Old Dominion University
ODU Digital Commons

Electrical & Computer Engineering Theses & Disssertations

Electrical & Computer Engineering

Summer 2007

Self-Assembly and Characterization of Germanium Quantum Dots on Silicon by Pulsed Laser Deposition

Mohammed S. Hegazy
Old Dominion University

Follow this and additional works at: https://digitalcommons.odu.edu/ece_etds

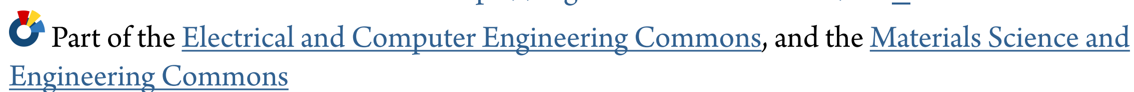
Part of the Electrical and Computer Engineering Commons, and the Materials Science and Engineering Commons

Recommended Citation
Hegazy, Mohammed S.. "Self-Assembly and Characterization of Germanium Quantum Dots on Silicon by Pulsed Laser Deposition" (2007). Doctor of Philosophy (PhD), dissertation, Electrical/Computer Engineering, Old Dominion University, DOI: 10.25777/6sr8-7f34
https://digitalcommons.odu.edu/ece_etds/75

This Dissertation is brought to you for free and open access by the Electrical & Computer Engineering at ODU Digital Commons. It has been accepted for inclusion in Electrical & Computer Engineering Theses & Disssertations by an authorized administrator of ODU Digital Commons. For more information, please contact digitalcommons@odu.edu.

SELF-ASSEMBLY AND CHARACTERIZATION OF Ge QUANTUM DOTS ON Si BY PULSED LASER DEPOSITION

By

Mohammed S. Hegazy
MS, Aug 2002, Old Dominion University
B.Sc., May 1997, Cairo University

A Dissertation Submitted to the Faculty of Old Dominion University in
Partial Fulfillment of the Requirement for the Degree of

DOCTOR OF PHILOSOPHY

ELECTRICAL ENGINEERING

OLD DOMINION UNIVERSITY

August 2007

Approved by:

Hani Elsayed-Ali (Director)

Sacharia Albin (Member)

Ravindra Joshi (Member)

Charles Sukenik (Member)

Reproduced with permission of the copyright owner. Further reproduction prohibited without permission.

ABSTRACT

SELF-ASSEMBLY AND CHARACTERIZATION OF Ge QUANTUM DOTS ON Si BY PULSED LASER DEPOSITION

Mohammed S. Hegazy
Old Dominion University, 2007
Director: Dr. Hani Elsayed-Ali

Self-assembled Ge quantum dots (QD) are grown on Si(100)-(2×1) by pulsed laser deposition (PLD). *In situ* reflection-high energy electron diffraction (RHEED) and post-deposition atomic force microscopy (AFM) are used to study the growth dynamics and morphology of the QDs. Several films of different thicknesses were grown at a substrate temperature of 400 °C using a Q-switched Nd:YAG laser (λ = 1064 nm, 40 ns pulse width, 23 J/cm^2 fluence, and 10 Hz repetition rate). At low film thicknesses, hut clusters that are faceted by different planes, depending on their height, are observed after the completion of the wetting layer. With increasing film thickness, the size of the clusters grows, and they gradually lose their facetation and become more rounded. With further thickness increase, the shape of these clusters becomes dome-like with some pyramids observed among the majority of domes. The effect of the laser fluence on the morphology of the grown clusters was studied. The cluster density was found to increase dramatically while the average cluster size decreased with the increase in the laser fluence. For a laser fluence of 70 J/cm^2, dome-shaped clusters that are smaller than the large huts formed at 23 J/cm^2 were observed. At a substrate temperature of 150 °C, misoriented three-dimensional (3D) clusters formed producing only a RHEED background. At 400 and 500 °C, huts and a lower density of domes formed, respectively. Above 600 °C, 3D clusters formed on top of a discontinuous textured layer.

Reproduced with permission of the copyright owner. Further reproduction prohibited without permission.

As an application, pulsed laser deposition is used to fabricate multilayered Ge quantum-dot photodetector on Si(100). Forty successive Ge quantum dot layers, each covered with a thin Si layer, were deposited. Deposition and growth are monitored by *in situ* reflection-high energy electron diffraction and the morphology is further studied by *ex situ* atomic force microscopy. The difference in the current values in dark and illumination conditions was used to measure the device sensitivity to radiation. Spectral responsivity measurements reveal a peak around 2 μm, with responsivity that increases three orders of magnitude as bias increases from 0.5 to 3.5 V.

The effects of laser-induced electronic excitations on the self-assembly of Ge quantum dots on Si(100)-2x1 grown by pulsed laser deposition are also studied. Electronic excitations, due to laser irradiation of the Si substrate and the Ge film during growth, are shown to decrease the roughness of films grown at a substrate temperature of ~120 °C. At this temperature, the grown films are nonepitaxial. However, electronic excitation results in the formation of an epitaxial wetting layer and crystalline Ge quantum dots at ~260 °C, a temperature at which no crystalline quantum dots form without excitation under the same deposition conditions.

Finally, the very early stages of formation of Ge hut clusters on Si(100) has been studied by UHV STM. Growth starts by the formation of a very low density of asymmetric huts with high aspect ratios. Further deposition results in a higher density of clusters characterized by their narrow size and height distributions. These clusters are almost of the same lateral size as those deposited at lower thicknesses.

Reproduced with permission of the copyright owner. Further reproduction prohibited without permission.

ACKNOWLEDGMENTS

I would like to present all kinds of gratitude and appreciation to my advisor, Dr. Hani Elsayed-Ali, for his help, guidance and direction for this research. Also, I would like to deeply thank Dr. Sacharia Albin (Electrical and Computer Engineering Department), Dr. Ravindra Joshi (Electrical and Computer Engineering Department), and Dr. Charles Sukenik (Physics Department) for kindly accepting to serve on my Ph.D. committee.

Appreciation should also go to my friends and laboratory mates Mohamed Hafez, Mohamed Zayed, Ibrahim Elkholy, Mohamed Moselhy, Ahmed Ismael, and Mahmoud Abdel-Fattah for their help and encouragement. Special thanks go to my friend Dr. Tamer Refaat for his cooperation, help, and support.

I would like to thank all of my family: my father, Dr. Samir Hegazy; mother, Fatmah Sheeha; brother, Islam Hegazy; and sisters, Faten and Eman Hegazy; back home in Egypt for their love, encouragement and support.

Finally, all kinds of love, regards, and appreciation should go to my wife, Doaa Teama; my daughter, Rawdah Hegazy; and my son, Ahmed Hegazy; for their continuing love and support and for their patience all the time, during which this work has been done.

Reproduced with permission of the copyright owner. Further reproduction prohibited without permission.

TABLE OF CONTENTS

LIST OF FIGURES viii

LIST OF TABLES xv

CHAPTER I. INTRODUCTION 1

- I.1. Introduction 1
- I.2. References 4

CHAPTER II. PULSED LASER DEPOSITION 9

- II.1. Introduction 9
- II.2. Laser ablation of matter 10
- II.3. Plume characteristics 14
- II.4. Particulates formation 18
- II.5. Pulsed laser deposition systems 20
- II.6. References 24

CHAPTER III. REFLECTION HIGH-ENERGY ELECTRON DIFFRACTION: THEORY AND EXPERIMENTAL CALCULATIONS 31

- III.1. Introduction 31
- III.2. RHEED setup and alternative 33
- III.3. RHEED Theories 35
  - III.3.A. Geometric model 35
  - III.3.B. Kinematical and dynamical model 38
- III.4. Transmission RHEED 45
- III.5. Some RHEED patterns 52
- III.6. Calculation of pure reflection RHEED patterns 54
  - III.6.A. Si(100) 54
  - III.6.B. Ge(100) 59
- III.7. Indexing transmission RHEED patterns 60
- III.8. References 65

CHAPTER IV. SELF-ASSEMBLY OF Ge QUANTUM DOTS ON Si 69

- IV.1. Introduction 69
- IV.2. Self-assembly of QD by Stranski-Krastanov (SK) growth 73
- IV.3. SK growth of Ge QD on Si 78
- IV.4. Experiment 79
- IV.5. Growth dynamics 81
- IV.6. Effect of laser fluence 95
- IV.7. Effect of substrate temperature 102
- IV.8. Conclusion 105

Reproduced with permission of the copyright owner. Further reproduction prohibited without permission.

IV.9. References 106

CHAPTER V. FABRICATION OF QUANTUM-DOT BASED INFRARED PHOTODETECTORS BY PULSED LASER DEPOSITION 114

V.1. Introduction 114
V.2. Theory of QDIP 116
V.3. Photodetector fabrication 121
V.4. Growth Characterization 123
V.5. Electrical and optical characterization 125
V.6. Conclusion 131
V.7. References 132

CHAPTER VI. NON-THERMAL LASER-INDUCED FORMATION OF CRYSTALLINE Ge QUANTUM DOTS ON Si(100) 135

VI.1. Introduction 135
VI.2. Electronic-induced bond breaking 138
VI.3. Experiment 142
VI.4. Results and discussion 145
VI.5. Conclusion 154
VI.6. References 155

CHAPTER VII. ULTRA HIGH VACUUM SCANNING TUNNELING MICROSCOPY STUDY OF PULSED LASER DEPOSITION OF Ge QD ON Si(100) 157

VII.1. Introduction 157
VII.2. Experiment 158
VII.3. Results and discussion 161
VII.4. Conclusion 172
VII.5. References 172

APPENDIX A. PULSED LASER DEPOSITION SYSTEM EQUIPPED WITH RHEED 174

A.1. System design and components 174
A.2. Pumping up and opening the system 175
A.3. Cleaning and changing the substrate 179
A.4. Changing the target 181
A.5. Pumping the system down and bakeout the system 182
A.6. Cleaning the Si(100) substrate to obtain the 2x1 reconstruction 184
A.7. RHEED gun schematics and operation 185
A.8. Nd:YAG laser operation 189

Reproduced with permission of the copyright owner. Further reproduction prohibited without permission.

APPENDIX B. PULSED LASER DEPOSITION SYSTEM EQUIPPED WITH SCANNING TUNNELING MICROSCOPE 193

B.1. System design and components 193
B.2. Pumping up and openıng the system 193
B.3. Changing the samples 195
B.4. Pumping the system down and bakeout the system 197
B.5. Cleaning the Si(100) substrate 200
B.6. Starting the STM and tip approach 201
B.7. Starting the STM scanning and data acquisition 206
B.8. Changing the tips 208

APPENDIX C. USEFUL CONTACT INFORMATION 209

VITA 210

Reproduced with permission of the copyright owner. Further reproduction prohibited without permission.

LIST OF FIGURES

Figure		Page
2.1	A schematic summarizing the thermal ablation of solid surfaces	11
2.2	Evolution of plume by laser ablation of solid materials: (a) before laser interaction, (b) laser absorption and surface temperature rise, (c) initial plume emission, (d-f) plume expansion as a function of time.	16
2.3	(a & b) The effect of laser pulse width on plume expansion: (a) fs pulses, (b) ns pulses. (c & d) The effect of laser fluence on plume expansion: (c) has more laser fluence then (d).	17
2.4	Mechanisms for formation of particulates: (a) splashing, (b) recoil pressure and (c) fracto-emission [After ref. 1].	18
2.5	A schematic diagram of the PLD system: (1) Target, (2) substrate (heated by direct current heating), (3) ablated species "Plume," (4) focused laser, (5) electron probe, (6) diffracted electrons, (7) electron gun, (8) phosphor screen, (9) CCD camera, (10) focusing lens, (11) ultrahigh vacuum chamber, (12) substrate manipulator, (13) target manipulator.	22
2.6	A schematic diagram of the PLD system equipped with UHV STM.	23
3.1	An illustration of the fundamentals of RHEED. The inset shows two kinds of reflection: transmission-reflection diffraction scattering by three-dimensional crystalline island (above) and surface scattering from flat surface (below).	32
3.2	RHEED sensitivity for surface structures and reconstructions. (a) Si(100)-1×1, (b) Si(100)-2×1 reconstructed surface.	33
3.3	Top view describing the origin of diffraction spots according to the geometrical model.	37
3.4	Comparison between (a) reflection diffraction from chemically cleaned Si(100) sample and (b) transmission-reflection diffraction pattern of Ge QD.	47
3.5	Different possibilities of transmission-reflection diffraction through thin crystals and the expected resulting diffraction patterns. (a) Transmission through high and wide crystal; (b) transmission through high and narrow crystal; (c) that through short and wide	48

Reproduced with permission of the copyright owner. Further reproduction prohibited without permission.

crystal; (d) diffraction from nearly flat asperities. [After ref. [9]].

3.6 IMFP of electrons in Ge as a function of electrons energy [Calculations are based on Ref. [24,25]]. 50

3.7 A schematic diagram represents the transmission-reflection geometry of RHEED. 51

3.8 Comparison of different reflection and transmission RHEED patterns and the originating surface structures. 53

3.9 (a) 3D illustration of the diamond structure of silicon showing its bonding structure, (b) sketch of the Si(100). [The free demonstration version of Crystal Maker[1] software was used to create both images]. 54

3.10 Real net of the Si(100). 55

3.11 Reciprocal net of Si(100). 56

3.12 A RHEED pattern for Si(100)-1×1 used to calculate the direction of incidence. 57

3.13 A RHEED pattern for Si(100)-2×1 used to calculate the average terrace width by calculating the splitting in the (00) peak. 58

3.14 Schematic of the vicinal surface used to calculate the miscut angle. 59

3.15 Expected XRD pattern of Ge crystal [The free demonstration version of Diamond software [36] was used to generate these data]. 61

3.16 Transmission RHEED pattern of Ge QD [obtained at 12 kV accelerating voltage]. 63

3.17 Indexed transmission pattern of Ge QD. 64

4.1 Schematic diagram of the density of states (DOS) for (a) 3D bulk semiconductor, (b) 2D quantum well, (c) 1D quantum wire, and (d) 0D quantum dot. 70

4.2 Schematics of the strain relief stages in the Stranski-Krastanov growth for the case of compressive strain: (a) Starting substrate, (b) growth of a psedumorphic smooth wetting layer, (b) formation of coherently strained 3D islands that are fully strained at the bottom and completely relaxed at the top, i.e. having the film lattice constant, (c) introduction of misfit dislocations in the 3D islands. 72

[1] CrystalMaker® : http:// www.crystalmaker.com

Reproduced with permission of the copyright owner. Further reproduction prohibited without permission.

The arrows indicate the direction of elastic strain relief.

4.3 RHEED patterns taken at different thicknesses for deposition at 400 °C, 23 J/cm^2, 10 Hz. Substrate (2×1) reconstruction pattern is shown in (a). Growth started epitaxially, as seen in the RHEED pattern taken after the deposition of ~3.3 ML shown in (b). At ~4.1 ML, (c), elongated transmission features with lines at the position of the second order streaks started to appear. In the pattern at ~6 ML, (d), the lines disappeared while the elongation of the transmission features increased. As the thickness was increased, the transmission features became well defined and the elongation decreased, as observed in (e) taken at ~9.3 ML. At ~13 ML, the transmission features became more round, (f). 81

4.4 Line profile measured along the (200)-(400) connecting line normal to the surface at different thicknesses. The transition from the elongated lines to sharp spots is shown. 83

4.5 3D AFM images of the clusters observed at different film thicknesses. Well-defined hut clusters observed at low thicknesses (a) and (b). As the film thickness was increased huts became more round (c) and (d). Some of these clusters grew into pyramids (e). The majority of clusters grew into domes (f). 88

4.6 Line scans performed across a couple of hut clusters, where the faceting angles are indicated. 89

4.7 Relation between major and minor lengths of the Ge QDs formed on Si(100)-2x1 at different film thicknesses. The solid line is the best fit to the data. 90

4.8 Lateral aspect ratio of clusters (major length/minor length) as a function of the minor length. The solid line is the best fit to the data. 91

4.9 Height of the QD as a function of both the major and minor lengths. Solid lines represent the best fits to the data. 92

4.10 Aspect ratio (major length/height) as a function of major length, fitted by the solid line 93

4.11 Contact angle that the bounding planes make with the substrate as a function of cluster's height. 94

4.12 RHEED patterns, AFM scans of three samples deposited at 400 °C, 10 Hz and column (a) 23 J/cm^2, column (b) 47 J/cm^2, column (c) 70 J/cm^2. 96

Reproduced with permission of the copyright owner. Further reproduction prohibited without permission.

4.13 3D AFM images of QDs corresponding to the 3 cases of the above figure and line scans along and across the clusters 97

4.14 Size distributions of the clusters formed on three different samples deposited at 400 °C, 10 Hz and column (a) 23 J/cm^2, column (b) 47 J/cm^2, column (c) 70 J/cm^2. The number of clusters in the scanned area, n, the average cluster size, d, the coverage ratio, θ, and the full width at half maximum FWHM of the distribution, f, are listed. 100

4.15 RHEED patterns of different samples ~9-ML thick deposited at 23 J/cm^2, 10 Hz and different substrate temperatures. 103

4.16 AFM scans corresponding to the samples of Fig. 5: (a) 150 °C, (b) 400 °C, (c) 500 °C, (d) 600 °C. 104

5.1 Structure of a typical QDIP, consisting of multilayers of QD sandwiched between the two heavily doped layers of emitter and collector. 115

5.2 Transitions in quantum confined heterostructures: (a) sub-band to sub-band, and (b) sub-band to continuum. 116

5.3 Schematics showing the operation principle of QDIP. 118

5.4 (Top) Side view schematics of the multi-layered Ge QD-based photodetector grown by PLD on Si(100). (Bottom) Top view schematics showing the film and the metal contacts. 122

5.5 (Left) RHEED diffraction pattern of the Si(100)-2×1 substrate. (Right) Transmission pattern formed when the growth of the first Ge QD layer is completed. 124

5.6 AFM scan of the Ge quantum dots. The major axis length distribution is shown as inset [scan area = 1.1×1.1 μm]. 124

5.7 Histogram showing the size distribution of the above figure. 125

5.8 A schematic of the detector characterization setup. 127

5.9 Dark current variation with bias voltage obtained at temperatures of 293.2, 283.2, 273.2, 263.2, 253.2, 160.0, 130.0 and 79.5 K from top to bottom, respectively. The inset shows a portion of the dark current at 293.2 K and it variation due to device illumination with 14.5 W/cm^2 radiation intensity. 128

5.10 Spectral response at different bias voltages, obtained at an operating temperature of 79.5 K. 130

Reproduced with permission of the copyright owner. Further reproduction prohibited without permission.

5.11	Measured and fitted noise variation with bias voltage and the corresponding detectivity (D*), obtained at an operating temperature of 79.5 K.	131
6.1	Summery of all possible results of the interaction of laser or electron beams with materials [From Ref. [6] with permission[2]].	136
6.2	Electron-hole pair generation due to laser absorption.	140
6.3	Side view of the atomic structure of Si(100)-2x1.	140
6.4	Electronic-induced bond breaking: (A) two-hole localization at first bond, (B) first bond breaking, (C) two-hole localization at second bond, (D) atom ejection due to a phonon kick.	141
6.5	Schematic of the laser excitation experimental setup.	143
6.6	Measurement of laser beam parameters: (a) laser pulse width, (b) ablation beam profile, and. (c) excitation beam profile.	144
6.7	RHEED patterns recorded at different deposition times for two samples deposited at ~120 °C by ablation laser energy density of 4.9 J/cm^2, and laser repetition rate of 50 Hz (a) under no laser excitation, (b) under 130±52 mJ/cm^2.	146
6.8	(a) RHEED patterns recorded at different deposition times for a sample grown under no laser excitation at temperature of ~260 °C by ablation laser energy density of 4.9 J/cm^2, and laser repetition rate of 50 Hz. (b) 3D STM image of the final film	147
6.9	(a) RHEED patterns recorded at different deposition times for the sample grown under excitation laser of 144±58 mJ/cm^2 at ~260 °C under laser ablation fluence 4.9 J/cm^2 and laser repetition rate of 50 Hz.	148
6.10	The ratio of the (111) peak intensity to the background intensity (measured between the (200) and the (111) peaks) as a function of deposition time.	149
6.11	The two assumed models for the ellipsometry thickness measurements.	150
6.12	STM images and cluster length distributions for samples grown ~260 °C under laser ablation fluence 4.9 J/cm^2 and laser repetition rate of 50 Hz under excitation laser fluence of (a) 144±58 mJ/cm^2 [d = 1.4x10^{11} cm^{-2}, CR = 10 & 15%], (b) 87±35 mJ/cm^2 [d = 1.7x10^{11} cm^{-2}, CR = 12%], (c) 50±20 mJ/cm^2 [d = 1.7x10^{11} cm^{-2}, CR = 31%].	152
7.1	Schematics showing the main components of the PLD deposition chamber equipped with Omicron UHV STM.	160

[2] The figure was redrawn and reorganized after the kind permission from both Dr. Stoneham and Dr. Itoh through personal communications.

Reproduced with permission of the copyright owner. Further reproduction prohibited without permission.

7.2 Main components inside the PLD chamber: (1) Ge target mounted on the target holder, (2) substrate holder equipped with direct heating, (3) ion gauge filament. 161

7.3 STM scans of the (a) Si substrate and of the Ge film after deposition of (b) 20 pulses, (c) 70 pulses, and (d) 220 pulses. The white lines show the locations of the line scans shown in Fig. 7.4. The lines marked x and y locate the locations of the line scans across the QD shown in Fig. 7.5. The square in (d) highlights the cluster shown in Fig. 7.6. 162

7.4 Line scans measured along the lines in Fig. 7.3. Lines (a), (b), (c), and (d) correspond to Fig. 7.3 (a), (b), (c), and (d), respectively. 163

7.5 Line scans measured along the lines marked x and y across the QD in Fig. 7.3 (c). 167

7.6 (a) The QD enclosed by the square in Fig. 7.3(d), (b) line scan across x, (b) line scan across y. 168

7.7 Aspect ratio, A, of the clusters in Fig. 7.3(d) as a function of their height, h. 169

7.8 Aspect ratio, A, of the clusters in Fig. 7.3(d) as a function of their major lengths, l_{maj}, (red circles) and minor lengths, l_{min}, (blue triangles). 169

7.9 Lateral aspect ratio, L, of the clusters in Fig. 7.3(d) as a function of their minor lengths, l_{min}. 170

7.10 Maximum faceting angle as a function of clusters' height. 170

7.11 (a) Major size histogram and (b) height histogram for the QD shown in Fig. 7.3(d). The most expected length, l_m, the most expected height, h_m, and both FWHM are indicated on the graphs. 171

A.1 Top view of the PLD system showing the main components: (1) target holder, (2) convectron gauge, (3) ion gauge, (4) phosphor screen, (5) sample (substrate) manipulator, and (6) RHEED gun. 174

A.2 Turbo pump with the vent valve highlighted by the circle. 176

A.3 Roughing mechanical pump. 176

A.4 Turbo pump controller: the circle highlights the ON/OFF button. 176

A.5 Ion pump controller: (1) ON/OFF button, (2) pressure, ionization current or voltage readout, (3) readout mode selector. 176

A.6 Butterfly valve manual control unit: clockwise closes, while anti-clockwise opens. 177

A.7 Right angle UHV valve. 177

A.8 Substrate holder: (1) direct heating current connector, (2) Thermocouple connector. 177

Reproduced with permission of the copyright owner. Further reproduction prohibited without permission.

A.9	The 8" flange holding the substrate manipulator.	178
A.10	Substrate manipulator: the circle highlights the direct current heated sample holder.	178
A.11	Direct current heated substrate holder.	178
A.12	Schematics showing the design of the directing heating substrate holder.	180
A.13	Magnetically rotated target holder.	181
A.14	Magnetically rotated target holder: (1) used Ge target, (2) magnetic shield.	182
A.15	Ion gauge controller: the circle highlights the mode selector.	184
A.16	Baking of the system by high power bulbs and covering the system by aluminum foil.	184
A.17	The home-made electron gun. (Top) back view showing the electrical connections. (Bottom) electron acceleration column. [A: anode, F: filament, N: ground, C: cup, X: x-deflector, Y: y-deflector, and U (the central connector): focus].	186
A.18	Electron gun control unit, including high voltage power supply, potential divider, X and Y deflectors.	187
A.19	Schematics of the high voltage potential divider.	188
A.20	Lumonics YAG Master (YM) 200 laser system.	190
A.21	External cooling water switch.	191
A.22	Mains power supply switch: (OFF) vertical position, (ON) horizontal position.	191
A.23	Local control unit.	192
B.1	Image of the PLD system equipped with UHV STM. (1) 48" magnetic transporter, (2) air compressor to controls the gate valve, (3) power supply to heat the substrate, (4) bellow to move the transporter in X and Y directions, (5) home-made target rotator mount on a Z-translator, (6) 12" spherical deposition chamber, (7) ion pump, (8) ion pump controller, (9) convectorn gauge, (10) turbo pump controller, (11) gate valve, (12) custom-made load lock, (13) Omicron bolt-on UHV STM chamber, (14) computer monitor to control the STM, (15) optics assembly to direct laser into the chamber, (16) shield to protect the system from the Nd:YAG laser.	194
B.2	Gate valve.	195
B.3	Right angle UHV valve connecting the deposition chamber to the STM chamber.	195

Reproduced with permission of the copyright owner. Further reproduction prohibited without permission.

B.4	8" flange on the load-lock	196
B.5	Tip/sample carousel in its housing in the UHV STM bolt-on.	196
B.6	Carousel outside the chamber	196
B.7	Directing heating sample holder.	196
B.8	Normal sample holder.	196
B.9	Tip holder.	196
B.10	(1) PPM, (2) connection to the Matrix control unit.	199
B.11	SPM preamplifier.	199
B.12	Bakeout short circuit plugs.	199
B.13	Right angle UHV valve connected to the deposition chamber.	199
B.14	Wobblestick.	200
B.15	Matrix power switch.	200
B.16	Communication is still in progress.	202
B.17	Communication is established.	202
A.18	Matrix software icon.	202
A.19	STM mode selection.	202
A.20	STM V-Spec mode selection, highlighted by the circle.	203
A.21	Matrix software interface.	203
A.22	Z regulation panel.	204
A.23	XY scanner control.	204
A.24	Matrix remote box.	204
A.25	Tip approaching the sample.	204

Reproduced with permission of the copyright owner. Further reproduction prohibited without permission.

LIST OF TABLES

Table		Page
3.1	Data extracted from Fig. 3.15 and the calculated interplaner distances, *d*, of the associated planes.	61
3.2	Interplaner distances calculated from the measurement of spot distances in Fig. 3.16.	64
3.3	Comparison of the calculated and measured values of angles between the index planes.	64
6.1	Summary of thickness monitor measurements, performed by placing the crystal at the location of the substrate at separate runs.	150
6.2	Summary of ellipsometry thickness measurements of three samples allowing for the variation of *n* and *k* from the bulk values.	151

Reproduced with permission of the copyright owner. Further reproduction prohibited without permission.

CHAPTER I

INTRODUCTION

I.1. Introduction

The study of the self-assembly and self-organization of nanostructures in heteroepitaxial systems is necessary for a fundamental understanding of the properties of reduced-size condensed matter systems and for the development of quantum dots (QD)-based devices [1,2]. From a basic physics point of view, Ge/Si is a model system for studying the growth dynamics of the Stranski-Krastanow (SK) mode. In such a system, growth starts by the formation of a two-dimensional (2D) wetting layer where the Ge film lattice constant adapts to that of the Si substrate [1,2]. However, due to the lattice mismatch of 4.2% between the film and the substrate, an elastic strain arises in the wetting layer, which increases linearly with the increase of the film thickness. When the thickness of the wetting layer reaches a critical value, which is estimated to be 4-6 monolayers (ML) (1 ML = 6.24×10^{14} atoms/cm^2), the film relieves its internal strain by three-dimensional (3D) nucleation [2].

The growth dynamics of Ge QDs on Si(100) was intensively studied for growth by molecular beam epitaxy (MBE) [3-8], chemical vapor deposition (CVD) [9,10], and liquid phase epitaxy (LPE) [11,12]. For the cases of MBE and CVD, 3D nucleation starts by the formation of {105}-faceted hut or pyramid clusters [2]. As the film coverage increases, multi-faceted domes, faceted by {113} and {102} planes, develop at the expense of the hut clusters. With further increase in thickness, large clusters or super-

Reproduced with permission of the copyright owner. Further reproduction prohibited without permission.

domes start to appear. The shape of the QDs depends on the deposition technique as well as the deposition conditions. When Sb was used as a surfactant in the MBE growth of Ge/Si(100), the initial island shape changed from {105}-faceted to {117}-faceted [13]. When Ge was grown by liquid phase epitaxy, {115}-faceted islands were first observed instead of the {105}-faceted ones. As the coverage was increased, {111}-faceted pyramids were formed [11,12]. However, detailed study of the growth of such a system by pulsed laser deposition was not presented before the current work.

PLD is a powerful technique for growing thin films from the vapor phase. A high power pulsed laser is focused onto a target of the material to be grown. As a result, a plume of vaporized material is emitted and then collected on the substrate. Among the interesting features of PLD are

(i) the high preservation of stoichiometry [15-17];

(ii) its adaptability to grow multicomponent or multilayered films [18,26];

(iii) the ability to grow a thin film out of any material regardless of its melting point;

(iv) the high energy of the ablated particles may have beneficial effects on film properties;

(v) PLD consists of periods of high deposition rate (on the microsecond time scale) followed by periods of no deposition (on the millisecond to the second time scale), allowing for surface relaxation that may lead to producing smoother films [19].

Reproduced with permission of the copyright owner. Further reproduction prohibited without permission.

The major drawbacks that delay its use in industry are the difficult techniques to achieve large area devices. However, some experimental recipes of producing large-area wafers by PLD have been reported [20,21].

From the application point of view, Ge QDs have interesting mid-infrared optical properties [22,23]. Therefore, they have been used in fabricating devices such as mid-infrared photodetectors [23-26], thermoelectric devices [27], and enhanced performance Si solar cells [28-30]. It was shown that the photoluminescence peak of a single Ge QD dot layer changes from 1.3 to 1.6 μm with increasing thickness from 5 to 9 ML [22]. Such wavelength tunability is one of the reasons behind the great interest in Ge QD-based devices. Generally, QD-based devices consist of tens of multilayers of doped or undoped QDs separated by spacing layers. Apparently, the first two features of PLD make it a strong candidate for growing multilayered devices. In this case, only targets of different materials in the desired stoichiometry and doping are required without the need for residual gases or doping sources. In order to design efficient Ge QD-based devices by PLD, a clear understanding of how to control their physical properties through controlling the deposition parameters is required. The physical parameters of QDs depend strongly on their shape and size distribution, while the device quantum efficiency is affected by the density and spatial distribution of the QDs. Besides the substrate temperature, laser parameters (fluence, repetition rate, and wavelength) are unique controlling parameters of PLD. The density and size distribution of QDs are mainly controlled both by the deposition rate and adatoms' kinetic energy, which affects surface diffusion [31]. In the case of PLD, adatom surface diffusion is controlled both by the substrate temperature and the laser fluence, while deposition rate is mainly controlled by

Reproduced with permission of the copyright owner. Further reproduction prohibited without permission.

the laser fluence and the repetition rate. The spatial distribution depends on the homogeneity of the atomic flux, which is governed by the laser fluence.

This dissertation is based on the journal publications [14,26,32-34] and is organized as follows. Chapter II presents an overview of PLD as a thin film deposition technique. The chapter also addresses the laser ablation of matter, the plume characteristics, and the problem of particular formation. Elements of reflection high-energy electron diffraction (RHEED), both theoretical and experimental, are discussed in chapter III. This chapter also contains detailed calculations of the Si(100) and Ge(100) reciprocal lattices and the indexing of the electron transmission pattern resulting from diffraction through the Ge QD formed by PLD. In chapter IV, the growth dynamics of the self-assembly of Ge QD on Si(100) by pulsed laser deposition is studied by in situ RHEED and ex situ AFM. The effects of the substrate temperature and laser on the growth dynamics and the morphology of the QD are studied. Chapter V presents the fabrication, by PLD, and the testing of a mid-infrared photodetector, consisting of layers of Ge QD embedded in successive layers of Si. In chapter VI, the effects of laser-induced electronic excitations on the self-assembly of Ge quantum dots on Si(100)-2x1 grown by pulsed laser deposition is discussed. Chapter VII presents an in situ UHV STM study on the initial formation of Ge QD huts grown by PLD on Si(100). Each chapter will be self-contained, having its own introduction, conclusion and list of references.

Reproduced with permission of the copyright owner. Further reproduction prohibited without permission.

I.2. References

[1] C. Teichert, "Self-organization of nanostructures in semiconductor heteroepitaxy," Phys. Rep. **365**, 335 – 432 (2002).

[2] B. Voigtländer, "Fundamental processes in Si/Si and Ge/Si epitaxy studied by scanning tunneling microscopy during growth," Surf. Sci. Rep. **43**, 127 – 254 (2001).

[3] V. Cimalla, K. Zekentes, and N. Vouroutzis, "Control of morphological transitions during heteroepitaxial island growth by reflection high-energy electron diffraction," Mater. Sci. Eng. B **88**, 186-190 (2002).

[4] I. Goldfarb, P. T. Hayden, J. H. G. Owen, and G. A. D. Briggs, "Nucleation of ``Hut" Pits and Clusters during Gas-Source Molecular-Beam Epitaxy of Ge/Si(001) in *In Situ* Scanning Tunnelng Microscopy," Phys. Rev. Lett. **78**, 3959-3962 (1997).

[5] Y.-W. Mo, D. E. Savage, B. S. Swartzentruber, M. G. Lagally, "Kinetic pathway in Stranski-Krastanov growth of Ge on Si(001)," Phys. Rev. Lett. **65**, 1020 (1990).

[6] A. I. Nikiforov, V. A. Cherepanov, O. P. Pchelyakov, A. V. Dvurechenskii, A. I. Yakimov, "In situ RHEED control of self-organized Ge quantum dots," Thin Solid Films **380**, 158-163 (2000).

[7] O. P. Pchelyakov, V. A. Markov, A. I. Nikiforov, and L. V. Sokolov, "Surface processes and phase diagrams in MBE growth of Si/Ge heterostuctures," Thin Solid Films **306**, 299-306 (1997).

[8] J. A. Floro, E. Chason, L.B. Freund, R. D. Twesten, R. Q. Hwang, and G. A. Lucadamo, "Novel SiGe Island Coarsening Kinetics: Ostwald Ripening and Elastic Interactions," Phys. Rev. B **59**, 1990 (1999).

Reproduced with permission of the copyright owner. Further reproduction prohibited without permission.

[9] T. I. Kamins, E. C. Carr, R. S. Williams, and S. J. Rosner, "Deposition of three-dimensional Ge islands on Si(001) by chemical vapor deposition at atmospheric and reduced pressures," J. Appl. Phys. **81**, 211 (1997).

[10] P. S. Chen, Z. Pei, Y. H. Peng, S. W. Lee, M.-J. Tsai, "Boron mediation on the growth of Ge quantum dots on Si(10 0) by ultra high vacuum chemical vapor deposition," Mater. Sci. Eng. B **108**, 213 (2004).

[11] M. Schmidbauer, T. Weibach, H. Raidt, M. Hanke, R. Köhler, H. Wawre, "Ordering of self-assembled $Si_{1-x}Ge_x$ islands studied by grazing incidence small-angle x-ray scattering and atomic force microscopy," Phys. Rev. B **58**, 10523-10531 (1998).

[12] W. Dorsch, S. Christiansen, M. Albrecht, P. O. Hansson, E. Bauser, and H. P. Strunk, "Early growth stages of Ge 0. 85 Si 0. 15 on Si (001) from Bi solution," Surf. Sci. **331–333**, 896 (1995).

[13] M. Horn-von Hoegen, B. H. Müller, A. Al Falou, M. Henzler, "Surfactant induced reversible changes of surface morphology," Phys. Rev. Lett. **71**, 3170 (1993).

[14] M. S. Hegazy and H. E. Elsayed-Ali, "Self-assembly of Ge quantum dots on Si(100) by pulsed laser deposition," Appl. Phys. Lett. 86, 243204 (2005). [Selected to appear on the Virtual Journal of Nanoscience and Technology, Vol. 11(24) (2005)].

[15] B. Dam, J. Rector, M. F. Chang, S. Kars, D. G. de Groot, and R. Griessen, "Laser ablation threshold of $YBa_2Cu_3O_{6+x}$" Appl. Phys. Lett. 65, 1581-1583 (1994).

[16] Y. Iijima, K. Kakimoto, and T Saitoh, "Fabrication and transport characteristics of long length Y-123 coated conductors processed by IBA and PLD," IEEE Trans. Appl. Supercon. **13**, 2466-2469 (2003).

Reproduced with permission of the copyright owner. Further reproduction prohibited without permission.

[17] J. C. Nie, H. Yamasaki, H. Yamada, K. Develos-Bagarinao, Y. Nakagawa and Y. Mawatari, "Improvements in the microstructure of $YBa_2Cu_3O_{7-\delta}$ films on sapphire with self-assembled CeO_2 buffer layers," Physica C **412-414**, 1272-1276 (2004).

[18] A. Ohtomo and A. Tsukazaki, "Pulsed laser deposition of thin films and superlattices based on ZnO," Semicond. Sci. Technol. **20**, S1-S12 (2005).

[19] P. P. Pronko, Z. Zhang, and P. A. VanRompay, "Critical density effects in femtosecond ablation plasmas and consequences for high intensity pulsed laser deposition," Appl. Surf. Sci. 208-209, 492-501 (2003).

[20] M. Lorenz, H. Hochmuth, D. Natusch, M. Kusunoki, V. L. Svetchnikov, V. Riede, I. Stanca, G. Kästner, and D. Hesse, "High-quality Y-Ba-Cu-O thin films by PLD-ready for market applications," IEEE Trans. Appl. Supercond. **11**, 3209-3212 (2001).

[21] B. Schey, T. Bollmeier, M. Kuhn, W. Biegel, and B. Stritzker, "Large area deposition of $YBa_2Cu_3O_{7-x}$ films by pulsed laser ablation, Rev. Sci. Inst. 69, 474-476 (1998).

[22] K K. Brunner, "Si/Ge nanostructures," Rep. Prog. Phys. **65**, 27-72 (2002).

[23] V. A. Egorov, G. É. Cirlin, A. A. Tonkikh, V. G. Talalaev, A. G. Makarov, N. N. Ledentosov, V. M. Ustinov, N. D. Zakharov, and P. Werner, "Si/Ge nanostructures for optoelectronics applications," Phys. Solid State **46**, 49-55 (2004).

[24] A. Elfving, G. V. Hansson, and W.-X. Ni, "SiGe (Ge-dot) heterojunction phototransistors for efficient light detection at 1.3-1.55 μm," Physica E **16**, 528 (2003).

[25] M. Elkurdi, P. Boucaud, S. Sauvage, G. Fishman, O. Kermarrec, Y. Campidelli, D. Bensahel, G. Saint-Girons, G. Patriarche, I. Sagnes, "Electromodulation of the interband

Reproduced with permission of the copyright owner. Further reproduction prohibited without permission.

and intraband absorption of Ge/Si self-assembled islands," Physica E 16, 450-454 (2003).

[26] M. S. Hegazy, T. F. Refaat, M. Nurul Abedin, H. E. Elsayed-Ali, "Fabrication of GeSi quantum dot infrared photodetector by pulsed laser deposition," Opt. Eng. **44**, 59702 (2005).

[27] J. L. Liu, A. Khitun, K. L. Wang, T. Borca-Tasciuc, W. L. Liu, G. Chen, and D. P. Yu, "Growth of Ge quantum dot superlattices for thermoelectric applications," J. Cryst. Growth **227-228**, 1111-1115 (2001).

[28] A. Alguno, N. Usami, T. Ujihara, K. Fujiwara, G. Sazaki, K. Nakajima, and Y. Shiraki, Appl. Phys. Lett. **83**, 1258 (2003).

[29] H. Presting, J. Konle, H. Kibbel, and F. Banhart, "Growth studies of Ge-islands for enhanced performance of thin film solar cells," Physica E 14, 249-254 (2002).

[30] J. Knole, H. Presting, H. Kibbel, Physica E **16**, 596 (2003).

[31] B. Hinnemann, H. Hinrichsen, and D. E. Wolf, "Unusual Scaling for Pulsed Laser Deposition," Phys. Rev. Lett. **87**, 135701 (2001).

[32] M. S. Hegazy and H. E. Elsayed-Ali, "Non-thermal laser induced formation of crystalline Ge quantum dots on Si(100)," Phys. Rev. Lett., *submitted.*

[33] M. S. Hegazy and H. E. Elsayed-Ali, "Quantum-dot infrared photodetector fabrication by pulsed laser deposition technique," J. Laser Micro/Nanoengineering **1**(2), 111 (2006).

[34] M. S. Hegazy and H. E. Elsayed-Ali, "Growth of Ge quantum dots on Si by pulsed laser deposition," J. Appl. Phys. 99, 054308 (2006) [Selected to appear on the Virtual Journal of Nanoscience and Technology, Vol. 13(11) (2006)].

Reproduced with permission of the copyright owner. Further reproduction prohibited without permission.

CHAPTER II

PULSED LASER DEPOSITION

II.1. Introduction

Pulsed laser deposition (PLD) is a powerful technique for growing thin films from the vapor phase. In PLD, a high-power pulsed laser beam is focused onto a target of the material to be grown. As a result, a plume of vaporized materials (atoms, ions, molten droplets and even particulates) is emitted and then deposited on the substrate to grow the film [1,2]. PLD has proved to be a powerful technique for growing high quality films of superconductors [3-6], magnetoresistant materials [7-10], semiconductors [11-15], ferroelectrics [16-19] and many others. The following are some of the unique and interesting features of PLD:

(1) Conceptually, it could be used to grow a thin film out of any material, regardless of its melting point.

(2) In most systems, the stoichiometry of the grown film is highly preserved [20-21].

(3) The high energy of the ablated particles may have beneficial effects on the film properties. Each type of the different emitted species has an energy distribution depending on the nature of its particles. Generally, the average energy increases as the laser fluence increases; however, such dependence is not yet fully understood. The energy could range from <0.1 eV for neutrals thermally desorbed at low fluences to 1 keV for ions emitted at higher fluences [22-24].

Reproduced with permission of the copyright owner. Further reproduction prohibited without permission.

(4) It could be easily employed to grow multicomponent/multilayer films and devices [25,26] as will be demonstrated in chapter VI.

(5) Most importantly, it consists of periods of high deposition rates (1-20 μs) followed by periods of no deposition (on the millisecond or the second scale), allowing for surface relaxation that may lead to enhancement of the properties of the grown film [27].

II.2. Laser Ablation of Matter

Materials ablation by lasers falls on a continuum between two extremes: thermal and non-thermal ablations. In thermal ablation, laser photons are absorbed and the resulting heat melts and vaporizes the material. For metal targets, laser absorption by free electrons takes place via an inverse Bremsstrahlung mechanism. Thermalization of these hot electrons takes place through (i) heat transport into the bulk by thermal diffusion and (ii) electron-phonon coupling by transferring their energy to the lattice, Fig. 2.1. The main parameters of interest in such an absorption mechanism are the peak surface temperature and the volume of the heated region, both of which are governed by the optical properties (reflectivity, R, and absorption coefficient, α), the thermal properties of the target (specific heat, C, the vaporization energy, and thermal conductivity, K), and the laser peak intensity, I_p. The rise in the substrate temperature, ΔT, is calculated using the heat diffusion equation:

Reproduced with permission of the copyright owner. Further reproduction prohibited without permission.

$$\rho C \frac{\Delta T(z,t)}{\Delta t} = K \frac{\Delta T(z_0 + \Delta z) - \Delta T(z_0)}{(\Delta z)^2} + (1-R)\alpha I_p \exp[-\alpha z].\exp[-\frac{t^2}{\tau^2}], \tag{2.1}$$

with

$$\tau = \frac{\tau_{FWHM}}{\sqrt{(4*\log(2)}}, \tag{2.2}$$

where τ_{FWHM} is the FWHM of the laser pulse. Ablation takes place when the laser energy dumped into the system exceeds a certain threshold to melt and vaporize the target.

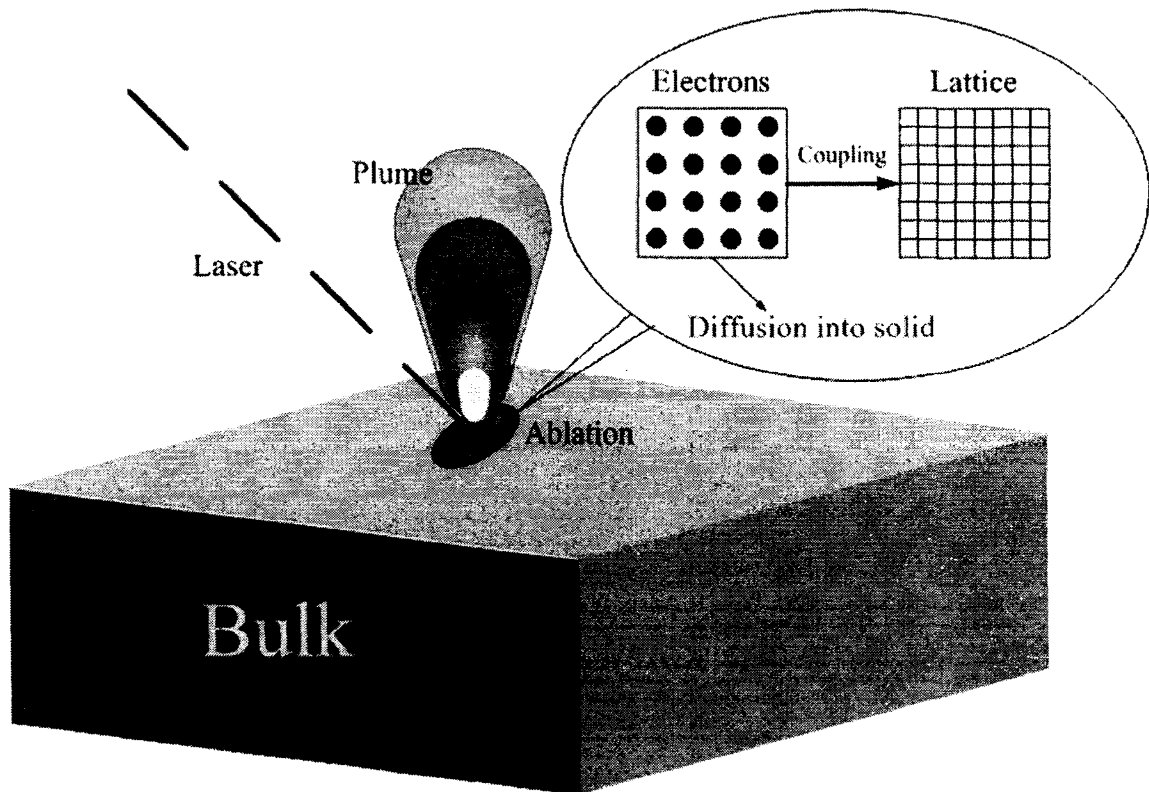

FIG. 2.1. A schematic summarizing the thermal ablation of solid surfaces

Reproduced with permission of the copyright owner. Further reproduction prohibited without permission.

In the other extreme, non-thermal ablation takes place by a variety of ways, depending on the properties of the laser and those of the substrate. Examples of the non-thermal ablation processes are:

(1) Desorption induced by electronic transitions (DIET): Photon absorption takes place by valance electrons, which causes their excitation into anti-bonding states. This results in the emission of atoms, molecules and ions [28,29].

(2) Collisional sputtering: This is an indirect process, in which plasma formed by laser interaction with mater bombards and sputters the surface of the material [30].

(3) Hydrodynamic sputtering: In this process, the target's surface is melted by the laser energy forming small droplets. Pressure waves caused by the motion of the liquid in the surface result in the ejection of such droplets from the surface [31,32].

(4) Fracto-emission: In this case, particles are emitted from freshly fractured surfaces by thermal or mechanical stresses [33].

These non-thermal processes, however, could not completely explain the ablation of matter by ultrafast lasers, e.g., femtosecond lasers. This is why this point currently receives a lot of attention. The important parameters determining the effect of the laser pulse length on the ablation process include: the heat diffusivity of the material, velocity of sound and the time scale for electron-electron thermalization and electron-phonon coupling, which was shown to be on the order of ~1 picosecond [34]. The important thermal processes, which occur in laser ablation, have been shown to be greatly modified once the laser pulses are shortened to a picosecond or femtosecond time scale [35,36].

Reproduced with permission of the copyright owner. Further reproduction prohibited without permission.

Due to their better spatial concentration compared to ns pulses, ultrashort (ps and fs) laser pulses decrease the required laser (threshold) fluence for ablation, increase the thermal gradient in the target, decrease the amount of energy lost to plasma and increase energy coupling to vaporize rather than melt the target. A time-resolved microscopic study showed that the actual ablation by ultrashort lasers takes much longer than the thermalization of the absorbed laser energy [37]. The same study showed that ablation of metals and semiconductors by ps and fs laser pulses occurs on the nanosecond time scale [37].

It is commonly assumed that the ablation process near the threshold is always initiated by the ultrafast melting of the material. However, a recent study on femtosecond laser ablation of silicon reported the occurrence of several physical processes, depending on the laser fluence [38]. These are, arranged in ascendant fluence order, oxidation, amorphization, re-crystallization, formation of bubbles due to boiling below the surface and ablation [38]. Another study on the physics of the fs laser ablation of wide band-gap materials reported two different ablation phases: a gentle phase with low ablation rates and a strong (etch) phase characterized by higher ablation rates but accompanied by a reduction of the degree of ionization [39]. Despite the large number of publications on the ablation of materials by ultrafast lasers, a lot of information is still missing in order to fully understand the physics involved in such a process.

Reproduced with permission of the copyright owner. Further reproduction prohibited without permission.

II.3. Plume characteristics

Exploring the nature of the plume and its dependence on the properties of the ablating laser is important in order to understand how to control the growth of thin films by PLD. A schematic diagram showing the steps of the plume evolution is shown in Fig. 2.2. Extensive theoretical and experimental work is being performed in order to study all the characteristics of the plume. Among these important characteristics are:

i) **Plume expansion**: This refers to the spatial expansion of the ablated species as a function of time. It is found to depend on the parameters of the ablating laser (wavelength, pulse width and fluence) [40], target material and ambient pressure. The effects of laser pulse width and fluence are outlined in Fig. 2.3. Regarding the laser pulse width, it was shown that fs lasers result in plumes with less lateral expansion (or more forward-directed) than those generated by the ns lasers [41], Fig(s). 2.3(a) and 2.3(b). However, increasing the laser fluence results in sharpening of the plume due to the interaction between the ablated particles [42], Figs. 2.3(c) and 2.3(d). Another interesting study showed that the plume sharpness increases with the target's atomic mass [43]. The plume angular dependence was shown to have the form

$$\frac{dN}{d\Omega} = a\cos\phi + b\cos^n\phi \tag{2.3}$$

where a, b, and n are material dependents, leading to film thickness variation of the form $\cos^n\theta$ with $n = 3k^2$ [43,44].

ii) **Energy (velocity) distributions**: It is understood that the ablated species are emitted with very high kinetic energies, ranging between 0.1-1000 eV. Each

Reproduced with permission of the copyright owner. Further reproduction prohibited without permission.

of the emitted species has its own energy (or velocity) distribution. Such distributions depend on the laser's fluence and pulse width as well as the target material itself. Regarding the pulse width, ablation by femtosecond pulses results in the ejection of highly energetic particles with velocities that can be an order of magnitude higher than those ablated in the nanosecond regime [41]. As for the laser fluence, its increase results in the increase of the ablated particles' mean velocities [45]. Depending on the laser fluence the composition of the plume changes significantly, since it can contain fine clusters when the applied laser fluence is much higher than the ablation threshold. Furthermore, depending on the composition and density of the plume, the velocity distribution can be described by a one-temperature shifted Maxwell–Boltzmann function or a two-temperature (parallel and perpendicular) distribution [46].

iii) **Effect of background (ambient) gas**: The velocities of the ablated species and the expansion dynamics strongly depend on the type and pressure of the background gas [41,47]. For example, the width of the angular distribution of Ag ions was found to increase with the Ar background pressure. On the other hand, in a He background the plume first narrows for a certain pressure range before it widens for higher pressures [47]. It was also shown that the length of the plume shortens when the ambient pressure is increased [48].

Reproduced with permission of the copyright owner. Further reproduction prohibited without permission.

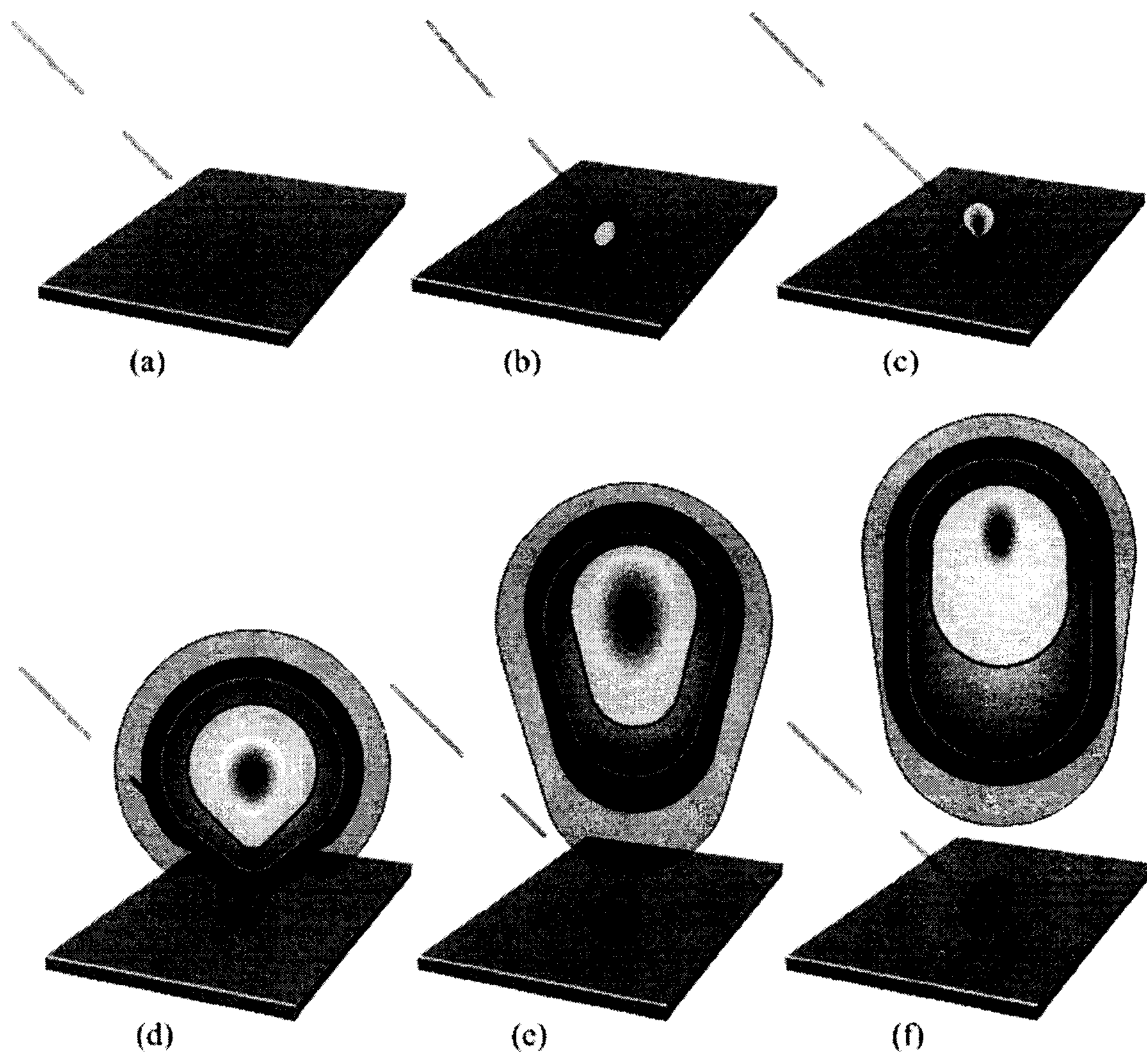

FIG. 2.2. Evolution of plume by laser ablation of solid materials: (a) before laser interaction, (b) laser absorption and surface temperature rise, (c) initial plume emission, (d-f) plume expansion as a function of time.

Reproduced with permission of the copyright owner. Further reproduction prohibited without permission.

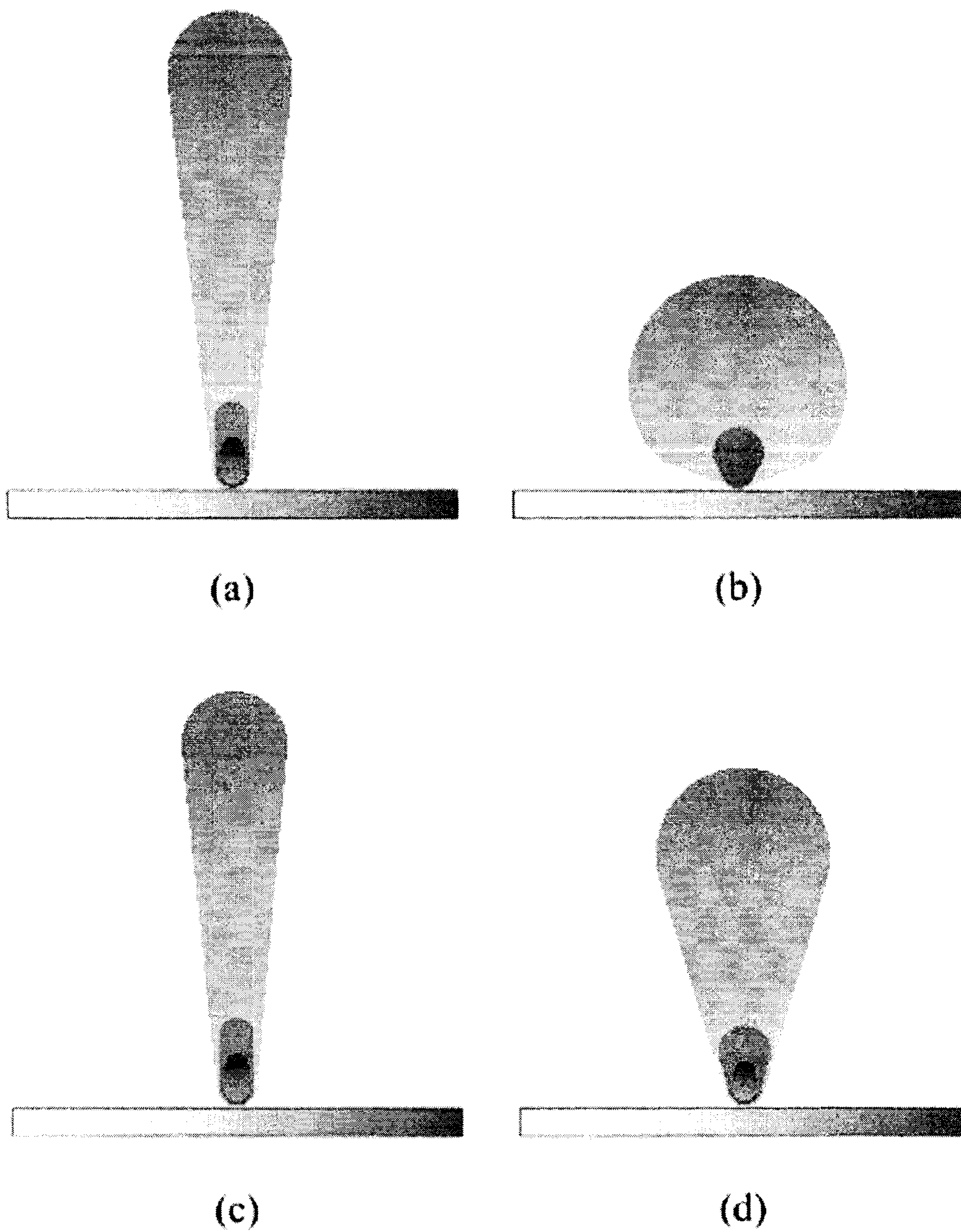

FIG. 2.3. (a & b) The effect of laser pulse width on plume expansion: (a) fs pulses, (b) ns pulses. (c & d) The effect of laser fluence on plume expansion: (c) has more laser fluence then (d)

Reproduced with permission of the copyright owner. Further reproduction prohibited without permission.

II.4. Particulates Formation

Despite its simplicity, PLD has some complications. The most challenging (and the most interesting, too, from a physics point of view) is the formation of particulates due to splashing of the molten surface layer. Their dimensions range from sub-micron to several micrometers [49]. Their crystallinity may vary as well; for example, for laser ablation of amorphous Si by ps YAG laser, both crystalline and amorphous particulates have been observed [50].

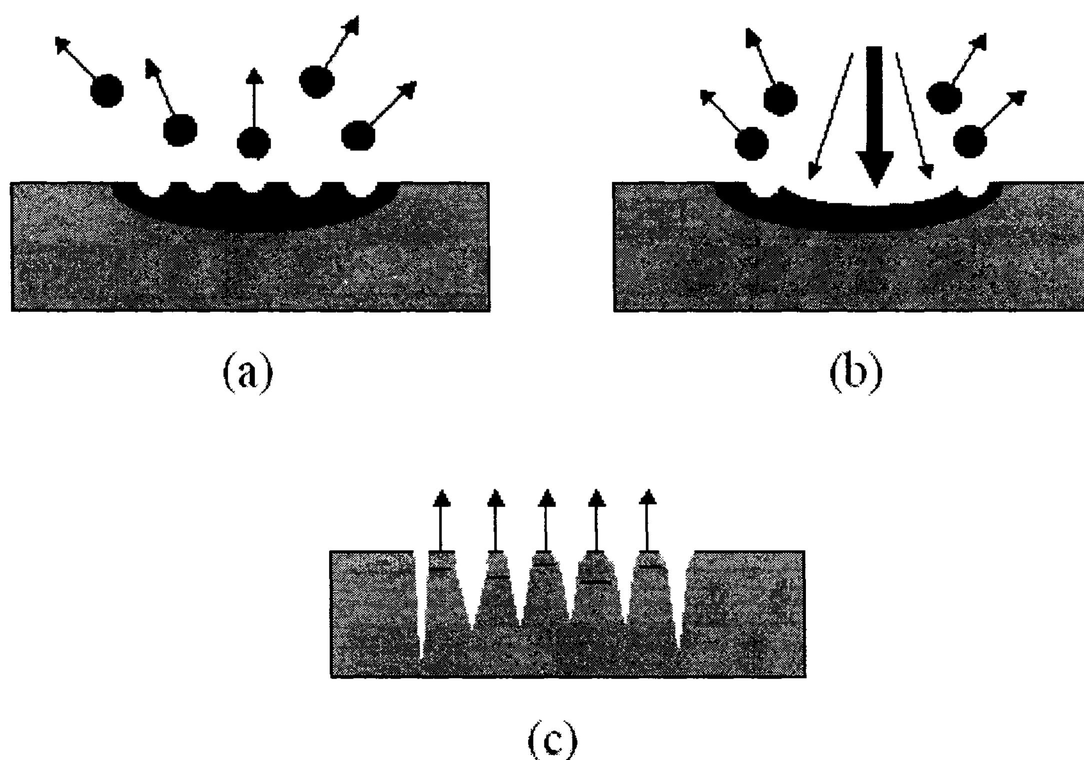

FIG. 2.4. Mechanisms for formation of particulates: (a) splashing, (b) recoil pressure and (c) fracto-emission [After ref. 1].

Reproduced with permission of the copyright owner. Further reproduction prohibited without permission.

Three mechanisms for forming particulates (splashing, recoil pressure and fracto-emission) are shown in Fig. 2.4. In splashing, a thin layer of the surface superheats above the vaporization temperature and a molten overlayer is blown off and disintegrates into liquid droplets [51-53]. However, in recoil pressure, vaporized materials exert some sort of pressure on the molten layer, formed by laser irradiation, and as a result liquid droplets are ejected [54]. Lastly, fracto-emission is the process in which emission from the microcracks in the target is caused by laser-induced thermal shocks [33].

Some mechanical filters have been used to prevent particulates from reaching the substrate; however, none of them could be considered as a universal solution for such problem. Particulates formation is affected by a number of parameters:

(1) Target density: increasing the target density can minimize the formation of particulates [55].

(2) Laser pulse duration and repetition rate: using ultrashort (fs and ps) lasers minimizes or eliminates particulates formation due to the lower thermal losses compared to the ns pulses, which causes a smaller amount of molten material and liquid droplets in the plume [56-58].

(3) Target surface quality: the probability of fractures emission from rough surfaces is quite high. Therefore, using rotated polished targets minimizes the particulates formation by expositing fresh target areas to laser all the time.

(4) Laser wavelength: YBC and BiSrCaCuO films deposited with 1.064 μm were rough in contrast to the smoother ones deposited with UV wavelengths [49,59]. However, the wavelength that yields the best film morphology depends on the target material.

Reproduced with permission of the copyright owner. Further reproduction prohibited without permission.

(5) Laser fluence: generally the particulates formation increases with the laser fluence. Particulate-free $CaZrO_3$ films were prepared by 0.64 J/cm^2 fluence, while SEM showed some particulates for those prepared with the same laser but with 16 J/cm^2 fluence [60].

II.5. Pulsed Laser Deposition Systems

Two PLD systems have been designed and assembled for the current research. A schematic diagram of the first system is shown in Fig. 2.5. An ultrahigh vacuum stainless steel chamber is used for deposition. With the aid of both turbo-molecular (Varian, 70 L/s) and ion (Perkin-Elmer, 300 l/s) pumps, a pressure of $\sim 5\times10^{-9}$ Torr can be reached without backing. If the system is backed, a base pressure of $<1\times10^{-10}$ Torr could be reached. A convectron (reading from 760 Torr down to 1×10^{-3} Torr) and an ion gauge (measuring from 1×10^{-3} Torr down to 1×10^{-11} Torr) are used to monitor the pressure at the different pressure ranges. A "homemade" sample holder, which is used to mount the substrate, was designed to heat the sample by means of direct heating, so that very high temperatures could be easily reached. The substrate holder is mounted on a manipulator (on a 4.5-inch conflat flange), which enables the azimuthial rotation of the sample by 360° and the adjustment of the sample-target distance. The target is mounted on an electrically rotated sample holder with a variable rotation speed. The rotation of the target minimizes the formation of particulates by exposing a fresh area to the laser all the time; thus, the probability of fracto-emission is minimized. The system is designed so that the

Reproduced with permission of the copyright owner. Further reproduction prohibited without permission.

laser, which enters the system through a 2.5-inch sapphire window, hits the target at ~ 45°. To monitor deposition, a CW-electron gun (Varian, mounted on 4.5-inch conflat flange) is used. An 8-inch phosphor screen is used to show the electron diffraction pattern, which is recorded by a CCD camera and later analyzed by image analysis software. A nanosecond Nd:YAG laser (Lumonics, 30-ns, 1064-nm and 1-1000 Hz) is used to ablate the Ge targets. More technical details of such a system are found in Appendix A.

The second PLD system is equipped with an *in situ* UHV STM. A schematic diagram of such a system is shown in Fig. 2.6. The system consists of an evaporation chamber, in which thin films could be grown by PLD or MBE. Film growth could be monitored by *in situ* RHEED. The chamber is pumped down to UHV via a roughing pump (Varian), a turbo pump (Varian, 70 l/s) and an ion pump (Varian, 300 l/s). This chamber is connected to a commercial UHV SPM (Omicron VT SPM) chamber via a custom-made load-lock and a gate valve. Samples are transferred between the two chambers by means of a magnetic transporter and a wobble stick. The magnetic transporter also serves as a manipulator that holds the sample holder, which is equipped with both resistive heating and direct heating mechanisms. For the case of PLD, the target is inserted from the top, while the laser beam enters the chamber from the bottom to ablate the target at an incident angle of ~45°. The target is mounted on an electrically rotated sample holder with a variable rotation speed. The nanosecond Nd:YAG laser (Lumonics, 30-ns, 1064-nm and 1-1000 Hz) is also used to ablate the Ge targets. More technical details of the system are found in appendix B.

Reproduced with permission of the copyright owner. Further reproduction prohibited without permission.

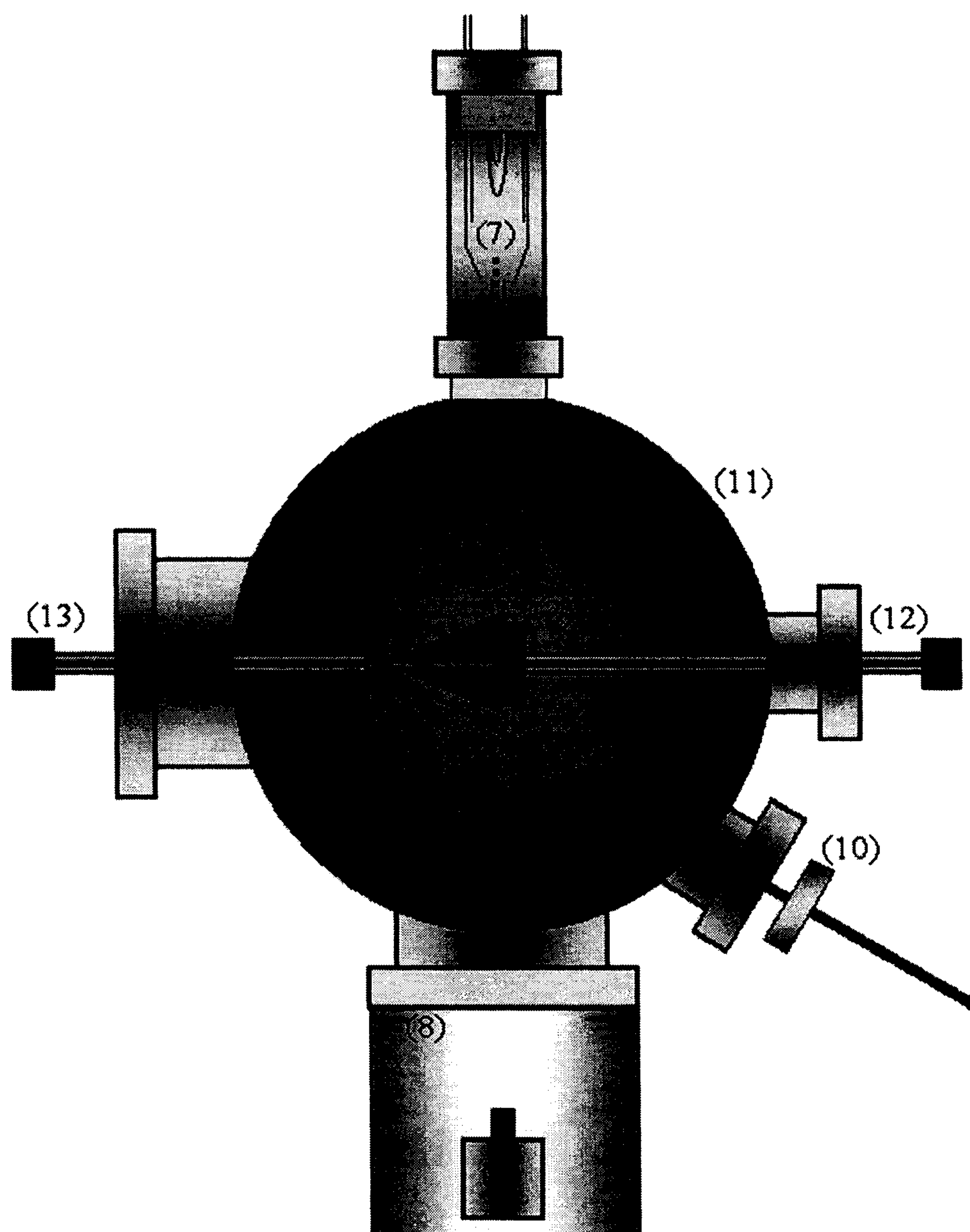

FIG. 2.5. A schematic diagram of the PLD system: (1) Target, (2) substrate (heated by direct current heating), (3) ablated species "Plume," (4) focused laser, (5) electron probe, (6) diffracted electrons, (7) electron gun, (8) phosphor screen, (9) CCD camera, (10) focusing lens, (11) ultrahigh vacuum chamber, (12) substrate manipulator, (13) target manipulator.

Reproduced with permission of the copyright owner. Further reproduction prohibited without permission.

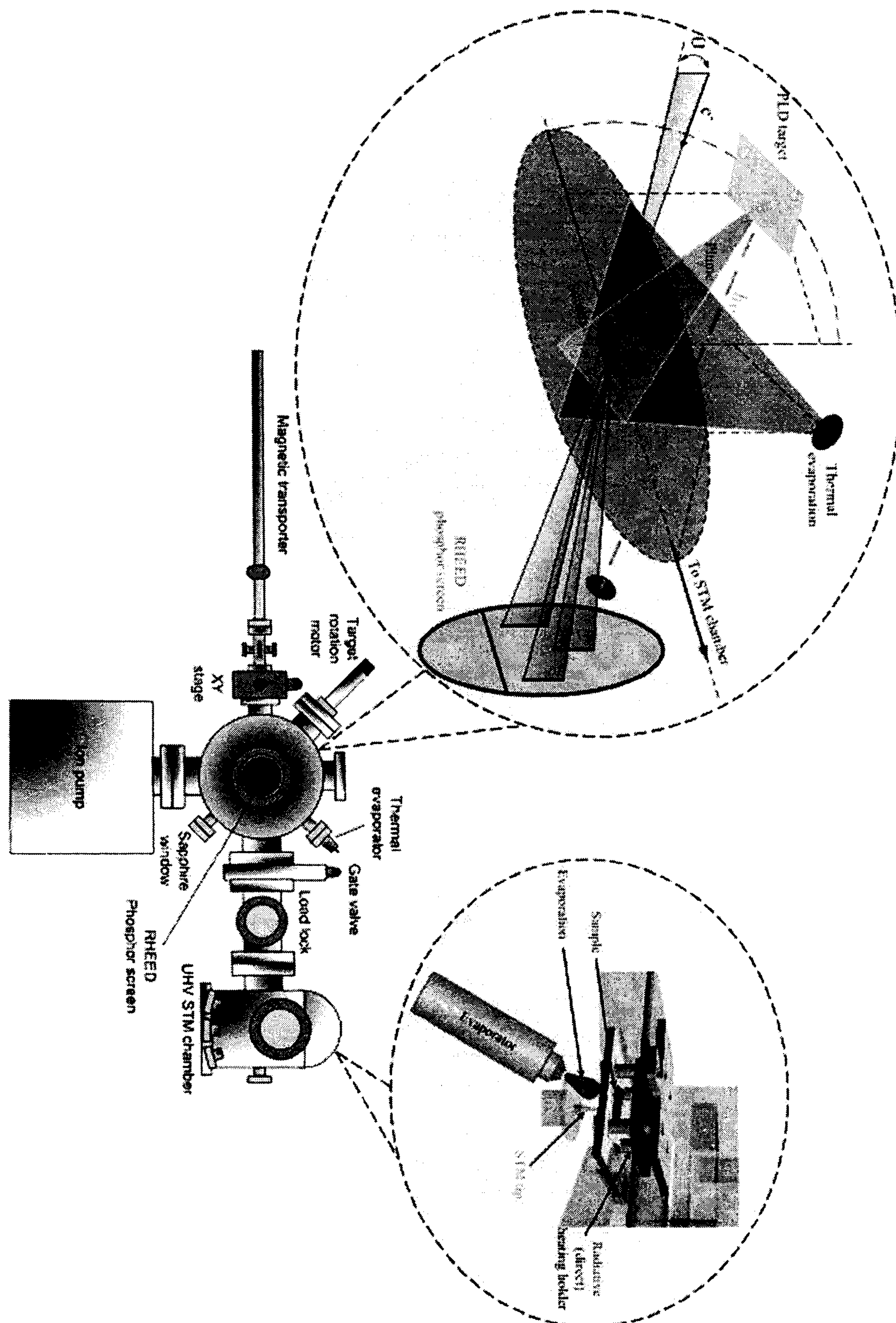

FIG. 2.6. A schematic diagram of the PLD system equipped with UHV STM.

Reproduced with permission of the copyright owner. Further reproduction prohibited without permission.

II.6. References

[1] K. L. Saenger, "Pulsed laser deposition Part I: A review of process characteristics and capabilities," Proc. Adv. Mat. **2**, 1-24 (1993).

[2] D. B. Chrisey and G. K. Hubler, editors, Pulsed laser deposition of thin films, Wiley, New York (1994).

[3] J. Schubert, M. Siegert, M. Fardmanesh, W. Zander, M. Prömpers, Ch. Buchal, Judit Lisoni, and C. H. Lei, "Superconducting and electro-optical thin films prepared by pulsed laser deposition technique," Appl. Surf. Sci. **168**, 208- 214 (2000).

[4] C-S. Kim, S. C. Song, and S. Yeol Lee, "Fabrication of novel 22 GHz hairpin type HTS micrpstrip filter using laser ablated thin films, Appl. Surf. Sci. **168**, 316- 319 (2000).

[5] P. Mele, K. Matsumoto, T. Horide, O. Miura, A. Ichinose, M. Mukaida, Y. Yoshida and S. Horii, "Tuning of the critical current in YBa2Cu3O7−*x* thin films by controlling the size and density of Y2O3 nanoislands on annealed SrTiO3 substrates," Supercond. Sci. Technol. **19**, 44–50 (2006).

[6] P. Badica, K. Togano, S. Awaji and K.Watanabe, "Growth of superconducting MgB2 films by pulsed-laser deposition using a Nd–YAG laser," Supercond. Sci. Technol. **19**, 242–246 (2006).

[7] A. Venimadhav, M. S. Hegde, R. Rawat, I. Das and M. El Marssi, "Enhancement of magnetoresistance in $La_{0.67}Ca_{0.33}MnO_3/Pr_{0.7}Ca_{0.3}MnO_3$ epitaxial multilayers," J. Alloys and Compounds 326, 270- 274 (2001).

[8] J. -M. Liu, Q. Huang, J. Li, C. K. Ong, X. Y. Chen, Z. G. Liu and Y. W. Du, "Low-field magneto-transport property of $La_{0.5}Sr_{0.5}MnO_3$ thin films deposited at low temperature by laser ablation," Mat. Lett. 50, 97- 102 (2001).

Reproduced with permission of the copyright owner. Further reproduction prohibited without permission.

[9] J. Miao, H. Yang, W. Hao, J. Yuan, B. Xu, X. Q. Qiu, L. X. Cao and B R Zhao, "Temperature dependence of the ferroelectric and dielectric properties of the Ba0.5Sr0.5TiO3/La0.67Sr0.33MnO3 heterostructure," J. Phys. D: Appl. Phys. **38**, 5–11 (2005).

[10] V. Ruckenbauer, F. F. Hau, S. G. Lu, K. M. Yeung, C. L. Mak, K. H. Wong, "Characteristics of BaxSr1–xTiO3 thin films grown by pulsed laser ablation of rotating split targets of BaTiO3 and SrTiO3," Appl. Phys. A 78, 1049–1052 (2004)

[11] J. Ohta, H. Fujioka, H. Takahashi, M. Sumiya and M. Oshima, "RHEED and XPS study of GaN on Si(1 1 1) grown by pulsed laser deposition," J. Crystal Growth 233, 779-784 (2001).

[12] M. Cazzanelli, D. Cole, J. Versluijs, J. F. Donegan and J. G. Lunney, "Pulsed laser deposition of GaN thin films," Mat. Sci. Eng. B 59, 89- 103 (1999).

[13] C. M. Rouleau and D. H. Lowndes "Growth of p-type ZnTe and n-type CdSe films on GaAs(001) by pulsed laser ablation," Appl. Surf. Sci. 127- 129, 418- 424 (1998).

[14] M. S. Hegazy and H. E. Elsayed-Ali, "Growth of Ge quantum dots on Si by pulsed laser deposition," J. Appl. Phys. **99**, 054308 (2006).

[15] M. S. Hegazy and H. E. Elsayed-Ali, "Self-assembly of Ge quantum dots on Si(100) by pulsed laser deposition," Appl. Phys. Lett. **86**, 243204 (2005).

[16] C. H. Hur, K. B. Han, K. A. Jeon and S. Y. Lee, "Enhancement of the dielectric properties of Pb(La,Ti)O_3 thin films fabricated by pulsed laser deposition," Thin Solid Films 400, 169- 171 (2001).

Reproduced with permission of the copyright owner. Further reproduction prohibited without permission.

[17] L. Goux, M. Gervais, F. Gervais, C. Champeaux and A. Catherinot, "Pulsed laser deposition of ferroelectric BST thin films on perovskite substrates: an infrared characterization," Int. J. Inorg. Mat. 3, 839- 842 (2001).

[18] I. B. Misirlioglu, A. L. Vasiliev, S. P. Alpay, M. Aindow, R. Ramesh, "Defect microstructures in epitaxial PbZr0.2Ti0.8O3 films grown on (001) SrTiO3 by pulsed laser deposition," J Mater. Sci. **41**, 697–707 (2006).

[19] M A Khan, A Garg, and A J Bell, "Pulsed laser deposition and characterization of (BiFeO3)0.7-(PbTiO3)0.3 thin films," J. Phys.: Conference Series **26,** 288–291 (2006).

[20] J. T. Cheung and H. Sankur, " Growth of thin films by laser-induced evaporation," CRC Critical Review of Solid State Materials **15**, 63-109 (1988).

[21] F. Ciabattari, F. Fuso, E. Arimondo, "Pulsed laser deposition of NiTi shape memory effect thin films," Appl. Phys. A **64**, 623–627 (1997).

[22] H. Sankur, J. DeNatale, W. Gunning, and J. G. Nelson, "Dense crystalline ZrO_2 thin films deposited by pulsed-laser evaporation," J. Vac. Sci. Tech. A 5, 2869 – 2874 (1987).

[23] P. D. Brewer, J. J. Zinck, and G. L. Olson, "Reversible modification of CdTe surface composition by excimer laser irradiation," Appl. Phys. Lett. 57, 2526 – 2528 (1990).

[24] L. Shi, H. J. Frankena, and H. J. van Elburg, "Mass composition and ion energy distribution in plasmas produced by pulsed laser evaporation of solid materials," Vacuum 40, 269 – 274 (1990).

[25] V. Braccini, D. Marre, A. Mollica, G. Grassano and A. S. Siri, "Deposition of (Ba, La)CuO_2/$CaCuO_2$ superconducting multilayers by pulsed laser deposition," Int. J. Mod. Phys. B 14 (25-27), 2713- 2718 (2000).

Reproduced with permission of the copyright owner. Further reproduction prohibited without permission.

[26] M. S. Hegazy, T. R. Refaat, M. N. Abedin, H. E. Elsayed-Ali, "Fabrication of GeSi quantum dot infrared photodetector by pulsed laser deposition," Optical Eng. Lett., **44(5)**, 59702 (2005).

[27] J. W. McCamy and M. Aziz, "Time-resolved RHEED studies of the growth of epitaxial ZnSe films on GaAs by pulsed laser deposition," Mat. Res. Soc. Symp. Proc. 441, 621- 626 (1997).

[28] J. Kanasaki, N. Mikasa, and K. Tanimura, "Laser-induced electronic desorption from InP surfaces studied by femtosecond nonresonant ionization spectroscopy," Phys. Rev. B **64**, 035414 (2001).

[29] P. Avouris and R. E. Walkup, "Fundamental mechanisms of desorption and fragmentation induced by electronic transitions at surfaces," Ann. Rev. Phys. Chem. **40**, 173-206 (1989).

[30] G. Falcone, "Ejection process in collisional sputtering," Phys. Rev. B **33**, 5054-5056 (1986).

[31] R. Kelly, J. J. Cuomo, P. A. Leary, J. E. Rothenberg, B. E. Braren, and C. F. Aliotta, Nucl. Inst. Meth. B **9**, 329-340 (1985).

[32] R. Kelly and A. Miotello, ``Mechanisms of Pulsed Laser Sputtering" in *Pulsed Laser Deposition of Thin Films*, D. B. Chrisey and G. K. Hubler (editors), John Wiley & Sons Inc., New York, 1994.

[33] E. E. Donaldson, J. T. Dickinson, and S. K. Bhattacharya, J. Adhesion **25**, 281 – 302 (1988).

Reproduced with permission of the copyright owner. Further reproduction prohibited without permission.

[34] H. E. Elsayed-Ali, T. B. Norris, M. A. Pessot, and G. Mourou, "Time-Resolved Observation of Electron-Phonon Relaxation in Copper," Phys. Rev. Lett. **58**, 1212-15 (1987).

[35] P. P. Pronko, S. K. Dutta, D. Du, and R. K. Singh, " Thermophysical Effects in Laser Processing of Materials with Picosecond and Femtosecond pulses," J. Appl. Phys. **78**, 6233-6240 (1995).

[36] P. P. Pronko, P. A. Van Rompay, and S. Sato, "Thin Film Synthesis with Ultrafast Lasers," Proc. SPIE- Intrational Society for Optical Engineering, vol. **3269**, 46-56 (1998).

[37] D. von der Linde and K. Sokolowski-Tinten, "The physical mechanisms of short-pulse laser ablation," Appl. Surf. Sci. **154-155**, 1- 10 (2000).

[38] J. Bonse, S. Baudach, J. Krüger, W. Kautek, M. Lenzner, "Femtosecond laser ablation of silicon-modification threshold and morphology," Appl. Phys. A **74**, 19- 25 (2002).

[39] I. V. Hertel, R. Stoian, D. Ashkenasi, A. Rosenfeld, and E. E. B. Campbell, "On the physics of material processing with femtosecond lasers," Riken Review **32**, 23- 30 (2001).

[40] M. W. Stapleton, A. P. McKiernan, and J.-P. Mosnier, "Expansion dynamics and equilibrium conditions in a laser ablation plume of lithium: Modeling and experiment," J. Appl. Phys. **97**, 064904 (2005).

[41] J. Perrière, E. Millon, W. Seiler, C. Boulmer-Leborgne, V. Craciun, O. Albert, J. C. Loulergue, and J. Etchepare, "Comparison between ZnO films grown by femtosecond and nanosecond laser ablation," J. Appl. Phys. **91**, 690-696 (2002).

Reproduced with permission of the copyright owner. Further reproduction prohibited without permission.

[42] N. N. Nedialkov, P. A. Atanasov, S. E. Imamova, A. Ruf, P. Berger, and F. Dausinger, "Dynamics of the ejected material in ultra-short laser ablation of metals," Appl. Phys. A **79**, 1121-1125 (2004).

[43] E Buttini, A Thum-Jäger and K Rohr, "The mass dependence of the jet formation in laser-produced particle beams," J. Phys. D: Appl. Phys. **31**, 2165–2169 (1998).

[44] S. I. Anisimov, D. Bäuerle, B. S. Luk'yanchuck, "Gas dynamics and film profiles in pulsed-laser deposition of materials," Phys. Rev. B **48**, 12078-12081 (1993).

[45] M. Ye and C. P. Grigoropoulos, "Time-of-flight and emission spectroscopy study of femtosecond laser ablation of titanium," J. Appl. Phys. **89**, 5183-5190 (2001).

[46] M. Zeifman, B. Garrison, and L. V. Zhigilei, "Combined molecular dynamics-direct simulation Monte Carlo computational study of laser ablation plume evolution," J. Appl. Phys. **92**, 2181-2193 (2002).

[47] S. Amoruso, B. Toftmann, and J. Schou, "Expansion of a laser-produced silver plume in light background gases," Appl. Phys. A **79**, 1311-1314 (2004).

[48] Z. Chen, D. Bleiner, and A. Bogaerts, "Effect of ambient pressure on laser ablation and plume expansion dynamics: A numerical simulation," J. Appl. Phys. **99**, 063304 (2006).

[49] G. Koren, A. Gupta, R. J. Baseman, M. I. Lutwyche and R. B. Laibowitz, "Laser wavelength dependent properties of $YBa_2Cu_3O_{7-\delta}$ thin films deposited by laser ablation," Appl. Phys. Lett. 55, 2450- 2452 (1989).

[50] W. Marine, J. M. Scotto D'Aniello, and J. Marfaing, Appl. Surf. Sci. 46, 239 – 244 (1990).

[51] J. F. Ready, Appl. Phys. Lett. **3**, 11-13 (1963).

Reproduced with permission of the copyright owner. Further reproduction prohibited without permission.

[52] R. K. Singh, D. Bhattacharya, and J. Narayan, "Subsurface heating effects during pulsed laser evaporation of materials," Appl. Phys. Lett. 57, 2022- 2024 (1990).

[53] D. Bhattacharya, R. K. Singh, and P. H. Holloway, "Laser-target interactions during pulsed laser deposition of superconducting thin films," J. Appl. Phys. 70, 5433 – 5439 (1991).

[54] H. Dupendant, J. P. Gavigan, D. Givord, A. Lienard, J. P. Rebouillat, and Y. Souche, Appl. Surf. Sci. 43, 369- 376 (1989).

[55] S. J. Barrington, T. Bhutta, D. P. Shepherd, R. W. Eason, "The effect of particulate density on performance of Nd:$Gd_3Ga_5O_{12}$ waveguide lasers grown by pulsed laser deposition," Opt. Comm. 185, 145- 152 (2000).

[56] F. Qian, R. K. Singh, S. K. Dutta, and P. P. Pronko, "Laser Deposition of Diamond-like Carbon Films at High Intensities," Appl. Phys. Lett. 67, 3120-3122 (1995).

[57] E. G. Gamaly, A. V. Rode, and B. Luther-Davies, "Ultrafast ablation with high-pulse-rate lasers. Part I: Theoretical considerations," J. Appl. Phys. 85, 4213- 4221 (1999).

[58] E. G. Gamaly, A. V. Rode, and B. Luther-Davies, "Ultrafast ablation with high-pulse-rate lasers. Part II: Experiments on laser deposition of amorphous carbon films," J. Appl. Phys. 85, 4222- 4230 (1999).

[59] A. Cheenne, J. Perriere, F. Kerherve, G. Hauchecorne, E. Fogarassy and C. Fuchs, "Laser assisted deposition of thin BiSrCaCuO films," Mat. Res. Soc. Symp. Proc. 191, 229- 234 (1990).

[60] M. Joseph, N. Sivakumar, P. Manoravi and S. Vanavaramban, "Preparation of thin film of $CaZrO_3$ by pulsed laser deposition," Sol. St. Ion. 144, 339-346 (2001).

Reproduced with permission of the copyright owner. Further reproduction prohibited without permission.

CHAPTER III

REFLECTION HIGH-ENERGY ELECTRON DIFFRACTION: THEORY AND EXPERIMENTAL CALCULATIONS

III.1. Introduction

Reflection high-energy electron diffraction (RHEED) [1] is a powerful technique for studying surface structures of flat surfaces [2] and surface phase transitions [3-5]. RHEED is sensitive to surface phenomena, not only structural changes but also deposition, adsorption and growth of 2D and 3D islands. Therefore, it is widely used as an *in situ* probe to monitor the growth of thin films both in research and in industry [6,7]. The concept of RHEED is quite simple, Fig. 3.1. An accelerated electron beam (5–100 keV) is incident on the solid's surface with a glancing angle of $\leq 3°$ and is reflected. The high energy of the electrons results in the increase in their penetration depth, but because of the glancing angle of incidence, only a few atomic layers are probed. This is the reason for the high surface sensitivity of RHEED. Upon reflection, electrons diffract, forming a diffraction pattern that depends on the structure and the morphology of the probed surface area. An example of the RHEED sensitivity is shown in Fig. 3.2, in which a comparison between RHEED patterns obtained from reconstructed and non-reconstructed surfaces is shown. Conceptually, perfectly flat surfaces should result in a diffraction pattern that consists of spots arranged on "Laue" rings, Fig. 3.2(b). However, because of the non-idealities in both the electron beam and the sample's surface, streaks appear instead of spots, Fig. 3.2(a).

Reproduced with permission of the copyright owner. Further reproduction prohibited without permission.

Most surfaces are not perfectly flat; hence, the diffraction pattern is produced by transmission through crystalline 3D structures or surface roughness (asperities); see the inset of Fig. 3.1. Despite the popularity of RHEED, there is no complete formal theory for it. However, a number of kinematical approaches have been introduced that are useful for understanding the basic idea of RHEED. They are sufficient for the determination of the unit cell dimension, crystal orientation and the crystal shape. The lack of a formal applicable theory is the reason behind the debate over the interpretation of some RHEED results [8].

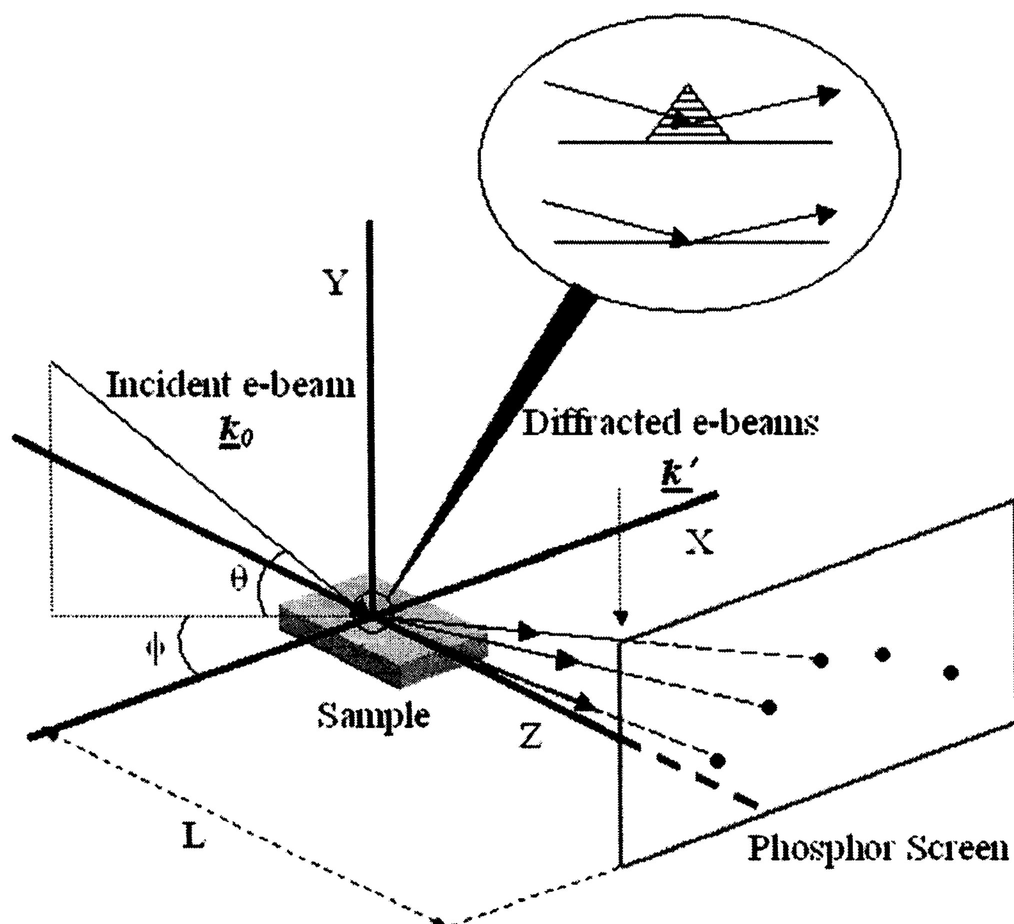

FIG. 3.1. An illustration of the fundamentals of RHEED. The inset shows two kinds of reflection: transmission-reflection diffraction scattering by three-dimensional crystalline island (above) and surface scattering from flat surface (below).

Reproduced with permission of the copyright owner. Further reproduction prohibited without permission.

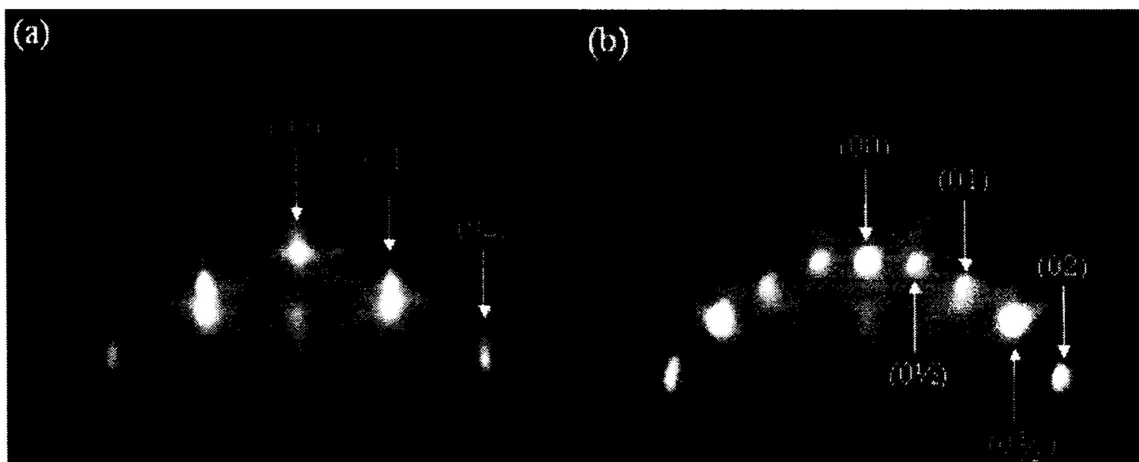

FIG. 3.2. RHEED sensitivity for surface structures and reconstructions. (a) Si(100)-1×1, (b) Si(100)-2×1 reconstructed surface.

III.2. RHEED Setup and Alternatives

The main advantages of RHEED as a surface science tool are its (1) simplicity (both setup and operation), (2) low cost (both price and maintenance), (3) real time (*in vivo*) and *in situ* surface monitoring ability, (4) high sensitivity to surface changes, and (5) compatibility with medium and ultrahigh vacuum environments [1,9,10]. It may be worthwhile to mention that high pressure versions of RHEED exist [11], in which the system's differential pumping is used and the electrons path in the high-pressure region is kept as short as possible.

The average RHEED system consists of the following components/parts:

(1) **Electron gun:** it produces, accelerates and collimates nearly mono-energetic electron beams with energies in the range 5-100 keV. The continuous wave (CW) electron gun is simply a tungsten filament that is heated via a radio frequency (rf) source to emit electrons. These electrons are then accelerated to high energies by

Reproduced with permission of the copyright owner. Further reproduction prohibited without permission.

a series of electrostatic dynodes and are focused by means of electrostatic or electromagnetic lenses. At the end of the accelerating column, two sets of electrostatic or electromagnetic deflectors are used to control the movement of the e-beam in two dimensions (see Appendix A for more details about the gun design).

(2) **Substrate**: it is the sample under study that causes the diffraction of the electron beam.

(3) **Phosphor screen**: it is used to transform the diffracted electrons into a visible diffraction pattern. Fast decay phosphor screens may be used for some time resolved studies.

(4) **Charge-coupled device (CCD) camera:** it is used to capture the diffraction patterns off the phosphor screen. High frame cameras may be used for time resolved studies.

Detailed information about the surface and the calculation of the surface potential could be obtained by obtaining different RHEED patterns at different azimuthal and incident angles [12]. Some groups have developed computer-controlled automated mechanisms to change the angle of incidence, via magnetic deflectors, and to record the data [13]. Using this technique, thermal surface phonons and some surface transitions have been studied [13-15]. Another RHEED alternative that automates the acquisition of the rocking curves is the convergent-beam RHEED (CB-RHEED). In such a technique, a cone-shaped, focused beam is used instead of the collimated e-beam [8,16,17]. Hence, it is possible to visualize the beam as a collection or ensemble of non-parallel sub-beams,

Reproduced with permission of the copyright owner. Further reproduction prohibited without permission.

each of which will result in a separate pattern. Therefore, the resultant pattern from a flat surface, for instance, consists of discs rather than spots in the ordinary RHEED [8].

Time-resolved RHEED is an important alternative to RHEED that enables the study of ultra fast surface phenomena, such as superheating, chemical reactions, and even the adatoms desorption during thin film growth [19,20]. In such a technique, laser interaction with some metal targets (cathode) results in the emission of the so called "photo-activated" e-beam instead of the thermally generated e-beam in ordinary RHEED. It is commonly used in pump-probe experiments, in which the laser beam is split into two beams, the first of which is used to pump the sample while the other is used to generate the electrons. By controlling the time lag between the two beams, different stages of the surface reactions can be studied.

III.3. RHEED Theory

III.3.A. Geometric Model

The simplest way to describe RHEED is the "geometric model" [1], in which diffraction of a plane wave (of wavevector k) by a single crystal is assumed. No interaction mechanism is taken into account in this treatment. Because of its simplicity, this theory is widely used for experimental calculations. In this theory, diffraction results when the Laue condition is satisfied, i.e.,

$$\vec{k}' - \vec{k}_0 = \vec{G}, \tag{3.1}$$

Reproduced with permission of the copyright owner. Further reproduction prohibited without permission.

where $\vec{k}'$ and $\vec{k}_0$ are the wave vectors for the diffracted and the incident beams, respectively, and G is the reciprocal-lattice vector. In the special case of elastic scattering; $|k'| = |k_0|$. This condition is satisfied by an infinite number of k' vectors pointing in all directions, which is the origin of the so-called Ewald sphere. An Ewald sphere is a sphere that has its origin as the origin of the k_0 and a radius $|k_0|$. Hence, the Laue condition may be re-formalized as "diffraction occurs for all k' connecting the origin of the sphere and a reciprocal-lattice point" [1,10]. The magnitude of the wavevector is given by the relativistic expression

$$k_0 = \frac{2\pi}{\lambda} = \frac{1}{\hbar}\sqrt{2m_0 qV + \left(\frac{qV}{c}\right)^2}, \tag{3.2}$$

where m_0 is the electron rest mass, q is its charge and V is the accelerating potential. Expression (3.2) is sometimes written as

$$\lambda = \frac{h}{\sqrt{2m_0 qV + \left(\frac{qV}{c}\right)^2}} \cong \frac{12.3}{\sqrt{V(1 + 1.95\times 10^{-6} V)}}, \tag{3.3}$$

where the wavelength λ is measured in Å and V is in volts.

The geometric model is successfully used to calculate the lattice spacing in the reciprocal space. A simple way to describe that is to consider Fig. 3.3, which is a top view showing the projection of the reciprocal space. The spots in the RHEED pattern are the result of the intersections of the Ewald's sphere with the reciprocal lattice rods. What is seen on the phosphor screen is the projection of these spots. By applying the principle

Reproduced with permission of the copyright owner. Further reproduction prohibited without permission.

of similar triangles to the two triangles at the bottom of the figure (the shadowed triangle and the bigger one), it is easy to see that $\frac{W}{L} \simeq \frac{a^*}{|k_0|}$. Hence,

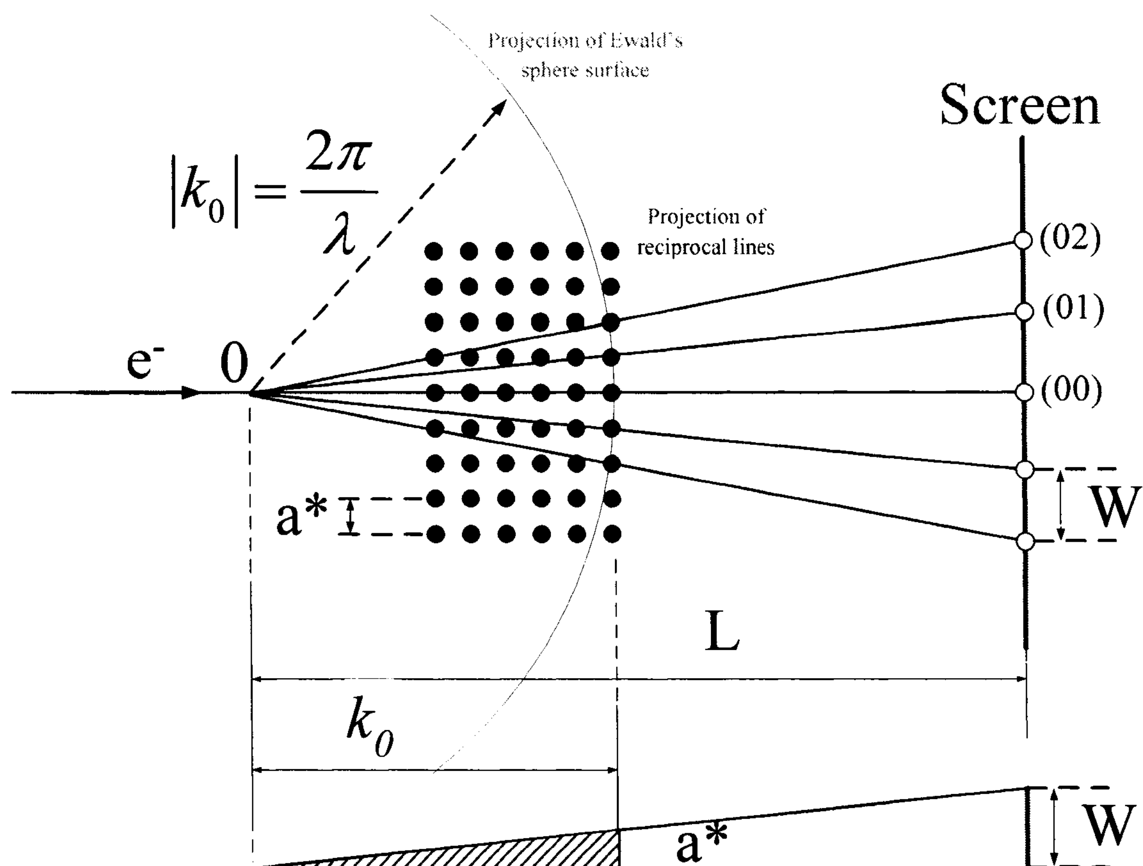

FIG. 3.3. Top view describing the origin of diffraction spots according to the geometrical model.

$$a^* = \frac{2\pi W}{\lambda L} , \tag{3.4}$$

where W is the streak separation, and L is the sample to screen distance. Now, changing the direction of incidence by changing the azimuthal angle would result in a completely different diffraction pattern, since the Ewald's sphere would intersect different rods. Depending on the lattice structure, most of the azimuths result in non-symmetric patterns.

Reproduced with permission of the copyright owner. Further reproduction prohibited without permission.

The rocking curves and the azimuthal plots, which are obtained by recording the intensities of a certain diffracted beam as a function of the azimuthal angle, are used to determine the atomic arrangement at the surface and surface symmetry [9,10,13,21].

The geometric model is good for a basic understanding of RHEED. It is also used in most of the RHEED calculations. However, it does not give any description of the mechanisms involved in the diffraction process. The following section is dedicated to understanding the physics behind RHEED.

III.3.B. Kinematical and Dynamical Model

The Schrödinger equation for the wavefunction of the scattered wave, $\psi(\underline{r})$, is given, in terms of effective potential $U(\underline{r})$, by [1,22]

$$\left(\frac{-\hbar^2}{2m}\nabla^2 + V(r)\right)\psi(r) = E\psi(r) \tag{3.5}$$

Or

$$\left(\nabla^2 + U(\underline{r}) + k_0^{\,2}\right)\psi(\underline{r}) = 0. \tag{3.6}$$

where

$$U(r) = \frac{2m}{\hbar^2}V(r), \text{ and } k_0 = \frac{2m}{\hbar^2}E \tag{3.7}$$

In almost all scattering problems, we deal with short-range potentials, i.e. $V(r) \approx 0$ beyond a certain distance, $|r| \sim a$, where a is the scatterer size. In all applications, including RHEED, we are interested in measuring the scattered electrons far

Reproduced with permission of the copyright owner. Further reproduction prohibited without permission.

away from the scattering center, i.e. $|r| \gg a$, which is realistic since the detector is always located at distances much larger than the scattering center. Hence,

$$\left(\nabla^2 + k_0{}^2\right)\psi(\underline{r}) = 0\,. \tag{3.8}$$

This is the plane wave (free particle) equation that has the eigenfunctions $\varphi(r) = e^{i\vec{k}\bullet\vec{r}}$ and the eigenvalues $E = \dfrac{\hbar^2 k^2}{2m}$.

Now, in the neighborhood of the scattering centers, we would like to find the modification of the eigenfunctions in the presence of the scattering potential. This is the well-known scattering problem, which is solved by different techniques [23-25]. Here, I will consider the "Lippmann-Schwinger" treatment, which is described in Ref. [23]. We start by rewriting equation (3.5) using the "ket" notation, viz. [23,24]

$$\left(H_0 + V\right)|\psi\rangle = E|\psi\rangle \tag{3.9}$$

Or

$$\left(E - H_0\right)|\psi\rangle = V|\psi\rangle \tag{3.9*}$$

Roughly, we may write

$$|\psi\rangle = \frac{V}{\left(E - H_0\right)}|\psi\rangle \tag{3.10}$$

To go around the pole of $1/\left(E - H_0\right)$, we may specify a boundary condition to the solution. We may write $1/\left(E - H_0 + i\varepsilon\right)$ where we take the limit $\varepsilon \to +0$ at the end of the calculations. In this notation, the plane wave solution away from the scattering center $|\varphi\rangle$ satisfies the equation $H_0|\varphi\rangle = E|\varphi\rangle$. Therefore, the solutions must satisfy the condition $|\psi\rangle \to |\varphi\rangle$ as $V \to 0$. Therefore, the solution could be written as

Reproduced with permission of the copyright owner. Further reproduction prohibited without permission.

$$|\psi\rangle = |\varphi\rangle + \frac{V}{\left(E - H_0 + i\varepsilon\right)}|\psi\rangle. \tag{3.11}$$

This is the so-called "Lippmann-Schwinger" equation. Multiplying Eq. (3.11) by the "bra" $\langle \vec{r}\,|$,

$$\langle \vec{r}\,|\psi\rangle = \langle \vec{r}\,|\varphi\rangle + \langle \vec{r}\,|\frac{V}{E - H_0 + i\varepsilon}|\psi\rangle \tag{3.12}$$

Now, it may be good to refresh our minds with some of the basic properties of the bra-ket notation [23]:

(1) The orthogonality of eigenkets states that $\langle r'|r''\rangle = \delta(r'-r'')$,

(2) The completeness, which follows right away from the orthogonality, is written as $\int_{-\infty}^{\infty}|x\rangle\langle x|dx = 1$

(3) From the orthogonality condition, any state $|A\rangle$ could be represented as $|A\rangle = \int_{-\infty}^{\infty}\langle r'|A\rangle|r'\rangle dr'$,

(4) The quantity $\langle r'|A\rangle = \psi_A(r')$ is the description of the complex eigenfunction of the position r',

(5) The inner product of any two eigenstates is defined as $\langle A|B\rangle = \int_{-\infty}^{\infty}\langle A|r'\rangle\langle r'|B\rangle dr' = \int_{-\infty}^{\infty}\psi_A^*(r')\psi_B(r')dr'$

(6) The expectation value of M with respect to the state α is given by $\langle M\rangle = \langle \alpha\,|\,M\,|\,\alpha\rangle$

Using the third property in Eq. (3.12), we may write

$$\psi(\vec{r}) = \varphi(\vec{r}) + \langle \vec{r}\,|\frac{V}{E - H_0 + i\varepsilon}|\psi\rangle \tag{3.12*}$$

Reproduced with permission of the copyright owner. Further reproduction prohibited without permission.

Or

$$\psi(\vec{r}) = \frac{e^{i\vec{k}.\vec{r}}}{(2\pi\hbar)^{3/2}} + \int \langle \vec{r} | \frac{1}{E - H_0 + i\varepsilon} | \vec{r}' \rangle \langle \vec{r} | V | \psi \rangle d\vec{r}'$$
$$= \frac{e^{i\vec{k}.\vec{r}}}{(2\pi\hbar)^{3/2}} + \int \langle \vec{r} | \frac{1}{E - H_0 + i\varepsilon} | \vec{r}' \rangle V(\vec{r}') \psi(\vec{r}') d\vec{r}' \quad (3.13)$$

Or

$$\psi(\vec{r}) = \frac{e^{i\vec{k}.\vec{r}}}{(2\pi\hbar)^{3/2}} + \int G(\vec{r},\vec{r}') V(\vec{r}') \psi(\vec{r}') d\vec{r}', \quad (3.13^*)$$

where

$$G(\vec{r},\vec{r}') = \langle \vec{r} | \frac{1}{E - H_0 + i\varepsilon} | \vec{r}' \rangle . \quad (3.14)$$

Equation (3.13') is called Helmholtz's equation and is solved by Green's function techniques. The problem, then, is reduced to finding the exact solution for the Green's function $G(\vec{r},\vec{r}')$. Using that $H_0 = \vec{P}/2m$, inserting a complete set of states in momentum space, and using the completeness property of momentum, i.e. $\int_{-\infty}^{\infty} |p'\rangle\langle p'| dp' = 1$ we may write Eq. (3.14) as,

$$G(\vec{r},\vec{r}') = \int \langle \vec{r} | \vec{p} \rangle \frac{1}{E - \vec{p}^2/2m + i\varepsilon} \langle \vec{p} | \vec{r}' \rangle d\vec{p} \quad (3.15)$$

Considering the momentum representative $\langle \vec{r} | \vec{p} \rangle$ and that $p = -i\hbar \frac{d}{dr}$, it is easy to see that $p\langle r | p \rangle = -i\hbar \frac{d}{dr} \langle r | p \rangle$,

and then the solution to this differential equation is

$$\langle r | p \rangle = e^{ipr/\hbar} . \quad (3.16)$$

Reproduced with permission of the copyright owner. Further reproduction prohibited without permission.

Hence, it is easy to see that

$$G(\vec{r},\vec{r}\,') = \int \frac{e^{i\vec{r}.\vec{p}/\hbar}}{(2\pi\hbar)^{3/2}} \frac{1}{E-\vec{p}^2/2m+i\varepsilon} \frac{e^{i\vec{r}\,'.\vec{p}/\hbar}}{(2\pi\hbar)^{3/2}} d\vec{p}$$
$$= \frac{1}{(2\pi\hbar)^3} \int e^{i(\vec{r}-\vec{r}\,').\vec{p}/\hbar} \frac{1}{E-\vec{p}^2/2m+i\varepsilon} d\vec{p} \tag{3.17}$$

Using the spherical polar coordinates for $\vec{p}$ and donating $\vec{r} = \vec{r} - \vec{r}\,'$

$$G(\vec{r}) = \frac{1}{(2\pi\hbar)^3} \int_0^\infty \int_{-1}^1 \int_0^{2\pi} \left[e^{ipr\cos\theta/\hbar} \frac{1}{E-\vec{p}^2/2m+i\varepsilon} \right] p^2 d(\cos\theta) dp d\varphi \tag{3.18}$$

Integrating over θ and φ, yields

$$G(\vec{r}) = \frac{2\pi}{(2\pi\hbar)^3} \int_0^\infty \frac{\left(e^{ipr/\hbar} - e^{-ipr/\hbar}\right)}{ipr/\hbar} \frac{1}{E-\vec{p}^2/2m+i\varepsilon} p^2 dp\,, \tag{3.19}$$

Now, performing the following simplification,

$$G(\vec{r}) = \frac{2\pi\hbar}{(2\pi\hbar)^3} \left(\int_0^\infty \frac{e^{ipr/\hbar}}{ir\left(E-\vec{p}^2/2m+i\varepsilon\right)} pdp - \int_0^\infty \frac{e^{-ipr/\hbar}}{ir\left(E-\vec{p}^2/2m+i\varepsilon\right)} pdp \right)$$
$$= \frac{2\pi\hbar}{(2\pi\hbar)^3} \left(\int_0^\infty \frac{e^{ipr/\hbar}}{ir\left(E-\vec{p}^2/2m+i\varepsilon\right)} pdp + \int_\infty^0 \frac{e^{-ipr/\hbar}}{ir\left(E-\vec{p}^2/2m+i\varepsilon\right)} pdp \right),$$
$$= \frac{2\pi\hbar}{(2\pi\hbar)^3} \left(\int_0^\infty \frac{e^{ipr/\hbar}}{ir\left(E-\vec{p}^2/2m+i\varepsilon\right)} pdp + \int_{-\infty}^0 \frac{e^{ipr/\hbar}}{ir\left(E-\vec{p}^2/2m+i\varepsilon\right)} pdp \right)$$

by writing $(-p) \to p$ in the second integral. Hence,

$$G(\vec{r}) = \frac{2\pi\hbar}{(2\pi\hbar)^3} \int_{-\infty}^\infty \frac{e^{ipr/\hbar}}{ir} \frac{-2m}{\vec{p}^2 - 2mE - i\varepsilon'} pdp \tag{3.19*}$$

where $\varepsilon' = 2m\,\varepsilon$. Rearranging and taking the perfect square of the denominator,

Reproduced with permission of the copyright owner. Further reproduction prohibited without permission.

$$G(\vec{r}) = \frac{1}{(2\pi\hbar)^2}\frac{2mi}{r}\int_{-\infty}^{\infty}\frac{pe^{ipr/\hbar}}{(p-\sqrt{2mE}-i\varepsilon')(p+\sqrt{2mE}+i\varepsilon')}dp\,, \tag{3.20}$$

where there is no need to consider the term $i\varepsilon'$ under the square, since it is infinitesimally small and will eventually go to zero.

Now, by using the residue theorem and by proper choice of the integration contour in the upper half plane to go along the real axis, the integral only has a pole at $p = \sqrt{2mE} + i\varepsilon' = \hbar k + i\varepsilon'$. Hence, the integration yields

$$G(\vec{r}) = \frac{1}{(2\pi\hbar)^2}\frac{2mi}{r}2\pi i\frac{\hbar k e^{ikr}}{2(\hbar k + i\varepsilon')} \tag{3.21}$$

Now, taking the limit that $\varepsilon' \to 0$ and arranging,

$$G(\vec{r}) = -\frac{2m}{4\pi\hbar^2}\frac{e^{ikr}}{r} \tag{3.22}$$

Substituting into Eq. (3.21) into Eq. (3.13) and using $\vec{r} = \vec{r} - \vec{r}\,'$, we get

$$\psi(\underline{r}) = \frac{e^{i\vec{k}.\vec{r}}}{(2\pi\hbar)^{3/2}} - \frac{2m}{\hbar^2}\int\frac{e^{ik|\underline{r}-\underline{r}'|}}{4\pi|\underline{r}-\underline{r}'|}V(\underline{r}')\psi(\underline{r}')d\underline{r}'\,. \tag{3.23}$$

Again, the first term in the above equation simply represents the incident plane wave, while the second represents the scattered wave. As mentioned earlier, in RHEED experiments, one is interested in the value of $\psi(\underline{r})$ evaluated at large distances compared to the dimensions of the scatterer, i.e., $|r - r'| \approx r$, hence Eq. (3.23) could be written as [1,22]

$$\psi(\underline{r}) = e^{i\underline{k}\bullet\underline{r}} - \frac{e^{ik'r}}{4\pi r}\frac{2m}{\hbar^2}\int e^{-i\underline{k}'\bullet\underline{r}'}V(\underline{r}')\psi(\underline{r}')d\underline{r}'\,. \tag{3.24}$$

Or

Reproduced with permission of the copyright owner. Further reproduction prohibited without permission.

$$\psi(\underline{r}) = e^{i\underline{k}\bullet\underline{r}} + \frac{e^{ik'r}}{r} f(k), \tag{3.24*}$$

where

$$f(\underline{k}) = -\frac{1}{4\pi}\frac{2m}{\hbar^2}\int e^{-i\underline{k}'\bullet\underline{r}'} V(\underline{r}')\psi(\underline{r}')d\underline{r}'. \tag{3.25}$$

is called the scattering amplitude and has the dimension of length. It is related to the scattering differential cross section by the relation

$$\frac{d\sigma}{d\Omega} = |f(k)|^2. \tag{3.26}$$

The scattering current scattered into a solid angle $d\Omega$ in the direction of (θ, ϕ) per unit current density in the incident wave is given by [1,22]

$$I(\theta,\phi)d\Omega = \frac{d\sigma}{d\Omega}d\Omega = |f(k)|^2 d\Omega. \tag{3.27}$$

To calculate the intensity distribution in the diffraction pattern in RHEED experiments, the effective potential should be assumed and the scattering amplitude integral (3.25) should be evaluated.

The so-called "kinematical theory" evolves when the Born approximation is used [1,2,22], i.e. the wave function inside the crystal is assumed to be that of the incident wave or $\psi(r') = e^{ik_0 r'}$. In this case, Eq. (3.25) is written as

$$f(\underline{K}) = -\frac{1}{4\pi}\int e^{-i\underline{K}\bullet r'} V(\underline{r}')d\underline{r}', \tag{3.28}$$

with $\underline{K} = \underline{k}' - \underline{k}_0$. In other words, the scattering amplitude is the Fourier transform of the scattering potential. A number of theoretical calculations have been made to calculate the scattering amplitude, assuming functional forms for $V(r)$ that take into account the

Reproduced with permission of the copyright owner. Further reproduction prohibited without permission.

periodicity of the crystal lattice. The main problem with the kinematical treatment is the oversimplified assumption that the wave function at the scatterer equals that of the incident plane wave, since this assumption overlooks the mutual interaction between the crystal and the incident electron beam.

A more elaborate theory, "dynamical theory," has been introduced to deal with the diffraction problem without the oversimplification of the kinematical theory [22]. For electron scattering from a crystal, the wave within the crystal may be represented by a sum of plane waves

$$\psi(r') = \sum_{l=0}^{N} \psi_l(r') e^{ik_l \bullet r'} . \tag{3.29}$$

Substituting (3.29) into (3.25) and using the Laue condition, $k_l - k_0 = 2\pi l$, the scattering amplitude could be written as

$$f(k) = \sum_{l=0}^{N} f_l(K_l) = -\frac{1}{4\pi} \sum_{l=0}^{N} \int_{scatterer} \psi_l(r') e^{-i(k'-k_0-2\pi l)\bullet r'} V(r') dr' . \tag{3.30}$$

Again in order to find the scattering amplitude, the integrals in Eq. (3.30) have to be solved. This difficulty is the reason why dynamical theory is not frequently used for analyzing RHEED data.

III.4. Transmission RHEED

In practice, most surfaces have three-dimensional features that differ in shape and height, which form during thin film deposition or chemical etching. Therefore,

Reproduced with permission of the copyright owner. Further reproduction prohibited without permission.

transmission diffraction through these features or structures is important [9,26]. The reflection (from relatively flat surfaces) and the transmission-reflection (3D structures) diffractions could be distinguished from the shape of the resulting diffraction pattern. The reflection diffraction pattern consists of spots (or streaks) that lie on arcs (the Laue rings), Fig. 3.4(a). On the other hand, in transmission-reflection diffraction, diffraction spots (not lines) lie along straight lines, Fig. 3.4(b). As the size of the crystal through which transmission occurs gets smaller, the diffraction spots gets broader. "A rough clean surface that is subsequently made smoother (by annealing or growth) initially shows spots (transmission pattern), then streaks, and finally sharp spots on arcs, if the surface can be made sufficiently well structurally" [9].

Figure 3.5 summarizes the four different possibilities of diffraction from thin 3D shapes and roughly predicts the resulting diffraction patterns [9]. Fig. 3.5(a) illustrates transmission through a high and wide 3D structure. In this case, a sharp transmission pattern, consisting of circular spots, is expected. For a high but narrow structure, 3.5(b), diffraction spots broaden parallel to the surface of the substrate. However, if the structure is short but wide, 3.5(c), the broadening of the spots will be normal to the substrate surface. Finally, for surfaces with flat terraces, 3.5(d), a combination of a reflection pattern superimposed on a transmission pattern is expected. This gives rise to a streaky reflection diffraction pattern. The shape of the transmission-reflection diffraction spot, therefore, is an indication of the shape of the 3D structure on the surface. Calculation of the 3D structure size from the diffraction pattern is, in most cases, not accurate because of two factors: 1) shadowing and 2) attenuation. For high density, 3D structures shadow each other both in the incident and the exiting beams. Attenuation not only acts to reduce

Reproduced with permission of the copyright owner. Further reproduction prohibited without permission.

the intensity of the transmitted beam but also introduces distortion to the beam shape if the asperity shape is not uniform. We are interested in studying the transmission diffraction from Ge quantum dots (QD). Therefore, we will focus our attention on that in the following discussion.

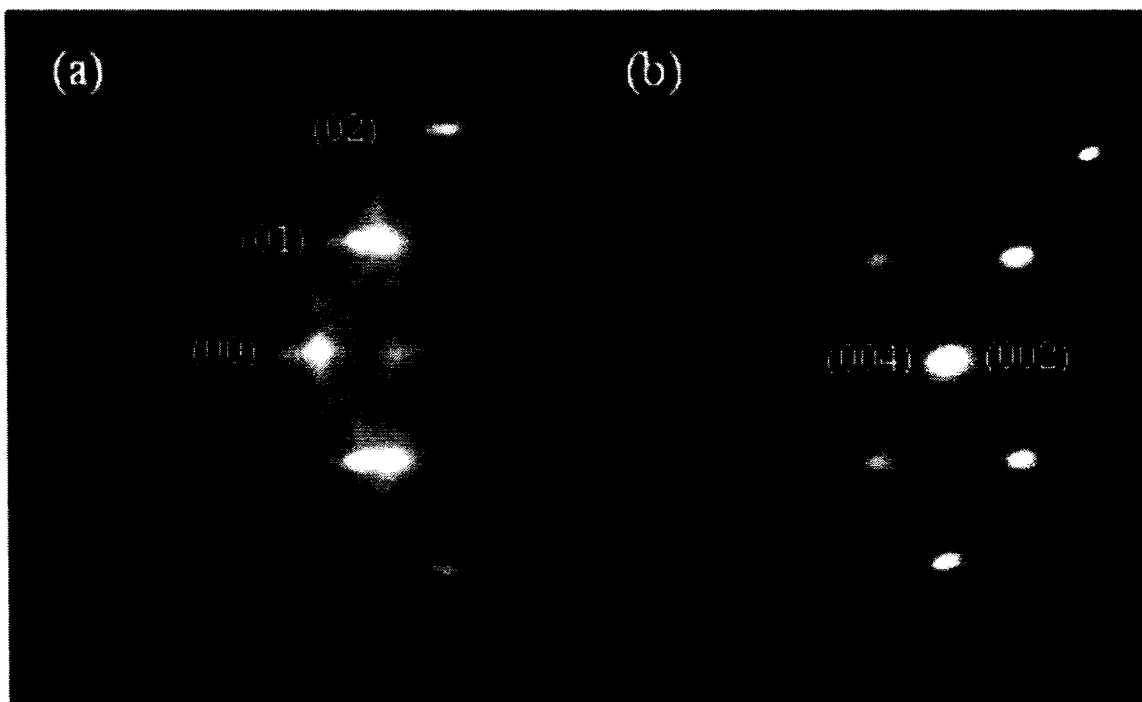

FIG. 3.4. Comparison between (a) reflection diffraction from chemically cleaned Si(100) sample and (b) transmission-reflection diffraction pattern of Ge QD.

RHEED is characterized by the small (glancing) angle of incidence that is responsible for (i) the very small electron momentum component normal to the surface (as compared to the parallel one) and (ii) the forward scattering of the e-beam [10]. These two characteristics act to enhance the transmission of the e-beam through the 3D structures, such as QD, resulting in transmission patterns. Such patterns consist of bright

Reproduced with permission of the copyright owner. Further reproduction prohibited without permission.

spots, arranged on lines parallel to the sample surface rather than rings, as is the case with reflection patterns. These patterns can give some useful structural information about the 3D structures.

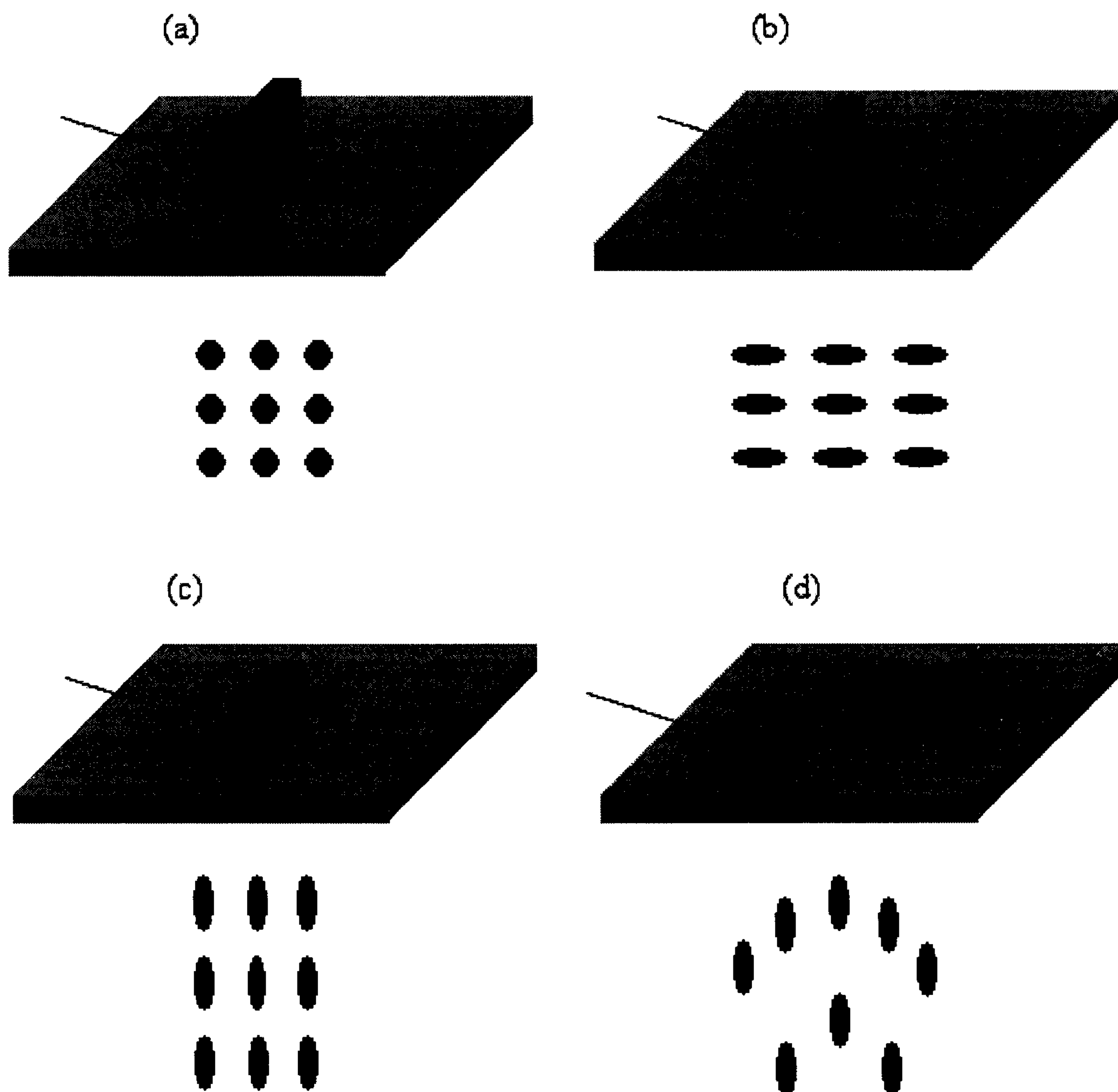

FIG. 3.5. Different possibilities of transmission-reflection diffraction through thin crystals and the expected resulting diffraction patterns. (a) Transmission through high and wide crystal; (b) transmission through high and narrow crystal; (c) that through short and wide crystal; (d) diffraction from nearly flat asperities. [After ref. [9]].

Reproduced with permission of the copyright owner. Further reproduction prohibited without permission.

However, the e-beam penetration through these structures is governed by the so-called inelastic mean free path (IMFP), which is defined as the average distance an electron traverses between successive inelastic collisions [27]. The value of the IMFP in a given material depends on the e-beam kinetic energy and the material's parameters (mainly, density and atomic number). Generally, the IMFP is given by [27-29],

$$\lambda_i = \frac{E}{E_p^2\left(\beta \ln(\gamma E) - \frac{C}{E} + \frac{D}{E^2}\right)}, \tag{3.31}$$

where λ_i is the IMFP, E is the electron energy, $\mathrm{E_p} = \sqrt{\rho N_v / M}$ is the generalized plasmon energy, N_v is the number of valence electrons, ρ is the density of the material and M is the atomic mass. The constants β, γ, C, and D are material dependent and can be estimated from some empirical or semi-empirical expressions [28]. For energies >100 eV, the above equation may be approximated as [27],

$$\lambda_i = \frac{E}{E_p^2 \beta \ln(\gamma E)}, \tag{3.32}$$

Figure 3.7 shows the IMFP electron energy curves calculated for Ge using different modifications of Eq. (3.31). The constants β, γ, C, and D are calculated from empirical relations given in Ref. [28]. From the figure, the IMFP in Ge 3D structures, at 12 keV, is 15±4 nm.

Reproduced with permission of the copyright owner. Further reproduction prohibited without permission.

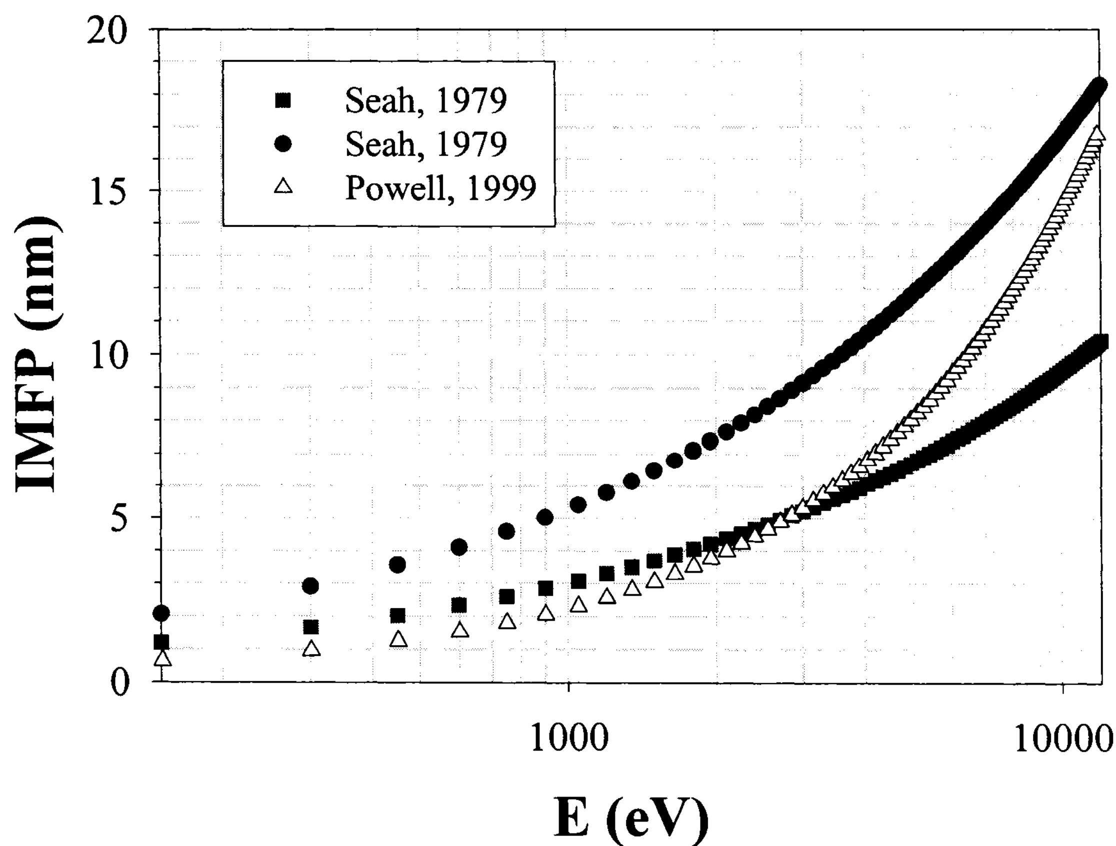

FIG. 3.6. IMFP of electrons in Ge as a function of electrons energy [Calculations are based on the data from Ref. [28,29]]

Figure 3.7 simplifies the geometry of transmission RHEED through surface roughness and crystalline 3D structures. Constructive interferences (or transmission spots) also follow Bragg's condition. For small angles of incidence, θ, $\sin\theta \cong \theta$; and hence Bragg's condition may be approximated as [30],

$$2d_{hkl} \cdot \theta_{hkl} = \lambda . \qquad (3.33)$$

Reproduced with permission of the copyright owner. Further reproduction prohibited without permission.

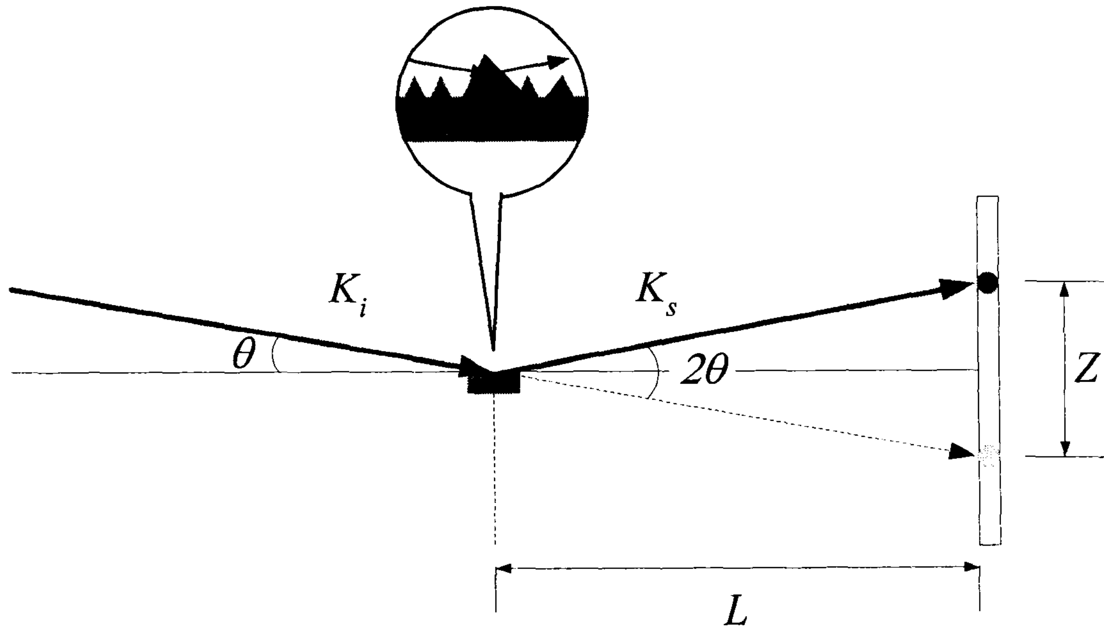

FIG. 3.7. A schematic diagram represents the transmission-reflection geometry of RHEED.

Considering the geometry in Fig. 3.7, θ can be written in terms of Z (origin-to-spot distance Z on screen) and L (sample-to-screen distance) as

$$2\theta_{hkl} = \frac{Z}{L}, \tag{3.34}$$

Substituting Eq. (3.34) into Eq. (3.33),

$$d_{hkl} = \frac{\lambda L}{Z}, \tag{3.35}$$

Each of the transmission spots accounts for a given plane (*hkl*) in the diffraction zone, which is the set of all planes normal to the e-beam direction of incidence and result in transmission conditions. All planes in the zone must satisfy the zone equation [30],

$$hu + kv + lw = 0, \tag{3.36}$$

Reproduced with permission of the copyright owner. Further reproduction prohibited without permission.

where (*hkl*) is any plane located in the [*uvw*] zone. The axis normal to the diffraction zone is parallel to the e-beam direction of incidence and is called the zone axis. It is very useful in the process of indexing the transmission patterns, as will be described and calculated in detail for Ge QD in section III.7.

III.5. Some RHEED patterns

Figure 3.8 shows different surface structures and the resulting diffraction and transmission patterns. Figures 3.8(a), (b) and (c) have been discussed in sections III.1 and III.4. For a polycrystalline surface, the RHEED pattern is the sum of the diffractions from all of the different crystalline regions [22]. This gives rise to a system of concentric rings. The reciprocal lattice of the whole specimen results from rotating the reciprocal lattice of the individual crystal around the origin. "Each reciprocal lattices point thus produces a sphere, which is intersected by the Ewald 'plane' in a circle" [22]. The ring pattern is sometimes referred to as the "Debye-Sherrer pattern," Fig. 3.8(d).

Sometimes the surface has domains that have a distribution of orientations but are largely near one value [22,31,32]. This kind of structure will give rise to the so-called "textured pattern," which consists of concentric broken rings or arcs, Fig. 3.8(d). The length of these arcs is a measure for the misorientation of the crystals about the electron beam direction of incidence. Similar patterns have been reported for the growth of TiN on Si(100) by 6-ns 355-nm laser at 750 °C [33]. The evolution of such patterns was attributed to the process of granular epitaxy and grain growth.

Reproduced with permission of the copyright owner. Further reproduction prohibited without permission.

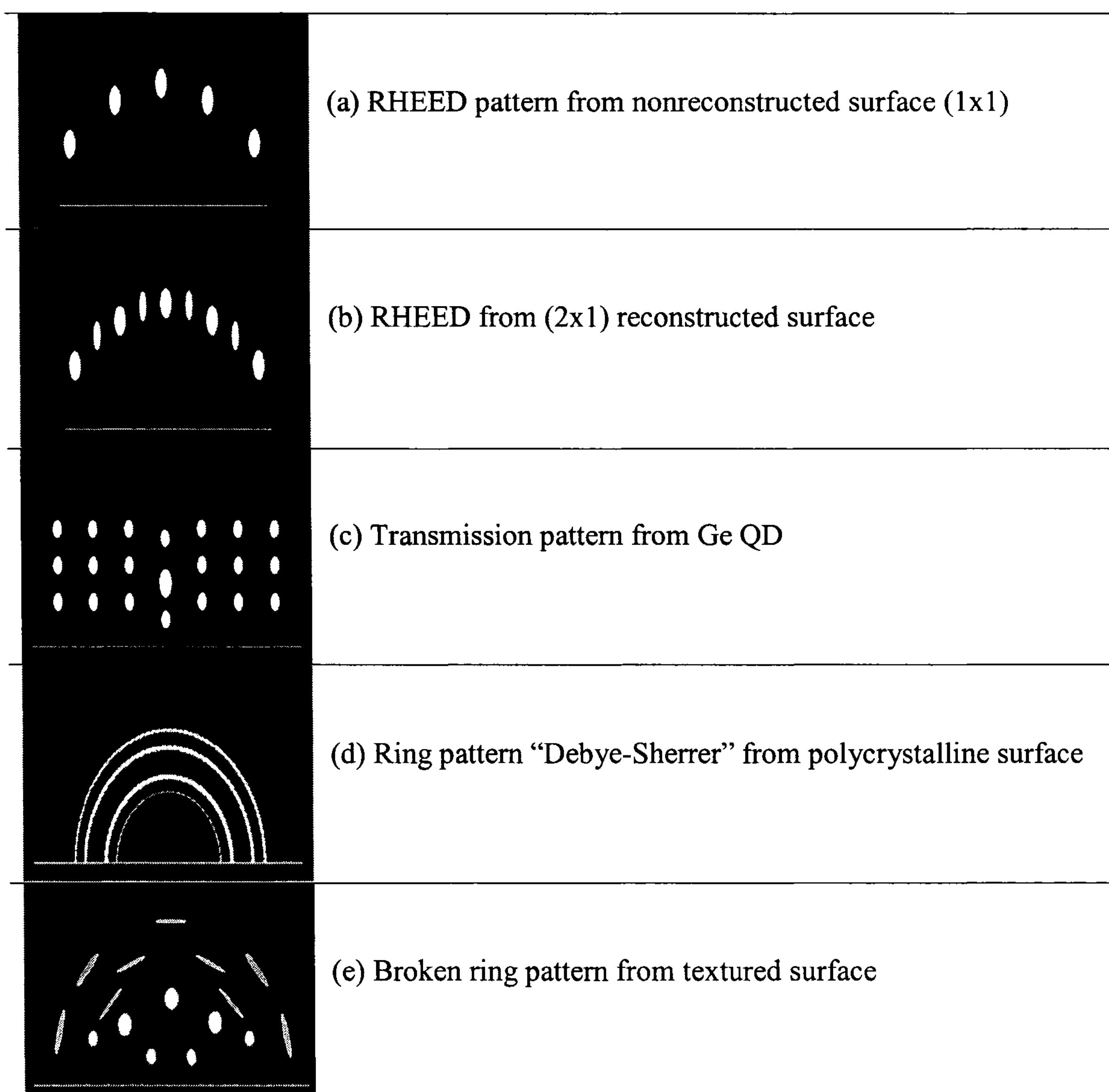

FIG. 3.8. Comparison of different reflection and transmission RHEED patterns and the originating surface structures.

Reproduced with permission of the copyright owner. Further reproduction prohibited without permission.

III.6. Calculation of pure reflection RHEED patterns

For pure reflection RHEED of a given surface of known orientation, 2D indexing is used. Recalling that RHEED is an image of the surface lattice in the reciprocal space, a pre-calculation of the reciprocal lattice mesh of that surface is needed. These calculations are necessary to determine the direction of the incident electron beam relative to the surface structure. In the case of an unknown crystal surface, calculations are performed for different crystal surfaces till a good match between the experimental and the calculated structure is found. Below, the reciprocal lattices of Si(100) and Ge(100) surfaces are calculated.

III.6.A. Si(100)

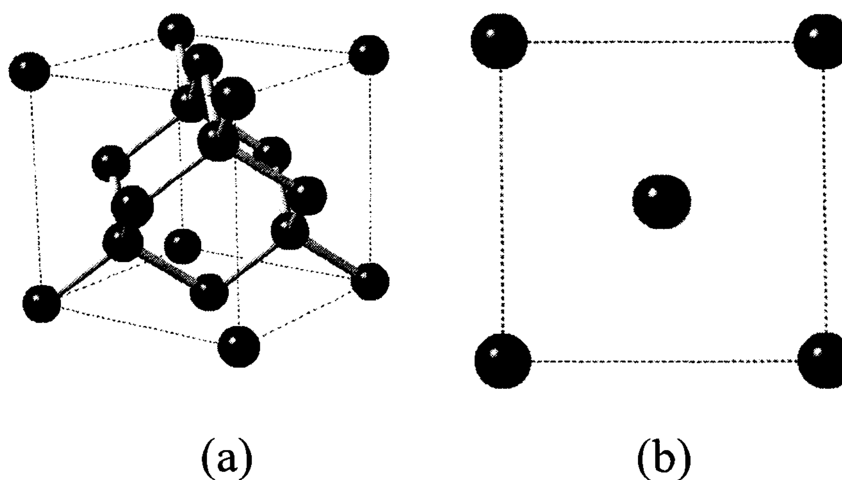

FIG. 3.9. (a) 3D illustration of the diamond structure of silicon showing its bonding structure, (b) sketch of the Si(100). [The free demonstration version of Crystal Maker[1] software was used to create both images].

---

[1] CrystalMaker® : http:// www.crystalmaker.com

Reproduced with permission of the copyright owner. Further reproduction prohibited without permission.

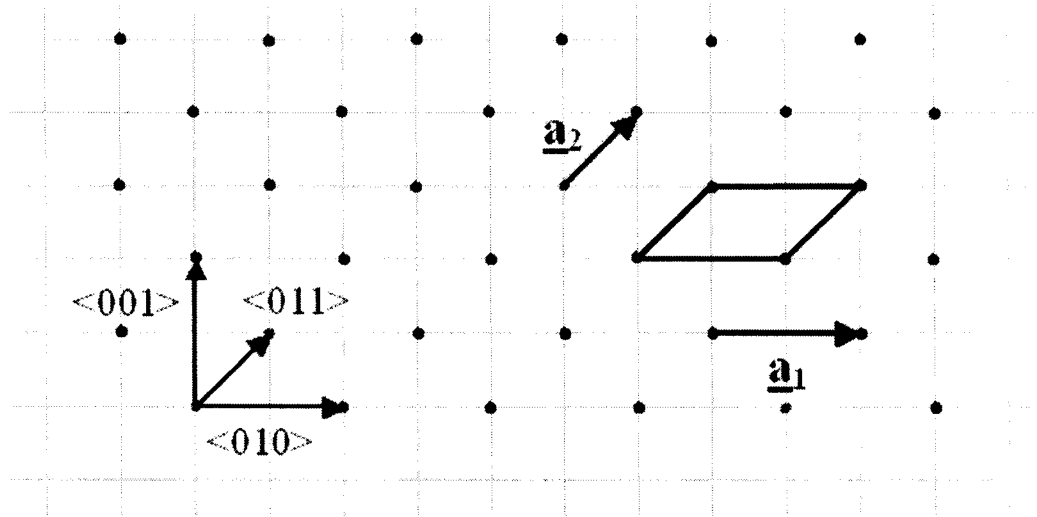

FIG. 3.10. Real net of the Si(100).

The reciprocal lattice basis vectors are defined as

$$\bar{a}_1^* = 2\pi \frac{\bar{a}_2 \times \hat{n}}{A} \tag{3.37}$$

$$\bar{a}_2^* = 2\pi \frac{\hat{n} \times \bar{a}_1}{A} \tag{3.38}$$

where the area A is

$$A = \bar{a}_1 \bullet (\bar{a}_2 \times \hat{n}) \tag{3.39}$$

Silicon has a diamond structure, which is shown in Fig 3.9. The lattice parameter is a = 5.431 Å. So, using Fig. 3.10, the real lattice vectors of Si(100) mesh are

$\underline{\mathbf{a}}_1 = 5.431 \ \langle 010 \rangle$ Å,

$\underline{\mathbf{a}}_2 = \frac{5.431}{\sqrt{2}} \frac{1}{\sqrt{2}} \langle 011 \rangle = 2.716 \ \langle 011 \rangle$ Å,

and the unit vector normal to the surface is $\underline{\mathbf{n}} = \langle 100 \rangle$.

Reproduced with permission of the copyright owner. Further reproduction prohibited without permission.

The inter-planer spacing between the {100} planes is a/4, i.e., 1.358 Å.

The area of the unit mesh is

$$A = \bar{a}_1 \bullet (\bar{a}_2 \times \hat{n}) = \frac{(5.431)^2}{2} \begin{vmatrix} 0 & 1 & 0 \\ 0 & 1 & 1 \\ 1 & 0 & 0 \end{vmatrix} = 14.748 \text{ Å}^2.$$

Hence, by substituting the values for the area and the lattice parameters in Eqs. (3.37) and (3.38), the reciprocal lattice parameters are

$$\bar{a}_1{}^* = 2\pi \frac{\bar{a}_2 \times \hat{n}}{A} = \frac{2\pi}{14.748}\left[2.7155 \ \langle 011 \rangle \times \langle 100 \rangle\right] = 1.157 \ \langle 01\bar{1} \rangle \ \text{Å}^{-1}$$

$$\Rightarrow \ | \ \bar{a}_1{}^* \ | = 1.636 \ \text{Å}^{-1}$$

$$\bar{a}_2{}^* = 2\pi \frac{\hat{n} \times \bar{a}_1}{A} = \frac{2\pi}{14.748}\left[5.431 \langle 100 \rangle \times \langle 010 \rangle\right] = 2.314 \langle 001 \rangle \ \text{Å}^{-1}$$

The reciprocal lattice would have the shape shown in Fig. 3.11.

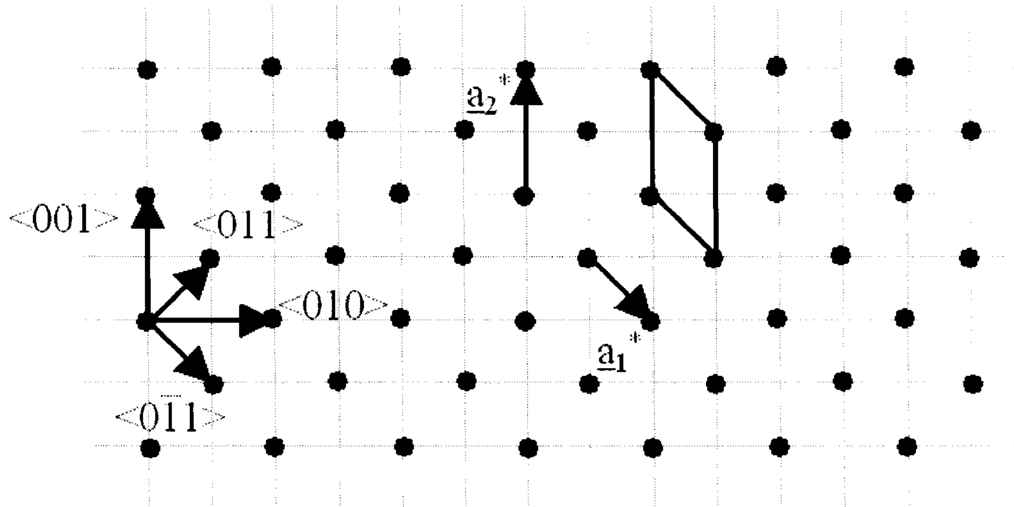

FIG. 3.11. Reciprocal net of Si(100).

Reproduced with permission of the copyright owner. Further reproduction prohibited without permission.

During the experimental work presented in this dissertation, only one direction of incidence will be used, unless otherwise stated. The reciprocal lattice parameter is given by

$$a^* = \frac{2\pi W}{\lambda L} \ , \qquad (3.40)$$

where W is the streak spacing on the screen, L is the screen-sample distance and λ is the wavelength of the electron wave given by Eq. (3.3). For electron accelerating voltage of 8.6 kV, λ is found to be 0.134 Å. Using Fig. 3.13, a^* is found to be 1.592 $Å^{-1}$ for W_1 and 1.622 $Å^{-1}$ for W_2. The average of both these values, accounting for the average value of a^*, is 1.61 $Å^{-1}$. Therefore, the direction of incidence of the electron beam is $\langle 01\bar{1} \rangle$.

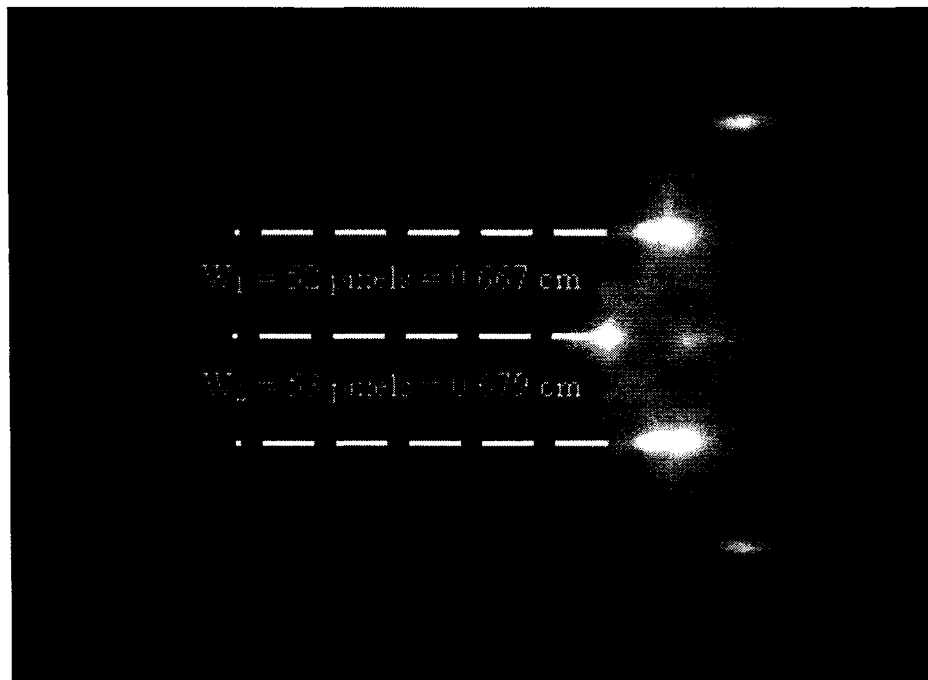

FIG. 3.12. A RHEED pattern for Si(100)-1×1 used to calculate the direction of incidence.

Reproduced with permission of the copyright owner. Further reproduction prohibited without permission.

When the electron beam is incident down the staircase of a vicinal surface, the intensity profile along the (00) streak shows split peaks due to interference from different terraces [34]. The split spacing is inversely proportional to the terrace width. Terrace width is given by $T = 2\pi/\delta$, where δ is (00) split spacing measured in $Å^{-1}$, after subtracting the instrumental response (given by the FWHM of the (00) peak in the in-phase condition measured normal to the surface) [34,35]. The splitting is better seen in the out-of-phase condition, but it is always there, even close to the in-phase condition [35]. Using Fig. 3.13, the (00) streak splitting spacing, δ, equals 0.398 $Å^{-1}$. Subtracting the instrumental response, which is found to be 0.367 $Å^{-1}$, the average terrace width is ~205 Å. Using Fig. 3.14, the miscut angle is given by $\theta = \sin^{-1}(d/T)$ ~0.38°.

FIG. 3.13. A RHEED pattern for Si(100)-2×1 used to calculate the average terrace width by calculating the splitting in the (00) peak.

Reproduced with permission of the copyright owner. Further reproduction prohibited without permission.

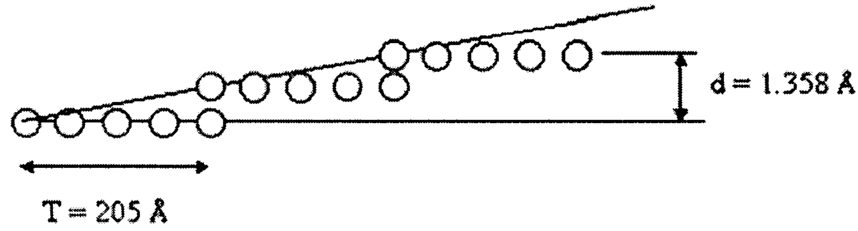

FIG. 3.14. Schematic of the vicinal surface used to calculate the miscut angle.

III.6.B. Ge(100)

Ge also has a diamond structure, with lattice parameter of a = 5.646 Å. So, using Fig. 3.10, the real lattice vectors of Ge(100) mesh are

$\underline{\mathbf{a}}_1 = 5.646 \langle 010 \rangle$ Å,

$\underline{\mathbf{a}}_2 = \frac{5.646}{\sqrt{2}} \frac{1}{\sqrt{2}} \langle 011 \rangle = 2.823 \langle 011 \rangle$ Å,

and the unit vector normal to the surface is $\underline{\mathbf{n}} = \langle 100 \rangle$.

The inter-planer spacing between the {100} planes is a/4, i.e., 1.412 Å.

The area of the unit mesh is

$$A = \bar{a}_1 \bullet (\bar{a}_2 \times \hat{n}) = \frac{(5.646)^2}{2} \begin{vmatrix} 0 & 1 & 0 \\ 0 & 1 & 1 \\ 1 & 0 & 0 \end{vmatrix} = 15.939 \text{ Å}^2.$$

Hence, by substituting the values for the area and the lattice parameters in Eqs. (3.37) and (3.38), the reciprocal lattice parameters are

$$\bar{a}_1^* = 2\pi \frac{\bar{a}_2 \times \hat{n}}{A} = \frac{2\pi}{15.939} \left[2.823 \ \langle 011 \rangle \times \langle 100 \rangle \right] = 1.113 \ \langle 01\bar{1} \rangle \text{ Å}^{-1}$$

$$\Rightarrow |\ \bar{a}_1^*\ | = 1.574 \text{ Å}^{-1}$$

Reproduced with permission of the copyright owner. Further reproduction prohibited without permission.

$$\bar{a}_2^* = 2\pi \frac{\hat{n} \times \bar{a}_1}{A} = \frac{2\pi}{15.939}\left[5.646\langle 100\rangle \times \langle 010\rangle\right] = 2.226\langle 001\rangle \text{ Å}^{-1}$$

The reciprocal lattice would have the shape shown in Fig. 3.11.

III.7. Indexing transmission RHEED patterns

Transmission RHEED patterns are indexed using three indices, similar to diffraction from bulk materials and selected area electron diffraction (SAED) [30]. Different alternatives can be used to index transmission patterns [30]. The following procedure is used to index transmission spots from Ge QD.

1. Use "Diamond" software [36] to generate the expected XRD pattern of Ge crystal, Fig. 3.15. You may also use "CaRIne" software [37] to generate similar powder diffraction patterns; however, some values may differ slightly.
2. From the graph, extract the angles associated with the diffraction planes.
3. Use these data to calculate the interplaner distances of the above planes, Table 3.1.
4. Obtain a RHEED diffraction pattern of Ge QD at a certain azimuth, Fig. 3.16.
5. Take one point as your (000) point. Here we take one point on the shadow edge.
6. Measure the distances of the transmission spots to the (000) point in "cm" and the angles they make with the line perpendicular to the surface and passing through the (000), Table 3.2.
7. Use Eq. 3.35 and the calculated electron wavelength to convert the above distances into *d*-values, Table 3.2.

Reproduced with permission of the copyright owner. Further reproduction prohibited without permission.

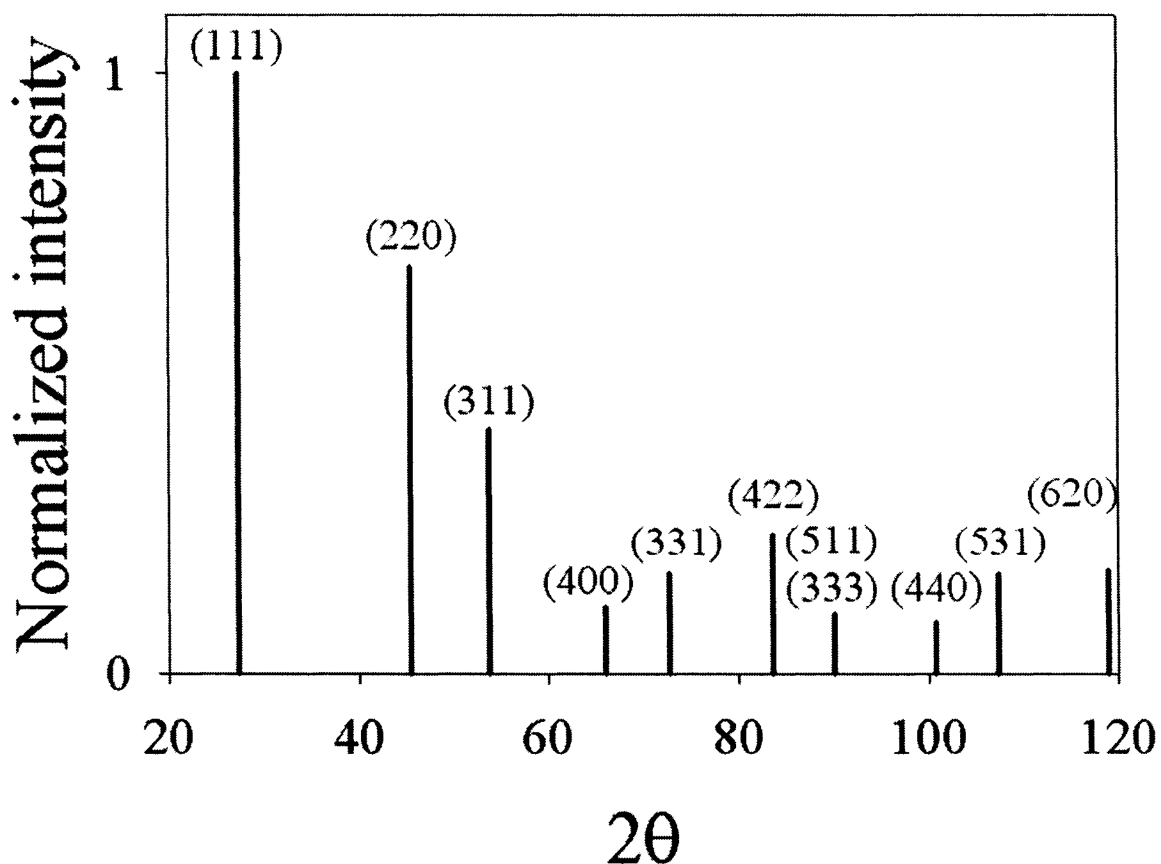

FIG. 3.15. Expected XRD pattern of Ge crystal [The free demonstration version of Diamond software [36] was used to generate these data].

Table 3.1. Data extracted from Fig. 3.15 and the calculated interplaner distances, *d*, of the associated planes.

Theoretical calculations					
(hkl)	**2θ**	**λ (Å)**	***d* (Å)**	***d*/2 (Å)**	**2*d* (Å)**
111	27.28	1.541	3.26894	1.63447	6.53788
220	45.3	1.541	2.001736	1.000868	4.003472
311	53.68	1.541	1.707333	0.853666	3.414666
400	65.99	1.541	1.415525	0.707763	2.83105
331	72.8	1.541	1.298976	0.649488	2.597952
422	83.66	1.541	1.905807	0.952903	3.811613
333/511	90.05	1.541	2.50377	1.251885	5.00754
440	100.73	1.541	2.949317	1.474658	5.898633
531	107.3	1.541	3.44106	1.72053	6.882119
620	118.86	1.541	3.799634	1.899817	7.599267

Reproduced with permission of the copyright owner. Further reproduction prohibited without permission.

8. Compare the measured values to the calculated ones to assign Miller indices to each spot. Tabulate all the possible indices, since it is normal to find more than one set for each spot.
9. You have to consider an error margin, Δd, in the measured values of *d-value* due to uncertainties in the spacing measurement and in the camera constant calibration.
10. For each possible *hkl* candidate, calculate the angles between these spots, α_{ij}, using the dot product rule, $\alpha_{ij} = cos^{-1} \frac{\bar{a}_i \bullet \bar{a}_j}{|a_i|.|a_j|}$.
11. Use the elimination process by comparing the measured and calculated angles, in order to assign the correct indices.
12. Determine the zone axis [*uvw*]. This is done by considering any two known [*hkl*] vectors within the diffracted zone such as finding out the components $u = k_1 l_2 - k_2 l_1$, $v = l_1 h_2 - l_2 h_1$, and $w = h_1 k_2 - h_2 k_1$.
13. Follow the same process to find the correct indexing for each spot, taking advantage of the already indexed ones and by making use of the calculated zone axis, since the zone equation, 3.36, is always satisfied.
14. Follow the above procedure until all spots are indexed.

By comparing Tables 3.1 and 3.2 and considering Fig. 3.16, the expected indices for spot (1) are (200) and (440), those for spot (2) are (400) and (880), for spot (3) are (111) and (531), and for spot (4) are (311) and (10,6,2). Considering first spots (1) and (3), the angles between (200) and (111), (200) and (531), (440) and (111), (440) and (531) are 54.7°, 32.3°, 65.9°, and 80°, respectively. It is clear that only the first pair has

Reproduced with permission of the copyright owner. Further reproduction prohibited without permission.

an angle value that agrees with the measured one, i.e., spot (1) is (200) and spot (3) is (111). This implies that the zone axis is $[0\bar{1}1]$. Using this value and making use of the zone equation, spots (2) and (4) should be (400) and (311), respectively. Also, using this information it is easy to index the rest of the spots. A comparison of the values of the measured and the calculated angles should be used to confirm the indices, Table 3.3. The final indexing is shown in Fig. 3.17.

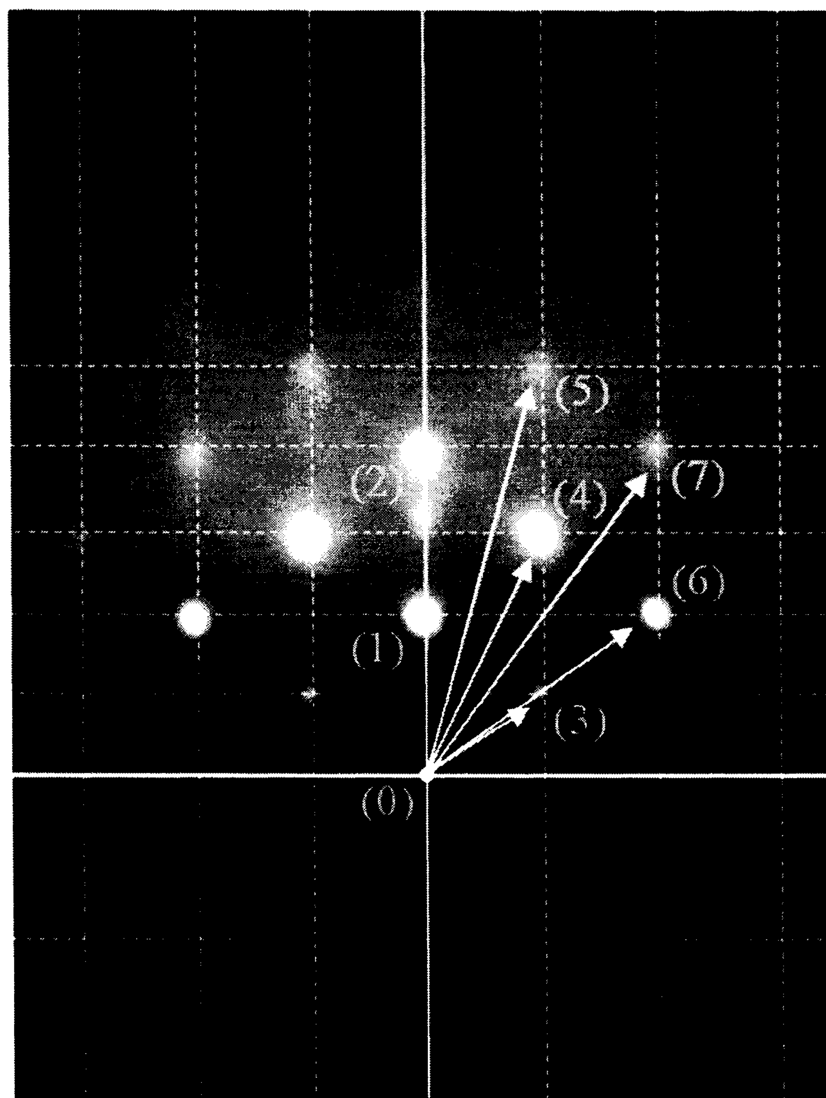

FIG. 3.16. Transmission RHEED pattern of Ge QD [obtained at 12 kV accelerating voltage].

Reproduced with permission of the copyright owner. Further reproduction prohibited without permission.

Table 3.2. Interplaner distances calculated from the measurement of spot distances in Fig. 3.16.

Experimental measurements						
Spot	**λ (Å)**	**R (cm)**	**α_{ij}**	***d* (Å)**	***d*/2 (Å)**	**2*d* (Å)**
1	0.111	**1.22619**	**0**	3.077825	1.538913	6.15565
2	0.111	**2.440476**	**0**	1.54642	0.77321	3.092839
3	0.111	**1.064345**	**52.8**	3.545842	1.772921	7.091684
4	0.111	**2.035714**	**25.2**	1.853895	0.926947	3.707789
5	0.111	**3.133333**	**15.2**	1.204468	0.602234	2.408936
6	0.111	**2.088333**	**53.6**	1.807183	0.903591	3.614366
7	0.111	**2.988095**	**34.8**	1.263012	0.631506	2.526024

Table 3.3. Comparison of the calculated and measured values of angles between the index planes.

Angles comparisons			
Spot	**Index**	**$\alpha_{calculated}$ (degrees)**	**$\alpha_{measured}$ (degrees)**
1	(200)	0	0
2	(400)	0	0
3	(111)	54.7	52.8
4	(311)	25.2	25.2
5	(511)	15.7	15.2
6	(222)	54.7	53.6
7	(422)	35.3	34.8

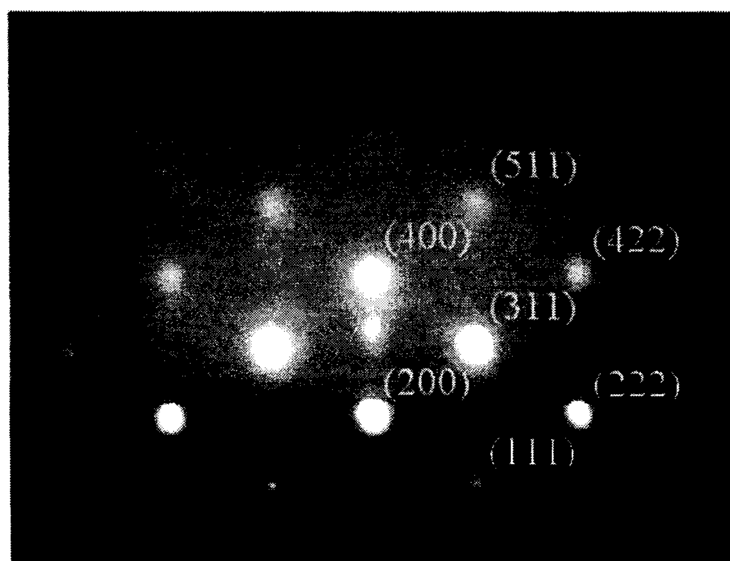

FIG. 3.17. Indexed transmission pattern of Ge QD.

Reproduced with permission of the copyright owner. Further reproduction prohibited without permission.

III.8. References

[1] W. Braun, "Applied RHEED," Springer-Verlag (1999).

[2] K. Britze and G. Meyer-Ehmsen, Surf. Sci. **77**, 131 (1978).

[3] X. Zeng, B. Lin, I. El-Kholy, and H. Elsayed-Ali, "Time-resolved reflection high-energy electron diffraction study of the Ge(111)-c(2×8) – (1×1) phase transition," Phys. Rev. B **59**, 14907- 14910 (1999).

[4] X. Zeng, B. Lin, I. El-Kholy, and H. Elsayed-Ali, "Time resolved structural study of the Ge(111) high-temperature phase transition," Surf. Sci. **439**, 95- 102 (1999).

[5] M. Itoh, "Relation between surface reconstructions and RHEED intensity oscillations," Phys. Rev. B **58**, 6716 – 6719 (1998).

[6] J. Y. Lee, J. Y. Juang, J. H. Ou, Y. F. Chen, K. H. Wu, T. M. Uen, and Y. S. Gou, "RHEED intensity oscillations in homoepitaxial growth of $SrTiO_3$ films," Physica B **284-288**, 2099- 2100 (2000).

[7] K. Inumaru, T. Ohara, S. Yamanaka, "Pulsed laser deposition of epitaxial titanium nitide on MgO(001) monitored by RHEED oscillation," Appl. Surf. Sci. **158**, 375-377 (2000).

[8] Z. Mitura and J. L. Beeby, "Theoretical studies on the quantitative interpretation of RHEED data," J. Phys.: Condens. Matter **8**, 8717- 8731 (1996).

[9] M. G. Lagally, D. E. Savage, and M. C. Tringides, "Diffraction from disordered surfaces: an overview," in "Reflection high-energy electron diffraction and reflection electron imaging of surfaces," eds. P. K. Larsen and P. J. Dobson, Plenum Press, New York (1988).

Reproduced with permission of the copyright owner. Further reproduction prohibited without permission.

[10] J. E. Mahan, K. M. Geib, G. Y. Robinson, and R. G. Long, "A review of the geometrical fundamentals of reflection high-energy electron diffraction with application to silicon surfaces," J. Vac. Sci. Technol. A **8(5)**, 3692- 3700 (1990).

[11] D. H. A. Blank, G. J. H. M. Rijnders, G. Koster, and H. Rogalla, "In-situ monitoring during pulsed laser deposition using RHEED at high pressure," Appl. Surf. Sci. **127**, 633–638 (1998).

[12] N. L. Yakovlev, P. A. Maksym, and J. L. Beeby, "Ionic potential analysis of RHEED rocking curves from fluoride structures," Surf. Sci. **529**, 319-328 (2003).

[13] Y. Shigeta and Y. Fukaya, "Structural phase transition and thermal vibration of surface atoms studied by reflection high-energy electron diffraction," Surf. Sci. **237**, 21-28 (2004).

[14] Y. Shigeta, Y. Fukaya, H. Mitsui, and K. Nakamura, "Observation of RHEED rocking curves during Si/Si(111) film growth," Surf. Sci. **402-404**, 313- 317 (1998).

[15] Y. Fukaya and Y. Shigeta, "Fast measurement of rocking curve of reflection high-energy electron diffraction by using quasi-1D convergent beam," Surf. Sci. **530**, 175-180 (2003).

[16] J. M. Zuo, U. Weierstall, L. M. Peng, and J. C. H. Spence, "Surface structural sensitivity of convergent-beam RHEED: Si(001)2×1 models compared with dynamical simulations ," Ultramicroscopy **81**, 235-224 (2000).

[17] U. Weierstall, J. M. Zuo, T. Kjørsvik, and J. C. H. Spence, "convergent-beam RHEED in a dedicated UHV diffraction camera and applications to Si reconstructed surfaces," Surf. Sci. **442**, 239-250 (1999).

Reproduced with permission of the copyright owner. Further reproduction prohibited without permission.

[18] P. Staib, W. Tappe, and J. P. Contour, "Imaging energy analyzer for RHEED: energy filtered diffraction patterns and In-situ electron energy loss spectroscopy," J. Crys. Growth **201**, 45-49 (1999).

[19] X. Zeng and H. E. Elsayed-Ali, "Time-resolved electron diffraction study of the Ge(100)-(2×1)–(1×1) phase transition," Surf. Sci. **497**, 373-384 (2002).

[20] P. Sandström, E. B. Svedberg, J. Birch, and J.-E. Sundgren, "Time-resolved measurements of the formation of single-domain epitaxial Ni films on MgO(111) substrates using in-situ RHEED analysis," Surf. Sci. **437**, L767–L772 (1999).

[21] M. Dabrowska-Szata, "Analysis of RHEED pattern from semiconductor surfaces," Mat. Chem. Phys. **81**, 257–259 (2003).

[22] E. Bauer, "Reflection electron diffraction (RED)," in "Techniques for the direct observation of structure and imperfections," ed. R. F. Bunshah, Techniques of metals research Vol. II, Part 2, p. 501, Interscience, New York (1969).

[23] J. J. Sakurai, "Modern Quantum Mechanics," Addison and Wesley (1994)

[24] J. E. G. Farina, "Quantum theory of scattering processes," Pergamon Press (1973)

[25] D. K. Ferry, "Quantum Mechanics: An Introduction for Device Physicists and Electrical Engineers," (2001).

[26] M. G. Lagally, "Diffraction techniques," in "Methods of experimental physics: surfaces," eds. R. L. Park and M. G. Lagally, Academic Press, Orlando, FL (1985).

[27] W. S. M. Werner, C. Tomastik, T. Cabela, G. Richter, and H. Störi, "Electron inelastic mean free path measured by elastic peak electron spectroscopy for 24 solids between 50 and 3400 eV," Surf. Sci. **470**, L123-L128 (2000).

Reproduced with permission of the copyright owner. Further reproduction prohibited without permission.

[28] J. Powell, A. Jablonski, I. S. Tilinin, S. Tanuma, and D. R. Penn, "Surface sensitivity of auger-electron spectroscopy and x-ray photoelectron spectroscopy," J. Elect. Spect. Rel. Phen. **98-99**, 1-15 (1999).

[29] M. P. Seah and W. A. Dench, "Quantitative electron spectroscopy of surfaces: A standard data base for electron inelastic mean free paths in solids," Surf. Interface. Anal.**1**, 2-11 (1979)

[30] M. De Graef, "Introduction to conventional transmission electron microscope," UK university press, Cambridge, (2003).

[31] D. Litvinov, T. O'Donnell, and R. Clarke, "*In situ* thin film texture determination," J. Appl. Phys. **85**, 2151–2156 (1999).

[32] S. Andrieu and P. Frechard, "What information can be obtained by RHEED applied on polycrystalline films," Surf. Sci **360**, 289 - 296 (1996).

[33] Z. Zhang, P. A. VanRompay, J. A. Nees, R. Clarke, X. Pan, P. P. Pronko, "Nitride film deposition by femtosecond and nanosecond laser ablation in low-pressure nitrogen discharge gas," Appl. Surf. Sci. 145- 155, 165-171 (2000).

[34] K. A. Elamrawi, M. A. Hafez, and H. E. Elsayed-Ali, "Atomic hydrogen-cleaned GaAs(100) negative electron affinity photocathode: Surface studies with reflection high-energy electron and quantum efficiency," J. Vac. Sci. Technol. A **18(3)**, 951–955 (2000).

[35] M. A. Hafez and H. E. Elsayed-Ali, "Atomic hydrogen cleaning of InP(100): Electron yield and surface morphology of negative electron affinity activated surfaces," J. Appl. Phys. **91**, 1256 –1264 (2002).

[36] Diamond version 3.1d: http://www.crystalimpact.com/diamond/

[37] CaRIne Crystallography 3.1: http://pros.orange.fr/carine.crystallography/index.html

Reproduced with permission of the copyright owner. Further reproduction prohibited without permission.

CHAPTER IV

SELF-ASSEMBLY OF Ge QUANTUM DOTS ON Si

IV.1. Introduction

The large number of publications reflects the great deal of attention being paid to the study of self-assembled nanostructures in heteroepitaxial systems. Self-assembly has been used to fabricate quantum dots (QD), which are mainly used in optical devices. Examples of such systems are Ge/Si [1-3], InAs/GaAs [4-6], and InSb/GaSb [7]. Magnetic QDs such as Fe-Pt, which are used in hard disks, have been self-assembled [8,9]. $Ga_xIn_{1-x}As$ quantum wires have also been self-assembled to serve as active media in infrared photodetectors [10,11]. The most important reason for the interest in such nanostructures is their electronic structure that differs from that of the bulk and its impact on their physical properties. The densities of states in 1, 2, 3 dimensional systems are given by the following equations, respectively, [12.13]

$$g_{0D} \propto \delta(E - E_i),\ i = 1,2,3... \tag{4.1}$$

$$g_{1D} = \sqrt{\frac{2\pi m}{h^2}} \frac{1}{\sqrt{E - E_{\min}}},\ for\ E > E_{\min} \tag{4.2}$$

$$g_{2D} = \frac{4\pi m}{h^2},\ for\ E > E_{\min} \tag{4.3}$$

$$g_{3D} = \frac{8\pi\sqrt{2}}{h^2} m^{3/2} \sqrt{E - E_{\min}},\ for\ E > E_{\min} \tag{4.4}$$

Reproduced with permission of the copyright owner. Further reproduction prohibited without permission.

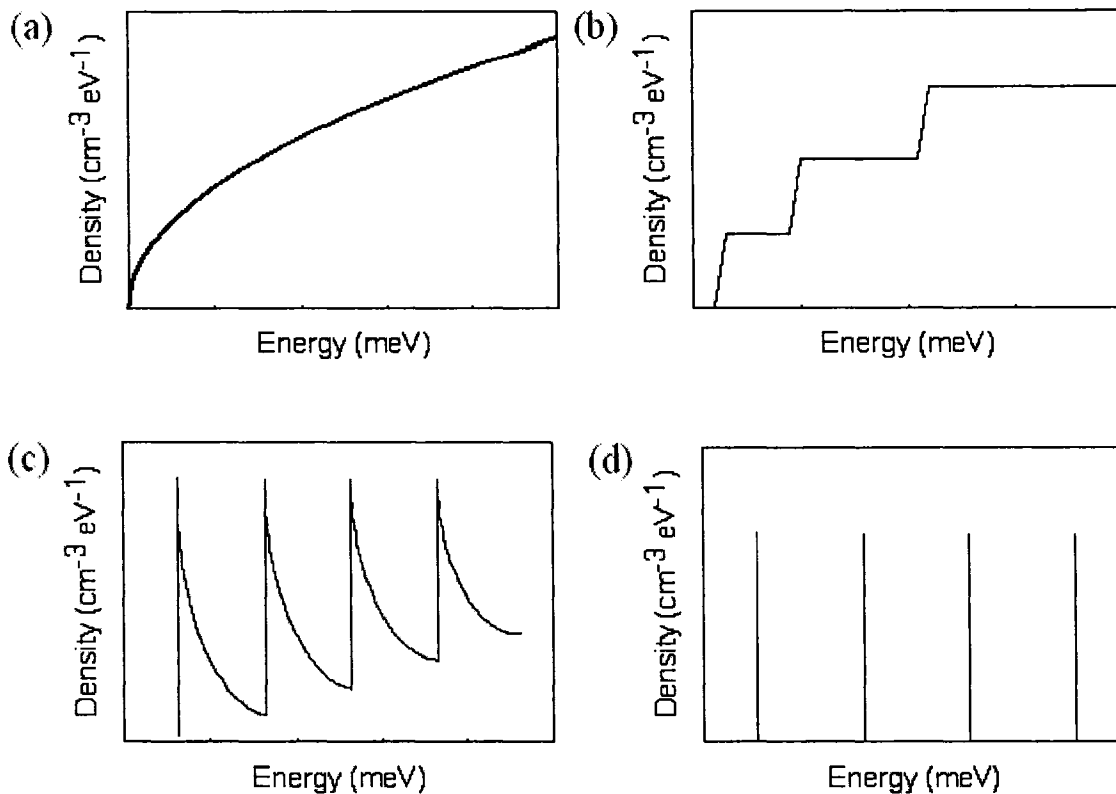

FIG. 4.1. Schematic diagram of the density of states (DOS) for (a) 3D bulk semiconductor, (b) 2D quantum well, (c) 1D quantum wire, and (d) 0D quantum dot.

A comparison between the densities of states of the three cases, along with the 0-dimensional case of QD, is given in Fig. 4.1. The electronic structure of the QDs consists of delta peaks, as shown in Fig. 4.1(d) [14,15]. Therefore, it is sometimes referred to as the quantum dots, which consists of $\sim 10^6$ atoms, as "superatoms."

Self-assembly of nanostructures takes place via the Stranski-Krastanow (SK) growth in lattice-mismatched systems. In some cases, such a technique represents an alternative to lithography-based techniques [16]. It may be worthwhile to mention that scanning probe microscopy (SPM) based techniques represent another alternative to optical lithography-based techniques in some cases [17,18]. Using self-assembly, it is

Reproduced with permission of the copyright owner. Further reproduction prohibited without permission.

expected to fabricate defect-free nanometer QD's and overcome some of the problems of lithography, such as contamination, defect formation, and poor interface quality. Also in this technique, no etching or implantation processes are required. However, some of its drawbacks are the size and spatial non-uniformity of the QD's. A thorough understanding of these two problems and their origin would enable their control, which is of great importance to technology. This is one of the motivations behind the extensive work on this topic.

The study of the self-assembly and self-organization of nanostructures in heteroepitaxial systems is important for a fundamental understanding of the properties of reduced-size condensed matter systems and for the development of quantum devices [1,17]. From a basic physics point of view, Ge/Si is a model system for studying the growth dynamics of the SK mode. Ge QDs were previously grown on Si(100) by molecular beam epitaxy (MBE) [19-24], chemical vapor deposition (CVD) [25,26], and liquid phase epitaxy (LPE) [27,28]. The shape and size distributions of the QDs were found to depend on the deposition technique as well as the deposition conditions. When Sb was used as a surfactant in the MBE growth of Ge/Si(100), the initial island shape changed from {105}-faceted to {117}-faceted [29]. When Ge was grown by liquid phase epitaxy, {115}-faceted islands were first observed instead of the {105}-faceted ones. As the coverage was increased, {111}-faceted pyramids were formed [27,28].

Ge QDs have interesting mid-infrared optical properties [29,30]. It was shown that the photoluminescence peak of a single Ge QD dot layer changes from 1.3 to 1.6 μm by increasing its thickness from 5 to 9 ML [30]. Such wavelength tunability is one of the reasons behind the great interest in Ge QD-based devices. Self-assembled Ge QDs grown

Reproduced with permission of the copyright owner. Further reproduction prohibited without permission.

on Si are used in fabricating devices such as mid-infrared photodetectors [31,32], thermoelectric devices [33], and enhanced performance Si solar cells [34-36]. Generally, QD-based devices consist of tens of multilayers of doped or undoped QDs separated by spacing layers. Apparently, the first two features of PLD make it a strong candidate for growing multilayered devices. In this case, only targets of different materials in the desired stoichiometry and doping are required without the need for residual gases or doping sources. In order to design efficient Ge QD-based devices by PLD, a clear understanding of how to control their physical properties through controlling the deposition parameters is required. The physical parameters of QDs depend strongly on their shape and size distribution, while the device's quantum efficiency is mainly affected by the density and spatial distribution of the QDs. Besides the substrate temperature, laser parameters (fluence, repetition rate, and wavelength) are unique controlling parameters of PLD. The density and size distributions of QDs are mainly controlled by both the deposition rate and adatoms' kinetic energy, which affects surface diffusion [37]. In the case of PLD, adatom surface diffusion is controlled by both the substrate temperature and the laser fluence, while deposition rate is mainly controlled by the laser fluence and the repetition rate. The spatial distribution depends on the homogeneity of the atomic flux, which is governed by the laser fluence. However, the dependence of the QD shape on deposition parameters has not been sufficiently explored for PLD. The current work aims to investigate the growth dynamics and the morphology of self-assembled Ge QDs on Si(100)-(2×1).

Reproduced with permission of the copyright owner. Further reproduction prohibited without permission.

IV.2. Self-assembly of QD by Stranski-Krastanov (SK) growth

The simplest model to describe thin film growth is the classical thermodynamical model. In such a model, depending on the relationship between the film surface energy γ_A, the substrate surface energy γ_B, and the interface energy γ^*, the film grows in one of three growth modes [38,39]:

(1) Frank-van der Merwe (layer-by-layer): arises when the deposited atoms are more strongly attracted to the substrate than they are to themselves (i.e. $\gamma_A < \gamma_B + \gamma^*$);

(2) Volmer-Weber (3D islands): occurs when the deposited atoms are more strongly attracted to themselves than they are to the substrate (i.e. $\gamma_A > \gamma_B + \gamma^*$);

(3) Stranski-Krastanow (SK): is a combination of the first two modes.

In the SK mode, growth starts by the formation of a two-dimensional (2D) "wetting layer," in which the film lattice constant adapts itself to that of the substrate, Fig. 4.2(b) [1,17,38]. Depending on the growth conditions, the 2D growth takes place by either two-dimensional nucleation (layer-by layer) or step-flow. However, due to the lattice mismatch between the film and the substrate, an elastic strain arises in the wetting layer that increases linearly with the increase of the film thickness. The lattice mismatch (or misfit) is defined as $\varepsilon = (a_A - a_B)/a_B$,[1] where a_A is the film lattice constant and a_B is that of the substrate. Apparently, there are two types of strain: (a) *tensile strain*, which occurs when the lattice constant of the substrate is larger than that of the film, and (b)

[1] In some publications, the mismatch is defined as $\varepsilon = (a_A - a_B)/a_A$, see for example Stoleru et al., 2002.

Reproduced with permission of the copyright owner. Further reproduction prohibited without permission.

compressive strain, which occurs when the lattice constant of the film is larger than that of the substrate.

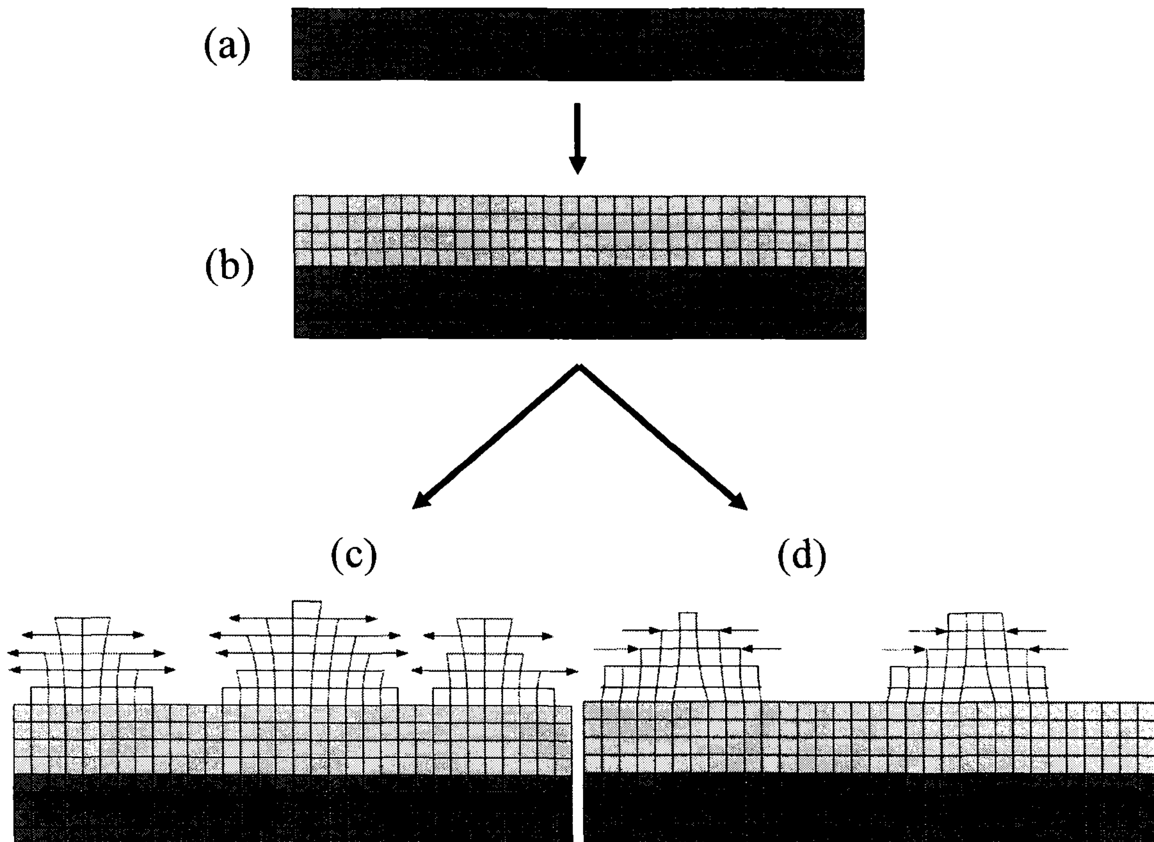

FIG. 4.2. Schematics of the strain relief stages in the Stranski-Krastanov growth for the case of compressive strain: (a) Starting substrate, (b) growth of a psedumorphic smooth wetting layer, (b) formation of coherently strained 3D islands that are fully strained at the bottom and completely relaxed at the top, i.e. having the film lattice constant, (c) introduction of misfit dislocations in the 3D islands. The arrows indicate the direction of elastic strain relief.

As the strain increases, the film seeks relaxation or "relief", which occurs by one of the following two routes:

Reproduced with permission of the copyright owner. Further reproduction prohibited without permission.

(a) Elastic relaxation that occurs by one of three mechanisms: (i) surface reconstruction of the wetting layer, (ii) step bunching of the wetting layer, or (iii) the formation of coherent (defect-free) 3D islands, Fig 4.2(c).

(b) Plastic relaxation that occurs by the formation of misfit dislocations in the wetting layer. In some systems misfit dislocations form in the 3D islands, if the formation of the 3D clusters is not enough to relax the system, Fig 4.2(d).

There is a competition between these two relief mechanisms and the value of the misfit is the key factor. It was shown that the barrier for 3D nucleation scales as ε^{-4}, while that for dislocation nucleation scales as ε^{-1} [40]. Therefore, for small ε misfit dislocations dominate, while 3D nucleation dominates for larger values of ε. This is the reason why pure Ge deposition on Si (large misfit of $\varepsilon = 0.042$) results in relaxation by 3D islands formation [1], while in the case of Ge_xSi_{1-x} (for example for $x = 0.15$, resulting in $\varepsilon = 0.006$) relaxation takes place by nucleation of misfit dislocations where the surface remains smooth with no 3D nucleation [41]. This shows the effect of interdiffusion, which depends mainly on the substrate temperature, on the smoothness or the morphology of the grown film. From the optical and magnetic applications point of view, defect-free coherent islands are mainly demanded. However, some researchers believe that the residual strain can have interesting effects on the electrical, optical and even magnetic properties of the semiconductor structures. This explains the interest in theoretically calculating and modeling the strain in the semiconductor nanosystems [42,43]. The three dimensional Schrödinger equation has been solved analytically for the "pyramidal" quantum dots of (In,Ga)As grown on GaAs, while the influence of strain on the band gap of the dots has been considered [44]. The strain was shown to modify the

Reproduced with permission of the copyright owner. Further reproduction prohibited without permission.

energy levels and the wave functions for the confined carriers, which affects the electronic structure and hence the electrical and optical properties of the dots. For example, the conduction band could be written as

$$E_c(\varepsilon) = E_c^0 + \delta E_c(\varepsilon)\,, \qquad (4.5)$$

where E_c^0 is the offset of the unstrained conduction band and δE_c is the strain-induced shift of the conduction band [46]. Though the effect of the strain on the valance band is more complicated [45], the strain was found to largely increase the band gap due to the considerable hydrostatic pressure.

An ideal strained heteroepitaxial system seeks relief by either the plastic or the elastic relaxation. However, in real systems a combination of both relaxation mechanisms takes place. For example, in the case of growing Ge on Si(100) by MBE, before the transformation into the 3D growth, the Ge wetting layer relieves its strain by the formation of a ($2\times N$) reconstruction in which every Nth dimmer of the (2×1) reconstruction is missing [1,46,47]. The distance between the trenches of the ($2\times N$) reconstruction decreases with the coverage, or, in other words, the periodicity, N, decreases with the coverage. Another example of the combination of both elastic and plastic relaxations is the introduction of misfit dislocations into the large 3D islands, Fig 4.2(d). This happens if the relaxation by 3D islands formation is not enough to relax the strain of the system.

When the thickness of the wetting layer reaches a critical value, h_c, which varies from one system to another, the strain becomes so critical that the film seeks relief by three-dimensional nucleation. The value of the "transition" critical thickness was

Reproduced with permission of the copyright owner. Further reproduction prohibited without permission.

estimated theoretically, assuming that the initial island shape is pyramidal, to have the form

$$h_c = \frac{5(1-\nu_e)\varepsilon_{sw}}{2Y[\ln(\frac{a_A}{a_B})]^2}\tan\theta, \tag{4.6}$$

where ν_e is Poisson's ratio, Y is Young's modulus, ε_{sw} vertical surface energy per unit area, and θ the angle between the ridgeline and the bottom surface of the pyramid [48]. More recently, the value of the critical thickness was shown to increase with the intermixing between the film and the substrate atoms [17]. In most systems, the formed nuclei are all of the same type or shape and they are free of defects and dislocations. In the case of growth by molecular beam epitaxy (MBE), the density of such coherent 3D islands varies with the substrate temperature T and the deposition flux F as

$$N \propto (F/D)^x, \tag{4.7}$$

where D is the diffusion constant and x is a positive number that depends on the details of the system [49]. The diffusion constant is given as

$$D = (\nu_d a^2/4)\ exp\text{-}(E_d/kT), \tag{4.8}$$

where E_d is the diffusion energy, the preexponential ν_d measures the jumping probability of an atom from one position to another at a distance a [38]. However, in some systems, as the film coverage increases other types of nuclei may develop. In others, defects and dislocations start to form in the 3D islands when they grow in size. The shape of the 3D islands may change from one deposition technique to another if a surfactant is used [17].

Reproduced with permission of the copyright owner. Further reproduction prohibited without permission.

IV.3. SK growth of Ge QD on Si

In the model system of the SK growth, i.e., deposition of Ge/Si(100) by MBE, nucleation starts by the formation of rectangular {105}-faceted three-dimensional islands (called "hut" clusters), [21]. As the film coverage increases, multi-faceted "dome" clusters that are faceted by {113} and {102} planes start to appear along with the {105} "hut" clusters. If the thickness increases more, large clusters called "super-domes" start to appear [25,50]. It was found that if Sb is used as a surfactant in the MBE growth of Ge/Si(100), the initial island shape changes from {105} to {117}-faceted with the increase of Sb concentration [51]. On the other hand, if Ge is grown on Si(100) by liquid phase epitaxy (LPE), {115} faceted islands are first observed instead of the {105}-faceted ones. As the coverage increases, pyramids bounded by {111} facets are formed [27,28]. The case is much simpler for the growth of Ge/Si(111), in which the three-dimensional islands were found to be all of the same type, i.e., coherent (dislocation-free) tetrahedrons with {113}-faceted sidewalls and flat {111}-faceted tops [53].

From the application point of view, arrays of organized, homogeneous (both in size and shape), ordered, and closely spaced quantum dots are required. To understand how to control the growth of self-assembled QDs, a large amount of work is published every year. A number of parameters are expected to affect the shape and size distribution of such dots:

1) Deposition technique: As mentioned above, the shape of the islands differs in the case of LPE from that of MBE. It was also reported that the growth dynamics

Reproduced with permission of the copyright owner. Further reproduction prohibited without permission.

differs in the case of chemical vapor deposition (CVD) from both of these techniques [1].

2) Substrate temperature: This affects the growth in a complex way, since temperature controls both surface diffusion and intermixing. As discussed above, interdiffusion acts to decrease the lattice mismatch, which increases the critical thickness of the 3D islands formation. Diffusion, on the other hand, is expected to increase the average island size.
3) Surfactants: As the case of Sb in the growth of Ge/Si(100), surfactants are expected to affect the equilibrium shape of the quantum dots, resulting in the change of their electronic structures and hence their physical properties [51].

IV.4. Experiment

An ultrahigh vacuum chamber is used for deposition. The Si substrate is heated by direct current to obtain high temperatures. The Ge target is mounted on a rotated sample holder with a variable rotation speed. Target rotation during PLD minimizes the formation of particulates by exposing a fresh area to the laser. An Nd:YAG laser (1064 nm, 40 ns, 10 Hz) is used to ablate the Ge target. The laser is focused on the rotating target with a spot size of ~330 μm (measured at 1/e of the peak value). The system is designed so that the laser is incident on the target at 45°. To *in situ* monitor the deposition, a 15-keV continuous electron gun is used to obtain reflection high-energy electron diffraction (RHEED) patterns during growth. A phosphor screen is used to

Reproduced with permission of the copyright owner. Further reproduction prohibited without permission.

display the electron diffraction pattern, which is recorded by a charge coupled detector (CCD) camera.

The Si(100) samples are first cleaned by chemical etching using a modification to the Shiraki method [51]. The samples are dipped into a solution of H_2SO_4 (97% wt): H_2O_2 (30% wt) = 4:1 (by volume) for 10 min, rinsed with ultrapure water for 10 min, then dipped into a solution of HF (50 wt %): H_2O = 1:10 (by volume) for 1 min. Unused clean samples are stored under Ethanol and are etched by HF just before being loaded into the chamber. The samples are loaded into the vacuum chamber within 5 minutes of chemical etching. The vacuum chamber is pumped down to $<1\times10^{-9}$ Torr. The chamber is baked at 300 °C for at least 12 hours while the substrate is kept at 500 °C during the baking. When baking is completed, the sample is kept at 800 °C for a few hours before being flashed to 1100 °C for about a minute. This procedure results in the observation of the Si(100)-(2x1) RHEED pattern.

Deposition takes place by focusing the laser beam onto the rotating Ge target, while the growth dynamics is studied by *in situ* RHEED. Later, the morphology of the grown films is studied by post deposition AFM. A series of films of different mean thicknesses was deposited at a substrate temperature of 400 °C using a laser of fluence of 23 J/cm^2 operating at 10 Hz. The growth dynamics and the morphology dependence on the cluster size were studied. Another series of films was grown at 400 °C with different laser fluences in order to study the effect of the laser fluence. Finally, several 9-ML films were grown at different substrate temperatures.

Reproduced with permission of the copyright owner. Further reproduction prohibited without permission.

IV.5. Growth dynamics

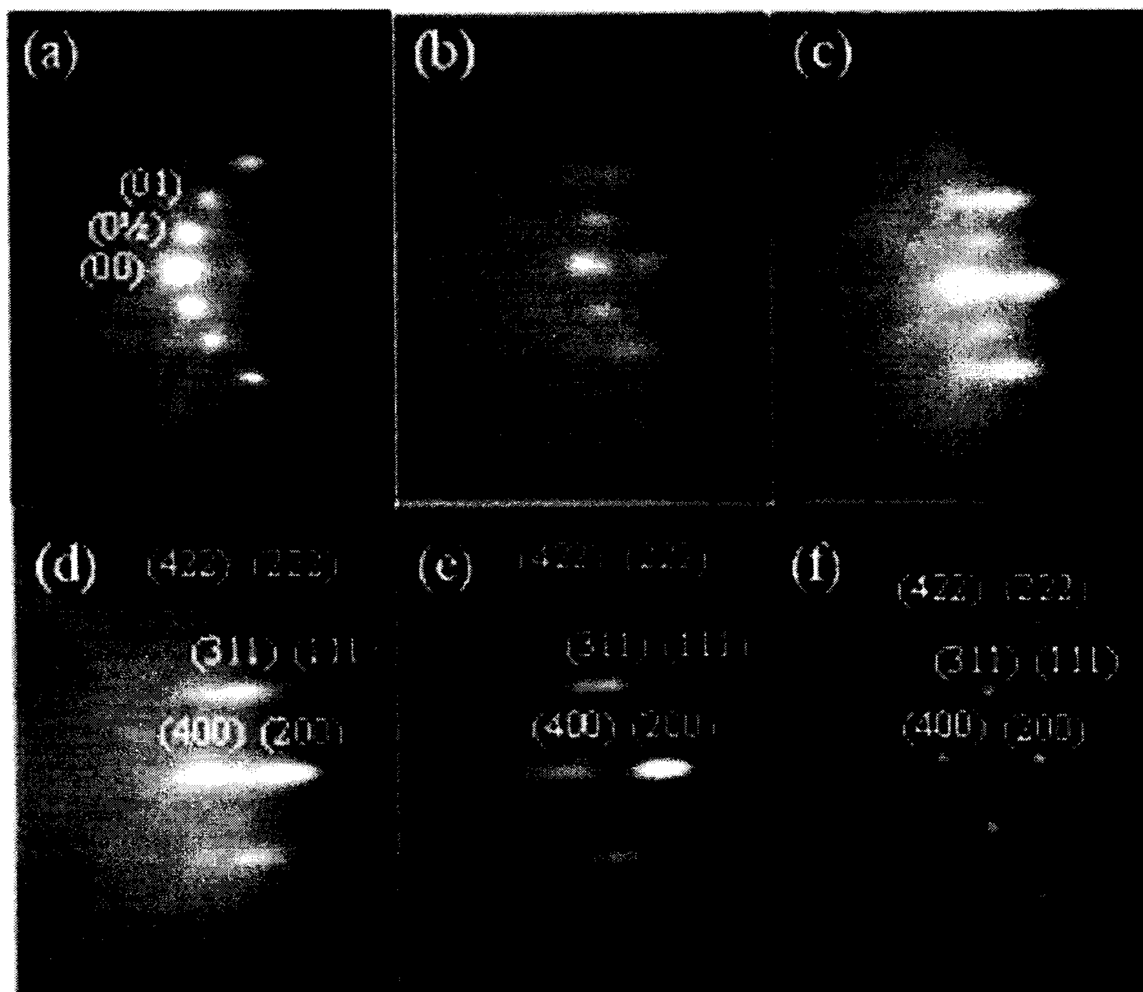

FIG. 4.3. RHEED patterns taken at different thicknesses for deposition at 400 °C, 23 J/cm^2, 10 Hz. Substrate (2×1) reconstruction pattern is shown in (a). Growth started epitaxially, as seen in the RHEED pattern taken after the deposition of ~3.3 ML shown in (b). At ~4.1 ML, (c), elongated transmission features with lines at the position of the second order streaks started to appear. In the pattern at ~6 ML, (d), the lines disappeared while the elongation of the transmission features increased. As the thickness was increased, the transmission features became well defined and the elongation decreased, as observed in (e) taken at ~9.3 ML. At ~13 ML, the transmission features became more round, (f).

Reproduced with permission of the copyright owner. Further reproduction prohibited without permission.

Ge films of different thicknesses were grown under the same deposition conditions (substrate temperature of 400 °C and a laser fluence of 23 J/cm^2 operated at a repetition arte of 10 Hz). Thickness calibration was done in separate runs by placing a crystal thickness monitor at the substrate's location. Figure 4.3 shows a series of RHEED patterns as the film mean thickness was increased. The Si(100)-(2x1) diffraction pattern features, shown in Fig. 4.3(a), remained unchanged during the first few seconds of deposition in which the epitaxial growth of the wetting layer occurs. Fig. 4.3(b), taken at ~3.3 ML, shows a RHEED pattern with equal streak spacing as in Fig. 4.3(a) but with reduced diffraction streak intensity. The epitaxial growth of the Ge wetting layer leads to a continuous increase in the lattice mismatch-induced internal strain as the film is grown. However, after depositing ~4 ML, elongated transmission features with lines at the positions of the second order strikes start to appear, as shown in Fig. 4.3(c). The appearance of such transmission features instead of the reflection ones indicates the beginning of the strain relief by the formation of 3D clusters. Elongated RHEED features result from transmission through asymmetric 3D clusters [54]. In the cases of growth by MBE and CVD, similar RHEED features were reported to correspond to the formation of {105}-faceted hut and pyramid clusters [19,21,54]. At ~6 ML, the lines at the positions of the second order strikes disappeared, while the elongated transmission features increased in intensity and elongation, as shown in Fig. 4.3(d). As the film thickness was increased, the transmission RHEED features split into well-defined features and their elongation started to decrease, as shown in Fig. 4.3(e) taken at ~9 ML. As the deposition continue, both the major (elongation) and minor lengths of the spot continued to decrease. Since the RHEED arrangement used probes an area of ~1 mm^2, such a decrease accounts for an

Reproduced with permission of the copyright owner. Further reproduction prohibited without permission.

increase in the Ge QDs' average size, within the limits of the electron penetration depth. This penetration depth is 15±4 nm in Ge at electron energy of 12 keV, as calculated by different inelastic mean free path (IMFP) models, see section III.4 [55,56]. Both the transmission spots' major and minor lengths decreased with the increase in the film thickness and the spots became more round.

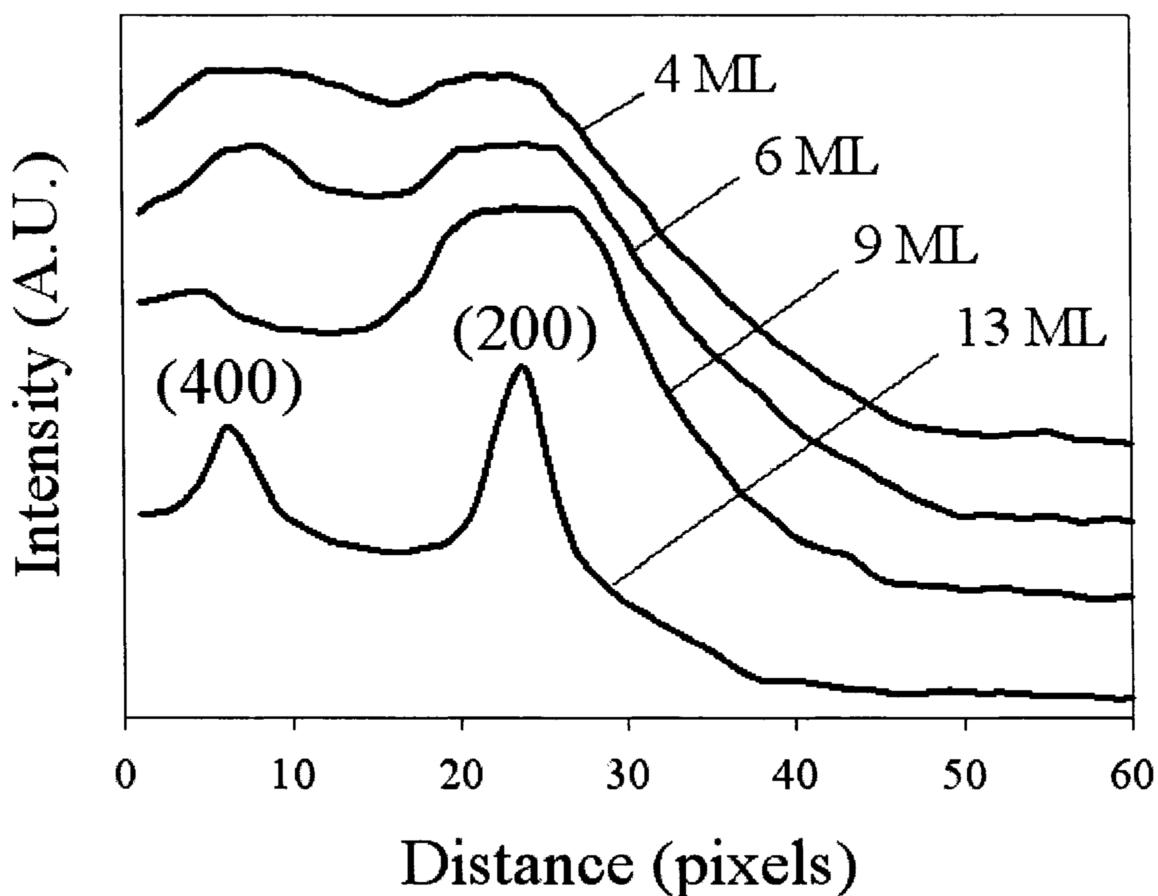

FIG. 4.4. Line profile measured along the (200)-(400) connecting line normal to the surface at different thicknesses. The transition from the elongated lines to sharp spots is shown.

Reproduced with permission of the copyright owner. Further reproduction prohibited without permission.

Figure 4.4 shows a set of line profiles taken at thicknesses corresponding to Figs. 4.3(c) through 4.3(f). The line scans, which are taken normal to the surface and measured along the (200)-(400) connecting line, show the decrease in the spots' major length with film thickness. Such observation predicts a transition from an asymmetric cluster shape to a more symmetric one. Finally, the transmission features in the case of ~13 ML appear to be fully rounded, as shown in Fig. 4.3(f). Rounded spots result from transmission through rounded clusters. A similar spotty transmission pattern, with chevron lines due to the facetation of the Ge clusters, were observed when multi-faceted "macroislands" clusters were formed (domes and superdomes faceted by {113} and {102} planes) [17,55]. In our study, we did not observe chevron lines, which could be due to the lack of well-defined facets in the PLD-formed dome clusters.

Ex situ AFM was used to study the morphology of the Ge QDs and to correlate the morphology with the RHEED observations. Figure 4.5 shows 3D AFM images of the cluster shapes observed at the different film thicknesses. Depending on the film thickness, three cluster shapes are observed: huts, pyramids and domes. Faceted hut clusters are observed to dominate at low film thicknesses with cluster sizes up to 400 nm and heights ranging up to 40 nm. Figures 4.5(a) and 4.5(b) show two representatives of these hut clusters. For larger film thicknesses, the huts (of lateral sizes > 400 nm) grew in size, became less defined, and lost their facetation. Figures 4.5(c) and 4.5(d) show two representatives of such clusters that are identified by their continuous round edges, indicating the lack of facetation.

By increasing the film thickness the hut clusters transformed into the dome-like shape, shown in Fig. 4.5(f), with a length/height ratio of ~4. The smoothness of the dome,

Reproduced with permission of the copyright owner. Further reproduction prohibited without permission.

which could be seen as a continuous distribution of faceting planes, is noticeable. This morphology is consistent with the lack of observation of chevron lines in RHEED [58]. The chevron lines arise from the intersection of two diffraction patterns, each originating from one faceting plane [54]. However, a small number of pyramid clusters, Fig. 4.5(e), are observed among the domes. These pyramids are slightly elongated and their main faceting planes are the {305} with contact angles of ~31°.

The observation of huts that are faceted by different planes, depending on their size, has not been previously reported. Also, the observation of huts that are faceted by planes of large contact angles with the substrate differ from those reported in the cases of MBE, CVD, and LPE [19,21,54]. Another new observation in the present PLD experiment is the formation of stable huts that are larger than those grown by the other deposition techniques. These observations could be attributed to PLD features, such as the high adatoms energies, plume density, and the periodic nature.

Line scans across and along the QD have been performed to measure their shape characteristics. Examples of such scans are shown in Fig. 4.6, where a couple of hut clusters of heights of ~3.7 and 63 nm are shown to be faceted with planes with slope angles of 3° and 31° with the substrate, respectively. Analyses of the quantitative measurements performed on the QDs are shown in Figs. 4.7-4.11. Figure 4.7 shows the relation between the major, l_{maj}, and minor, l_{min}, lengths of the QDs. The best fit of the data was found to follow the relation:

$$l_{\min} = 17753.577 - 8925.051 \ln(l_{maj}) + 1460.366 \ln(l_{maj})^2 - 76.198 \ln(l_{maj})^3 . \quad (4.9)$$

Reproduced with permission of the copyright owner. Further reproduction prohibited without permission.

The data of the above figure have been used to generate Fig. 4.8, showing the lateral aspect ratio, L, (= major length/minor length) as a function of the cluster's minor length. The best fit to the data was found to follow the exponential relation

$$L = (1.125)\exp\left(\frac{37.157}{l_{\min} - 34.974}\right). \tag{4.10}$$

Figures 4.7 and 4.8 show that small hut clusters are asymmetric in shape, where the asymmetry decreases with the lateral size increase. As they grew in size, they became more laterally symmetric, as shown in Fig. 4.8, in which the lateral aspect ratio asymptotically reaches ~1.2. The height, h, of the QDs as a function of both the major and minor lengths is shown in Fig. 4.9, where the best fitting function of the data was found to be

$$h = h_0 + \frac{a}{1 + \exp\left(-\frac{x - x_0}{b}\right)}, \tag{4.11}$$

where a, b, x_0, and h_0 have the values of 107.112, 77.702, 337.920, and 6.364 for the major length case and 108.675, 92.304, 373.593, and -3.949 for the case of minor length. The aspect ratio, A, (major length/height) as a function of major length is shown in Fig. 4.10, where the fitting function is

$$A = 6.085 + 97.751\,e^{-0.009\,l_{maj}}. \tag{4.12}$$

Figures 4.9 and 4.10 indicate that for small clusters the rate of height increase is faster than that of lateral size increase. However, both rates become comparable as the cluster increases in size. This growth anisotropy may be attributed to the cluster's internal strain. Increasing the lateral size is expected to result in increasing the internal strain due to the lattice mismatch. On the contrary, increasing the cluster's height leads to more strain

Reproduced with permission of the copyright owner. Further reproduction prohibited without permission.

relief through the adjustment of the lattice spacing in the growing layers, and therefore is favored over the lateral growth [17]. The aspect ratio asymptotically decreases to the value of ~4, which indicates that spherical cluster cannot be obtained under the considered deposition conditions. Finally, the contact angle, θ, of the clusters' bounding planes with the Si(100) substrate as a function of the cluster's height is shown in Fig. 4.11. The best fit function for the whole range is

$$\theta = 1.846(1 - e^{-0.241h}) + 28.132(1 - e^{-0.039h}), \tag{4.13}$$

where the linear fitting for the first region is

$$\theta = (4.995) + (0.556)h. \tag{4.14}$$

The contact angle increases linearly for clusters with heights less than 40 nm. This leads to the continuous change of the planes faceting the clusters. For example, the huts shown in Figs. 4.5(a) and 4.5(b), are mainly faceted by planes having contact angles of ~10° and ~18°, respectively, which account for the faceting planes of {811} and {310}. The slope of the clusters' edges asymptotically reached the value of ~31°, which assumes that both the height and the lateral size increased almost at the same rate.

Reproduced with permission of the copyright owner. Further reproduction prohibited without permission.

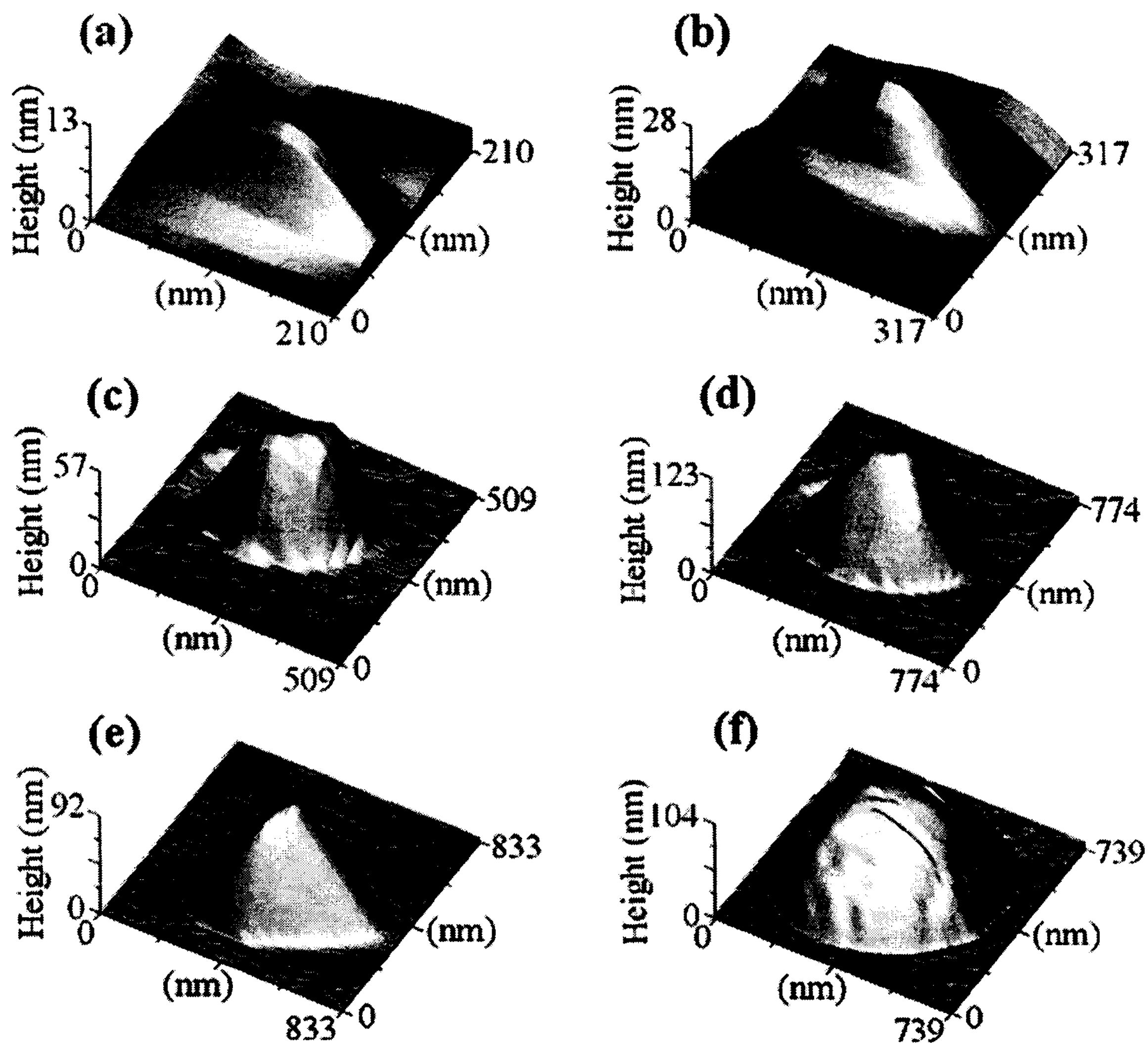

FIG. 4.5. 3D AFM images of the clusters observed at different film thicknesses. Well-defined hut clusters observed at low thicknesses (a) and (b). As the film thickness was increased huts became more round (c) and (d). Some of these clusters grew into pyramids (e). The majority of clusters grew into domes (f).

Reproduced with permission of the copyright owner. Further reproduction prohibited without permission.

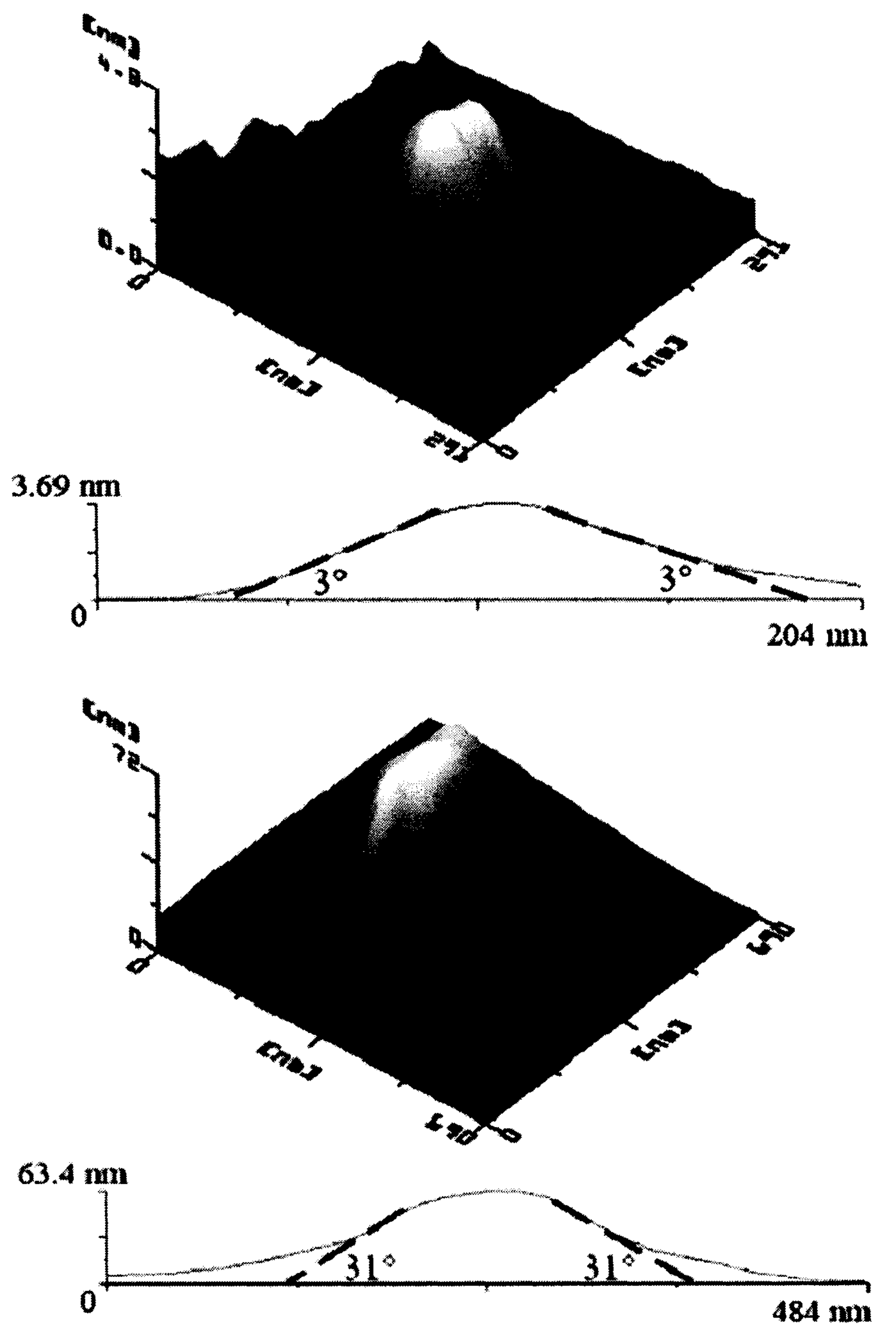

FIG. 4.6. Line scans performed across a couple of hut clusters, where the faceting angles are indicated.

Reproduced with permission of the copyright owner. Further reproduction prohibited without permission.

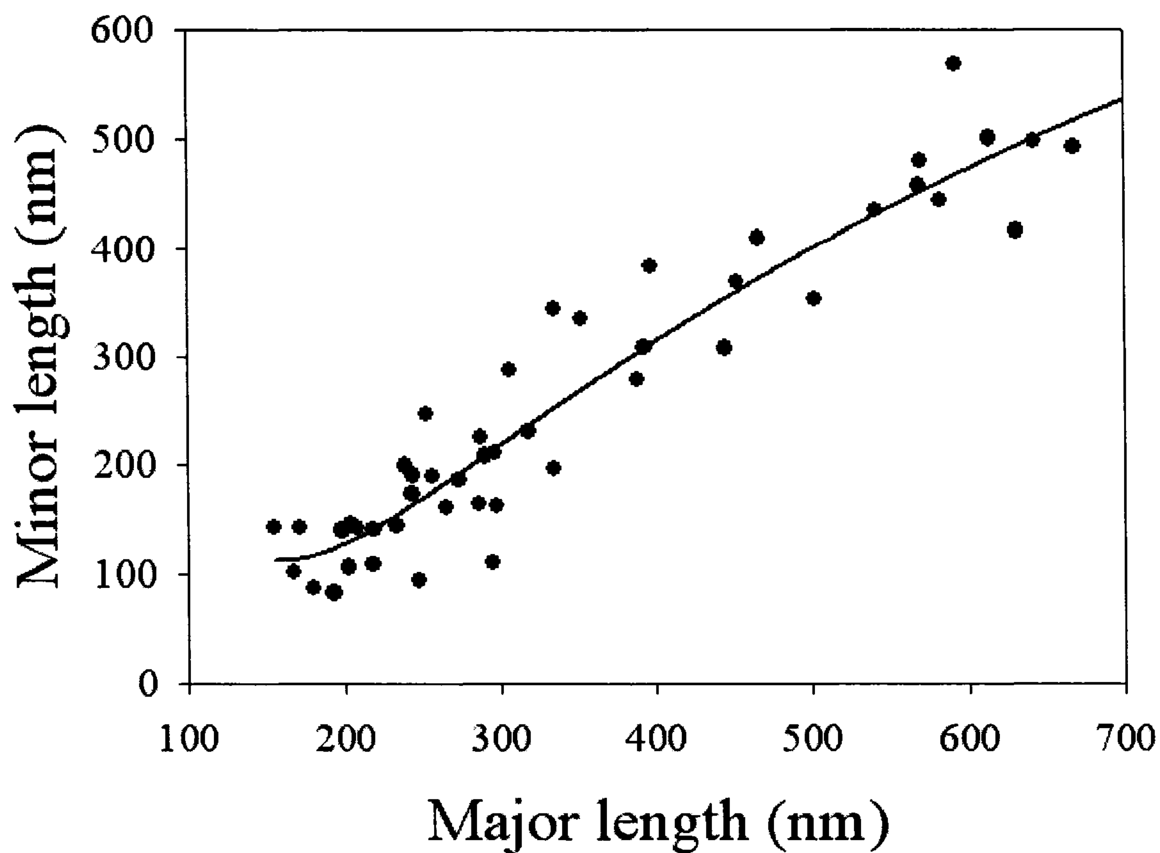

FIG. 4.7. Relation between major and minor lengths of the Ge QDs formed on Si(100)-2x1 at different film thicknesses. The solid line is the best fit to the data.

Reproduced with permission of the copyright owner. Further reproduction prohibited without permission.

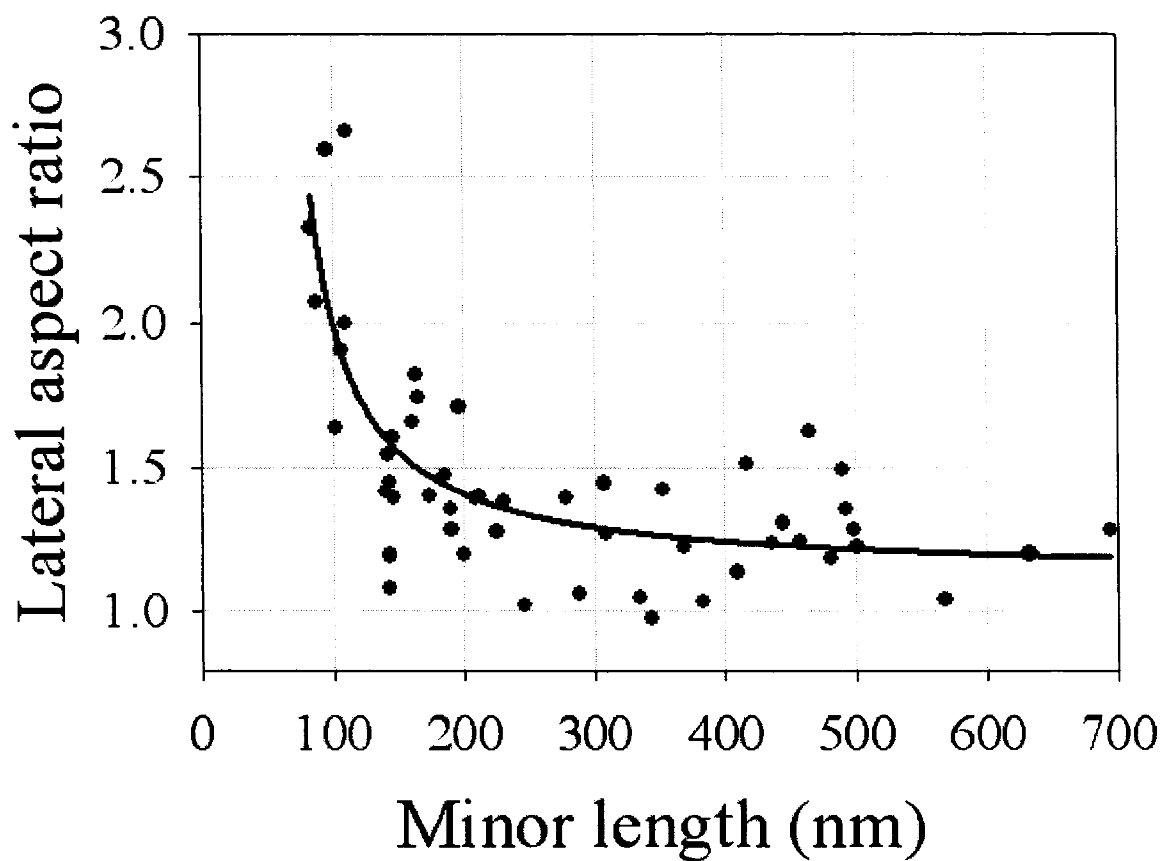

FIG. 4.8. Lateral aspect ratio of clusters (major length/minor length) as a function of the minor length. The solid line is the best fit to the data.

Reproduced with permission of the copyright owner. Further reproduction prohibited without permission.

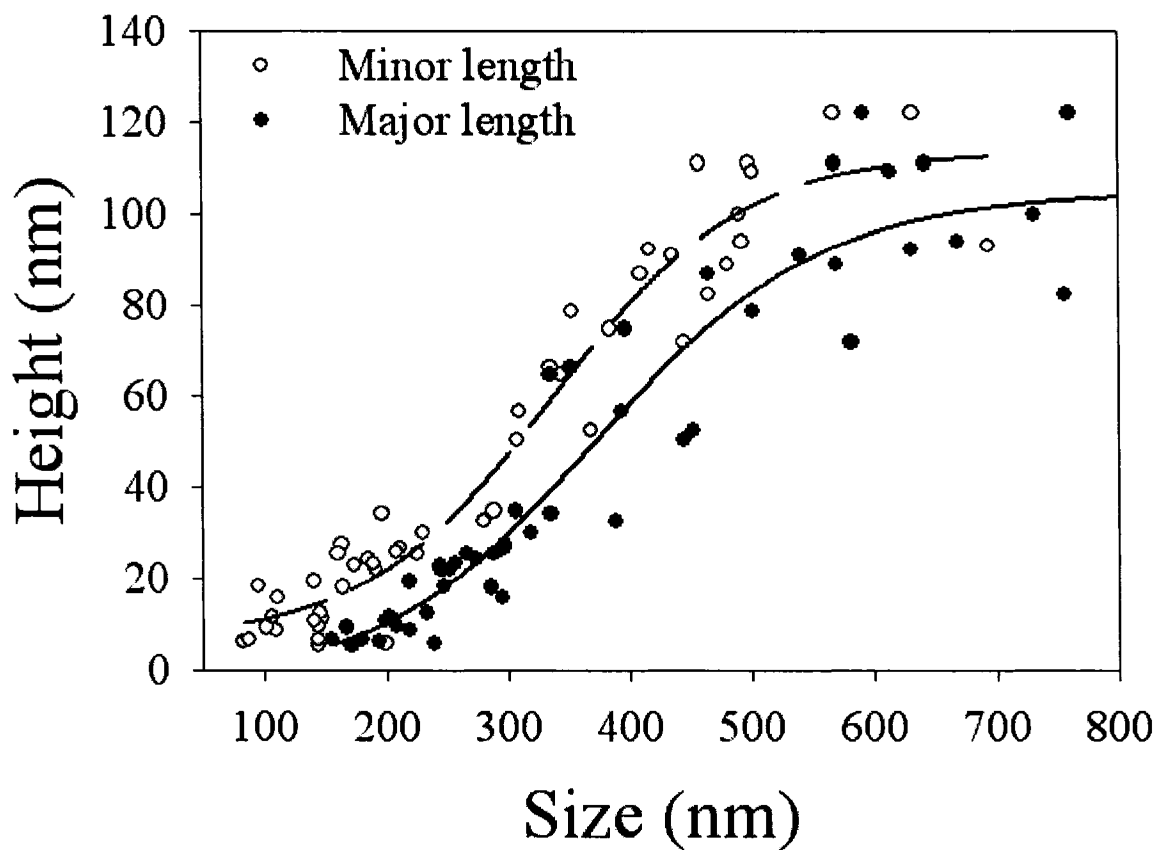

FIG. 4.9. Height of the QD as a function of both the major and minor lengths. Solid lines represent the best fits to the data.

Reproduced with permission of the copyright owner. Further reproduction prohibited without permission.

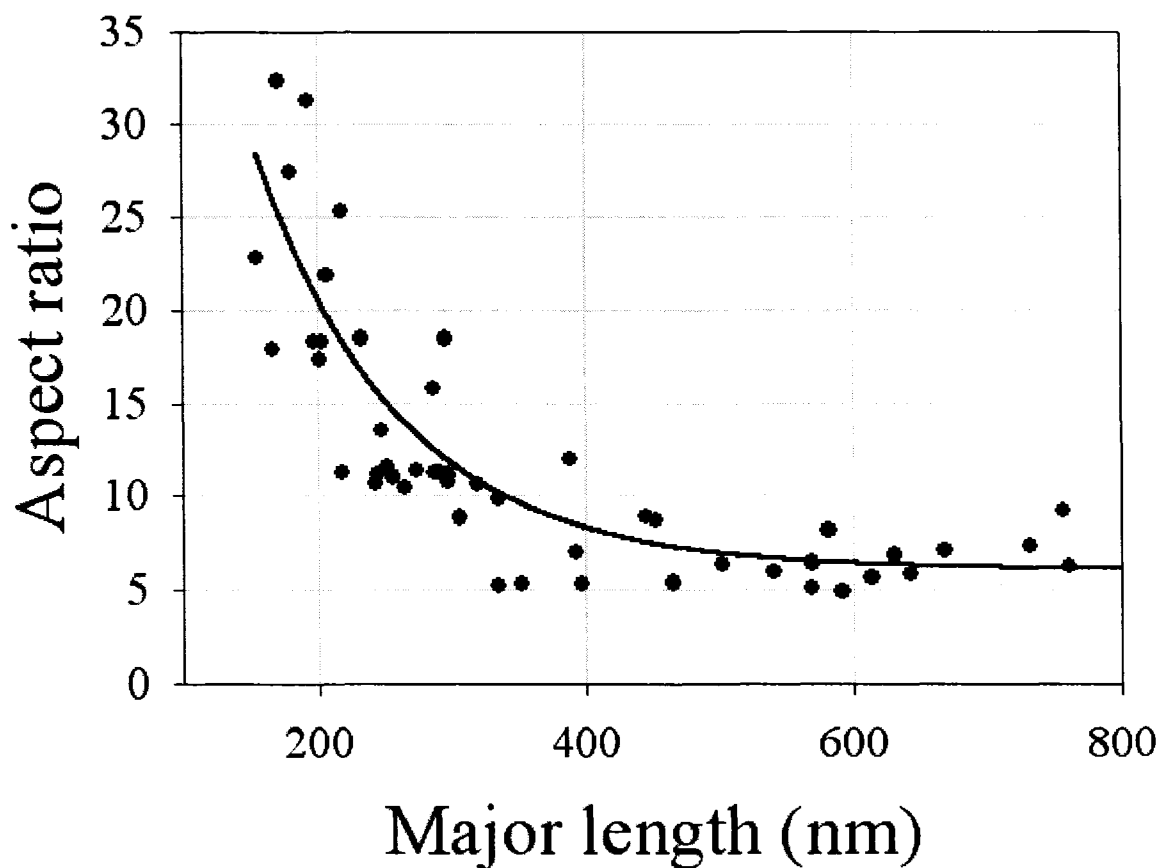

FIG. 4.10. Aspect ratio (major length/height) as a function of major length, fitted by the solid line.

Reproduced with permission of the copyright owner. Further reproduction prohibited without permission.

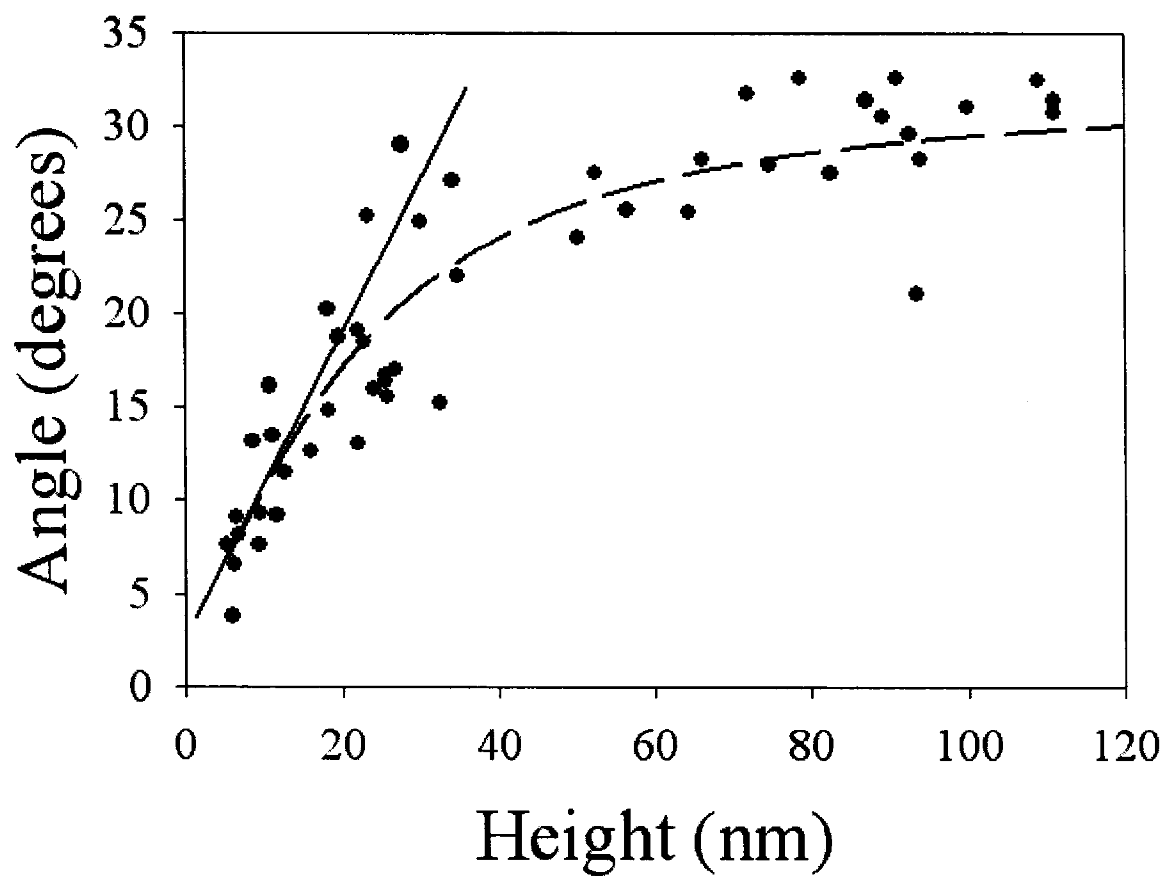

FIG. 4.11. Contact angle that the bounding planes make with the substrate as a function of cluster's height.

Reproduced with permission of the copyright owner. Further reproduction prohibited without permission.

IV.6. Effect of Laser Fluence

Controlling thin film growth by changing the laser parameters, namely fluence and repetition rate, is a unique feature of PLD. Figure 4.12 shows the AFM scans and the resulting RHEED patterns obtained after depositing Ge on Si(100)-(2×1) for 80 s at 400 °C, 10 Hz but at different laser fluences (23, 47, and 70 J/cm^2). The corresponding line scans along and across the clusters are shown in Fig. 4.13. For 23 J/cm^2, column (a), shows that the origin of the elongated transmission streaks is the elongated hut clusters. Notice the low clusters' density in this case. When the laser fluence was increased to 47 J/cm^2, represented in column (b), the cluster density increased while cluster sizes decreased. The 3D image of a representative cluster shows that the clusters became more symmetric in shape. This decreased the transmission RHEED streak elongation. When the fluence was increased to 70 J/cm^2, cluster density was seen to increase dramatically while the average size cluster decreased further. The shape of the clusters became almost symmetric, as seen in the 3D image, which resulted in round transmission RHEED spots. The cluster heights are much larger than those observed by other techniques [25]. The observation of domes for a laser fluence 70 J/cm^2 that are smaller in size than the huts observed for a fluence of 23 J/cm^2 differs from other deposition methods. These observations show that the effect of the laser fluence is not only on the size and spatial distributions of the clusters but also on their morphology.

Reproduced with permission of the copyright owner. Further reproduction prohibited without permission.

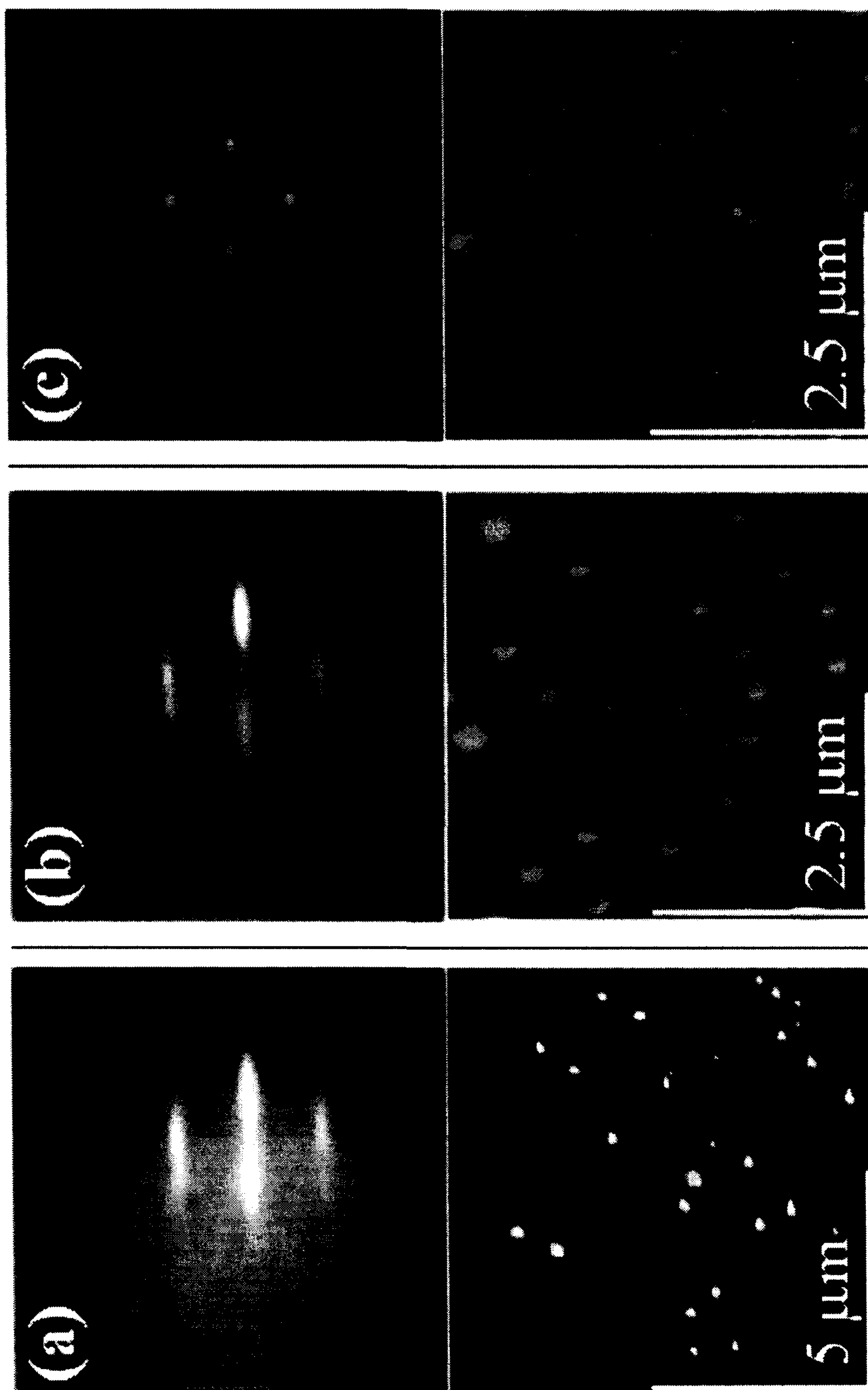

FIG. 4.12. RHEED patterns, AFM scans of three samples deposited at 400 °C, 10 Hz and column (a) 23 J/cm^2, column (b) 47 J/cm^2, column (c) 70 J/cm^2.

Reproduced with permission of the copyright owner. Further reproduction prohibited without permission.

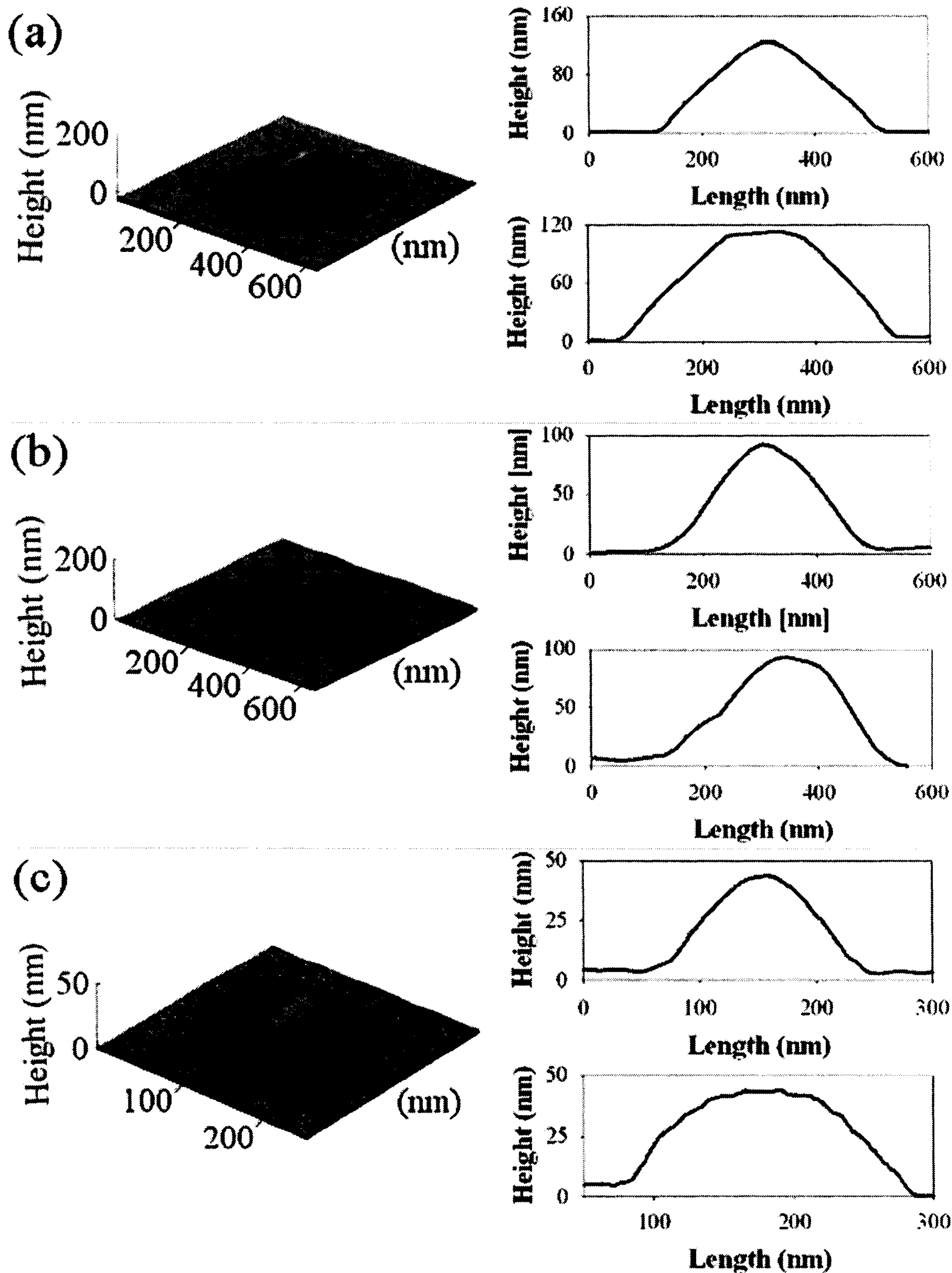

FIG. 4.13. 3D AFM images of QDs corresponding to the 3 cases of the above figure and line scans along and across the clusters.

Reproduced with permission of the copyright owner. Further reproduction prohibited without permission.

Figure 4.14 presents some statistics calculated from the above AFM scans. The number of clusters in the scanned area *n*, the average cluster size *d*, the coverage ratio θ, and the full width at half maximum FWHM of the distribution *f* are listed. With the increase of the laser fluence, the cluster density is seen to increase dramatically (from 3×10^7 cm^{-2} for 23 J/cm^2 to 1.3×10^8 cm^{-2} and 6.3×10^8 cm^{-2} for 47 and 70 J/cm^2, respectively), while the average cluster size decreased (~362, 287, and 107 nm for 23, 47 and 70 J/cm^2, respectively). One may notice that the cluster density is at least an order of magnitude less than that observed in other deposition techniques under standard deposition conditions [26,34,59]. This could be attributed to the higher kinetic energy of the adatoms in the case of PLD. The dependence of the FWHM of the size distribution on the laser fluence is complicated. It is known that on samples with different cluster shapes, each cluster shape has its own size distribution. This is the reason for the bimodal distributions observed in some systems [25,60,61]. The shapes of the clusters are different in these 3 cases. However, one may easily see that films prepared at 70 J/cm^2 have the narrowest distribution.

In vapor phase deposition, the nucleation density and the clusters' sizes are determined through the competition between the atomic flux *F* (atoms/area.time) and adatoms' diffusion coefficient *D* (area/time), given as $D = D_0 \exp[E_d / k_B T]$, where E_d is the diffusion barrier [37,62]. The density of stable islands is given by [63,64]

$$N = \eta(\Theta)(D_0 / F)^{-\chi} \exp(-\frac{\chi E_d}{k_B T}), \qquad (4.15)$$

where $\eta(\Theta) \cong \Theta^{1/3}$ is the coverage Θ dependent factor and χ is the scaling factor. Therefore, a high flux results in high supersaturation of adatoms leading to a large

Reproduced with permission of the copyright owner. Further reproduction prohibited without permission.

nucleation density of small clusters. On the other hand, high substrate temperatures increase the adatom diffusion coefficient favoring the formation of low density of larger clusters. In PLD, the nucleation density is expected to be dependent on the laser's repetition rate and pulse duration in addition to the parameters in Eq. 4.15. Rate equations were solved numerically and the number of stable islands was found as a function of D/F for the case of PLD for different deposition duration and laser repetition rate and was compared to the case of MBE [64]. According to these models, both MBE and PLD result in the same island density N for very low values of D/F, while PLD yields higher values of N for larger D/F.

The effect of the laser fluence on nucleation density is complex since changing the laser fluence affects both the atom flux F and the kinetic energy of the ablated species [65], which ranges from 0.1 to 1000 eV. Therefore, the diffusion coefficient D is expected to depend on the particles' kinetic energy as well as the substrate temperature. Moreover, the effect of the particles' kinetic energy on D is further complicated by the interaction between the incident particles and the adatoms [66]. Although the functional dependence of F on the laser fluence is not known, it is not expected to be linear, since increasing the fluence results in increasing the ablation yield and a more directional plume [65].

Reproduced with permission of the copyright owner. Further reproduction prohibited without permission.

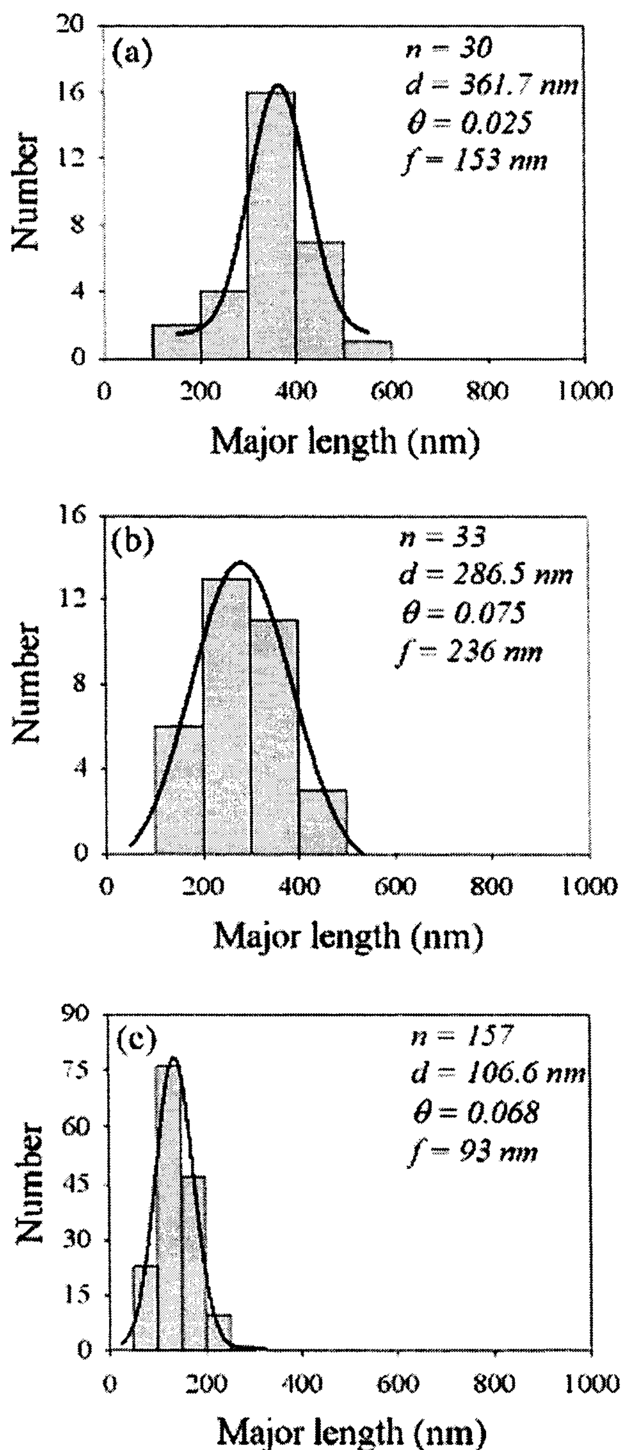

FIG. 4.14. Size distributions of the clusters formed on three different samples deposited at 400 °C, 10 Hz and column (a) 23 J/cm^2, column (b) 47 J/cm^2, column (c) 70 J/cm^2. The number of clusters in the scanned area, n, the average cluster size, d, the coverage ratio, θ, and the full width at half maximum FWHM of the distribution, f, are listed.

Reproduced with permission of the copyright owner. Further reproduction prohibited without permission.

One model showed that the growth behaviors of PLD and MBE are equivalent at very small plume intensities, I, which is the plume intensity in units of atoms/area [37,38]. In this regime, the nucleation density follows the relation $N \propto (D/F)^{-\gamma}$ and, therefore, depends on the laser fluence through the competition between D and F, since they are both functions of I. The exponent γ is a positive constant, the value of which depends on the nucleation and growth mechanisms. However, above a certain critical intensity, I_c, PLD shows no dependence on F and D but rather on I according to the relation $N \propto I^{\nu}$, where ν is some exponent [37,67]. The reason for the change in behavior at I_c is that the huge number of deposited atoms in each pulse leads to high nucleation probability even before the effects of the change in D and F take place. Therefore, the nucleation density in the case of PLD may be formulated intuitively as [37]

$$N \propto (D/F)^{-\gamma} f(I/I_c), \tag{4.16}$$

where

$$f(I/I_c) \sim \begin{cases} const. & I \ll I_c \\ (I/I_c)^{\nu} & I_c \gg I \end{cases}. \tag{4.17}$$

Therefore, increasing the plume intensity, by increasing the laser fluence, acts to increase the nucleation density. The drawback of this model is the assumption that atoms are deposited at thermal energies, which is not the case in PLD. However, it gives a decent picture of how the nucleation density and the average cluster size are dependent on D, F, and I.

Because of the current lack of understanding of the dependence of F, kinetic energy distribution, and I on the laser fluence, the dependence of the cluster density and average cluster size on the laser fluence is not well explained. In our current situation, if

Reproduced with permission of the copyright owner. Further reproduction prohibited without permission.

we assume that the studied laser fluences result in plume intensities above the critical value (i.e., $I > I_c$), the nucleation density will be a power function of the intensity. If this is not the case (i.e., $I < I_c$), the increase in the density with the laser fluence indicates that the effect of the increase in the plume density overwhelms that due to the increase in the adatoms' kinetic energy.

IV.7. Effect of Substrate Temperature

Figure 4.15 shows the RHEED patterns obtained after the deposition of ~9 ML of Ge on Si(100)-(2×1) at different substrate temperatures along with the pattern obtained from the substrate before deposition. Figure 4.16 shows the AFM scans corresponding to the samples of Fig. 4.15. For growth at 150 °C, the (2×1) diffraction pattern becomes dimmer continuously during the growth of the Ge film resulting in the shown diffused pattern indicating that the grown clusters are misoriented. AFM imaging of this sample, Fig. 4.16(a), shows the formation of randomly distributed 3D clusters, which produces the diffuse RHEED pattern in Fig. 4.15. Similar results were observed for the Si homoepitaxy at low temperatures [53]. For deposition at 400 °C, formation of elongated hut clusters was observed as shown in Fig. 4.16(b). These clusters give an elongated transmission RHEED pattern shown in Fig. 4.15. The RHEED transmission pattern with rounded spots obtained for deposition at 500 °C indicates the formation of dome clusters as shown in the AFM in Fig. 4.16(c). Comparing AFM images in Figs. 4.16(b) and (c) shows the effect of the substrate temperature on the cluster morphology, nucleation

Reproduced with permission of the copyright owner. Further reproduction prohibited without permission.

density, and cluster spatial distribution. The cluster morphology changed from the asymmetric hut shape to the symmetric dome shape. The decrease in the cluster density is consistent with the general behavior described by Eq. 4.16, in which the nucleation density decreases with the increase of the diffusion coefficient due to the increase in temperature. For growth at 600 °C a transmission RHEED pattern is seen on top of broken rings, as shown in Fig. 4.15. The incomplete concentric rings usually result from textured structures, i.e., surfaces with domains that have a distribution of orientations but are largely near one value [68,69]. Figure 4.16(d) is the AFM image corresponding to the sample grown at 600 °C, which shows 3D clusters formed on top of a discontinuous layer.

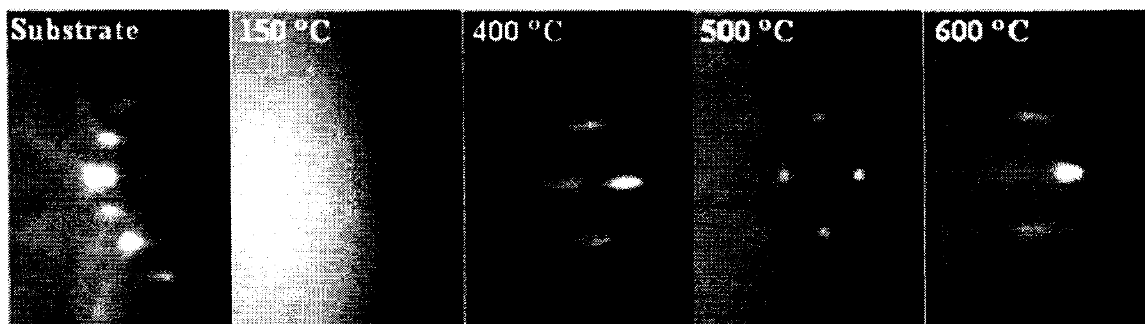

FIG. 4.15. RHEED patterns of different samples ~9-ML thick deposited at 23 J/cm^2, 10 Hz and different substrate temperatures.

Reproduced with permission of the copyright owner. Further reproduction prohibited without permission.

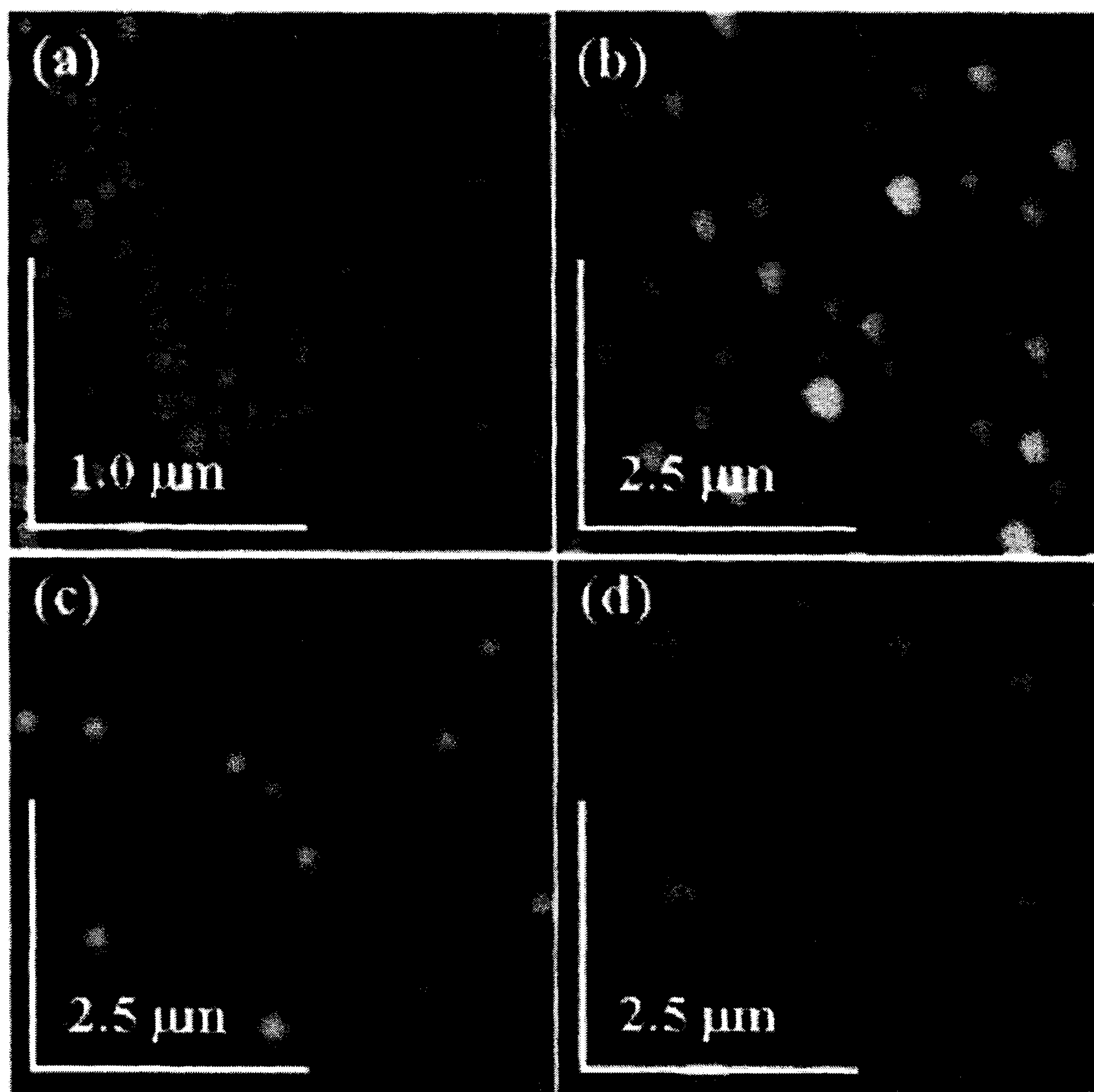

FIG. 4.16. AFM scans corresponding to the samples of Fig. 4.15: (a) 150 °C, (b) 400 °C, (c) 500 °C, (d) 600 °C.

Reproduced with permission of the copyright owner. Further reproduction prohibited without permission.

IV.8. Conclusion

The growth dynamics and the morphology of Ge QDs grown on Si(100)-(2×1) by PLD were studied by RHEED and AFM. After the completion of the wetting layer, Ge was observed to form hut clutters faceted by planes having contact angles with the substrate that increase with the height of the cluster. As the cluster size increased with further deposition, they lost their facetation and became rounded forming a dome shape. The effect of the laser fluence on the growth dynamics and cluster morphology was studied. As the laser fluence was increased, the clusters' density increased dramatically, while the average cluster sizes were reduced. At a substrate temperature of 150 °C, misaligned clusters formed giving a diffuse RHEED pattern. At 400 and 500 °C, transmission RHEED patterns were observed indicating the growth of oriented clusters. Around 600 °C, the QDs were formed on top of textured surfaces.

Reproduced with permission of the copyright owner. Further reproduction prohibited without permission.

IV.9. References

[1] B. Voigtländer, "Fundamental processes in Si/Si and Ge/Si epitaxy studied by scanning tunneling microscopy during growth," Surf. Sci. Rep. **43**, 127 – 254 (2001).

[2] A. Elfving, G. V. Hansson, and W.-X. Ni, "SiGe (Ge-dot) heterojunction phototransistors for efficient light detection at 1.3-1.55 μm," Physica E **16**, 528 (2003).

[3] P. Castrucci, R. Gunnella, N. Pinto, and M De Crescenzi, "Structural and photoluminescence properties of Ge-Si ultra-thin films and heterostructures," J. Phys.: Condens. Matter **14**, 8333 – 8351 (2002).

[4] M. V. Alves, M. J. Semenzato, E. Marega Jr., and P. P. Gonzalez-Borrero, "Light emitting diodes based on self-organized InAs quantum dots grown on GaAs(311)A surfaces using only Si as a doping material," Phys. Stat. Sol. (b) **232(1)**, 32 – 36 (2002).

[5] J. C. Galzerani, and Y. A. Puesep, "Raman spectroscopy characterization of InAs self-assembled quantum dots," Physica B **316–317**, 455–458 (2002).

[6] V.-G. Stoleru, D. Pal, and E. Towe, "Self-assembled (In,Ga)As/GaAs quantum-dot nanostructures: starin distribution and electronic structure," Physica E **15**, 131–152 (2002).

[7] E. Alphandéry, R. J. Nicholas, N. J. Mason, S. G. Lyapin, and P. C. Klipstein, "Photoluminescence of self-assembled InSb quantum dots grown on GaSb as a function of excitation power, temperature, and magnetic field," Phys. Rev. B **65**, 115322-1 – 115322-7 (2002).

[8] J. I. Martín, J. Nogués, K. Liu, J. L. Vicent, I. K. Schuller, "Ordered magnetic nanostructures: fabrication and properties," J. Magnetism and Mag. Mat. **256**, 449-501.

Reproduced with permission of the copyright owner. Further reproduction prohibited without permission.

[9] S. Anders, S. Sun, C. B. Murray, C. T. Rettner, M. E. Best, T. Thomson, M. Albrecht, J.–U. Thiele, E. E. Fullerton, and B. D. Terris, "Lithography and self-assembly for nanometer scale magnetism," Microelectronic Eng. **61–62**, 569–575 (2002).

[10] L.-X. Li, S. Sun, Y.-C. Chang, "Optical properties of self-assembled quantum wires for application in infra-red detection," Infrared Phys. Tech. **44**, 57 – 67 (2003).

[11] D. E. Wohlert and K. Y. Cheng, "Temperature dependent polarization switching and band-gap anomalies in strained $Ga_xIn_{1-x}As$ quantum wire heterostructures," Appl. Phys. Lett. **76**, 2247 – 2249 (2002).

[12] M. S. Lundstrom, "Fundamentals of Carrier Transport," Cambridge University Press (2000).

[13] R. W. Kelsall, M. Geoghegan, I. W. Hamley, "Nanoscale Science and Technology," John Wiley and Sons (2005).

[14] V. A. Shchukin, and D. Bimberg, "Spontaneous ordering of nanostructures on crystal surfaces," Rev. Mod. Phys. **71**, 1125 – 1171 (1999).

[15] S. M. Reimann, "Electronic structure of quantum dots," Rev. Mod. Phys. **74**, 1283 – 1342 (2002).

[16] M. Henini, "Quantum dot nanostructures," Materialstoday, June, 48 – 53 (2002).

[17] C. Teichert, "Self-organization of nanostructures in semiconductor heteroepitaxy," Phys. Rep. **365**, 335 – 432 (2002).

[18] A. D. Kent, D. M. Shaw, S. V. Molnar, D. D. Awschalom, "Growth of high aspect ratio nanometer-scale magnets with chemical vapor deposition and scanning tunneling microscopy," Science **262**, 1249 – 1252 (1993).

Reproduced with permission of the copyright owner. Further reproduction prohibited without permission.

[19] V. Cimalla, K. Zekentes, and N. Vouroutzis, "Control of morphological transitions during heteroepitaxial island growth by reflection high-energy electron diffraction," Mater. Sci. Eng. B **88**, 186-190 (2002).

[20] I. Goldfarb, P. T. Hayden, J. H. G. Owen, and G. A. D. Briggs, "Nucleation of ``Hut" Pits and Clusters during Gas-Source Molecular-Beam Epitaxy of Ge/Si(001) in *In Situ* Scanning Tunnelng Microscopy," Phys. Rev. Lett. **78**, 3959-3962 (1997).

[21] Y.-W. Mo, D. E. Savage, B. S. Swartzentruber, M. G. Lagally, "Kinetic pathway in Stranski-Krastanov growth of Ge on Si(001)," Phys. Rev. Lett. **65**, 1020 (1990).

[22] A. I. Nikiforov, V. A. Cherepanov, O. P. Pchelyakov, A. V. Dvurechenskii, A. I. Yakimov, "In situ RHEED control of self-organized Ge quantum dots," Thin Solid Films **380**, 158-163 (2000).

[23] O. P. Pchelyakov, V. A. Markov, A. I. Nikiforov, and L. V. Sokolov, "Surface processes and phase diagrams in MBE growth of Si/Ge heterostuctures," Thin Solid Films **306**, 299-306 (1997).

[24] J. A. Floro, E. Chason, L.B. Freund, R. D. Twesten, R. Q. Hwang, and G. A. Lucadamo, "Novel SiGe Island Coarsening Kinetics: Ostwald Ripening and Elastic Interactions," Phys. Rev. B **59**, 1990 (1999).

[25] T. I. Kamins, E. C. Carr, R. S. Williams, and S. J. Rosner, "Deposition of three-dimensional Ge islands on Si(001) by chemical vapor deposition at atmospheric and reduced pressures," J. Appl. Phys. **81**, 211 (1997).

[26] P. S. Chen, Z. Pei, Y. H. Peng, S. W. Lee, M.-J. Tsai, "Boron mediation on the growth of Ge quantum dots on Si(10 0) by ultra high vacuum chemical vapor deposition," Mater. Sci. Eng. B **108**, 213 (2004).

Reproduced with permission of the copyright owner. Further reproduction prohibited without permission.

[27] M. Schmidbauer, T. Weibach, H. Raidt, M. Hanke, R. Köhler, H. Wawre, "Ordering of self-assembled $Si_{1-x}Ge_x$ islands studied by grazing incidence small-angle x-ray scattering and atomic force microscopy," Phys. Rev. B **58**, 10523-10531 (1998).

[28] W. Dorsch, S. Christiansen, M. Albrecht, P. O. Hansson, E. Bauser, and H. P. Strunk, "Early growth stages of Ge 0. 85 Si 0. 15 on Si (001) from Bi solution," Surf. Sci. **331–333**, 896 (1995).

[29] V. A. Egorov, G. É. Cirlin, A. A. Tonkikh, V. G. Talalaev, A. G. Makarov, N. N. Ledentosov, V. M. Ustinov, N. D. Zakharov, and P. Werner, "Si/Ge nanostructures for optoelectronics applications," Phys. Solid State **46**, 49-55 (2004).

[30] K. Brunner, "Si/Ge nanostructures," Rep. Prog. Phys. **65**, 27-72 (2002).

[31] M. Elkurdi, P. Boucaud, S. Sauvage, G. Fishman, O. Kermarrec, Y. Campidelli, D. Bensahel, G. Saint-Girons, G. Patriarche, I. Sagnes, "Electromodulation of the interband and intraband absorption of Ge/Si self-assembled islands," Physica E 16, 450-454 (2003).

[32] M. S. Hegazy, T. F. Refaat, M. Nurul Abedin, H. E. Elsayed-Ali, "Fabrication of GeSi quantum dot infrared photodetector by pulsed laser deposition," Opt. Eng. **44**, 59702 (2005).

[33] J. L. Liu, A. Khitun, K. L. Wang, T. Borca-Tasciuc, W. L. Liu, G. Chen, and D. P. Yu, "Growth of Ge quantum dot superlattices for thermoelectric applications," J. Cryst. Growth **227-228**, 1111-1115 (2001).

[34] A. Alguno, N. Usami, T. Ujihara, K. Fujiwara, G. Sazaki, K. Nakajima, and Y. Shiraki, Appl. Phys. Lett. **83**, 1258 (2003).

Reproduced with permission of the copyright owner. Further reproduction prohibited without permission.

[35] H. Presting, J. Konle, H. Kibbel, and F. Banhart, "Growth studies of Ge-islands for enhanced performance of thin film solar cells," Physica E 14, 249-254 (2002).

[36] J. Knole, H. Presting, H. Kibbel, Physica E **16**, 596 (2003).

[37] B. Hinnemann, H. Hinrichsen, and D. E. Wolf, "Unusual Scaling for Pulsed Laser Deposition," Phys. Rev. Lett. **87**, 135701 (2001).

[38] J. A. Venables, *Introduction to surface and thin film processes*, Cambridge University Press (2000).

[39] G. Le Lay, and R. Kern, "Physical methods used for the characterization of modes of epitaxial growth from the vapor phase," J. Crystal. Growth **44**, 197 – 222 (1978).

[40] J. Tersoff, and F. K. LeGouse, "Competing relaxation mechanisms in strained layers," Phys. Rev. Lett. **72**, 3570 – 3573 (1994).

[41] F. K. LeGoues, B. S. Meyerson, J. F. Morar, and P. D. Kirchner, "Mechanism and conditions for anomalous strain relaxation in graded thin films and superlattices," J. Appl. Phys. 71, 4230 – 4243 (1992).

[42] S. Christiansen, M. Albrecht, H. P. Strunk, and H. J. Maier, "Strained state of Ge(Si) islands on Si: Finite element calculations and comparison to convergent beam electron-diffraction measurement," Appl. Phys. Lett. **64**, 3617 – 3619 (1994).

[43] J. Tersoff, "Step Energies and Roughening of Strained Layers," Phys. Rev. Lett. 74, 4962 (1995).

[44] V.-G. Stoleru, D. Pal, and E. Towe, "Self-assembled (In,Ga)As/GaAs quantum-dot nanostructures: starin distribution and electronic structure," Physica E **15**, 131 – 152 (2002).

Reproduced with permission of the copyright owner. Further reproduction prohibited without permission.

[45] G. Cipriani, M. Rosa-Clot, and S. Taddei, "Electronic-level calculations for semiconductor quantum dots: Deterministic numerical method using Green's functions," Phys. Rev. B **61**, 7536 – 7544 (2000).

[46] F. Wu, M. G. Lagally, "Ge-induced reversal of surface stress anisotropy on Si(001)," Phys. Rev. Lett. **75**, 2534 – 2537 (1995).

[47] F. Iwawaki, M. Tomitori, O. Nishikawa, "STM study of initial stage of Ge epitaxy on Si(001)," Ultramicroscopy 42 – 44, 902 – 909 (1992).

[48] A. Sasaki, E. R. Weber, Z. Liliental-Weber, S. Ruvimov, J. Washburn, Y. Nabetani, "Transition thickness of semiconductor heteroepitaxy," Thin Solid Films **367**, 277 – 280 (2000).

[49] A. R. Woll, P. Rugheimer, and M. G. Lagally, "Strain engineering, self-assembly, and nanoarchitectures in thin SiGe films on Si," Mat. Sci. Eng. B **96**, 94 – 101 (2002).

[50] O. P. Pchelyakov, V. A. Markov, A. I. Nikiforov, and L. V. Sokolov, "Surface processes and phase diagrams of Si/Ge heterostructures," Thin Solid Films **306**, 299 – 306 (1997).

[51] M. Horn-von Hoegen, B. H. Müller, A. Al Falou, M. Henzler, "Surfactant induced reversible changes of surface morphology," Phys. Rev. Lett. **71**, 3170 (1993).

[52] B. Voigtländer, A. Zinner, "Simultaneous molecular beam epitaxy growth and scanning tunneling microscopy imaging during Ge/Si epitaxy," Appl. Phys. Lett. **63**, 3055-3057 (1993).

[53] M. S. Hegazy, H. E. Elsayed-Ali, "Observation of step-flow growth in femtosecond pulsed laser deposition of Si on Si(100)-2x1," J. Vac. Sci. Technol. A **20**, 2068 (2002).

[54] C. E. Aumann, Y.-W. Mo, and M. G. Lagally, Appl. Phys. Lett. **59**, 1061 (1991).

Reproduced with permission of the copyright owner. Further reproduction prohibited without permission.

[55] J. Powell, A. Jablonski, I. S. Tilinin, S. Tanuma, and D. R. Penn, "Surface sensitivity of auger-electron spectroscopy and x-ray photoelectron spectroscopy," J. Elect. Spect. Rel. Phen. **98-99**, 1-15 (1999).

[56] M. P. Seah and W. A. Dench, "Quantitative electron spectroscopy of surfaces: A standard data base for electron inelastic mean free paths in solids," Surf. Interface. Anal.**1**, 2-11 (1979).

[57] J. W. Lee, D. Schuh, M. Bichler, and G. Abstreiter, "Advanced study of various characteristics found in RHEED patterns during the growth of InAs quantum dots on GaAs (0 0 1) substrate by molecular beam epitaxy," Appl. Surf. Sci. **228**, 306 (2004).

[58] M. D. Kim, T. W. Kim, and Y. D. Woo, "Dependence of the growth modes and the surface morphologies on the As/In ratio and the substrate temperature in InAs/GaAs nanostructures," J. Cryst. Growth **265**, 41 (2004).

[59] S. W. Lee, L. J. Chen, P. S. Chen, M. –J. Tsai, C. W. Liu, W. Y. Chen, and T. M. Hsu, "Improved growth of Ge quantum dots in Ge/Si stacked layers by pre-intermixing treatments," Appl. Surf. Sci. **224**, 152 (2004).

[60] Anders, C. S. Kim, B. Klein, M. W. Keller, R. P. Mirin, A. G. Norman, "Bimodal size distribution of self-assembled $In_xGa_{1-x}As$ quantum dots," Phys. Rev. B **66**, 125309 (2002).

[61] V. Le Thanh, P. Boucaud, D. De Débarre, and Y. Zheng, "Nucleation and growth of self-assembled Ge/Si(001) quantum dots," Phys. Rev. B **58**, 211 (1998).

Reproduced with permission of the copyright owner. Further reproduction prohibited without permission.

[62] Z. Zhang and M. G. Lagally, "Atomistic Processes in the Early Stages of Thin-Film Growth," Science 276, 377 (1997).

[63] J. Shen, Z. Gai, J. Kirschner, "Growth and magnetism of metallic thin films and multilayers by pulsed-laser deposition," Surf. Sci. Rep. 52, 163 (2004).

[64] P.-O. Jubert, O. Fruchart, C. Meyer, "Nucleation and surface diffusion in pulsed laser deposition of Fe on Mo(110)," Surf. Sci. **552**, 8-16 (2003).

[65] N. N. Nedialkov, P. A. Atanasov, S. E. Imamova, A. Ruf, P. Berger, F. Dausinger, "Dynamics of the ejected material in ultra-short laser ablation of metals," Appl. Phys. A **79**, 1121 (2004).

[66] D. M. Zhang, L. Guan, Z. H. Li, G. J. Pan, H. Z. Sun, X. Y. Tan, and L. Li, "Influence of kinetic energy and substrate temperature on thin film growth in pulsed laser deposition," Surf. Coatings Technol. **200**, 4027-4031 (2006).

[67] B. Hinnemann, H. Hinrichsen, and D. E. Wolf, "Epitaxial growth with pulsed deposition: Submonolayer scaling and Villain instability," Phys. Rev. E **67**, 11602 (2003).

[68] D. Litvinov, T. O'Donnell, and R. Clarke, "*In situ* thin-film texture determination," J. Appl. Phys. **85**, 2151–2156 (1999).

[69] S. Andrieu and P. Frechard, "What information can be obtained by RHEED applied on polycrystalline films?,"Surf. Sci. 360, 289-296 (1996).

Reproduced with permission of the copyright owner. Further reproduction prohibited without permission.

CHAPTER V

FABRICATION OF QUANTUM-DOT BASED INFRARED PHOTODETECTORS BY PULSED LASER DEPOSITION

V.1. Introduction

Devices that are based on Ge QD have received significant attention in the past few years. Ge QD have proved very promising for fabricating infrared photodetectors [1,2], thermoelectric devices [3], and enhancing the performance of solar cells [4]. QD infrared photodetectors (QIPD) were first proposed by Ryzhii in 1996 [5] and were shown to have better sensitivity to normal incidence photoexcitation, broader IR response, high photoconductive gain, high extraction efficiency, lower dark current, elevated operation temperatures, and higher photoelectric gain than quantum well infrared photodetectors (QWPD) [6-8]. Unlike the case of single crystal photodetectors, controlling the QD material composition, size distribution, spatial distribution, shape and density can be used to tune the device detection band and to control the spectral response of the QDIP in a broad range through IR [1,6,9].

A typical QDIP device consists of a multiple of two-dimensional arrays of QDs separated by spacing layers and sandwiched between two heavily doped layers: emitter and collector, Fig. 5.1. The device, however, can have any junction structure, such as P-N, N-P-N, P-I-N, etc. In most cases, QDs are grown via self-assembly in lattice mismatched semiconductors, e.g. Ge/Si and InGaAs/GaAs. As discussed in chapter IV, Ge growth on Si follows the Stranski-Krastanow (SK) mode, in which Ge atoms form

Reproduced with permission of the copyright owner. Further reproduction prohibited without permission.

few epitaxial monolayers (wetting layer) before developing "self-assembled" QDs, in order to relieve the strain caused by the lattice mismatch [10]. The amount of that strain and the deposition conditions control the shape, size and spatial distributions of the QDs; therefore allows for the tuneability of the detected wavelength band.

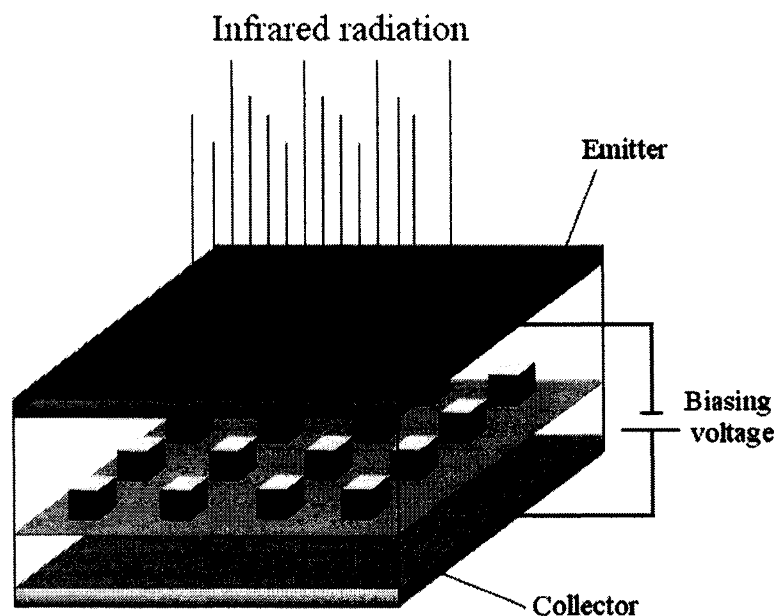

Fig. 5.1. Structure of a typical QDIP, consisting of multilayers of QD sandwiched between the two heavily doped layers of emitter and collector.

Ge QDs were grown on Si by molecular beam epitaxy (MBE) [11], chemical vapor deposition (CVD) [12], and liquid phase epitaxy (LPE) [2]. However, very few groups have used PLD to grow Ge on Si and to fabricate optical and electrical devices. Among the attractive features of PLD, as discussed in Chapter II, are the preservation of stoichiometry and the ease of growing multilayered films. These two features would enable the growth of multilayered devices of different materials or dopings without the

Reproduced with permission of the copyright owner. Further reproduction prohibited without permission.

need for residual gases or doping sources; only targets with the desired doping are used. This should lead to a reduction in the fabrication time and cost. In this chapter, PLD is used to fabricate a multi-layered infrared photodetector that is based on Ge QDs grown on Si(100) substrate.

V.2. Theory of QDIP

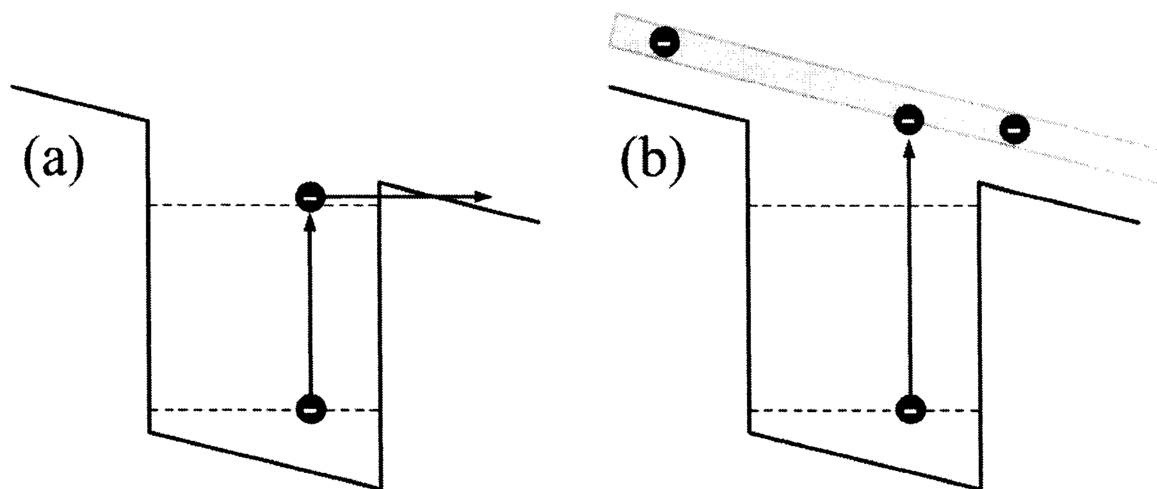

Fig. 5.2. Transitions in quantum confined heterostructures: (a) sub-band to sub-band, and (b) sub-band to continuum.

Generally, optically induced transitions in photodetectors, based on quantum-confinement structures, involve sub-band to sub-band or sub-band to continuum absorption, Fig. 5.2 [13]. For the case of QDIP, radiation is detected through intraband transitions in the conduction band. The absorption of IR radiation is associated with the electron bound-to-continuum or bound-to-quasibound transitions, which results in

Reproduced with permission of the copyright owner. Further reproduction prohibited without permission.

photoionization of QDs and free electrons. Figure 5.3 summarizes the operation aspects of QDIP. Electrons are injected from the emitter into the active region with QDs, where electrons could be captured by QDs or drifted toward the collector. When photoexcited by IR photons, the emitted electrons drift toward the collector by the electric field provided by the applied bias, resulting in photocurrent [7,14]. Bound electrons accumulated in QDs create a significant space charge which modifies the electric field distribution in the active region. The process of photoionization of QDs under IR illumination results in a redistribution of the electric field in the active region, which gives rise to a change in the injected current. The total current across the photodetector is the sum of both the current caused by electrons emission from QDs (by thermoemission and/or photoemission) and the injected current from the emitter. The QDIP operation is associated with the current across the device active region limited by the bound space charge which is controlled by incident IR radiation [15].

The absorption of the IR radiation takes place via intraband transitions in QDIP. The absorption coefficient depends on the energy of states of the QD, which depend mainly on the shape of the QD. Therefore, the QD shape and size distribution should be controlled in such a way to optimize absorption of the desired wavelength. However, due to the size and shape fluctuations of the QD, the spectral response is broadened. Experiments and theoretical calculations showed higher absorption for the in-plane polarized light compared to the perpendicularly polarized one [16]. Another result is the strong normal incidence absorption, which is connected with the QD size. Therefore, the QD have to be small in the lateral and in the growth direction [16]. High absorption efficiency is required for good detectors, which is achieved by high QD density.

Reproduced with permission of the copyright owner. Further reproduction prohibited without permission.

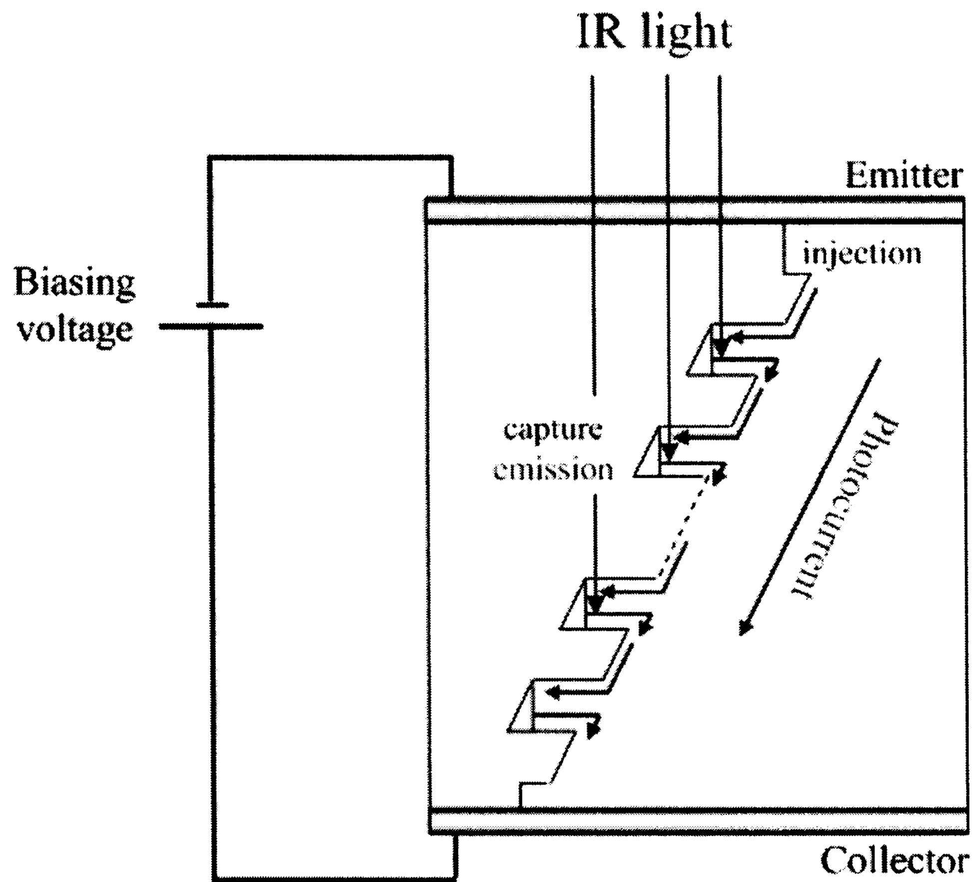

Fig. 5.3. Schematics showing the operation principle of QDIP.

Without illumination, small dark current flows across the device. The amount of such a current depends on the generation-recombination origin in the carrier trapping and thermionic emission from QD and thermionic emission from emitter in the active region of the device [7]. Thermal dark current is approximated by [5,17]

$$j_{th} = e\sum_k \frac{G_k}{P_k} \approx \frac{eG_{th}}{p_c}, \tag{5.1}$$

where e is the electron charge, G_{th} is the rate of thermoemission per unit area of QD layer and p_c is the average capture probability for free electrons. QDIP should have lower dark

Reproduced with permission of the copyright owner. Further reproduction prohibited without permission.

currents by decreasing thermionic emission through increasing the carriers' life times and decreasing the capture probability. Dark current optimization depends on the density of QD, doping level of the active region, and the applied bias [17].

Under IR illumination, photoemission (via bound-to-continuum transition) dominates thermoemission, giving rise to photocurrent, which is estimated by [5,6,13,16]

$$j_{ph} = \frac{eG_{ph}}{p_c} = \frac{e\sigma_{QD}\langle n\rangle\Phi}{p_c} = e\Phi\eta g, \tag{5.2}$$

where G_{ph} is the photoemission rate per unit area of the QD layer, σ_{QD} is the photoemission cross section, $\langle n\rangle$ is the average sheet density of electrons in the QD layer, Φ is the incident photons flux, η is the detector's quantum efficiency, and g is the photoconductive gain. The photoconductive gain is defined as the ratio of the total flux of injected electrons to the total rate of thermoemission (under dark conditions) or photoemission (under illumination) from all QD. It is then defined as [6,13,16]

$$g \approx \frac{1}{MFp_c(1+p_c)}, \tag{5.3}$$

where M is the number of QD layers, F is the filling factor (given by the covering area of QD layer). Expression (5.3) is valid under the condition $p_c << 1$, which is true for QD. Another expression for the gain is [6,16]

$$g = \frac{\tau_{eff}}{\tau_{tr}}, \tag{5.4}$$

where τ_{eff} is the effective carrier life time and τ_{tr} is the carrier transit time across the active region.

Reproduced with permission of the copyright owner. Further reproduction prohibited without permission.

An important parameter that measures the QDIP quality is its responsivity, which is defined as the photocurrent per unit light power (in Watts). If the photoemission is much larger than thermoemission, we may write [5,6]

$$R = \frac{(j_{ph} - j_{th})}{\hbar\omega\Phi} \approx \frac{e\sigma_{QD}\langle n \rangle}{\hbar\omega\Phi}, \tag{5.5}$$

where $\hbar\omega$ is the energy of the incident photons. It may be important to point out that it is not just enough for the value of the responsivity to be high and to increase with the applied bias, as the dark current also increases with the bias.

The signal-to-noise ratio, SNR, of photodetectors is measured by the detectivity (measured in units of $cm\sqrt{Hz}W^{-1}$), which is expressed as [6,13]

$$D^* = R\frac{\sqrt{A\Delta f}}{I_n} = R\frac{\sqrt{A\Delta f}}{\sqrt{4egI_{th}\Delta f}}, \tag{5.6}$$

where A is the detector area, Δf is the measured bandwidth, and I_n is the noise current. In terms of thermoemission and photoemission rates, the detectivity may be written as [6,13]

$$D^* = \frac{G_{ph}}{\hbar\omega\Phi\sqrt{G_{th}}}. \tag{5.7}$$

Reproduced with permission of the copyright owner. Further reproduction prohibited without permission.

V.3. Photodetector fabrication

Si substrates are chemically cleaned as described in section IV.5 prior to being loaded into the vacuum chamber. The chamber is pumped down to a pressure of $<1\times10^{-8}$ Torr and baked for 12-24 hours before flashing the substrate to ~1100 °C in order for the 2×1 reconstruction to develop. The Si substrate is kept at 773 K during deposition in a base pressure $<1\times10^{-9}$ Torr. A 40-ns Nd:YAG laser (16 J/cm^2, 50 Hz) is used to ablate the rotating target, which is in the form of two semi-circular disks placed together to form a circle; one is Si (p-type, 1×10^{19} cm^{-3}) and the other is undoped Ge. During target rotation, PLD minimizes the formation of particulates by exposing a fresh area to the laser; thus, the probability of fracto-emission is minimized. The laser is focused on the rotating target with a spot size of 330 μm (measured at 1/e of the peak value). The system is designed in such a way that the laser hits the target at 45°. A thickness of ~0.6 nm Ge is first deposited, followed by depositing ~0.4 nm Si. The process is repeated for 40 revolutions. A Si capping layer of ~1 nm is deposited before a mask is used to deposit about 100-nm thick Al contacts. The deposition of the 40-layered device, without the metal contacts, took ~500 s, which is much less than the time needed to fabricate similar devices by other deposition techniques. A schematic diagram of the device is shown in Fig. 5.4.

Reproduced with permission of the copyright owner. Further reproduction prohibited without permission.

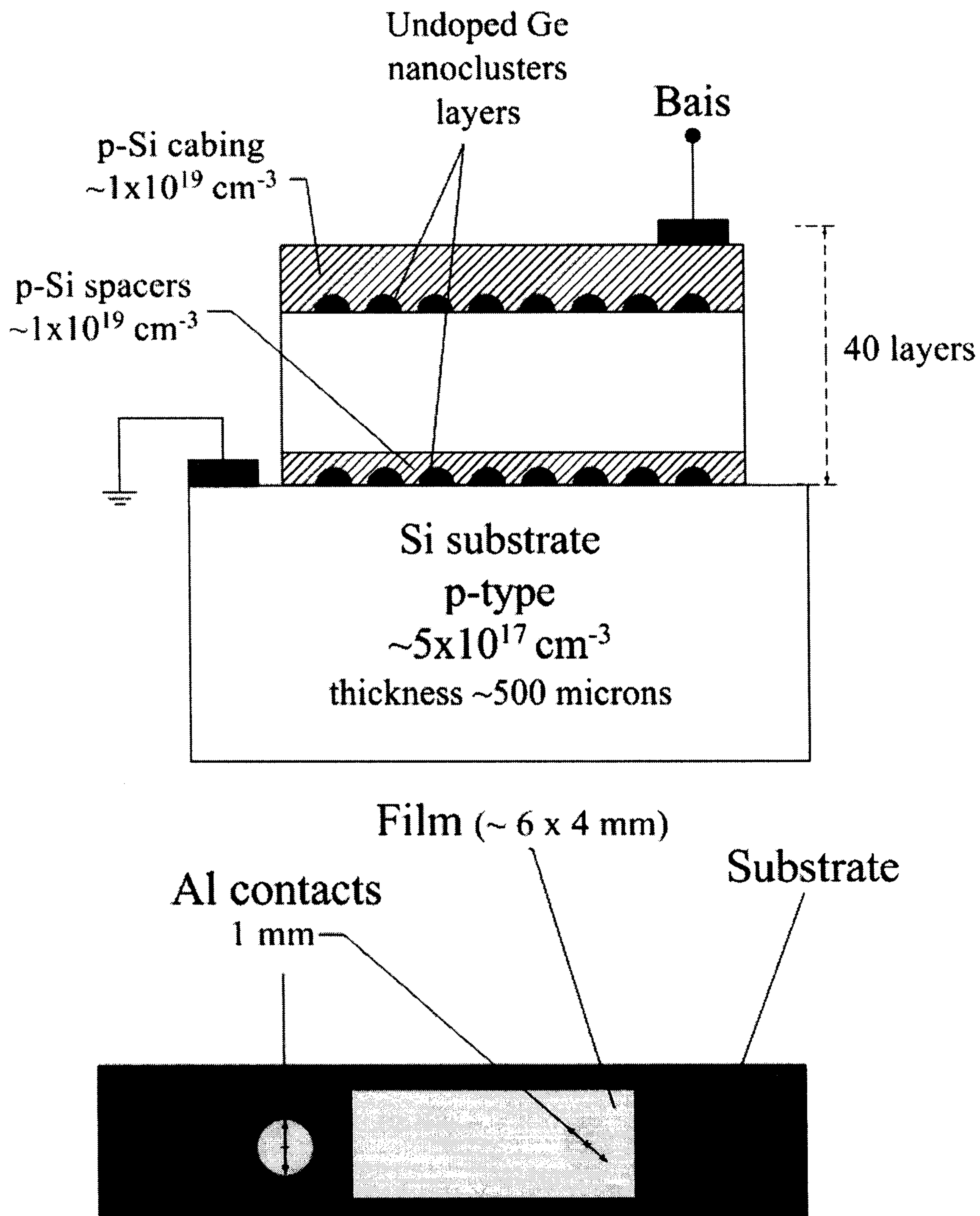

Fig. 5.4. (Top) Side view schematics of the multi-layered Ge QD-based photodetector grown by PLD on Si(100). (Bottom) Top view schematics showing the film and the metal contacts.

Reproduced with permission of the copyright owner. Further reproduction prohibited without permission.

V.4. Growth characterization

To *in situ* monitor the deposition, a 15-keV CW electron gun is used. A phosphor screen is used to display the electron diffraction pattern, which is recorded by a CCD camera. During the initial stages of deposition, the Si(100)-2×1 diffraction pattern, Fig. 5.5 (left), does not change, which accounts for the formation of the 2D wetting layer. In such 2D growth, the Ge film grows having the Si lattice constant. Upon the completion of the first Ge layer, the RHEED diffraction pattern transforms into a transmission pattern, Fig. 5.5 (right), indicating the formation of elongated (hut) Ge QDs. Ge QDs form to relieve the internal strain inside the film due to the lattice mismatch between Ge and Si. Such a transmission pattern is taken as an indication for the formation of QD to start the deposition of the Si spacing layer. As the capping layer is being grown, the transmission pattern does not change in shape, but decreases in intensity.

The morphology of the Ge film is studied by *ex situ* AFM (Digital Instruments; Nanoscope 3100). For this purpose, a Ge film of the same thickness as the first QD layer, was grown under the same deposition conditions. Figure 5.6 shows the formation of the Ge QDs, which are distributed homogeneously over the substrate. A detailed study of the Ge QD formation on Si(100)-2×1 showed that under similar deposition conditions at the same thickness hut clusters are formed [18,19], as described in chapter IV. The size distribution of the Ge QDs of Fig. 5.6 is shown in Fig. 5.7, indicating a FWHM of ~35 nm.

Reproduced with permission of the copyright owner. Further reproduction prohibited without permission.

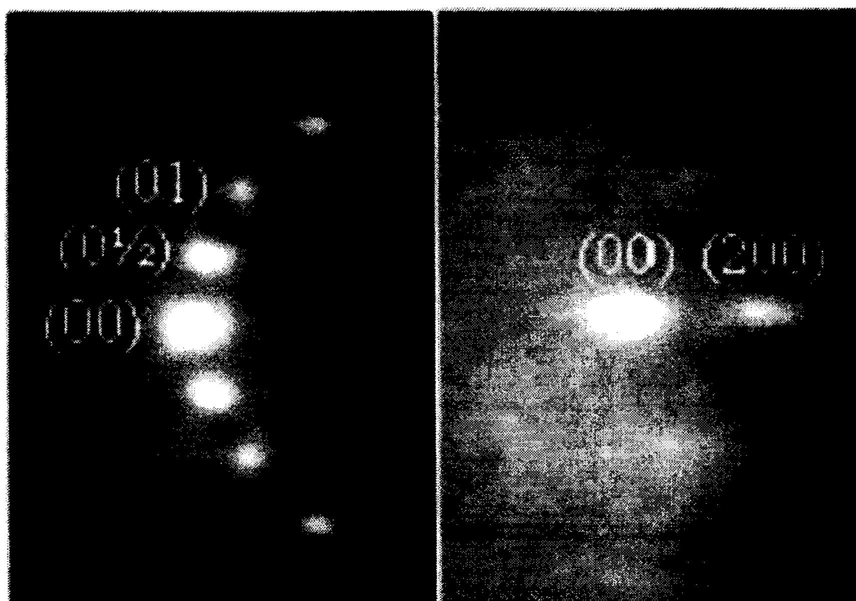

Fig. 5.5. (Left) RHEED diffraction pattern of the Si(100)-2×1 substrate. (Right) Transmission pattern formed when the growth of the first Ge QD layer is completed.

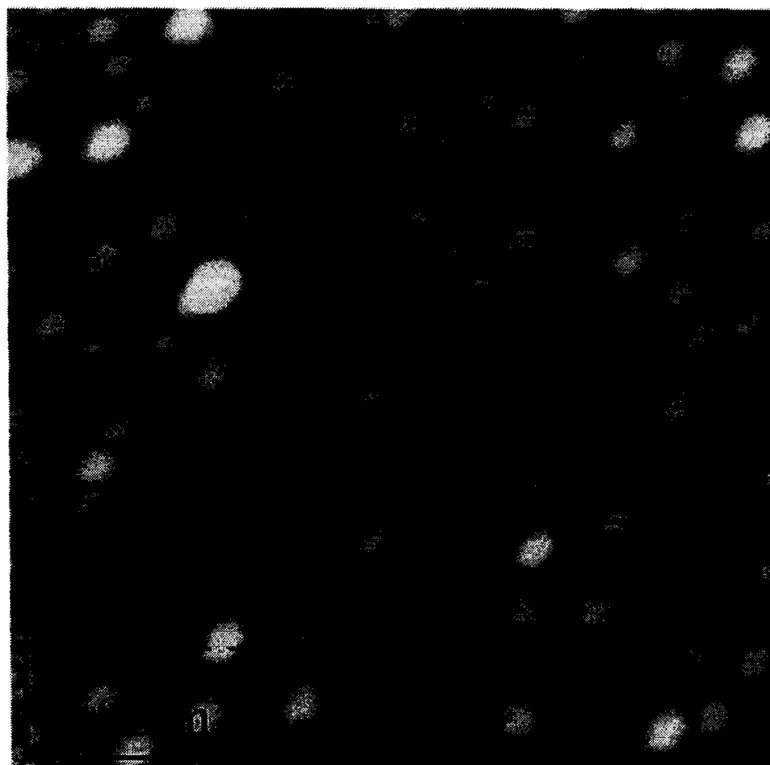

Fig. 5.6. AFM scan of the Ge quantum dots. The major axis length distribution is shown as inset [scan area = 1.1×1.1 μm].

Reproduced with permission of the copyright owner. Further reproduction prohibited without permission.

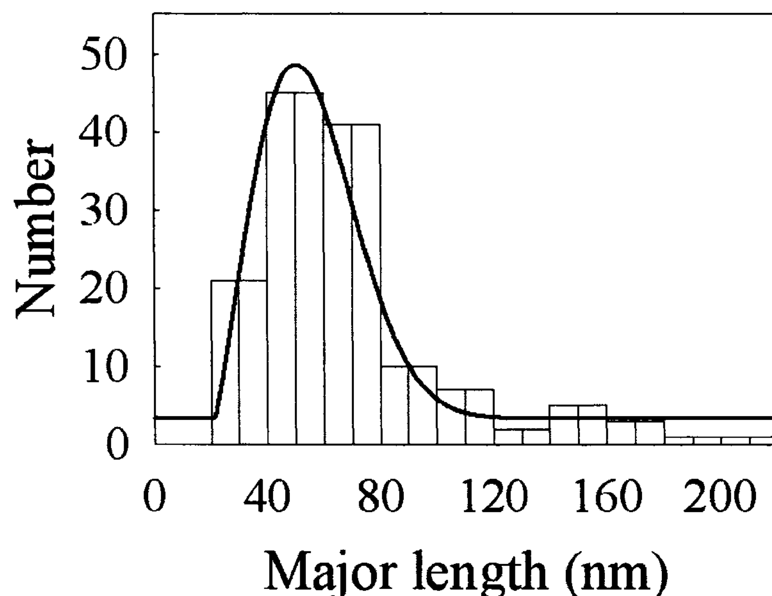

Fig. 5.7. Histogram showing the size distribution of the above figure.

V.5. Electrical and optical characterization

Silver epoxy was used to mount the QD detector sample on an aluminum sample holder and to fix the connecting wires to the Al pads. Figure 5.8 shows a schematic of the characterization setup [20]. The setup consists mainly of optical, electrical and mechanical sections. The mechanical section is used to mount the device while conditioning its operation in terms of alignment, temperature and bias voltage. The sample holder was mounted on the cold-finger of a vacuum sealed cryogenic chamber (dewar). The chamber was cooled by liquid nitrogen and the required temperature was obtained using a temperature controller (Lake Shore; Autotuning Temperature Controller 330). The controller senses the temperature using a Si diode (Lake Shore; DT-470) and modifies it using resistive heaters. Vacuum isolation (~10^{-6} Torr) was used with the

Reproduced with permission of the copyright owner. Further reproduction prohibited without permission.

chamber to preserve temperature stability using a vacuum pumping system (Pfeiffer; Vacuum Pump System TSU071E). For the spectral response measurements, an optical signal was applied to the detector using the optical section. The optical section consists of a current controlled (Optronic Laboratories; Programmable Current Source OL65A) radiation source (Halogen lamp) the output of which is modulated using an optical chopper and analyzed using a monochromator (Optronic Laboratories; Monochromator OL750-S). The electrical section was integrated to measure the device output for a certain operating condition. A lock-in amplifier (Stanford Research Systems; DSP Lock-in Amplifier SR850) was used to measure the output signal for a given radiation input. A spectrum analyzer (Stanford Research Systems; 2 Channel dynamic Signal Analyzer SR785) was used for noise measurements. A semiconductor characterization system (Keithly; 4200) was used for the I-V measurements. All of these instruments are linked to a personal computer for data acquisition and control. The instruments are synchronized using the chopper controller. A preamplifier (Stanford Research Systems; SR570) is used to convert the detector current into a voltage signal.

Reproduced with permission of the copyright owner. Further reproduction prohibited without permission.

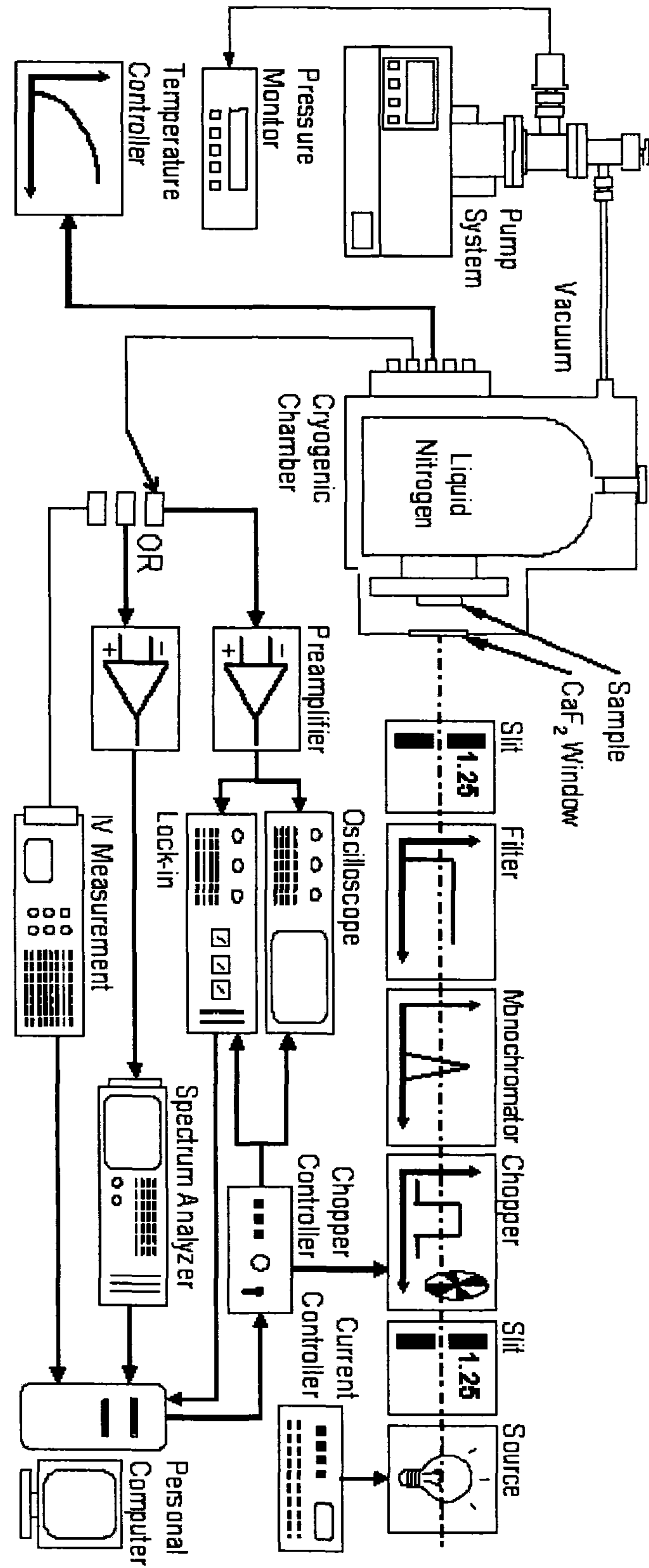

Fig. 5.8. A schematic of the detector characterization setup.

Reproduced with permission of the copyright owner. Further reproduction prohibited without permission.

Figure 5.9 shows the I-V characteristics of the device at different operating temperatures. The I-V characteristics reveal the diode behavior of the sample, which confirms the Schottky structure. Cooling down the device slightly reduces the dark current, suggesting the domination of the leakage current due to the tunneling process. The inset of Fig. 5.9 zooms in to a part of the 293.2 K characteristics. The inset compares the curves obtained in dark and illumination conditions. A current shift of about 5 μA with 14.5 W/cm^2 incident intensity suggests the sensitivity of the device to radiation. In order to quantify this sensitivity a spectral response measurements were carried out.

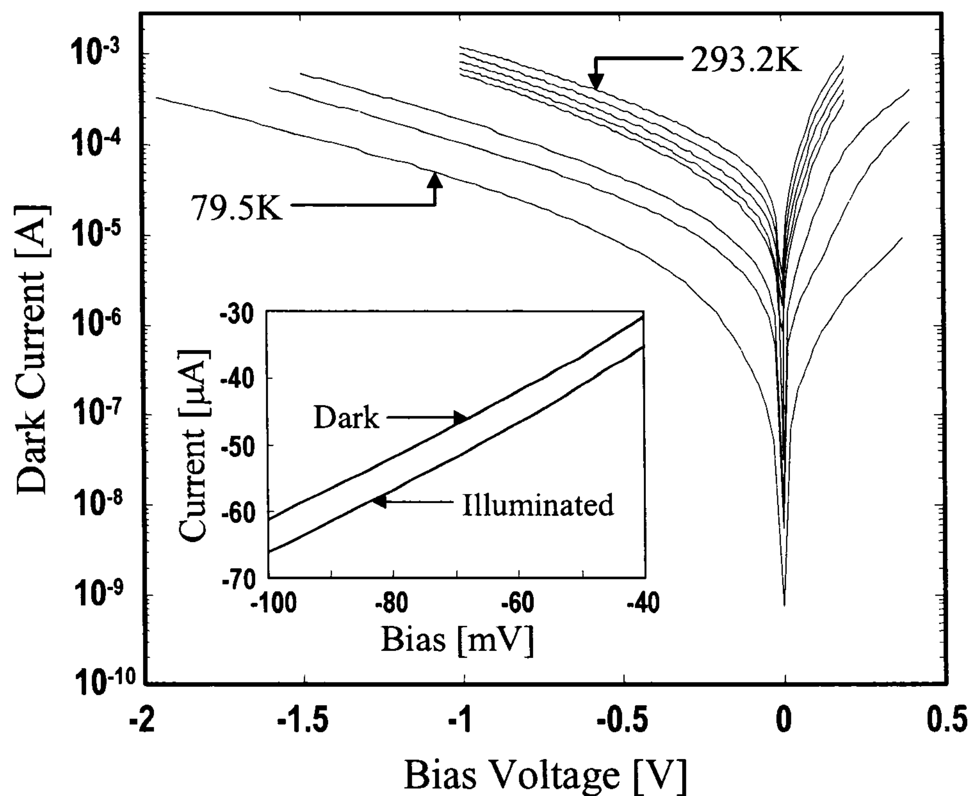

Fig. 5.9. Dark current variation with bias voltage obtained at temperatures of 293.2, 283.2, 273.2, 263.2, 253.2, 160.0, 130.0 and 79.5 K from top to bottom, respectively. The inset shows a portion of the dark current at 293.2 K and it variation due to device illumination with 14.5 W/cm^2 radiation intensity.

Reproduced with permission of the copyright owner. Further reproduction prohibited without permission.

The spectral response of the QD photodetector sample is shown in Fig. 5.10. The characteristics assume 20-nm wavelength resolution with 10 averages. The characteristics were obtained in the wavelength range of 1.0 to 3.2 μm at 79.5 K operating temperature and different bias voltages. The spectral range is compatible with the optical section limitation. Lower temperatures have been used to minimize the device noise since the responsivity is very low. The applied bias voltage was limited not to breakdown the device. The spectral response reveals peak responsivity around 2 μm wavelength with ~1.8 and ~2.2 μm cut-on and cut-off wavelengths, respectively. The presence of this peak is attributed to the type-II band lineup with interband transitions observed in Si/Ge QDs. Tuneability of this peak can be potentially achieved by controlling the composition, size, and size distribution of the QDs through varying the deposition parameters. These deposition parameters include growth temperature, laser fluence and repetition rate, and thickness of the Si spacers. PLD growth of Ge QDs and the control of their size and spatial distributions are reported elsewhere [18,19]. Another possible peak at a longer wavelength with a cut-on around 3 μm is visible in the figure. High responsivity at 1 μm dominates the maximum at 0.5 V due to absorption in the Si substrate. The responsivity increases almost three orders of magnitude (from ~5×10^{-6} A/W to ~3×10^{-3} A/W at 2 μm) by increasing the bias from 0.5 to 3.5 V. Although this might be attributed to an internal gain mechanism, it is associated with a high increase in the noise level. This fact is clarified in Fig. 5.11, where the noise is plotted against the operating bias voltage. For comparison, the device detectivity (D*) is calculated and plotted in the same figure. Knowing the mean responsivity, R, at a certain bias voltage, and by measuring the noise current density, i_n, at the same voltage, the detectivity is calculated using the relation

Reproduced with permission of the copyright owner. Further reproduction prohibited without permission.

$$D^* = \frac{i_n}{R} \cdot \sqrt{A},$$

where A is the area of the sensitive element. The figure reveals a poor detectivity compared to typical infrared detectors operating at the same wavelength range, even at room temperature. Nevertheless, the results indicate a promising device, with a wavelength tunability option. The poor detectivity is attributed to the poor responsivity associated with QD detectors in general. Thus, research efforts should focus on the gain behavior and should try to increase it.

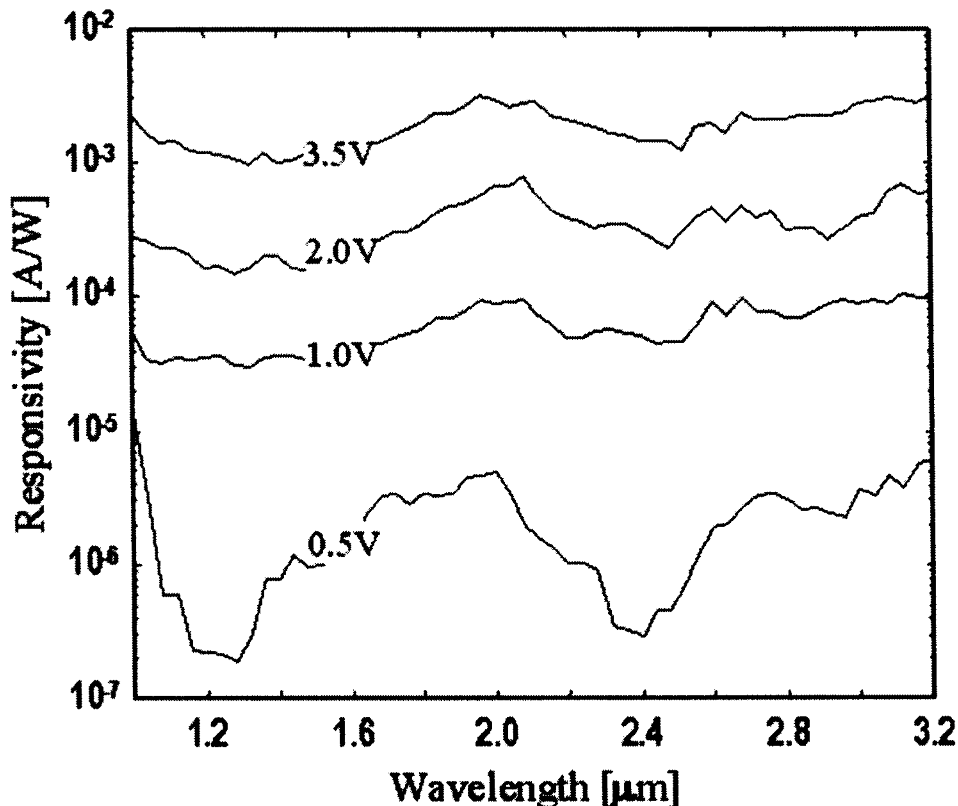

Fig. 5.10. Spectral response at different bias voltages, obtained at an operating temperature of 79.5 K.

Reproduced with permission of the copyright owner. Further reproduction prohibited without permission.

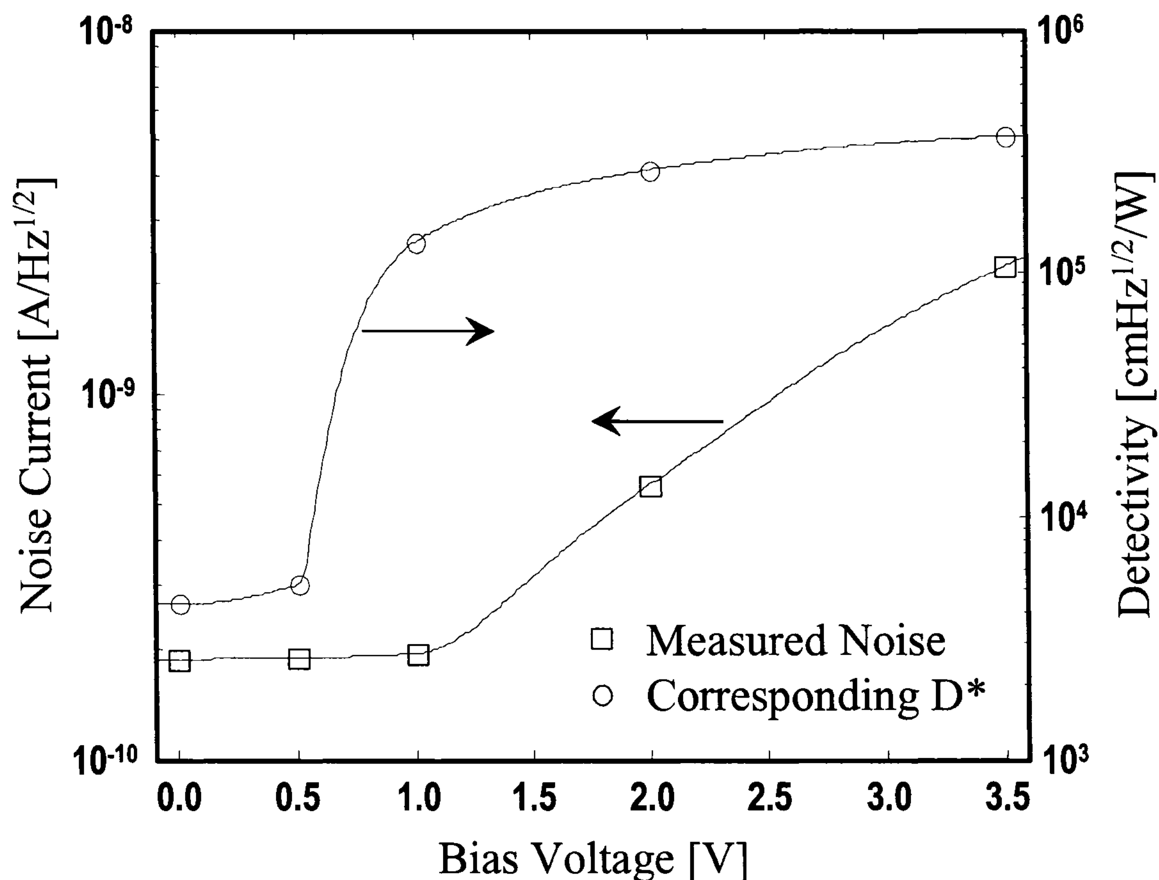

Fig. 5.11. Measured and fitted noise variation with bias voltage and the corresponding detectivity (D*), obtained at an operating temperature of 79.5 K.

V.6. Conclusion

In summary, the fabrication of a mid-infrared photodetector by PLD is reported. The device consists of 40 successive Ge QD layers separated by 39 Si spacers and a topmost Si capping layer. The fabrication time of the device, without the metal contacts, takes ~500 s. The growth was studied by *in situ* RHEED to identify the formation of Ge

Reproduced with permission of the copyright owner. Further reproduction prohibited without permission.

QDs, while *ex situ* AFM is used to study the morphology of the QDs and their size and spatial distributions. The difference in the current values in dark and illumination conditions shows the device is sensitive to radiation. Spectral responsivity measurements reveal a peak around 2 μm, the responsivity of which increases three orders of magnitude as the bias increases from 0.5 to 3.5 V. However, the low detectivity requires some design improvements.

V.7. References

[1] V. A. Egorov, G. É. Cirlin, A. A. Tonkikh, V. G. Talalaev, A. G. Makarov, N. N. Ledentosov, V. M. Ustinov, N. D. Zakharov, and P. Werner, Phys. Solid State 46, 49 (2004).

[2] A. Elfving, G. V. Hansson, and W.-X. Ni, Physica E. 16, 528 (2003).

[3] J. L. Liu, A. Khitun, K. L. Wang, T. Borca-Tasciuc, W. L. Liu, G. Chen, and D. P. Yu, J. Cryst. Growth 227-228, 1111 (2001).

[4] A. Alguno, N. Usami, T. Ujihara, K. Fujiwara, G. Sazaki, K. Nakajima, and Y. Shiraki, Appl. Phys. Lett. 83, 1258 (2003).

[5] V. Ryzhii, "The theory of quantum quantum-dot infrared phototransistors," Semicond. Sci. Technol. **11**, 759-765 (1996).

[6] M. Maksimović, "Quantum dot infrared photodector as an element of free-space optics communication systems," XI Telekomunikacioni Forum Telefor, 2003.

Reproduced with permission of the copyright owner. Further reproduction prohibited without permission.

[7] E. Towe and D. Pan, "Semiconductor quantum-dot nanostructures: their application in a new class of infrared photodetectors," IEEE J. Sel. Top. In QE **6(3)**, 408-421 (2000).

[8] H. C. Liu, "Quantum dot infrared photodetectors," Optoelectronics Rev. **11(1)**, 1-5 (2003).

[9] C. Miesner, O. Röthing, K. Brunner, G. Abstreiter, Physica E 7, 146 (2000).

[10] K. Brunner, Rep. Prog. Phys. 65, 27-72 (2002).

[11] V. Cimalla, K. Zekentes, and N. Vouroutzis, Mater. Sci. Eng. B 88, 186 (2002).

[12] P. S. Chen, Z. Pei, Y. H. Peng, S. W. Lee, M.-J Tsai, Mat. Sci. Eng. B 108, 213 (2004).

[13] J. Phillips, P. Bhattacharya, S. W. Kennerly, D. W. Beekman, and M. Dutta, "Self-assembled InAs-GaAs quantum-dot intersubband detectors," IEEE J. Quan. Elect. **35(6)**, 936-943(1999).

[14] C. Miesner, K. Brunner, G. Abstreiter, "Lateral photodetectors with Ge quantum dots in Si," Infrared Phys. and Technol. **42**, 461-465 (2001).

[15] V. Ryzhii, I. Khmyrova, M. Ryzhii, and V. Mittin, "Comparison of dark current, responsivity and detectivity in different intersubband infrared photodetectors," Semicond. Sci. Technol. **19**, 8-16 (2003).

[16] B. Kochman, A. D. Stiff-Roberts, S. Chakrabarti, J. D. Philips, S. Krishna, J. Singh, P. Bhattacharya, "Absorption, Carrier Lifetime, and Gain in InAs-GaAs Quantum-Dot Infrared Photodetectors," IEEE J. Quant. Elect. **39,** 459-466 (2003).

[17] M. B. El Mashade, M. Ashry, A. Nasr, "Theoretical analysis of quantum dot infrared photodetectors," Semicon Sci. Technol.**18**, 891-900 (2003).

Reproduced with permission of the copyright owner. Further reproduction prohibited without permission.

[18] M. S. Hegazy and H. E. Elsayed-Ali, "Self-assembly of Ge quantum dots on Si(100) by pulsed laser deposition," Appl. Phys. Lett. 86, 243204 (2005). [Selected to appear on the Virtual Journal of Nanoscience and Technology, Vol. 11(24) (2005)].

[19] M. S. Hegazy and H. E. Elsayed-Ali, "Growth of Ge quantum dots on Si by pulsed laser deposition," J. Appl. Phys. 99, 054308 (2006) [Selected to appear on the Virtual Journal of Nanoscience and Technology, Vol. 13(11) (2006)].

[20] T. F. Refaat, M. N. Abedin, O. V. Sulima, U. N. Singh and S. Ismail, In IEDM Tech. Dig., page 355-358, 2004.

Reproduced with permission of the copyright owner. Further reproduction prohibited without permission.

CHAPTER VI

NON-THERMAL LASER-INDUCED FORMATION OF CRYSTALLINE Ge QUANTUM DOTS ON Si(100)

VI.1. Introduction

Electronic excitations by laser or electron beam interaction with surfaces have been shown to modify surface properties [1-5]. Figure 6.1 summarizes all of the possible material modifications due to electronic excitations induced by laser or electron beams [6]. Electronic-induced surface processes include selective removal of surface atoms, surface layer modifications, and the alternation of rates of some surface processes [6]. Removal of surface atoms occurs due to bond breaking as a result of single or multiple photon excitations. In semiconductors, bond breaking by laser pulses below melting and ablation thresholds is purely electronic [7]. Even what was thought of as purely thermal desorption was recently reported to involve electronic excitations [8].

In Si(100)-2x1, bond breaking takes place due to the localization of two photo-generated surface holes at dimmer sites [7]. The number of the electronically-removed atoms, due to laser excitations, depends on the laser wavelength and is a superlinear function of laser fluence but is independent of the material's temperature [5,6].

Reproduced with permission of the copyright owner. Further reproduction prohibited without permission.

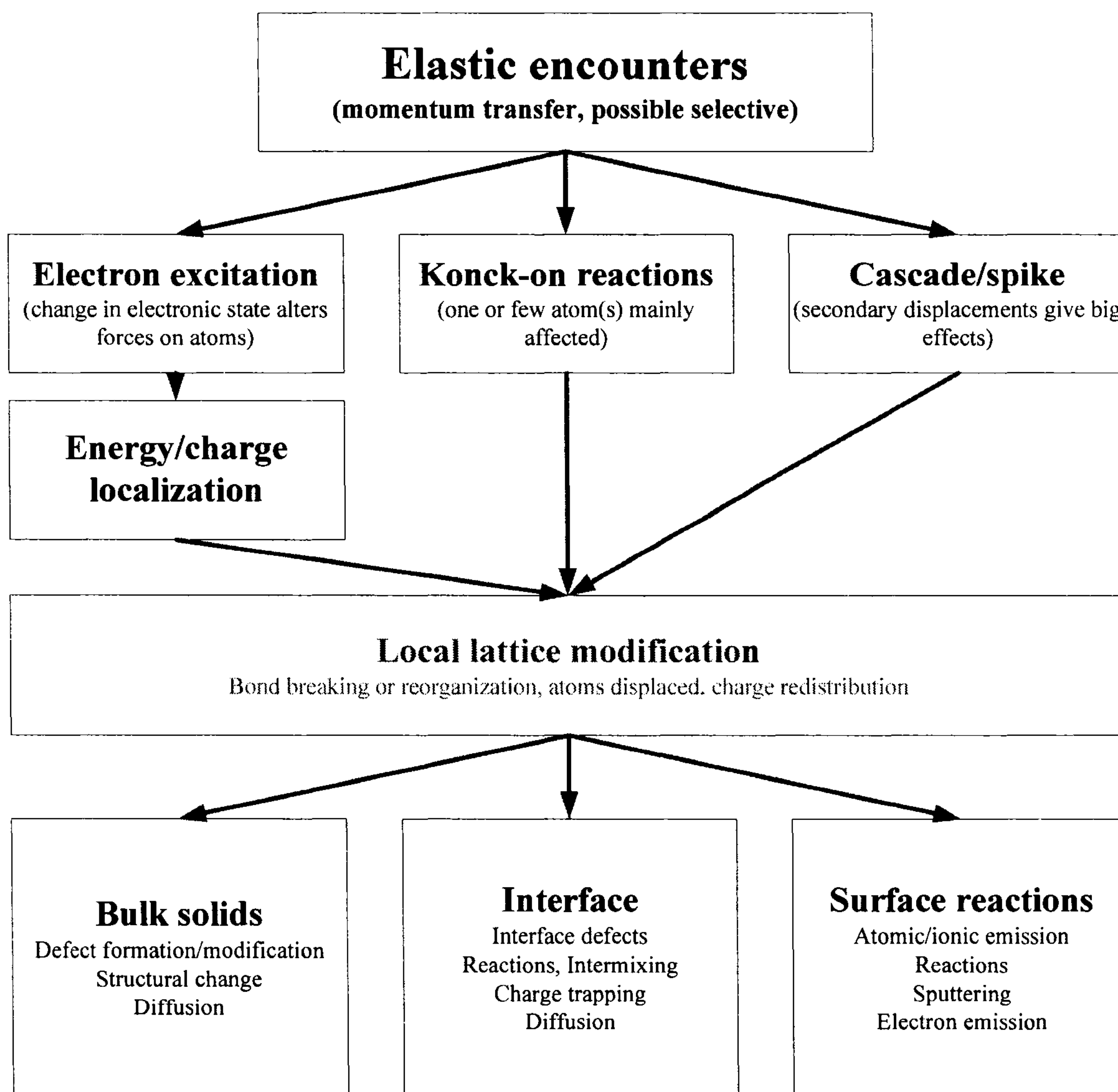

FIG. 6.1. Summery of all possible results of the interaction of laser or electron beams with materials [From Ref. [6] with permission[1]].

It is believed that energetic particles such as ions, electrons, and photons can transfer sufficient energy to enhance the migration of adsorbed atoms and/or molecules and hence enhance the nucleation and growth [4]. Despite that, a few publications have

[1] The figure was redrawn and reorganized after the kind permission from both Dr. Stoneham and Dr. Itoh through personal communications.

Reproduced with permission of the copyright owner. Further reproduction prohibited without permission.

considered the effects of the electronic excitations on the growth of thin films and nanostructures. Illumination of silica substrates with a low-fluence diode laser during deposition has been reported to enhance the shape and size distribution of Ga nanoparticles at ~100 °C [9] Illumination of silica substrates with a low-fluence diode laser during deposition has been reported to unify the cluster's shape and narrow the size distribution of Ga nanoparticles grown at ~100 °C [9]. Recently, our group has achieved homoepitaxy of Si(111)-7x7 via step flow at room temperature by exciting the substrate with femtosecond laser pulses during pulsed laser deposition (PLD) [10]. The growth process was attributed to the dynamic competition between the nonthermal laser-induced desorption of surface atoms and the adsorption of the new atoms [9,10]. On the other hand, irradiation by electron beams, of a few hundreds of eV, has been reported to enhance the epitaxy of CeO_2 on Si at 100 °C lower than that required for epitaxy [4].

It has to be noted that "light-controlled growth" techniques differ from the pulsed laser induced epitaxy (PLIE) of growing epitaxial layers of GeSi alloys, in which amorphous Ge or SiGe films are deposited at low temperatures before being rapidly melted and recrystallized via irradiation with high-power ns or ps UV laser pulses, leading to enhanced epitaxy and the redistribution of the Si and Ge contents [11].

In this chapter, we show that laser irradiation during the PLD of Ge on Si(100)-2x1 enhances the crystallinity of quantum dots (QD) and lessens the temperature required for their formation, which is ~400 °C as shown in Chapter IV.

Reproduced with permission of the copyright owner. Further reproduction prohibited without permission.

VI.2. Electronic-induced bond breaking

Removal of surface atoms occurs due to bond breaking as a result of single or multiple photon excitations. In semiconductors, bond breaking by laser pulses below melting and ablation thresholds is of a purely electronic nature [7]. In fact, it has been recently reported that even thermally-excited charge carriers are responsible for bond breaking of adsorbed atoms [8]. Due to the low surface absorption coefficients, photoexcitation takes place in bulk, resulting in a high density of electron-hole pairs, Fig 6.2, which can transfer to the surface electronic systems via electron-electron and/or electron-phonon coupling. Hole localization onto particular surface sites results in bond breaking (rupture) and, consequently, the ejection of atoms, via phonon kicks, with translational energy. In Si(100)-2x1, bond breaking has been reported to take place due to the localization of two photo-generated holes at the same surface bond of given dimer sites [7]. Figure 6.3 is a side view showing the bond structure of Si(100)-2x1, while the cartoon in Figure 6.4 summarizes the process of bond breaking via two-hole localization and atom ejection via phonon kick. The rate of the "two-hole" localization onto a particular lattice site is approximated by [12]

$$P = A[\exp(n_h) - 1]^2, \tag{6.1}$$

where A is a constant and

$$n_h = \frac{\text{concentration of photo-generated holes}}{\text{effective \# of free-hole surface valence band states}}. \tag{6.2}$$

The number of electronically-removed atoms depends on the laser wavelength and is a superlinear function of laser fluence, Φ, but it is independent of temperature [5,6]. For the

Reproduced with permission of the copyright owner. Further reproduction prohibited without permission.

"two-hole" localization mechanism, the yield of desorption, Y, has been calculated to have the form [12]

$$Y = Y_0[\exp(B\Phi) - 1]^2. \tag{6.3}$$

It has been observed that electronic-induced bond breaking processes have some common features [5,6,7]:

(1) Bond rupture takes place for atoms at perfect surface sites,

(2) Desorption of neutral atoms only takes place,

(3) Bond breaking rate is sensitive to surface sites and atomic species, which may result from the localization process and/or the bond breaking reaction,

(4) The desorption rate depends superlinearly on the excitation laser fluence for photon energies between 1 and 4 eV.

Reproduced with permission of the copyright owner. Further reproduction prohibited without permission.

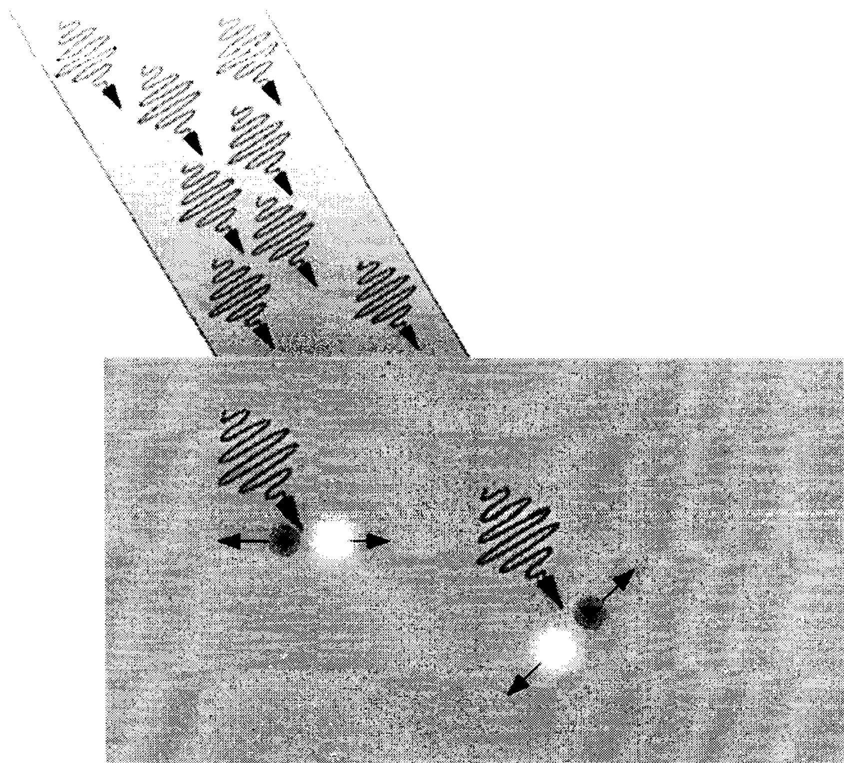

FIG. 6.2. Electron-hole pair generation due to laser absorption.

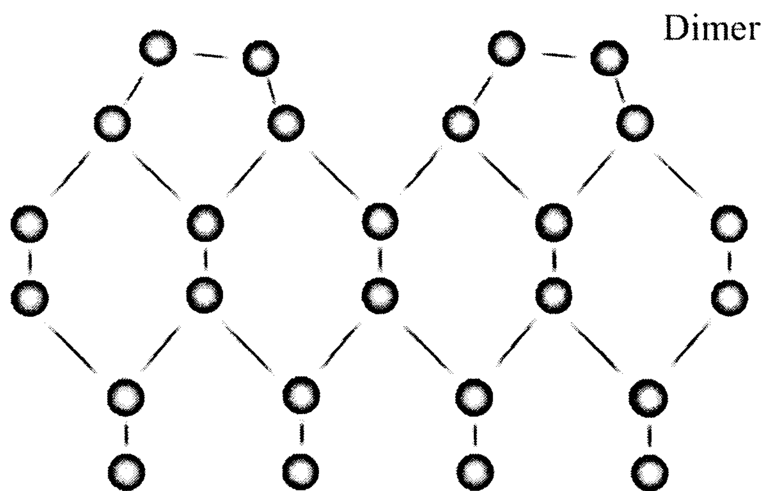

FIG. 6.3. Side view of the atomic structure of Si(100)-2x1.

Reproduced with permission of the copyright owner. Further reproduction prohibited without permission.

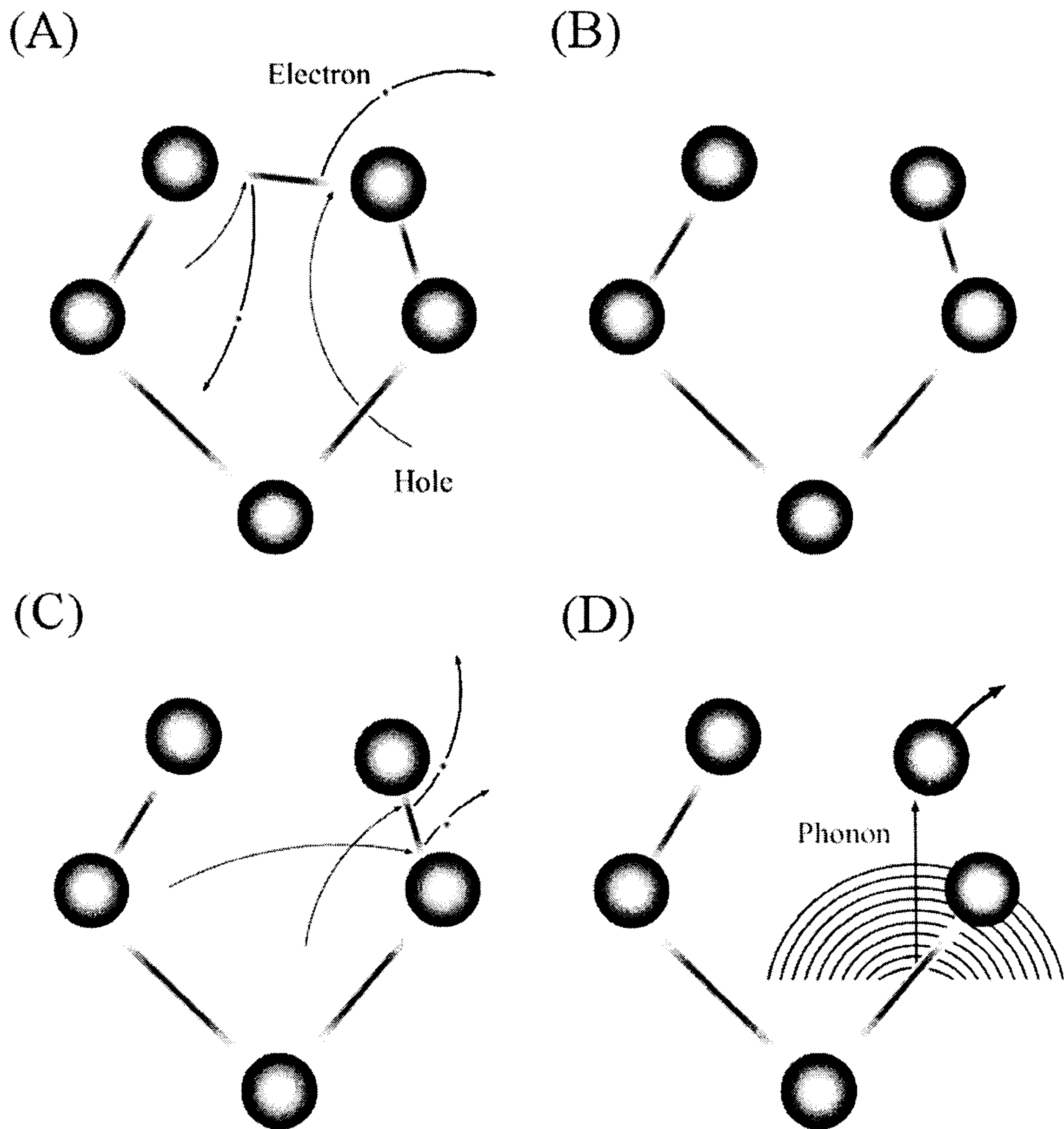

FIG. 6.4. Electronic-induced bond breaking: (A) two-hole localization at first bond, (B) first bond breaking, (C) two-hole localization at second bond, (D) atom ejection due to a phonon kick.

Reproduced with permission of the copyright owner. Further reproduction prohibited without permission.

VI.3. Experiment

Ge on Si(100)-2x1 was grown by PLD in an ultrahigh vacuum chamber, in which the Si substrate was heated by direct current, Fig. 2.5. The Ge target was mounted on a rotated holder with a variable rotation speed. Target rotation during PLD is necessary to minimize the formation of particulates. Before being loaded into the vacuum, the Si(100) substrates (with dimensions of 3-4 mm x 10 mm) were cleaned by chemical etching using a modification to the Shiraki method, as discussed in Chapter 4. The vacuum system was then pumped down, baked for at least 12 hours, and the sample was then flashed to 1100 °C in order for the 2×1 reconstruction to form. The chamber pressure was maintained $<1\times10^{-9}$ Torr.

A schematic of the experimental setup is shown in Fig. 6.5. A Q-switched Nd:YAG laser (1064 nm, FWHM of ~40 ns, Fig 6.6(a), repetition rate of 50 Hz) is split into an ablation beam and an excitation beam of non-equal powers by means of a half wave-plate and a polarizing beam splitter. The P-polarized ablation beam is focused on the rotating Ge target to a spot size of 330 μm (measured at 1/e of the peak value, Fig 6.6(b)) resulting in a laser fluence of 4.9 J/cm^2. The S-polarized excitation beam, however, is left unfocused, with a beam diameter of 5.8 mm (measured at 1/e of the peak value, Fig 6.6(c)), to shine the Si(100) substrate and the Ge film during deposition. A 12-keV RHEED electron gun is used to monitor growth dynamics during deposition, while a phosphor screen displays the electron diffraction pattern, which is recorded by means of a charge-coupled device (CCD) camera. Post deposition STM is used to study the morphology of the grown films. Several Ge films were grown on Si(100)-2x1 at different

Reproduced with permission of the copyright owner. Further reproduction prohibited without permission.

substrate temperatures and different laser excitation conditions but with the same ablation laser fluence. The growth dynamics and morphology of the films grown under the laser excitation are compared to those grown at the same deposition conditions without laser excitation.

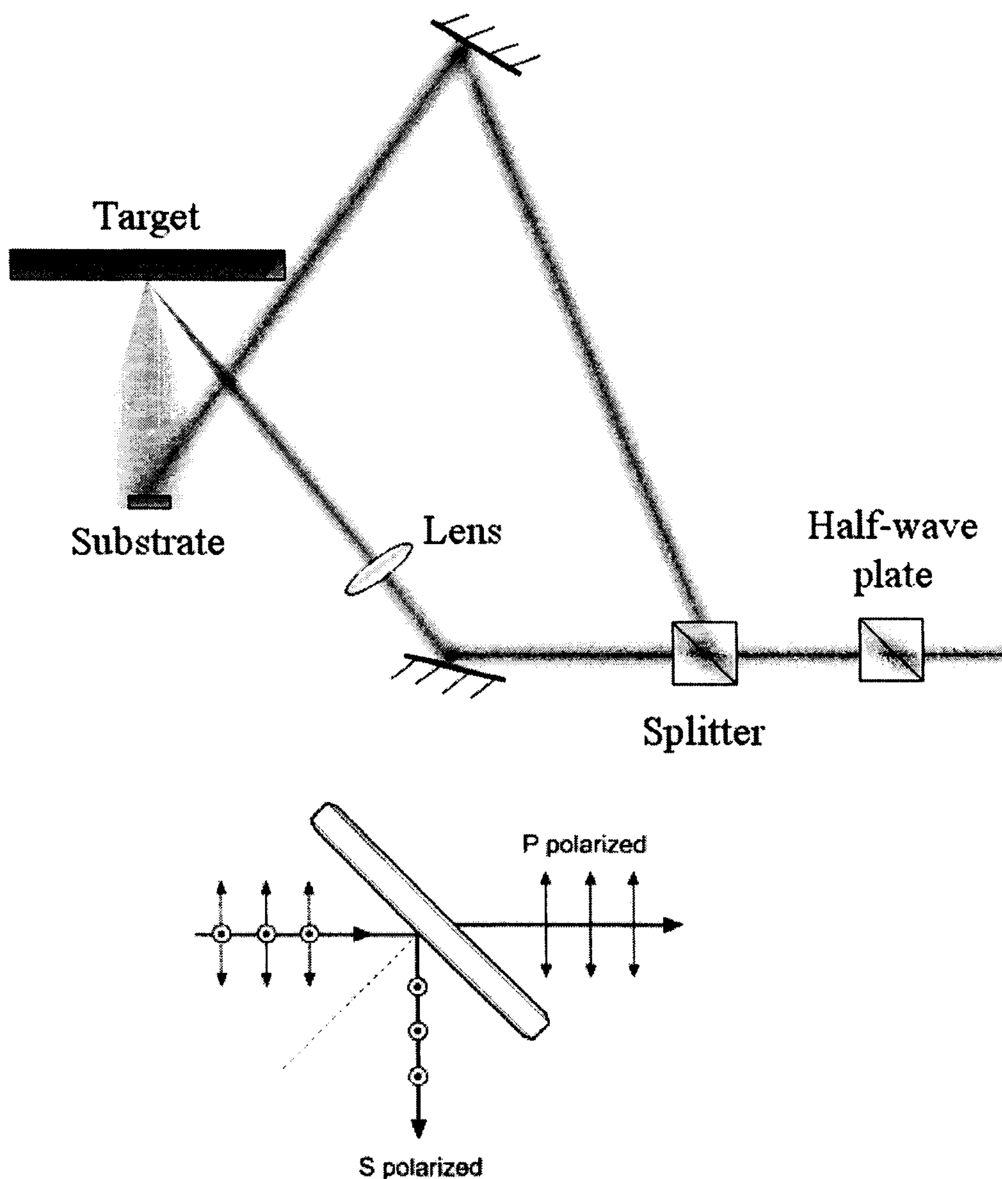

FIG. 6.5. Schematic of the laser excitation experimental setup.

Reproduced with permission of the copyright owner. Further reproduction prohibited without permission.

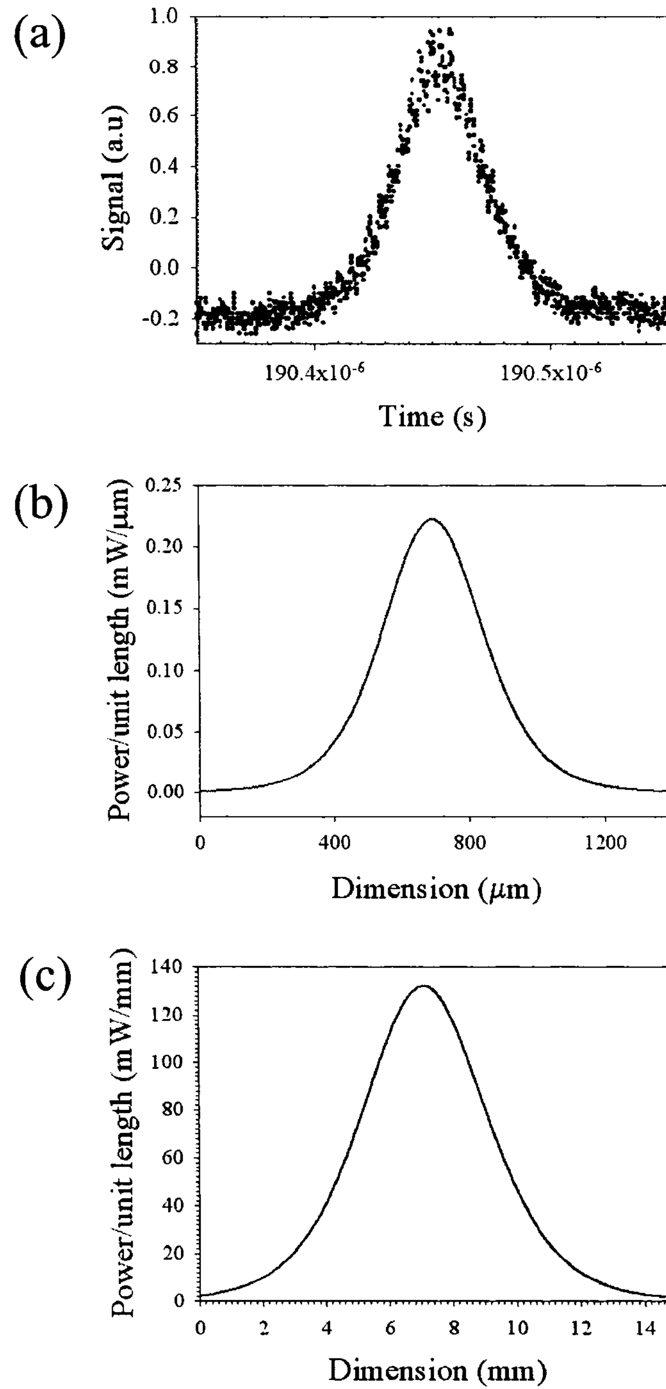

FIG. 6.6. Measurement of laser beam parameters: (a) laser pulse width, (b) ablation beam profile, and. (c) excitation beam profile.

Reproduced with permission of the copyright owner. Further reproduction prohibited without permission.

VI.4. Results and discussion

For the case of PLD of Ge QD on Si(100), without laser excitation of the substrate, we have shown in Chapter 4 that the Ge RHEED transmission diffraction patterns only show for samples grown above ~400 °C [13]. This indicates the formation of crystalline Ge QD, which starts by the formation of hut clusters that are faceted by different planes, depending on the cluster height [13]. As these huts grow in size, they gradually lose their facetation until they become non-faceted domes [13]. For samples grown at substrate temperatures lower than ~400 °C the intensity of the Si(100)-2x1 RHEED spots decays continuously with deposition time until they completely disappear, resulting in a diffuse pattern, after a given thickness that increases with the substrate temperature. This indicates the formation of three-dimensional (3D) structures that collectively lack long range order, as confirmed by RHEED and atomic force microscopy (AFM) [13].

In order to study the effect of the laser-induced electronic excitations on the PLD of Ge on Si(100)-2x1, a set of samples was deposited under the same laser conditions but at a substrate temperature of ~120 °C. All samples of this set show continuous intensity decay until the complete disappearance of the RHEED patterns, Fig. 6.7. However, the time required for the disappearance of the RHEED pattern for the laser irradiated films, Fig. 6.7(b), is ~180 s (8.93±0.4 ML), which is ~9 times that required for the non-irradiated ones (~20 s or 0.99±0.044 ML), Fig. 6.7(a). The decay in the RHEED spots intensity and the increase in the background are associated with an increase in the film roughness. The faster the decay of the pattern, the rougher the surface. Therefore, laser

Reproduced with permission of the copyright owner. Further reproduction prohibited without permission.

irradiation of the substrate decreases the roughness of the film, even though epitaxy is not achieved. This indicates that some energy transfer takes place from the excitation laser to the adsorbed atoms that is acting to increase their surface diffusion.

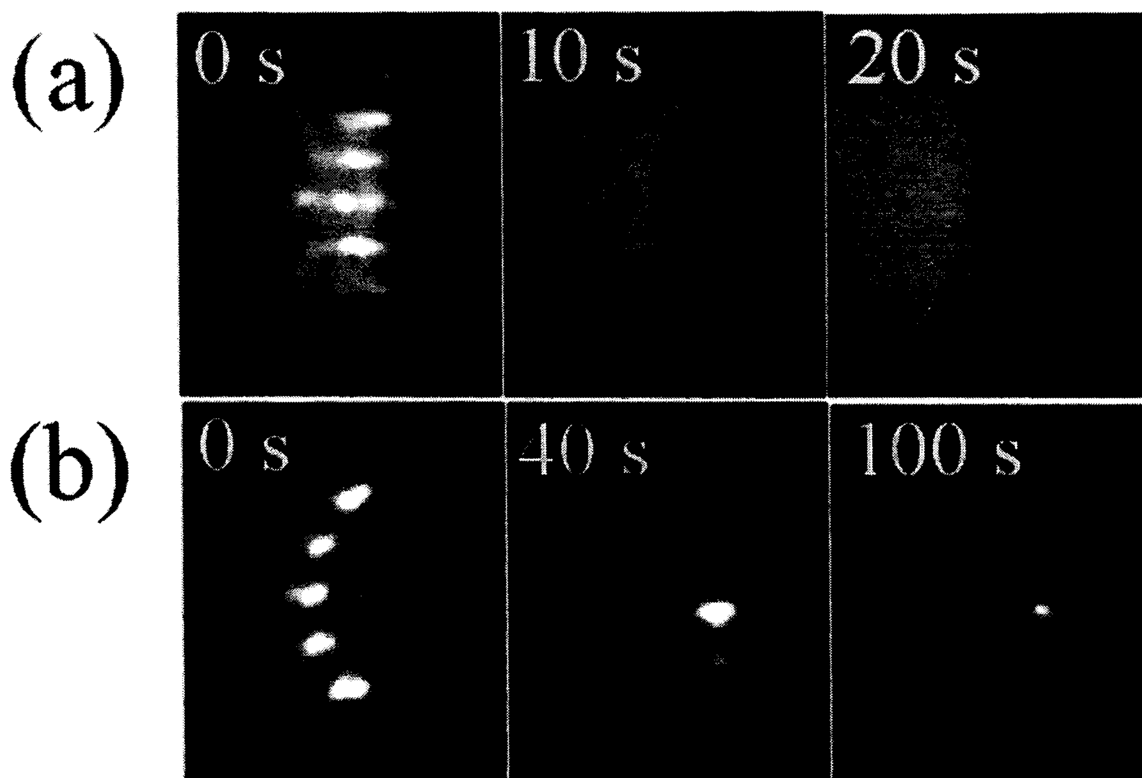

FIG. 6.7. RHEED patterns recorded at different deposition times for two samples deposited at ~120 °C by ablation laser energy density of 4.9 J/cm^2, and laser repetition rate of 50 Hz (a) under no laser excitation, (b) under 130±52 mJ/cm^2.

Another set of samples was grown at a substrate temperature of ~260 °C for 160 s (8000 pulses). Some of these samples were deposited under no laser excitation, while the rest were been deposited under substrate excitation by laser beams of different fluences (ranging between 30±12 and 230±93 mJ/cm^2). The large error in the fluence arises from the visual alignment of the excitation laser on the substrate and variation of the laser

Reproduced with permission of the copyright owner. Further reproduction prohibited without permission.

energy density on the substrate. Figure 6.8 shows the disappearance of the Si(100)-2x1 RHEED pattern during the growth of a Ge film under no laser excitation, while Fig. 2(b) shows an *ex situ* STM scan, obtained over 1.2x1.2 μm, of the resulting film. The film could be described as a collection of 3D structures, characterized by the randomness in their shape, size and spatial distributions. This is usually attributed to the slow surface diffusion of the adsorbed atoms, which is expected at this relatively low temperature.

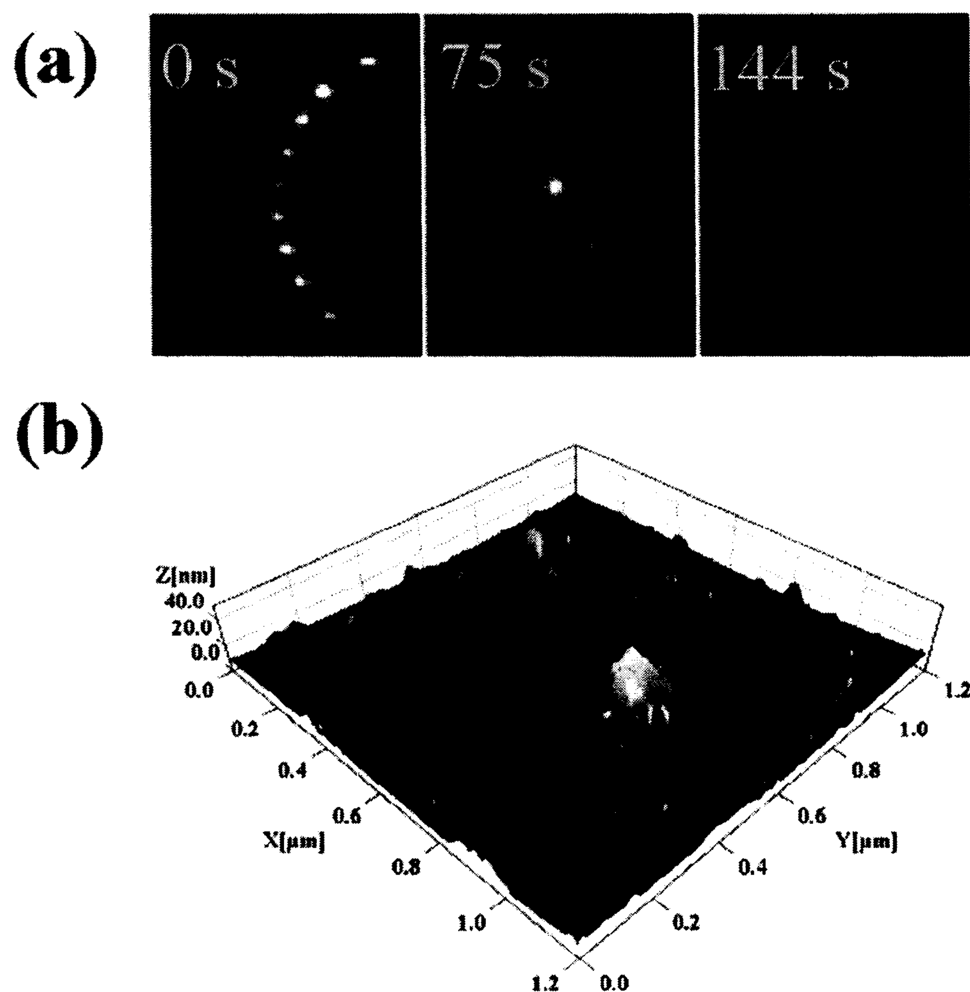

FIG. 6.8. (a) RHEED patterns recorded at different deposition times for a sample grown under no laser excitation at temperature of ~260 °C by ablation laser energy density of 4.9 J/cm^2, and laser repetition rate of 50 Hz. (b) 3D STM image of the final film.

Reproduced with permission of the copyright owner. Further reproduction prohibited without permission.

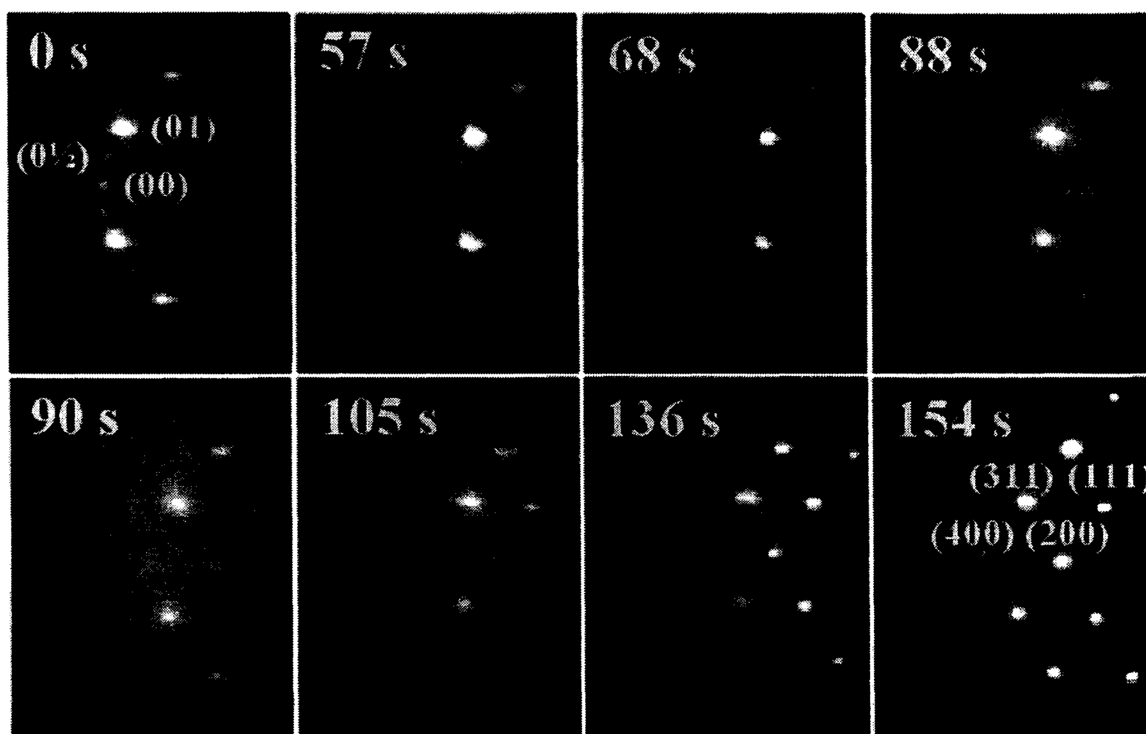

FIG. 6.9. (a) RHEED patterns recorded at different deposition times for the sample grown under excitation laser of 144±58 mJ/cm^2 at ~260 °C under laser ablation fluence 4.9 J/cm^2 and laser repetition rate of 50 Hz.

Figure 6.9 shows the RHEED patterns for a sample grown under laser excitation with a fluence of 144±58 mJ/cm^2. Initially, the substrate's 2x1 RHEED pattern did not change during the first few seconds of deposition, which corresponds to the epitaxial growth of the wetting layer. At ~61 s (3.027±0.136 ML), the reflection RHEED pattern transformed into an elongated transmission pattern, indicating the initial formation of the hut QD. To estimate this transition time, the intensity of the transmission (111) peak, normalized to the background between the (111) and the (200) peaks is ploted as a function of the deposition time, Fig 6.10. The intersection of the data fitting with the background is the 2D-3D transition time. As the film thickness was increased further,

Reproduced with permission of the copyright owner. Further reproduction prohibited without permission.

these spots became more intense before they became rounded in shape, indicating the formation of the dome QD.

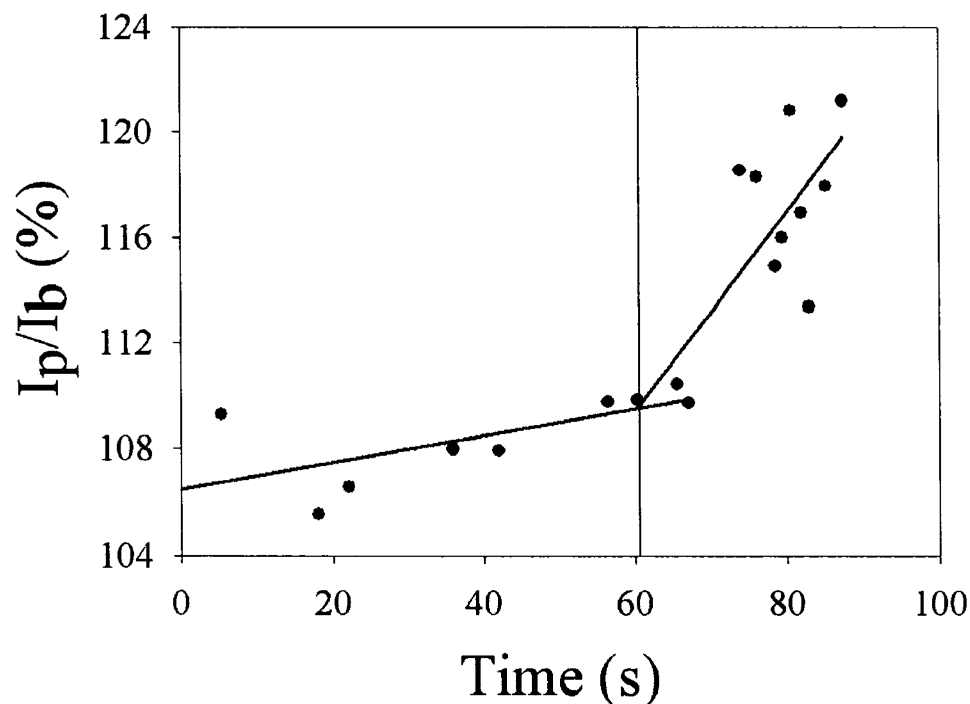

FIG. 6.10. The ratio of the (111) peak intensity to the background intensity (measured between the (200) and the (111) peaks) as a function of deposition time.

For PLD, *in situ* measurement of the film thickness by a crystal thickness monitor is not usually possible due to the high directionality of the plume. The deviation of the highly energetic adatoms' sticking coefficient to the Au-coated crystal from that to the substrate also presents another complication. We have placed a crystal thickness monitor in the location of the substrate in separate PLD runs to estimate the deposition per pulse. The results are shown in Table 6.1. The average rate of deposition measured this way was $(2.13\pm0.16)\mathrm{x}10^{-3}$ Å/pulse. The error range considered only the standard deviation due to repeating the calibration several times and did not consider the variation of the sticking

Reproduced with permission of the copyright owner. Further reproduction prohibited without permission.

coefficient of Ge to the Au-coated crystal from that for Si, nor did it consider the plume nonuniformity over the 50-mm^2 area of the crystal. The thickness calibration was also performed by a spectroscopic ellipsometry (Woollam M44 ellipsometer). Due to the low coverage ratio of the QD, as will be shown later, we used a model of a thin flat Ge layer on the 0.5 mm Si wafer, Fig. 6.11. The results of such measurements are shown in Table 6.2. The average deposition rate in this case was found to be $(1.34\pm0.06)\times10^{-3}$ Å/pulse. The error range included was that from fitting the measured data to the assumed model considering the variation of the optical properties of the film from the bulk values. We rely on the thickness calibration by the ellipsometer because we believe it is more accurate than that obtained from the crystal thickness monitor.

Table 6.1. Summary of thickness monitor measurements, performed by placing the crystal at the location of the substrate at separate runs.

# pulses	Φ (J/cm^2)	Thick. (Å)	Thick. (ML)	Per pulse (Å)
15000	4.655705872	36	26.66666667	0.0024
15000	4.655705872	32	237.037037	0.002133333
18000	4.655705872	37	274.0740741	0.002055556
21000	4.655705872	43	318.5185185	0.002047619
15000	4.655705872	30	22.22222222	0.002
			Average	**0.002127302**

(a)

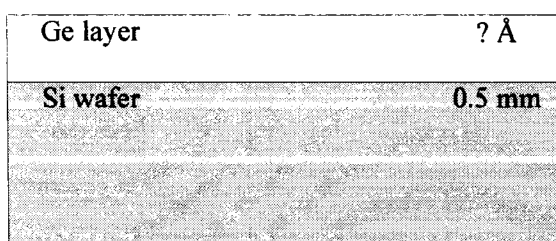

(b)

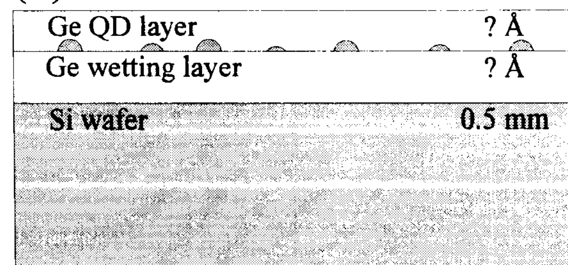

FIG. 6.11. The two assumed models for the ellipsometry thickness measurements.

Reproduced with permission of the copyright owner. Further reproduction prohibited without permission.

Table 6.2. Summary of ellipsometry thickness measurements of three samples allowing for the variation of n and k from the bulk values.

# pulses	Φ (J/cm^2)	Thick. (Å)	Error (Å)	Thick. (ML)	Per pulse (Å)
7500	0.144	9.496	0.989	7.034074074	0.001266133
4500	0.22	7.3904	0.0529	5.47437037	0.001642311
8350	0.22	9.236	0.25	6.841481481	0.001106108
				Average	**0.001338184**

Figure 6.12 compares the STM images of three samples grown for 160 s (7.94±0.36 ML) for laser excitation energy density of 50±20, 87±35 and 144±58 mJ/cm^2. The length histograms of each STM image are shown. The size distributions for samples deposited with laser excitation using an energy density of 50±20 and 87±35 mJ/cm^2 are unimodal with most expected length, L_m, of 10.4±0.3 and 10.7±0.2 nm, and FWHM of 9 and 6 nm, respectively. However, that for the sample deposited with 144±58 mJ/cm^2 excitation energy density is bimodal with L_m = 10.6±0.5 nm and 28.4±0.9 nm and the corresponding FWHM of 9 and 8 nm. Hence, L_m is about the same for the three samples, if the higher lengths distribution is neglected. For the excitation energy density of 144±58 mJ/cm^2, the coverage ratio CR (defined as $\sum \text{cluser areas/total scanned area}$) is ~11 for the lower size unimodal distribution and ~18% for the combined distributions. This becomes ~31% when the excitation is decreased to 50±20 mJ/cm^2. The corresponding cluster density d decreases with increased energy density from ~4.1x10^{11} cm^{-2} to ~1.4x10^{11} cm^{-2}. This trend could be thought of as a diffusion boost due to laser energy coupling to adatoms.

Reproduced with permission of the copyright owner. Further reproduction prohibited without permission.

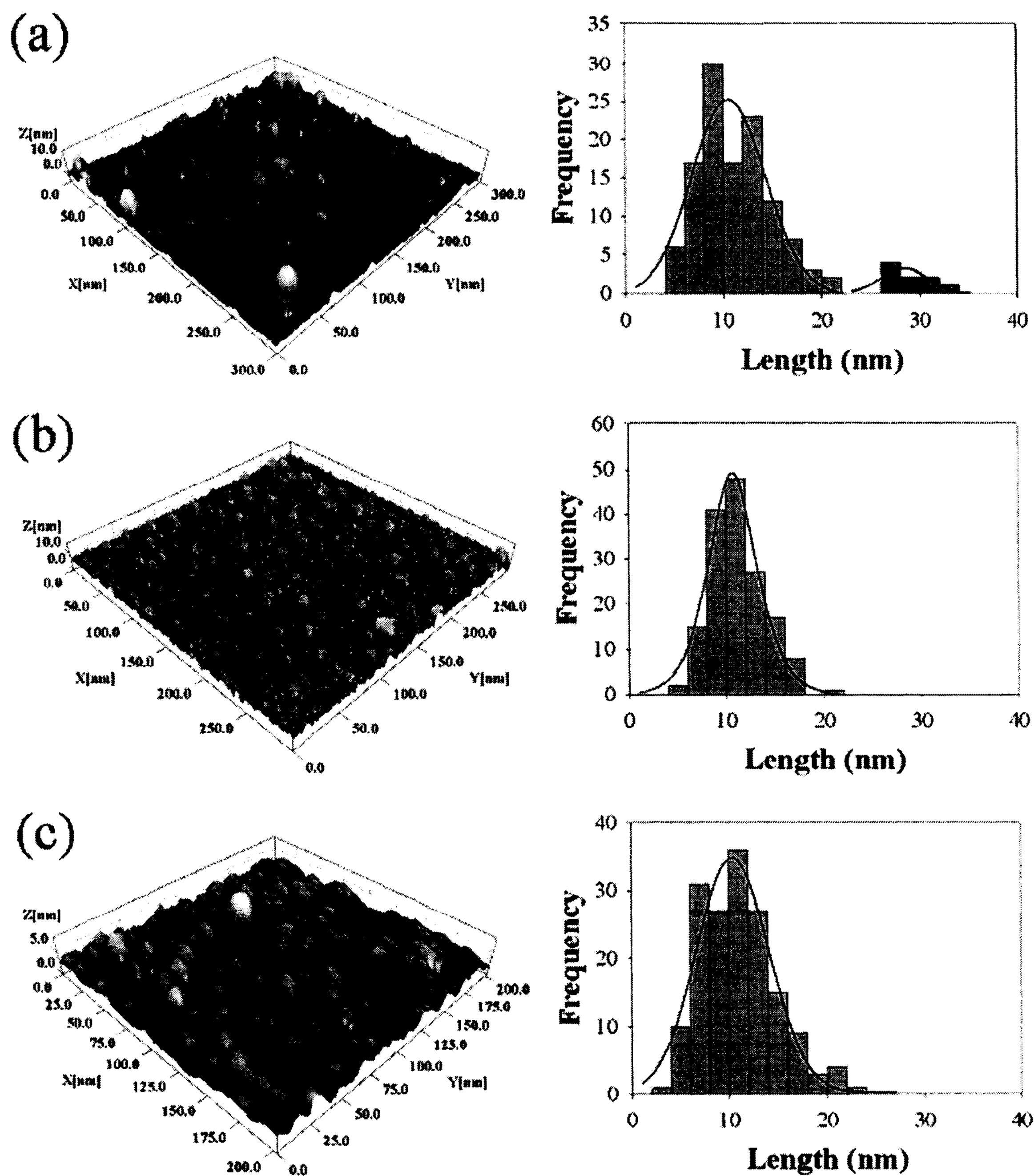

FIG. 6.12. STM images and cluster length distributions for samples grown ~260 °C under laser ablation fluence 4.9 J/cm^2 and laser repetition rate of 50 Hz under excitation laser fluence of (a) 144±58 mJ/cm^2 [d = 1.4x10^{11} cm^{-2}, CR = 11 & 18%], (b) 87±35 mJ/cm^2 [d = 1.7x10^{11} cm^{-2}, CR = 12%], (c) 50±20 mJ/cm^2 [d = 4.1x10^{11} cm^{-2}, CR = 31%].

Reproduced with permission of the copyright owner. Further reproduction prohibited without permission.

The enhancement of QD crystallinity under laser excitation is not expected to be associated with a temperature rise due to laser absorption in the Si substrate. According to a one-dimensional heat diffusion model, the maximum temperature rise due to the absorption of the 1064-nm excitation laser in the skin depth of Si (~60 μm) is ~11 °C for laser conditions similar to those used with the highest energy density in the present experiments. This temperature excursion decays to almost the substrate temperature in ~0.1 ms. For Ge, the skin depth for 1064 nm is 200 nm and the maximum temperature rise, if bulk Ge is irradiated with the same laser energy density, is 121 °C. Thus for several ML of Ge on Si, the temperature excursion and its duration is too small to play a role in the much slower processes occurring on the surface that affect the growth mode.

Two mechanisms are probably responsible for the enhancement of QD crystallinity under laser irradiation. The first is a dynamic competition between nonthermal laser-induced desorption of surface atoms, at temperatures significantly below the melting and ablation thresholds, and the adsorption of new adatoms. The yield of the Si atoms, nonthermally removed via laser-induced electronic excitations, have been reported to depend superlinearly on the laser fluence [5,7]. Due to the low surface absorption coefficient, photoexcitation takes place in bulk [1], resulting in a high density of electron-hole pairs that can transfer to the surface electronic systems via electron-electron and/or electron-phonon coupling [7]. Hole localization onto particular surface sites results in selective bond breaking via a proposed two-hole mechanism [1,7]. Consequently, these atoms are ejected via a phonon kick (from local heating due to a nonradiative electron-hole pair recombination mechanism) with a distribution of translational energy that starts from a given onset [5]. In growth of Ge on Si, such

Reproduced with permission of the copyright owner. Further reproduction prohibited without permission.

translational energy gain of the Ge adatoms is expected to lead to increasing adatom diffusion and hence affect the QD morphology. Also, the resultant vacancies may act as favorable nucleation sites for the adatoms. It is also possible that the same mechanism may lead to increased detachment rates from the forming QD, leading to cluster size limitations.

The second mechanism involves an energy transfer from the laser-generated hot electrons to the adsorbed and/or surface atoms. It has been reported that substrate irradiation by an electron beam, of energy of a few hundred eV, during deposition of CeO_2 reduces the required temperature for epitaxial growth on Si(100) by more than 100 °C [4]. These electrons ionize surface atoms and adatoms. This results in the enhancement of adatom diffusion toward lattice sites via Coulomb interaction [4]. Electron beam irradiation was also found to increase the epitaxial recrysallization rates in amorphous $SrTiO_3$ by orders of magnitude compared to thermal effects [2]. A mechanism was proposed based on localized excitations affecting local atomic bonds by lowering the energy barrier to defect recovery [2].

VI.5. Conclusion

The effect of the laser-induced electronic excitation of the PLD of Ge QD grown on Si(100)-2x1 was studied. Electronic excitation by laser irradiation of the substrate changes film morphology and reduces the temperature required for the formation of crystalline QD. Thermal effects are clearly not responsible for these observations. The

Reproduced with permission of the copyright owner. Further reproduction prohibited without permission.

mechanisms involved could be the proposed dynamic competition between laser-induced desorption of surface atoms and the adsorption of new atoms, and energy coupling from the laser-generated hot electrons to adatoms. The present results show that surface electronic excitation can be used to effectively alter the growth mode and produce low temperature epitaxy.

VI.6. References

[1] K. Tanimura, E. Inami, J. Kanasaki, and W. P. Hess, "Two-hole localization mechanism for electronic bond rupture of surface atoms by laser-induced valence excitation of semiconductors," Phys. Rev. B **74**, 035337-1-8 (2006).

[2] Y. Zhang, J. Lian, C. M. Wang, W. Jiang, R. C. Ewing, and W. J. Weber, "Ion-induced damage accumulation and electron-beam-enhanced recrystallization in $SrTiO_3$," Phys. Rev. B **72**, 094112-1-8 (2005).

[3] N. Itoh and A. M. Stoneham, "Treatment of Semiconductor surfaces by laser-induced electronic excitation," J. Phys.: Condens. Matter **13**, R489-R503 (2001).

[4] T. Inoue, Y. Yamamoto, and M. Satoh, "Electron-beam-assisted evaporation of epitaxial CeO_2 thin films on Si substrates," J. Vac. Sci. Technol. A **19(1)**, 275-279 (2001).

[5] J. Kanasaki, K. Iwata, and K. Tanimura, "Translational Energy Distribution of Si Atoms Desorbed by Laser-Induced Electronic Bond Breaking of Adatoms on Si(111)-7x7," Phys. Rev. Lett. **82**, 644-647 (1999).

Reproduced with permission of the copyright owner. Further reproduction prohibited without permission.

[6] A. M. Stoneham and N. Itoh, "Materials modification by electronic excitation," Appl. Surf. Sci. **168**, 186-193 (2000).

[7] J. Kanasaki, K. Katoh, Y Imanishi, K. Tanimura, "Electronic bond rupture of Si-dimers on Si(001)-2x1 induces by pulsed laser excitation," Appl. Phys. A **79**, 865-868 (2004).

[8] B. R. Trenhaile, V. N. Antonov, G. J. Xu, K. S. Nakayama, J. H. Weaver, "Electron-stimulated desorption from an unexpected source: internal hot electrons for Br-Si(100)-(2x1)," Surf. Sci. Lett. **583**, L135-L141 (2005).

[9] V. A. Fedotov, K. F. MacDonald, N. I. Zheludev, and V. I. Emel'yanov, "Light-controlled growth of gallium nanoparticles," J. Appl. Phys. **93**, 3540-3544 (2003).

[10] I. El-Kholy and H. E. Elsayed-Ali, "Ultrafast laser enhanced homoeptiaxial growth of Si on Si(111)-7x7 at room temperature," *to be published.*

[11] G. Padeletti and R. Larciprete, "Atomic force microscopy study of the morphological modifications induced by laser processing of $Si_{(1-x)}Ge_x$/Si samples," J. Vac. Sci. Technol. B **16(3)**, 1762-1766 (1998).

[12] H. Sumi, "Theory on laser sputtering by high-density valence-electron excitation of semiconductor surfaces," Surf. Sci. **248**, 382 (1991).

[13] M. S. Hegazy and H. E. Elsayed-Ali, "Growth of Ge quantum dots on Si by pulsed laser deposition," J. Appl. Phys. **99**, 054308 (2006).

Reproduced with permission of the copyright owner. Further reproduction prohibited without permission.

CHAPTER VII

ULTRA HIGH VACUUM SCANNING TUNNELING MICROSCOPY STUDY OF PULSED LASER DEPOSITION OF Ge QD ON Si(100)

VII.1. Introduction

The growth of Ge QD on Si(100) by MBE and CVD has been extensively studied by in situ ultrahigh vacuum scanning tunneling microscopy (UHV STM) and atomic force microscopy (AFM) [1-5]. For the case of MBE, after the formation of the wetting layer, nucleation starts by the formation of {105}-faceted hut clusters [5]. As the film coverage increases, multi-faceted "dome" clusters (faceted by {113} and {102} planes) start to appear along with the {105} huts. With further increases, large clusters called "super-dome" islands start to appear [3,6]. It was reported that if Sb is used as a surfactant in the MBE growth of Ge/Si(100), the initial hut facetation changes from {105} to {117} [7]. On the other hand, if Ge is grown on Si(100) by liquid phase epitaxy (LPE), {115} faceted islands are first observed instead of the {105}-faceted ones. As the coverage increases, pyramids bounded by {111} facets are formed [8,9]. This indicates that the growth dynamics depend on the deposition technique as well as the substrate temperature and deposition conditions. However, no detailed study on the formation of Ge QD on Si by PLD has been performed by in situ STM or AFM.

In Chapter 4, we studied the PLD of the Ge QD and Si(100)-2x1 by RHEED and ex situ AFM, and we showed that nucleation initiates via the formation of faceted hut clusters. The facetation of such clusters was shown to change during deposition due to

Reproduced with permission of the copyright owner. Further reproduction prohibited without permission.

the increase of the contact angle that the faceting planes make with the (100) substrate. As they grow in size, they gradually lose their facetation in the route of their transition to non-faceted domes. In that study, the smallest observed cluster length and height were ~150 and 4 nm, respectively. Therefore, no information was available about the very early stages of the formation of the huts. In this chapter, the early stages of the formation of the Ge huts on Si(100) by PLD will be studied using ultrahigh vacuum scanning tunneling microscopy (UHV STM).

VII.2. Experiment

The growth is conducted in a special home-made UHV PLD chamber that is equipped with an Omicron UHV STM bolt-on, Figs. 2.6 and 7.1. The geometry of this system is different from that used in Chapters 4, 5 and 6. The ablation laser enters the chamber from the bottom 2¾ inch sapphire window. Figure 7.2 shows the arrangement of the target and the substrate. The substrate holder is equipped with a commercial direct heating facility, while the Ge target is mounted on a home-made mechanically rotated target holder. The chamber pressure is maintained at $<1\times10^{-9}$ Torr. More technical details about the system are found in Appendix B.

Sample cleaning, system baking and sample preparation to obtain the Si(100)-2x1 reconstruction are mentioned in Chapter 4. A Q-switched Nd:YAG laser (1064 nm, FWHM ~40 ns, 5 Hz) is focused on Ge to a spot size of 400 μm (measured at 1/e of the peak value), resulting in a laser fluence of 50 J/cm^2. Deposition by a few laser pulses is

Reproduced with permission of the copyright owner. Further reproduction prohibited without permission.

conducted in the deposition chamber at substrate temperature of ~400 °C. The substrate temperature is cooled to room temperature, at a rate of 2-6 °C per second, before being transferred into the UHV STM bolt-on by means of a 48" magnetic transporter. The sample is moved to the STM stage by means of a wobble-stick. The substrate is scanned at different marked areas at different magnifications. The sample is then returned to the PLD chamber for more deposition. These deposition-scanning cycles are repeated several times in order to study the early stages of Ge QD formation. It has to be noted that moving the sample in and out of the scanning stage for the sake of deposition, results in a negligible probability of scanning the same area again. However, we try to minimize that to a few micrometers by using surface features that result in different surface reflections as seen by the CCD camera monitoring the sample, as landmarks.

Reproduced with permission of the copyright owner. Further reproduction prohibited without permission.

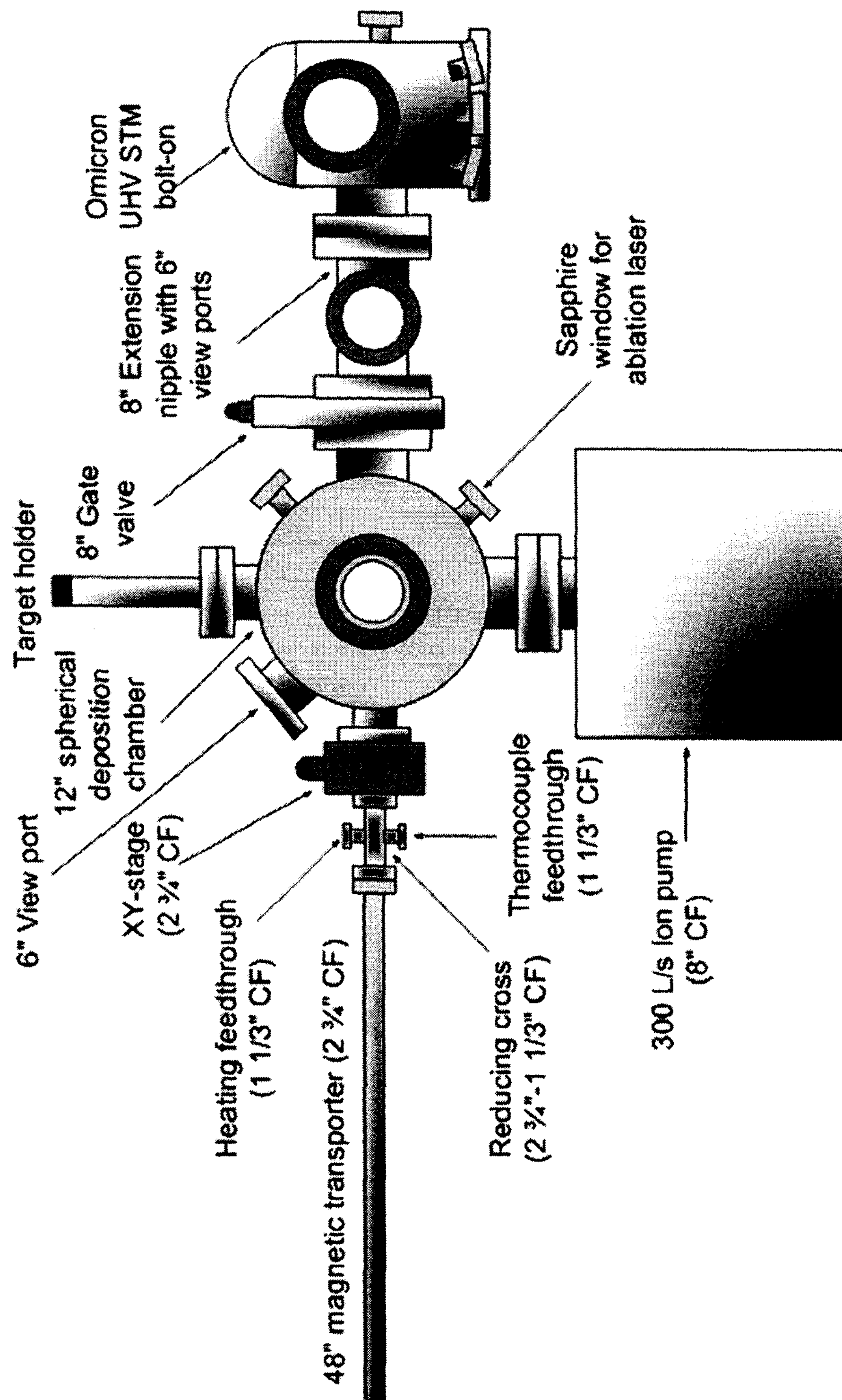

FIG. 7.1. Schematics showing the main components of the PLD deposition chamber equipped with Omicron UHV STM.

Reproduced with permission of the copyright owner. Further reproduction prohibited without permission.

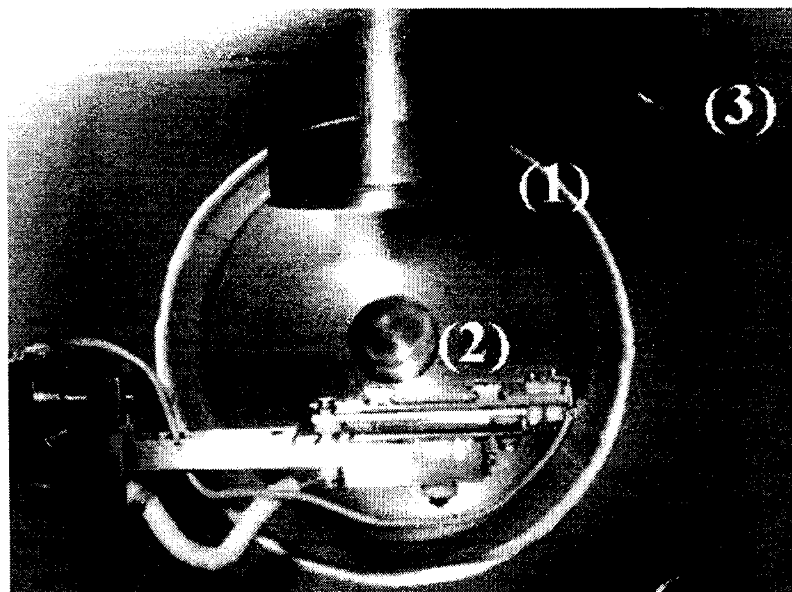

FIG. 7.2. Main components inside the PLD chamber: (1) Ge target mounted on the target holder, (2) substrate holder equipped with direct heating, (3) ion gauge filament.

VI.3. Results and discussion

Figure 7.3 shows STM images recorded for the Si(100) substrate, Fig. 7.3(a), and for Ge films grown at different deposition times. The flat film in Figs. 7.3(b), deposited for 20 pulses, account for the epitaxial formation of the wetting layer. After deposition by 70 pulses, a very small density (~10 per 300x300 nm^2 area or ~$1x10^{10}$ cm^{-2}) of tiny clusters of almost the same size are seen on a flat surface. Figure 7.3(c) zooms down to 60x60 nm^2 to show one of these isolated clusters. With the increase in film thickness, the density of the clusters is seen to increase. Figure 7.3(d) shows a 200x200 nm^2 STM image of the Ge film after deposition by 220 laser pulses. The figure shows an ensemble of clusters distributed almost homogenously over the scanned area.

Reproduced with permission of the copyright owner. Further reproduction prohibited without permission.

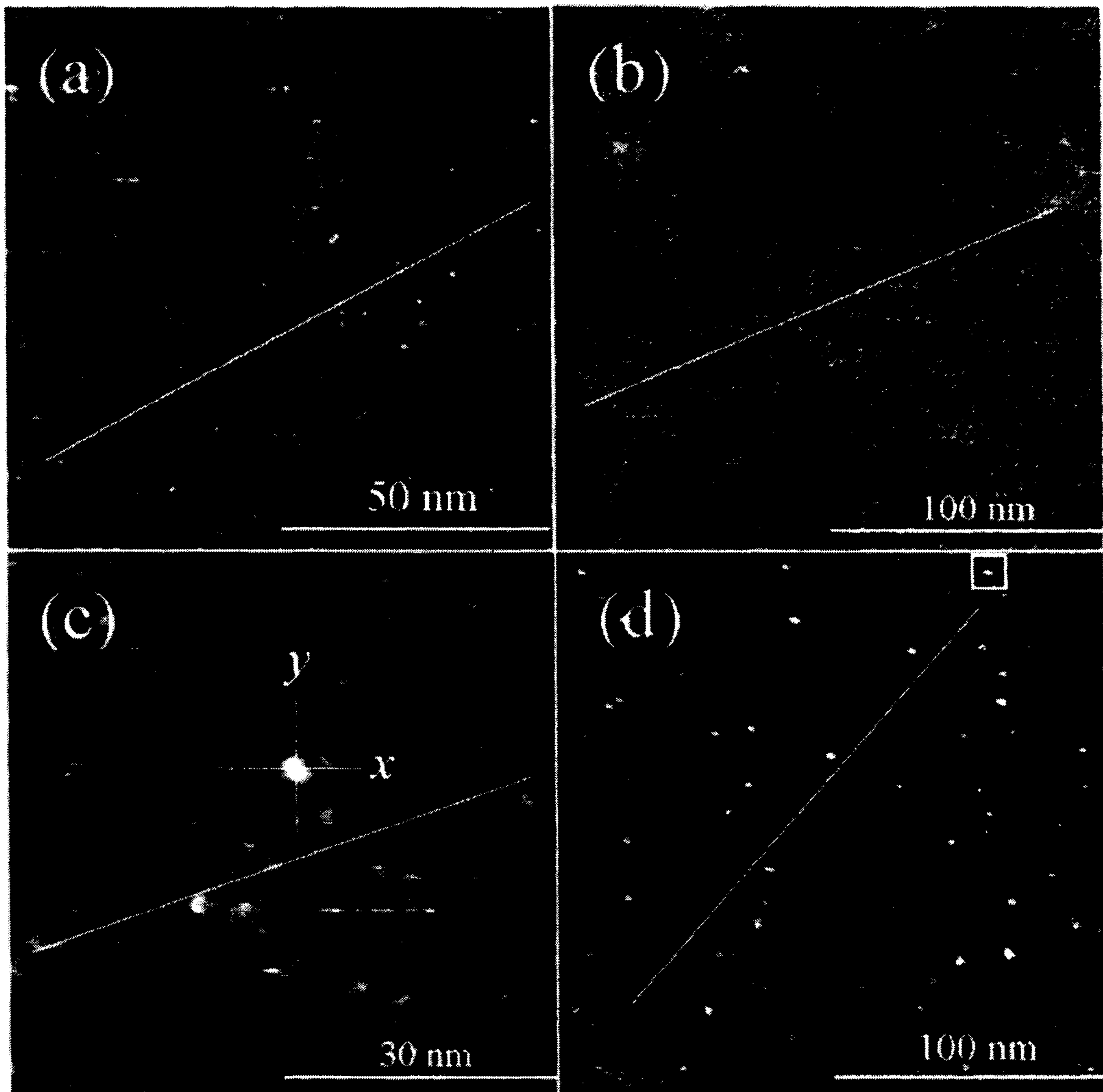

FIG. 7.3. STM scans of the (a) Si substrate and of the Ge film after deposition of (b) 20 pulses, (c) 70 pulses, and (d) 220 pulses. The white lines show the locations of the line scans shown in Fig. 7.4. The lines marked x and y locate the locations of the line scans across the QD shown in Fig. 7.5. The square in (d) highlights the cluster shown in Fig. 7.6.

The changes in the surface roughness during the growth of the Ge film is studied by performing line scans (white lines in the images of Fig. 7.3) along some flat areas of the films that are compared to the roughness of the Si(100) substrate. Figure 7.4 shows

Reproduced with permission of the copyright owner. Further reproduction prohibited without permission.

the results of the line scans along the 4 lines in Fig. 7.4. Constant values have been added to lines (b), (c) and (d) in order to make it easy to compare the results. This will not affect the result since we are only interested in the amplitude of the fluctuations. The fluctuations along the line scan measured over the Si(100) substrate, line (a), do not exceed ±0.21 nm. However, for the case of Ge films, the fluctuation extreme limits increase to the values of ±0.40, ±0.31, and ±0.65 nm around the main value for the cases of deposition by 20, 70 and 220 laser pulses, respectively. Such increase in roughness is expected since epitaxy nucleation for the second and third layers starts before the completion of the first one. Also, we have to consider the larger atomic size of the Ge as compared to Si, which is also expected to be responsible for part of these fluctuations.

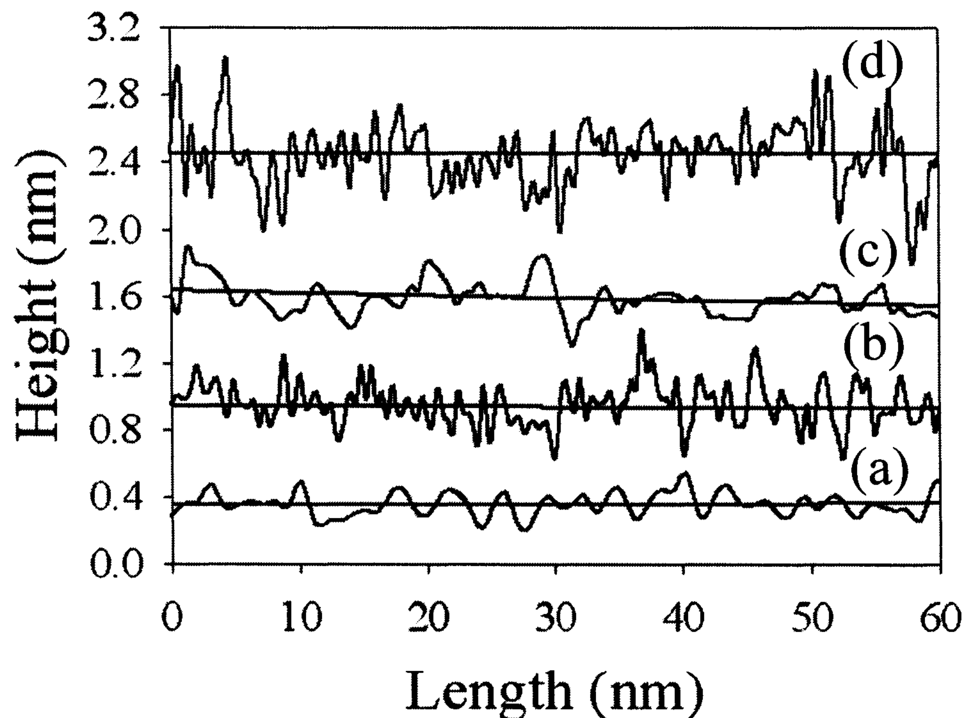

FIG. 7.4. Line scans measured along the lines in Fig. 7.3. Lines (a), (b), (c), and (d) correspond to Fig. 7.3 (a), (b), (c), and (d), respectively.

Reproduced with permission of the copyright owner. Further reproduction prohibited without permission.

Figure 7.5 shows the line profiles of the single cluster in Fig. 7.3(c) measured along the lines designated as x and y. The profiles show that the cluster has lengths of ~4.8 and ~4.4 nm in the x and y directions, respectively, and a height of ~0.7 nm (corresponding to ~5 ML of Ge). These values result in a lateral aspect ratio, L (defined as major length/minor length), of 1.1 and an aspect ratio, A (defined as major length/height), of ~6.9. This indicates that at the very early stages of the cluster formation, the cluster grows laterally faster than vertically, as will be confirmed later. The cluster is seen to be a multi-faceted cluster with planes making different angles with the (100) substrate. Due to the error in calculating the angle, which is not expected to exceed 1°, for each single measured angle, there corresponds a set of expected planes. For example, the left faceting plane of the cluster in Fig. 7.5(a) makes an angle of 18.3±1°. Therefore, within our error, the family of planes {922}, {712}, {301}, and {903} are all possible. However, we only consider the facets with the smallest Miller indices, since they are the most stable facets; therefore, the {301} are only considered in the figure. The other plane identified as {801} makes an angle of ~6.8±1°. For the profile along the y-direction, the faceting planes make angles of 16.1±1°, 27.6±1°, and 28.6±1° with the (100) substrate and hence are identified as {702}, {613}, and {613}, respectively.

For the larger film thickness, deposited at 220 pulses, Fig. 7.3(d), the cluster enclosed in the white square is shown in Fig. 7.6(a). Line profiles along the x and y lines are shown in Figs 7.3(b) and (c), respectively. The profiles show that the cluster has developed a hut shape with major and minor lengths of ~3.6 and ~3.3 nm, respectively, and a height of ~2.2 nm. These values result in a lateral aspect ratio and aspect ratio of

Reproduced with permission of the copyright owner. Further reproduction prohibited without permission.

~1.1 and 1.6, respectively. Although we cannot derive conclusions from comparisons of only two different clusters, it is clearly seen that the aspect ratio drops considerably.

Figure 7.7 shows the relation between aspect ratio and the height, h, of the clusters in Fig. 7.3(d). The best fitting for the function is

$$A = 1.152 + 9.070\exp[-1.238h]. \tag{7.1}$$

The dependence of the aspect ratio on the major and minor lengths, however, is shown in Fig. 7.8. The linear fit for the functions is

$$A = A_0 + a\eta, \tag{7.2}$$

where η stands for both l_{min} and l_{maj}, and the fitting values for A_0 are 2.082 and 0.2101, respectively, and for a are 0.2327 and 0.6741 nm^{-1}, respectively. From these equations, the rate of change of the aspect ratio with respect to the height, dA/dh, is $-11.229e^{-1.238h}$ nm^{-1} and the rate of change with respect to the major length, dA/dl_{maj}, is 0.6741 nm^{-1}. Therefore, $|dA/dh| > |dA/dl_{maj}|$, which indicates that the vertical growth of these clusters is favored over the lateral one. As discussed in Chapter 4, this growth anisotropy may be attributed to the cluster's internal strain. Increasing the lateral size is expected to result in increasing the internal strain due to the lattice mismatch. On the contrary, increasing the cluster's height leads to more strain relief through the adjustment of the lattice spacing in the growing layers, and, therefore, is favored over the lateral growth [1].

The lateral aspect ratio as a function of the clusters' height is shown in Fig. 7.9. Small hut clusters are seen to be laterally asymmetric in shape. Such asymmetry decreases with the lateral size increase. The best fit to the data was found to have the form

Reproduced with permission of the copyright owner. Further reproduction prohibited without permission.

$$L = (-0.1865) + (5.540)\exp[-(0.6117)l_{\min}] + (0.1885)l_{\min}. \tag{7.3}$$

The lateral aspect ratio asymptotically reaches 1, i.e. complete symmetry. To achieve such symmetry, adsorption to the shorter cluster side should be favorable over that to the longer one.

Since the clusters are multifaceted, the maximum faceting angle, θ_{max}, of the clusters' faceting planes with the Si(100) substrate as a function of the cluster's height is shown in Fig. 7.10. The best fit function is the linear equation

$$\theta = (31.26) + (13.83)h. \tag{7.4}$$

Figure 7.11 presents major length (size) and height histograms of the clusters in Fig. 7.3(d). The best fit for both histograms is the Gaussian of the forms

$$F_{l_{maj}} = (0.8979) + (38.91)\exp\left[-0.5\left(\frac{l_{maj} - 2.82}{0.8891}\right)\right] \tag{7.5}$$

for size distribution and

$$F_h = (1.288) + (57.76)\exp\left[-0.5\left(\frac{h - 1.39}{0.224}\right)\right] \tag{7.6}$$

for the height. From these fitting functions, the most expected size and height are 2.82 and 1.39 nm, respectively, while the FWHM for both distributions are 2.5 and 0.6 nm, respectively. Both distributions are considered narrow. The average density of clusters as calculated over 200x200 nm areas, scanned over different locations within 2x2 mm area, is ~2.3×10^{11} cm^{-2}. An interesting remark is that the clusters seen after the deposition by 70 pulses, similar to that in Fig. 7.3(c), can nicely fit in both the size and height histograms of Fig. 7.3(d). This might lead to the conclusion that, in this growth regime, some limiting force acts to limit the size and heights of the clusters and favor nucleation

Reproduced with permission of the copyright owner. Further reproduction prohibited without permission.

of new clusters. As mentioned above, strain due to mismatch would be that controlling force.

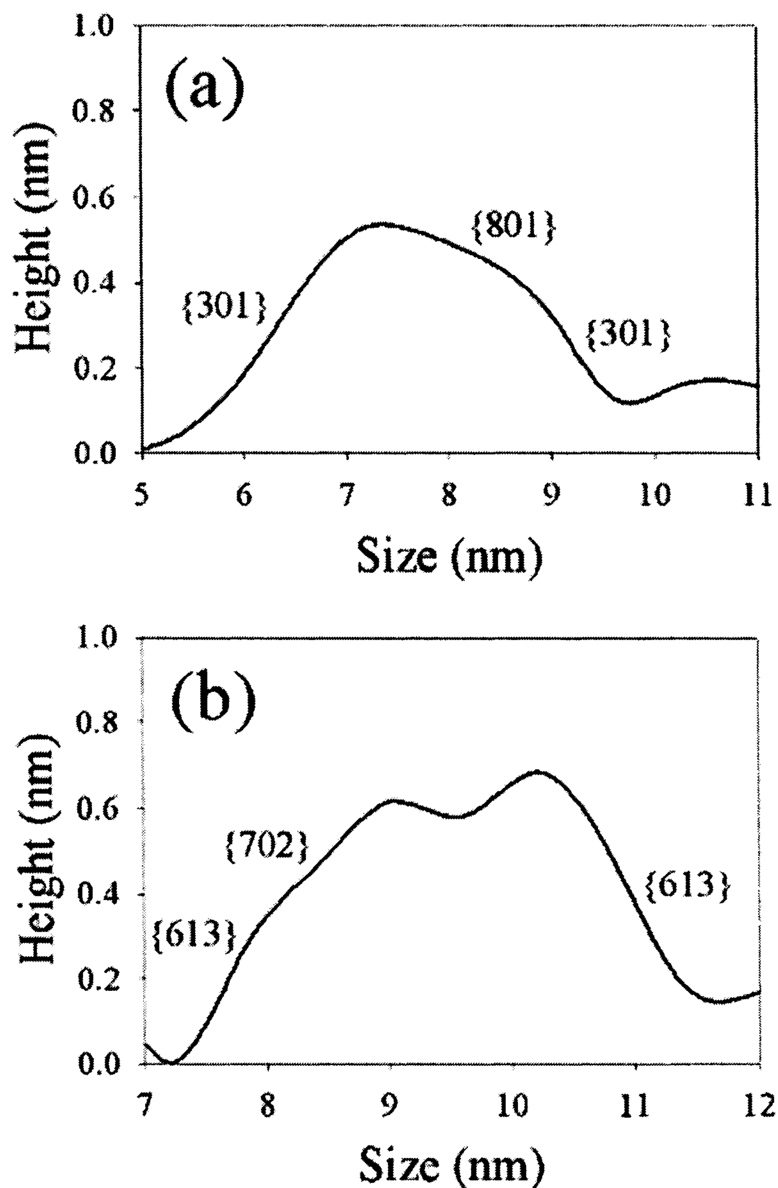

FIG. 7.5. Line scans measured along the lines marked x and y across the QD in Fig. 7.3 (c).

Reproduced with permission of the copyright owner. Further reproduction prohibited without permission.

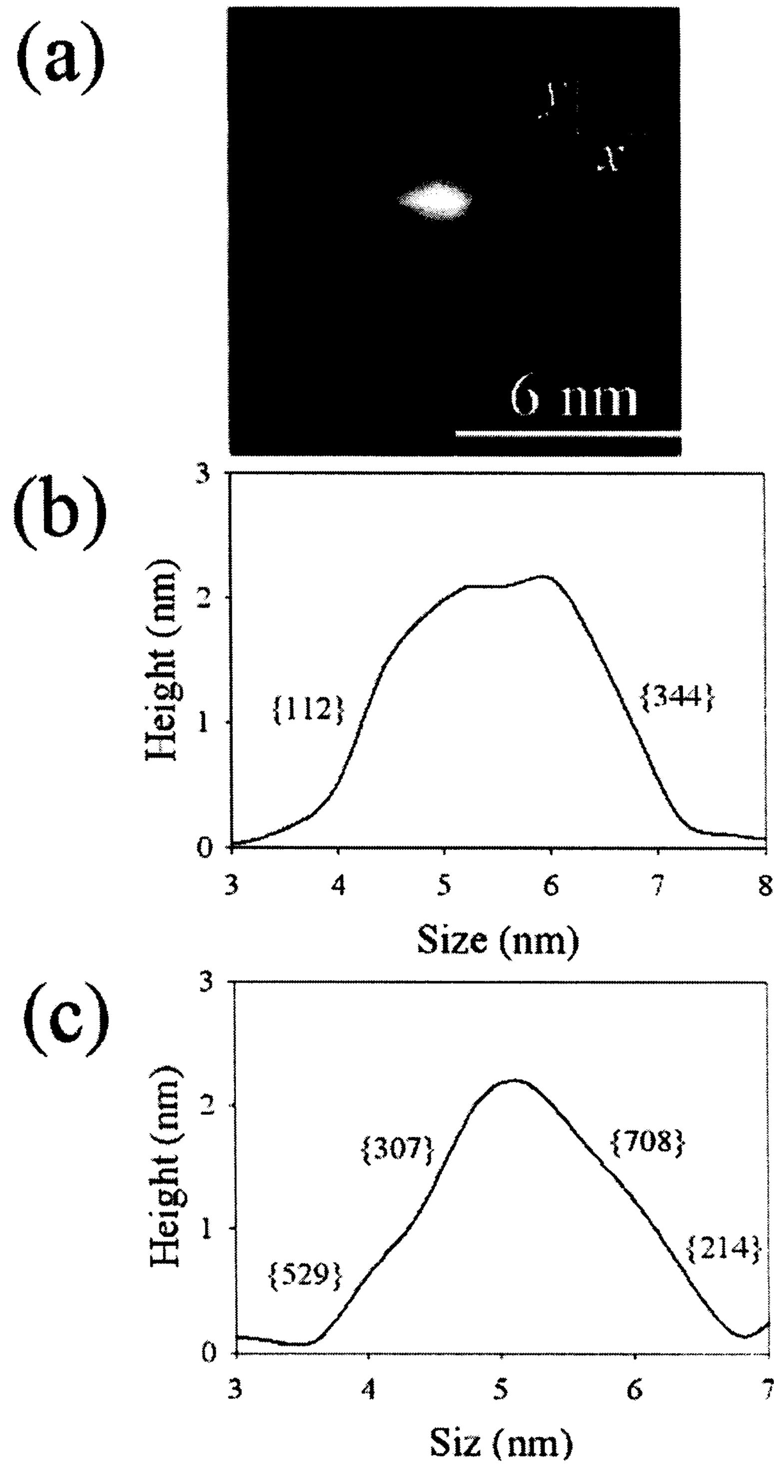

FIG. 7.6. (a) The QD enclosed by the square in Fig. 7.3(d), (b) line scan across x, (b) line scan across y.

Reproduced with permission of the copyright owner. Further reproduction prohibited without permission.

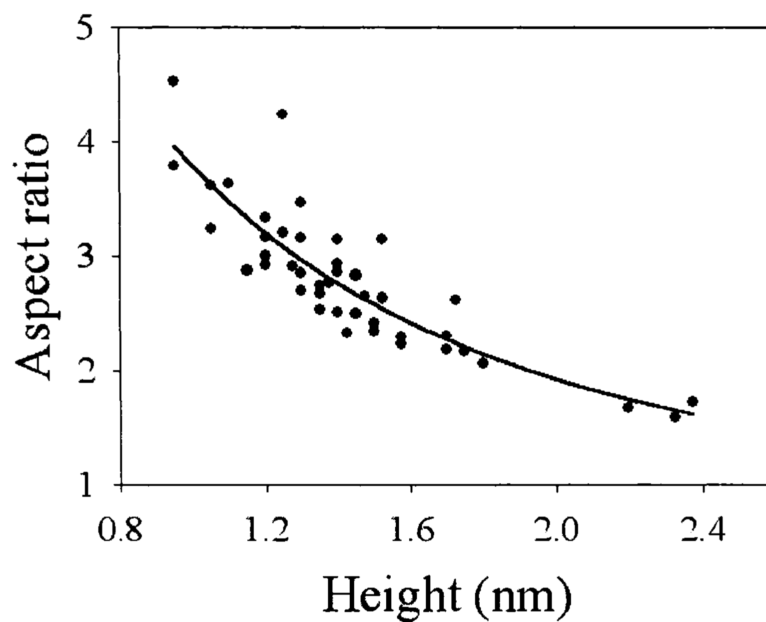

FIG. 7.7. Aspect ratio, A, of the clusters in Fig. 7.3(d) as a function of their height, h.

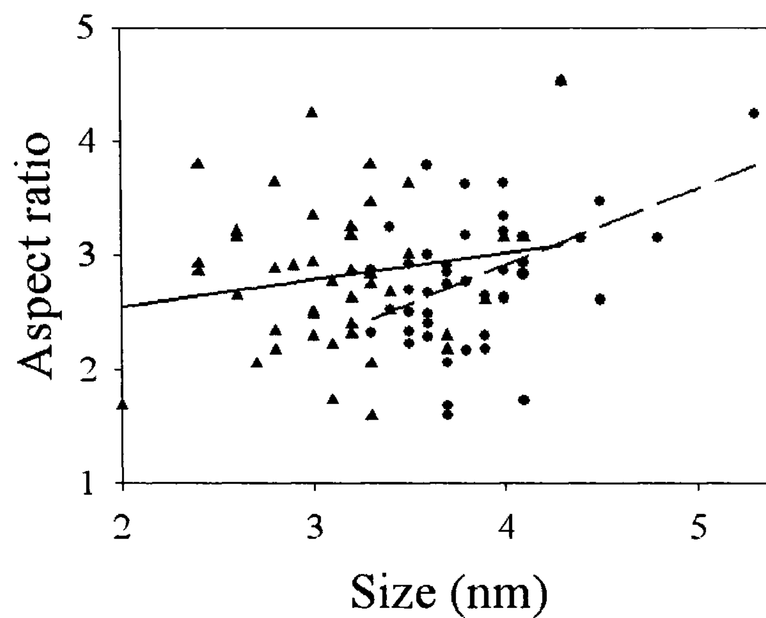

FIG. 7.8. Aspect ratio, A, of the clusters in Fig. 7.3(d) as a function of their major lengths, l_{maj}, (red circles) and minor lengths, l_{min}, (blue triangles).

Reproduced with permission of the copyright owner. Further reproduction prohibited without permission.

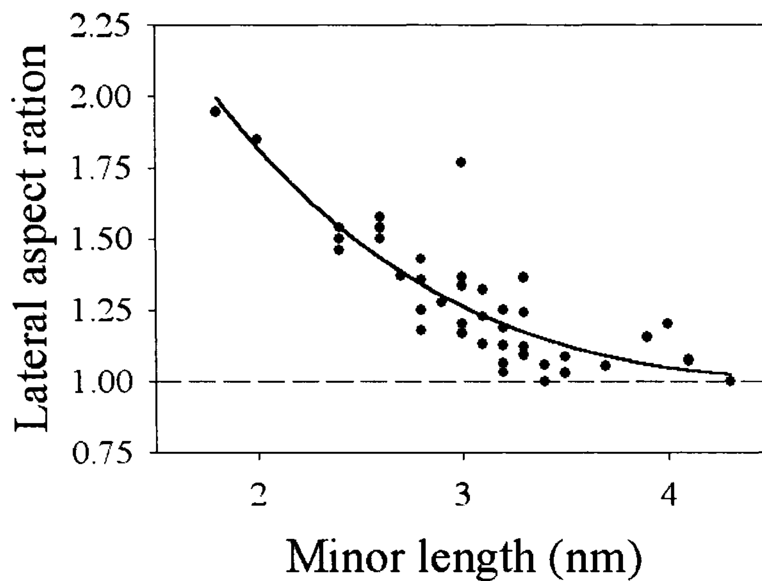

FIG. 7.9. Lateral aspect ratio, L, of the clusters in Fig. 7.3(d) as a function of their minor lengths, l_{min}.

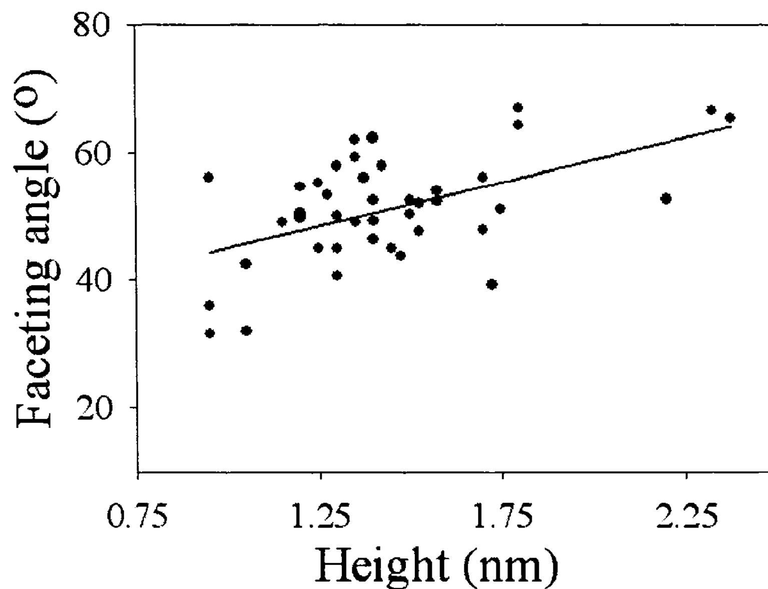

FIG. 7.10. Maximum faceting angle as a function of clusters' height.

Reproduced with permission of the copyright owner. Further reproduction prohibited without permission.

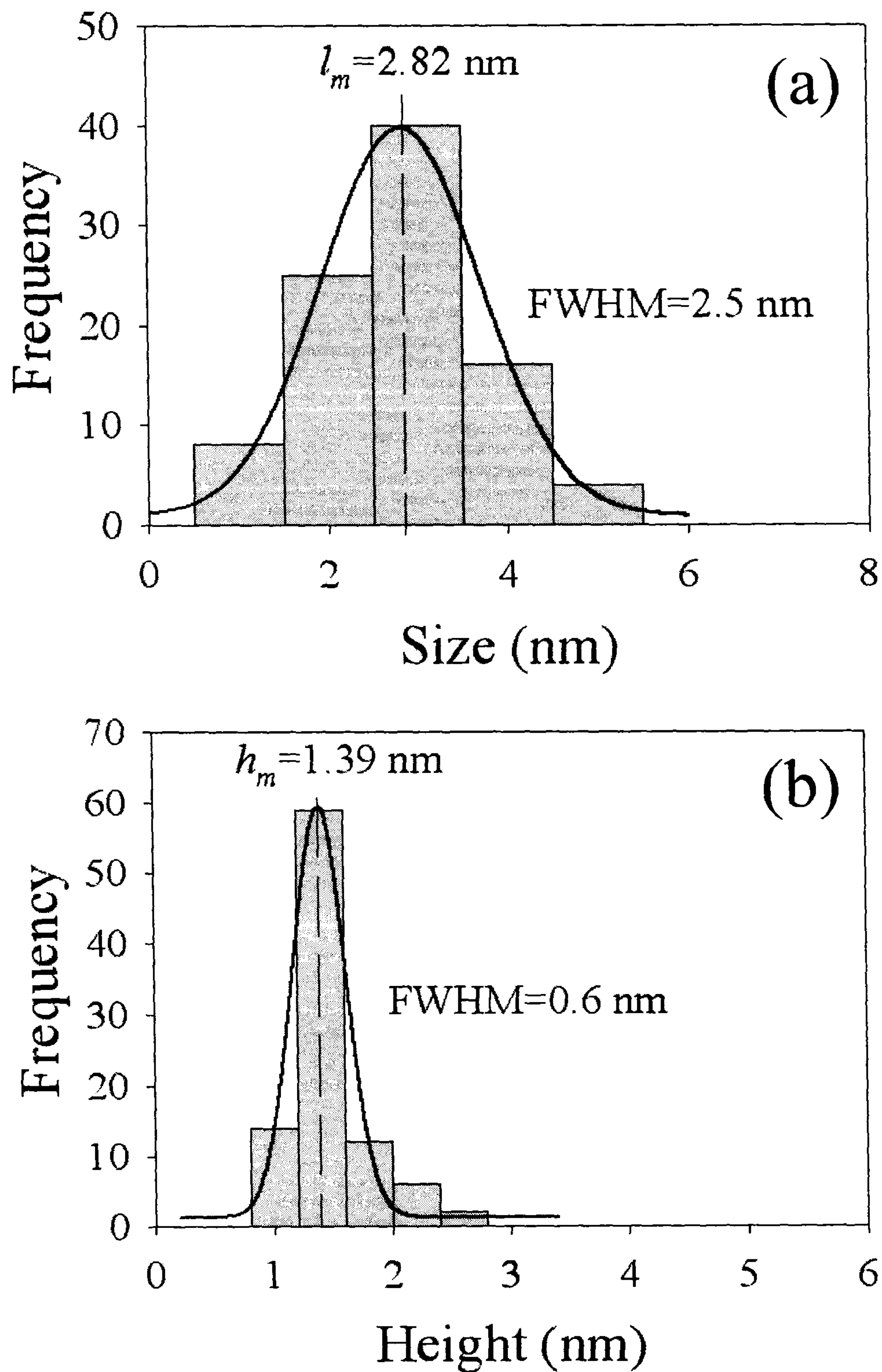

FIG. 7.11. (a) Major size histogram and (b) height histogram for the QD shown in Fig. 7.3(d). The most expected length, l_m, the most expected height, h_m, and both FWHM are indicated on the graphs.

Reproduced with permission of the copyright owner. Further reproduction prohibited without permission.

VI.4. Conclusion

The early stages of formation of the Ge hut QD on Si(100) has been studied by UHV STM. Growth starts by the formation of a very low density of asymmetric huts with high aspect ratios. Further deposition results in a higher density of clusters characterized by their narrow size and height distributions. These clusters are almost of the same lateral size as those deposited at lower thicknesses.

VI.5. References

[1] C. Teichert, "Self-organization of nanostructures in semiconductor heteroepitaxy," Phys. Rep. **365**, 335 – 432 (2002).

[2] B. Voigtländer, "Fundamental processes in Si/Si and Ge/Si epitaxy studied by scanning tunneling microscopy during growth," Surf. Sci. Rep. **43**, 127 – 254 (2001).

[3] O. P. Pchelyakov, V. A. Markov, A. I. Nikiforov, and L. V. Sokolov, "Surface processes and phase diagrams in MBE growth of Si/Ge heterostuctures," Thin Solid Films **306**, 299-306 (1997).

[4] A. I. Nikiforov, V. A. Cherepanov, and O. P. Pchelyakov, "Oscillation of in-plane lattices constant of Ge islands during molecular beam epitaxy growth on Si," Mat. Sci. Eng. B **89**, 180 – 183 (2002).

Reproduced with permission of the copyright owner. Further reproduction prohibited without permission.

[5] Y.-W. Mo, D. E. Savage, B. S. Schwartzentruber, and M. G. Lagally, "Kinetic pathways in Stranski-Krastanow growth of Ge on Si(001)," Phys. Rev. Lett. **65**, 1020 – 1023 (1990).

[6] T. I. Kamins, E. C. Carr, and R. S. Williams, "Deposition of three-dimensional Ge islands on Si(001) by chemical vapor deposition at atmospheric and reduced pressures," J. Appl. Phys. **81**, 211 – 219 (1997).

[7] M. Horn-von Hoegen, B. H. Müller, A. Al Falou, M. Henzler, "Surfactant induced reversible change of morphology," Phys. Rev. Lett. **71**, 3170 – 3173 (1993).

[8] W. Dorsch, S. Christiansen, M. Albrecht, P. O. Hansson, E. Bauser, and H. P. Strunk, "Early growth stages of $Ge_{0.85}Si_{0.15}$ on Si(001) from Bi solution," Surf. Sci. **331 – 333**, 896 – 901 (1995).

[9] M. Schmidbauer, T. Wiebach, H. Raidt, M. Hanke, R. Köhler, H. Wawre, "Ordering of self-assembled $Si_{1-x}Ge_x$ islands studied by grazing incidence small-angle X-ray scattering and atomic-force microscopy," Phys. Rev. B **58**, 10,523 – 10,531 (1998).

Reproduced with permission of the copyright owner. Further reproduction prohibited without permission.

APPENDIX A

PULSED LASER DEPOSITION SYSTEM EQUIPPED WITH RHEED

A.1. System design and components

The main components of the system are shown in Fig. A.1. Images for the rest of the components will appear later in the operation description.

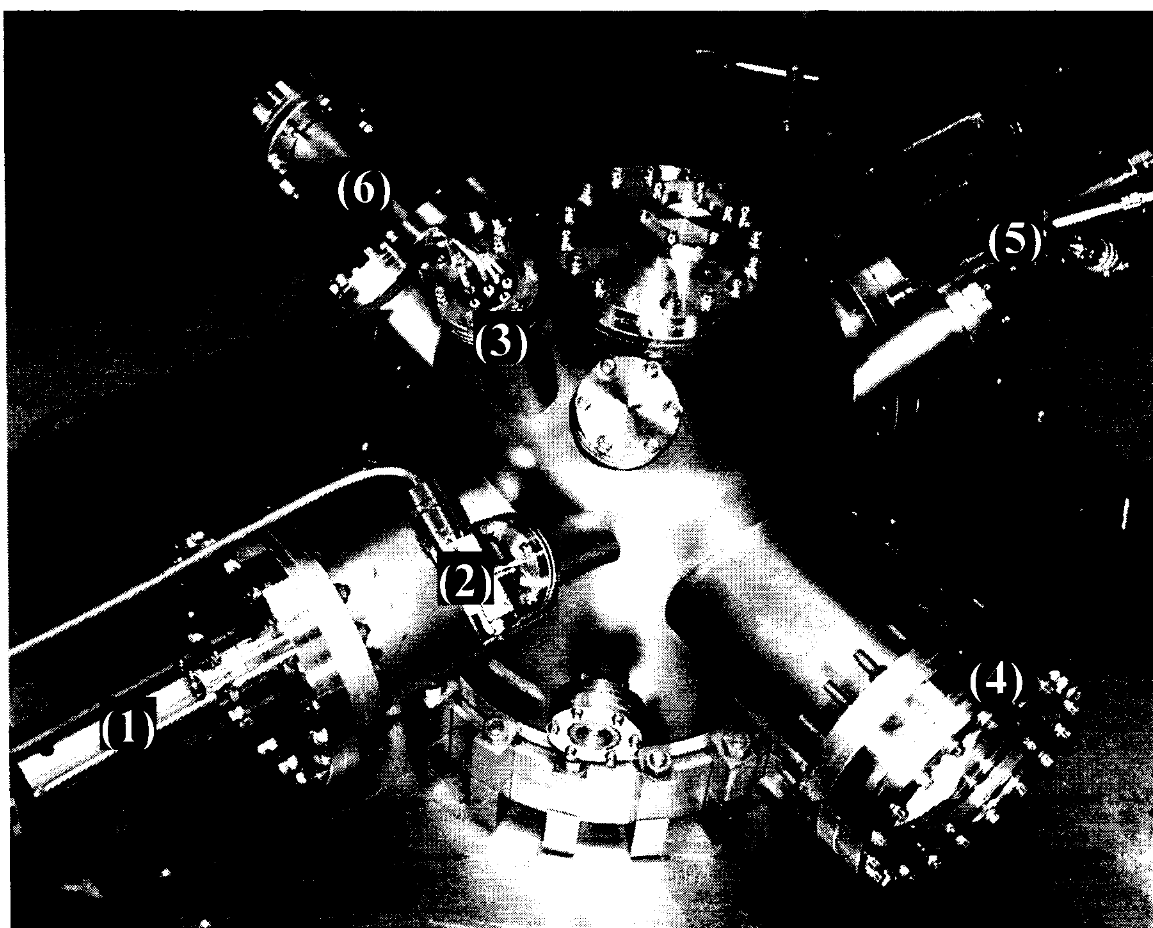

FIG. A1. Top view of the PLD system showing the main components: (1) target holder, (2) convectron gauge, (3) ion gauge, (4) phosphor screen, (5) sample (substrate) manipulator, and (6) RHEED gun.

Reproduced with permission of the copyright owner. Further reproduction prohibited without permission.

A.2. Pumping up and opening the system

1. Make sure that vent valve of the turbo is closed, Fig A.2.

2. Turn ON the roughing mechanical pump, Fig. A.3; after few seconds turn ON the turbo pump, Fig. A.4.

3. Turn OFF the ion pump, Fig. A.5.

4. Close the butterfly valve to separate the ion pump from the chamber, Fig. A.6.

5. When pressure in the chamber reaches $>10^{-7}$ Torr, open the right angle UHV valve slowly, Fig. A.7. (**Caution:** don't open the valve all the way out).

6. Wait for a few minutes while the system is pumped by the turbo and the roughing pump.

7. Turn off the turbo and then the mechanical pump.

8. After a few seconds open the turbo vent valve, Fig. A.2, very slowly until the turbo stops and the chamber is completely filled by air.

9. Disconnect thermocouple and the direct heating connections, Fig. A.8

10. Unscrew the screws of the 8" flange holding the sample manipulator, Fig. A.9.

11. Take the sample manipulator out, place it on a clean bench, Fig. A.10, and close the open port with a plastic cap (**Caution:** be careful when taking the sample manipulator out. It should not be sharply bent in order not to hit it inside the chamber.

Reproduced with permission of the copyright owner. Further reproduction prohibited without permission.

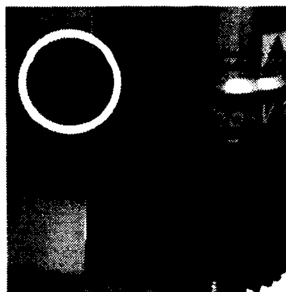

FIG. A.2. Turbo pump with the vent valve highlighted by the circle.

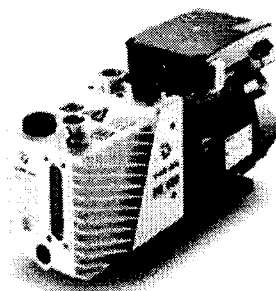

FIG. A.3. Roughing mechanical pump.

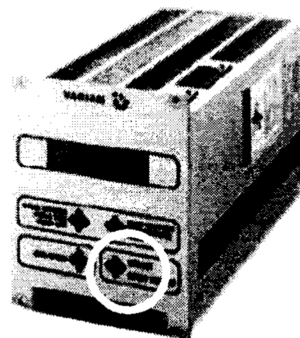

FIG. A.4. Turbo pump controller: the circle highlights the ON/OFF button.

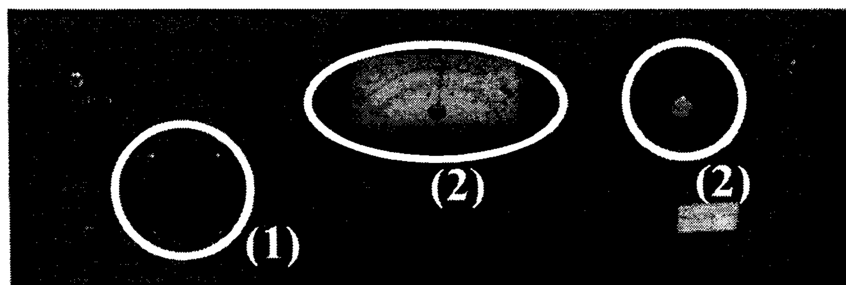

FIG. A.5. Ion pump controller: (1) ON/OFF button, (2) pressure, ionization current or voltage readout, (3) readout mode selector.

Reproduced with permission of the copyright owner. Further reproduction prohibited without permission.

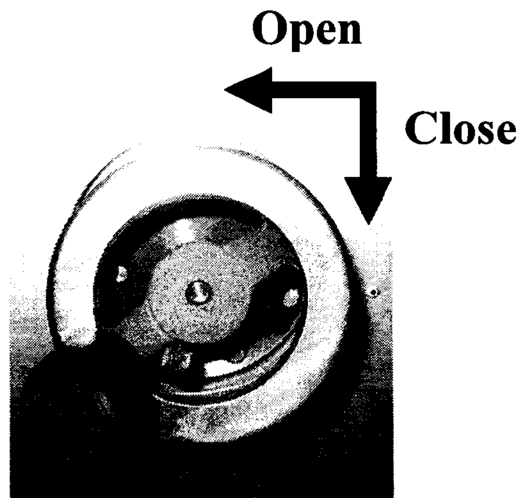

FIG. A.6. Butterfly valve manual control unit: clockwise closes, while anti-clockwise opens.

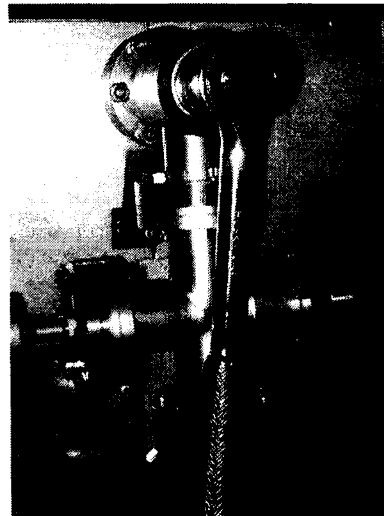

FIG. A.7. Right angle UHV valve.

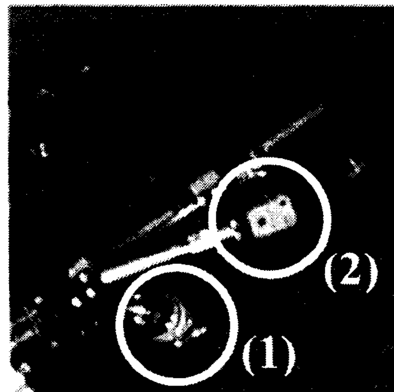

FIG. A.8. Substrate holder: (1) direct heating current connector, (2) Thermocouple connector.

Reproduced with permission of the copyright owner. Further reproduction prohibited without permission.

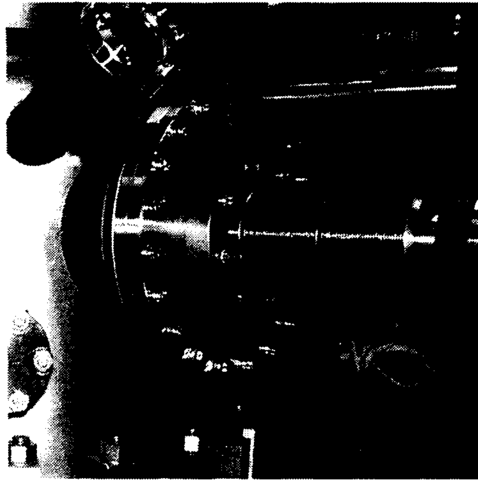

FIG. A.9. The 8" flange holding the substrate manipulator.

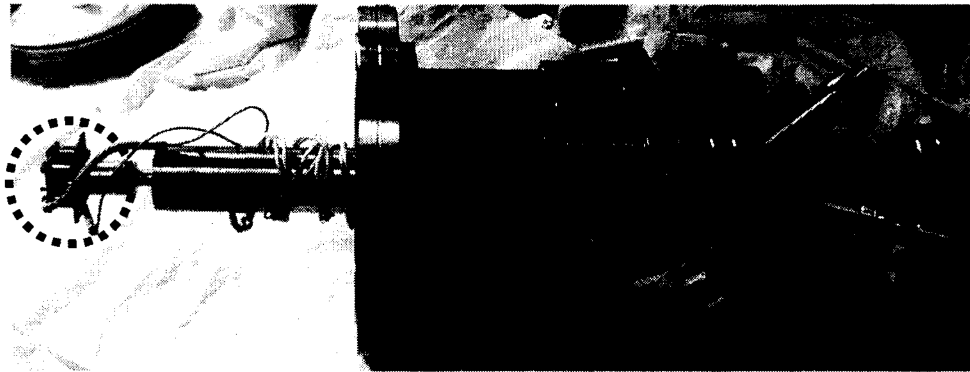

FIG. A.10. Substrate manipulator: the circle highlights the direct current heated sample holder.

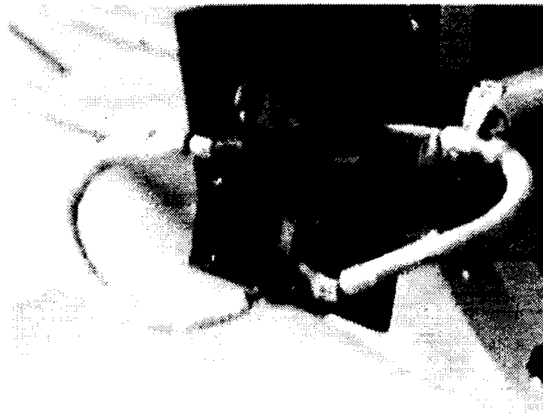

FIG. A.11. Direct current heated substrate holder.

Reproduced with permission of the copyright owner. Further reproduction prohibited without permission.

A.3. Cleaning and changing the substrate

1. Using a diamond scriber, cut Si wafer into substrates of dimensions of ~ 3 mm x 1 cm.

2. Clean the substrates, using the following method: The samples are dipped into a solution of H_2SO_4 (97% wt): H_2O_2 (30% wt) = 4:1 (by volume) for 10 min, rinsed with ultra pure water for 10 min, then dipped into a solution of HF (50% wt): H_2O = 1:10 (by volume) for 1 min. **Caution: HF is a very dangerous solution, avoid direct exposure to skin and do NOT inhale its fumes**. Unused clean samples are stored under ethanol and are etched by HF just before being loaded into the chamber.

3. Take one of the samples and lightly etch its surface by dipping it a few times in diluted HF.

4. Unscrew the screw holding the sample holder from the manipulator, Fig A.11. Figure A.12 shows a schematic drawing of the sample holder.

5. Unscrew the screws holding the clips and remove any installed sample.

6. Install the new sample and put the thermocouple between the clips and the sample so that it firmly touches the sample's surface.

7. Install the sample holder back to the manipulator. Make sure to measure the resistance of the sample and make sure that there is no short circuit anywhere.

8. Install the sample manipulator back to the system and securely fastened all screws. Remember to change the gasket. **Caution: Do NOT risk scratching the knife edge of the conflat flange when changing the gasket.**

Reproduced with permission of the copyright owner. Further reproduction prohibited without permission.

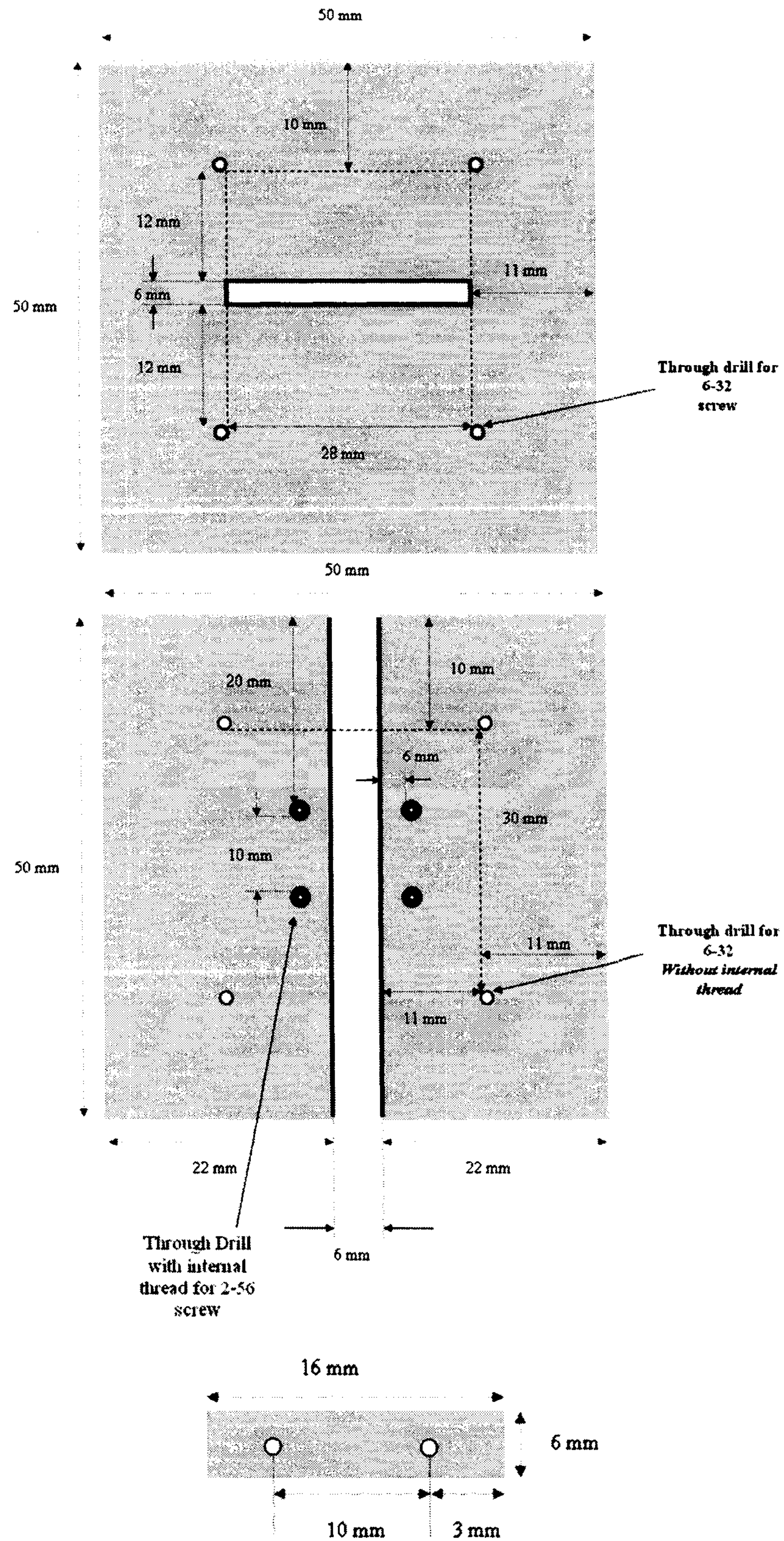

FIG. A.12. Schematics showing the design of the directing heating substrate holder.

Reproduced with permission of the copyright owner. Further reproduction prohibited without permission.

A.4. Changing the target

Note: the target can serve many months, depending on the usage load. Therefore, you do NOT change it every time you change the sample. ONLY change it when required.

1. Unscrew the 8" flange holding the target holder, Fig. A.13.

2. To remove the installed target, hold your fingers around the target, Fig. A.14, and rotate it clockwise, then pull it out.

3. Place the target upside-down on a clean surface.

4. Using a heat gun, heat the target-holder interface for a few minutes until the "Torr Seal" completely cures and the target is detached from the base holder. You will need to heat the entire circumference uniformly by directing the heat gun to different areas.

5. Prepare and clean your target. The cleaning process depends on the target material. For Ge, wet a clean tissue with ethanol and place the Ge wafer upside-down, then rotate it gently on the wet tissue (**Caution: DO NOT apply vertical pressure on the wafer**).

6. Install the target holder base to its location and rotate it counter-clockwise.

7. Install the flange back and tighten all the screws.

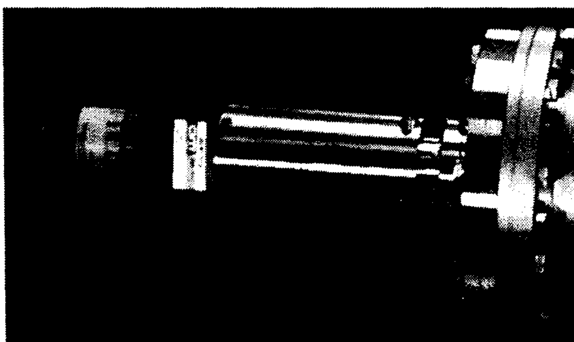

Fig. A.13. Magnetically rotated target holder.

Reproduced with permission of the copyright owner. Further reproduction prohibited without permission.

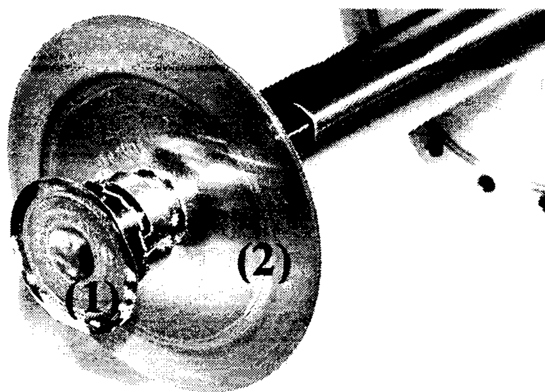

FIG. A.14. Magnetically rotated target holder: (1) used Ge target, (2) magnetic shield.

A.5. Pumping the system down and bakeout the system

1. Make sure that you have installed new gaskets and tightly screwed all screws. Also, double check that the turbo vent valve is tightly closed. **Remember: Make sure that the antiseize compound is applied to screws the first time they are used. Reapply compound every few months.**

2. Turn on the roughing pump and turbo pump. Watch the speed and temperature of the turbo during pumping down.

3. When the turbo reaches its maximum pumping speed, turn ON the ion gauge, Fig. A.15, by selecting "UHV" using the mode selector. Press the "1" button to select the filament used in this chamber. Press "1/T 3" button to activate this filament.

4. When the pressure reaches the low 10^{-4} Torr range, open the butterfly valve, Fig. A.6. Do so very slowly until the valve is all the way open. You should be watching the pressure at all times. Leave the whole system to be pumped by the turbo for 3-6 hours.

Reproduced with permission of the copyright owner. Further reproduction prohibited without permission.

5. When the pressure is in the 10^{-7} range (lower pressure is always better), tightly (but not too tight in order not to destroy the seal) close the right angle UHV valve, Fig. A.7.

6. Turn ON the ion pump, while watching the pressure. At the beginning, the pressure will go up before going down within several seconds. Observe the pressure for several minutes.

7. When the ion pump is operating normally, shut down the turbo pump, then shut down the mechanical pump.

8. Wait for a few hours. When the pressure reaches the low 10^{-8} Torr range, you may start baking the system. Surround the system with high power light bulbs and cover everything with aluminum foil, Fig A.16. (**Caution: before baking the system, make sure that it is not surrounded by anything that can be burned. Also, cover all mirrors and/or lenses that are very close to the system with aluminum foil. In doing so, be careful not to scratch them**). The system should be baked for 12-24 hours. You have to watch the pressure during the early stages of baking. It is normal for the pressure to increase by an order of magnitude during baking. Monitor the chamber bakeout temperature with a thermocouple. It should be ~150 °C.

7. During baking, the Si substrate should be kept at ~300 °C.

8. After the baking period, turn off all the bulbs and remove the foil and leave the system to cool down. It may take several minutes to cool down to room temperature.

Reproduced with permission of the copyright owner. Further reproduction prohibited without permission.

FIG. A.15. Ion gauge controller: the circle highlights the mode selector.

FIG. A.16. Baking of the system by high power bulbs and covering the system with aluminum foil.

A.6. Cleaning the Si(100) substrate to obtain the 2x1 reconstruction

1. After baking, wait until the system cools down and the pressure goes down to its minimum value, which should be ~$1x10^{-9}$ Torr or better. During that time, keep the sample temperature the same as during baking, i.e. ~300 °C.

Reproduced with permission of the copyright owner. Further reproduction prohibited without permission.

2. Start heating the sample gradually at a very slow rate by increasing the heating current until you reach ~800 °C. Leave the sample at that temperature for a few hours. You have to watch the pressure at all times, keeping it in the 10^{-9} Torr range.

3. Quickly flash the sample to 1100 °C for a few seconds, and then quickly bring the temperature back to ~800 °C. I used to use the Leader power supply (18 V, 20 A) to heat the samples. For most of the Si samples used, ~8 A results in a temperature of ~800 °C, and the samples are flashed to a current of 13-16 A. Please make sure to draw a temperature calibration curve, by drawing a relation between the heating power (= voltage x current) and the resulting equilibrium temperature.

4. You may need to repeat the flashing cycles several times, depending on the resulting RHEED pattern.

A.7. RHEED gun schematics and operation

The home-made electron gun that is used in this system is shown in Fig. A.17. The main components of the gun are shown in the figure. The electron gun control unit is shown in Fig. A.18, while Fig. A.19 shows schematics of the potential divider circuit.

Turn ON procedure:

1. Make sure that the high voltage is set to zero. Set the filament current to 2 A.

2. Turn ON the high voltage, the filament current, and the X- and Y-deflector power supplies.

3. Watch the pressure increase due to the increase in the filament current.

Reproduced with permission of the copyright owner. Further reproduction prohibited without permission.

4. After a few minutes start increasing the high voltage and the current very gradually until you reach the desired values. To avoid discharges do not exceed 14 kV.

5. Use the X and Y deflectors to manipulate the beam and to obtain a pattern of the substrate.

Turn OFF procedure:

1. Decrease the values of both the current and the high voltage gradually until you reach zero Volt and 2 A.

2. Turn off all power supplies.

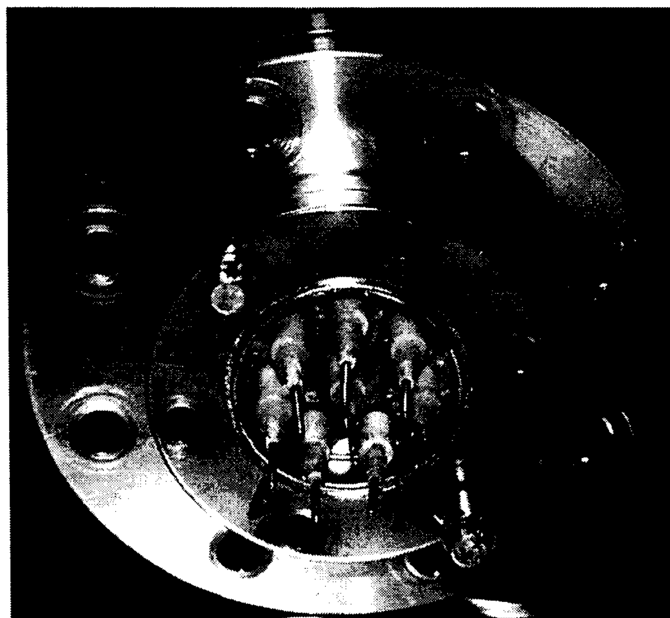

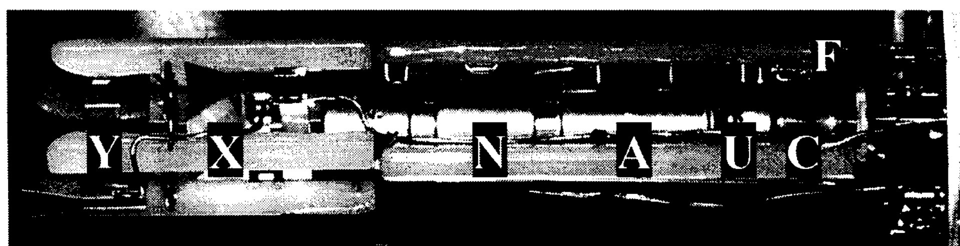

FIG. A.17. The home-made electron gun. (Top) back view showing the electrical connections. (Bottom) electron acceleration column. [A: anode, F: filament, N: ground, C: cup, X: x-deflector, Y: y-deflector, and U: focus].

Reproduced with permission of the copyright owner. Further reproduction prohibited without permission.

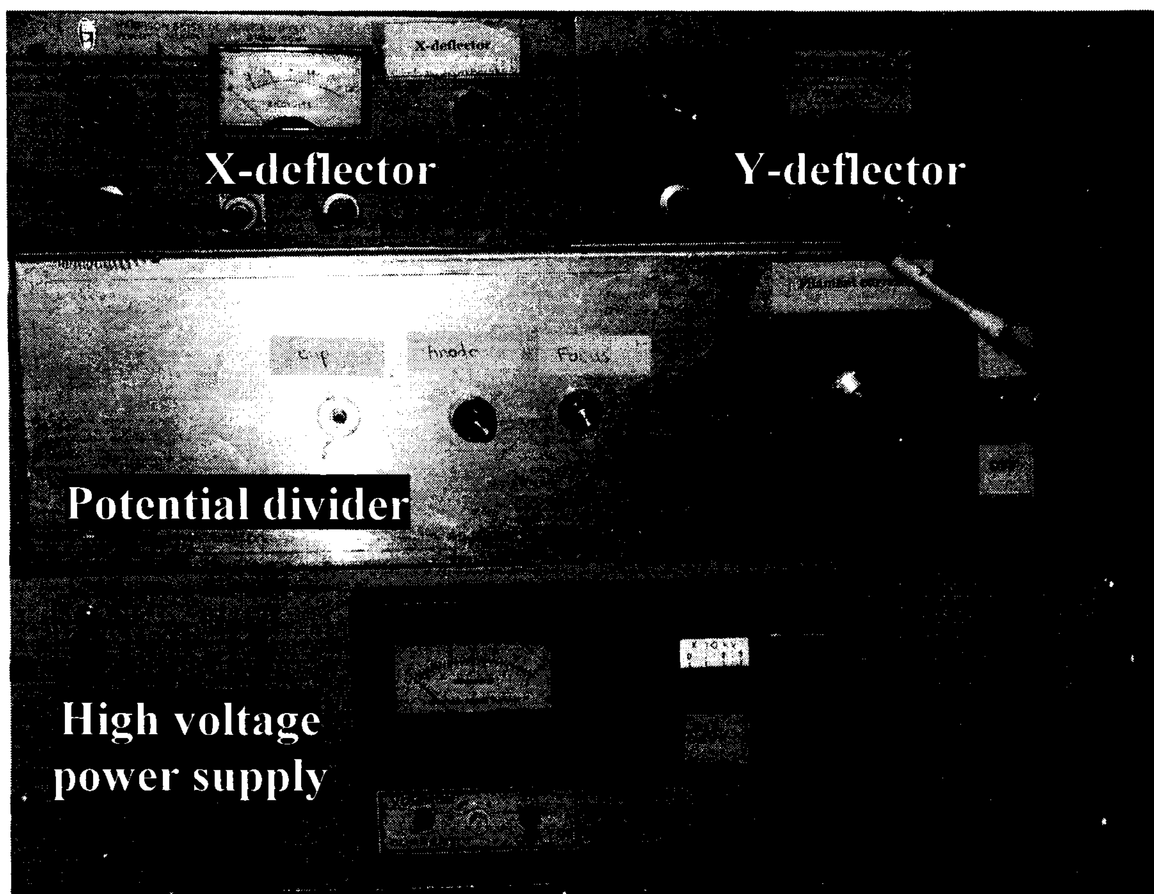

FIG. A.18. Electron gun control unit, including high voltage power supply, potential divider, X and Y deflectors.

Reproduced with permission of the copyright owner. Further reproduction prohibited without permission.

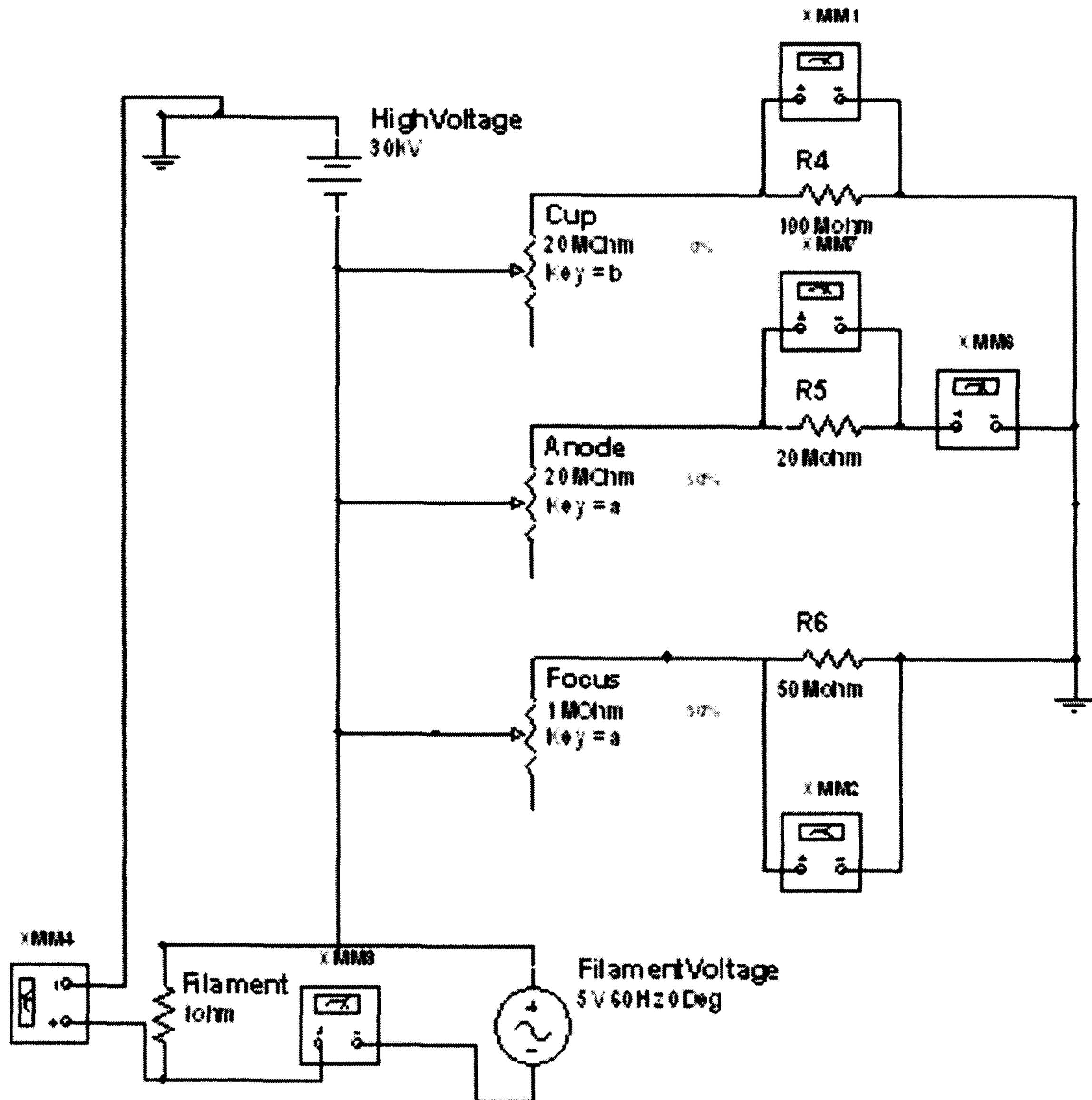

FIG. A.19. Schematics of the high voltage potential divider.

Reproduced with permission of the copyright owner. Further reproduction prohibited without permission.

A.8. Nd:YAG laser operation

The Lumonics YAG Master 200 laser is shown in Fig. A.20. For laser specifications please refer to the laser manual.

Turn ON procedure:

1. Make sure that you and everyone within sight of the laser is wearing laser eye protection.

2. Turn ON the external cooling city water supply, Fig. A.21.

3. Rotate the "red" mains to ON position, Fig. A.22. The cooler pump will start.

4. Allow at least 30 minutes for the coolant and the HGA ovens to reach the operating temperature.

5. Turn the ENABLE key switch on the control unit clockwise to the horizontal ON position, Fig. A.23.

6. After a delay of 5 seconds the power supply is enabled and the ON LED, Fig. A23, next to the key switch will light up indicating the start of the flashlamp.

7. From the pockels cell divider buttons, push the button to deliver the requested frequency (by diving the default 50 Hz).

8. Using the "oscillator" flashlamp selector, choose the required value.

9. Press the shutter "OPEN" button.

10. Press the oscillator "ON" button; the flashlamp will begin to pulse.

11. Check, using an IR viewer, along the beam path that there are no unwanted reflections and that the beam is safely contained.

12. To momentarily stop the beam, simply press the OPEN shutter pushbutton.

Reproduced with permission of the copyright owner. Further reproduction prohibited without permission.

Turn OFF procedure:

1. Press the Oscillator OFF pushbutton and press the shutter CLOSE button.

2. Turn the ENABLE key switch to the vertical OFF position.

3. Leave the cooler pump ON for at least 30 minutes to cool down the system.

4. Switch OFF the cooler.

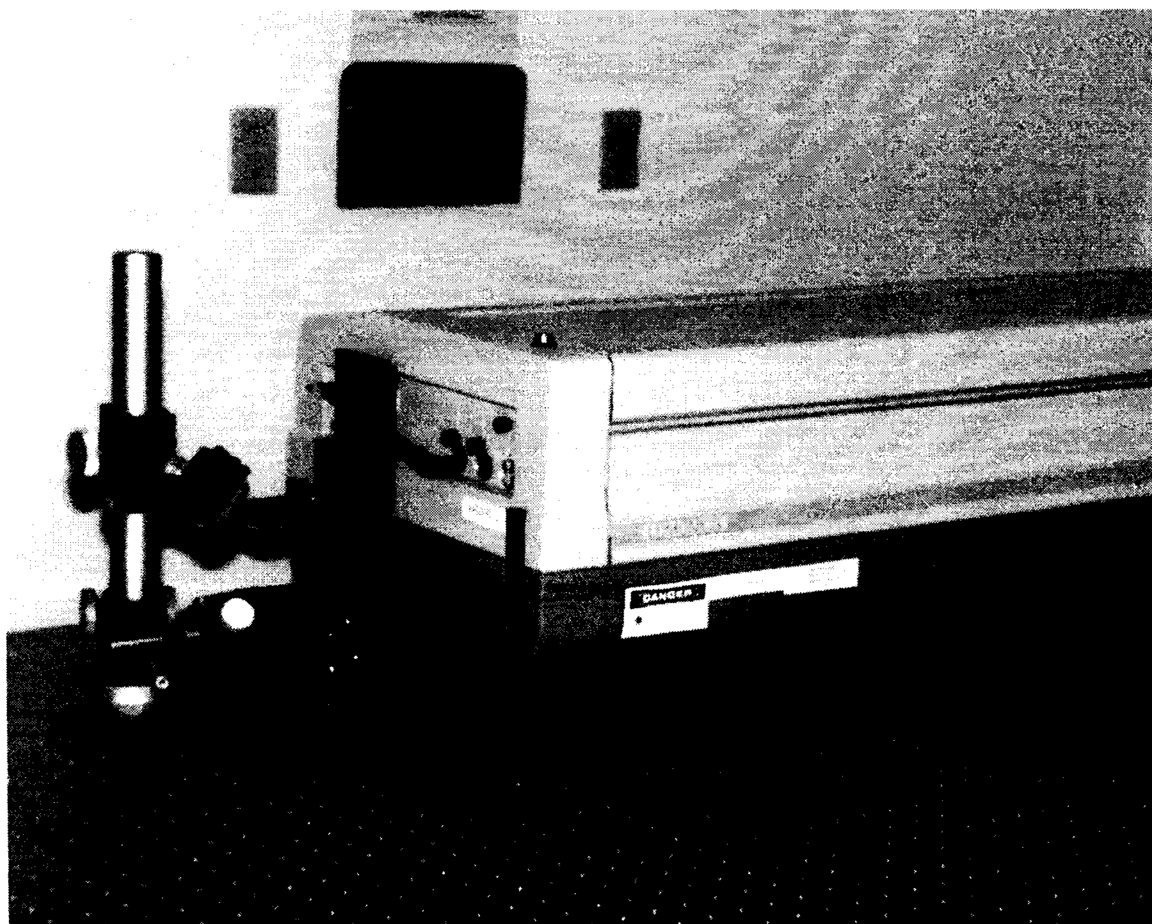

FIG. A.20. Lumonics YAG Master (YM) 200 laser system.

Reproduced with permission of the copyright owner. Further reproduction prohibited without permission.

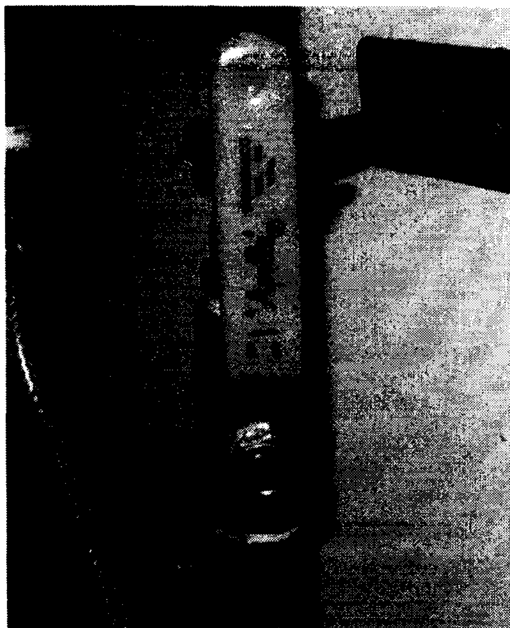

FIG. A.21. External cooling water switch.

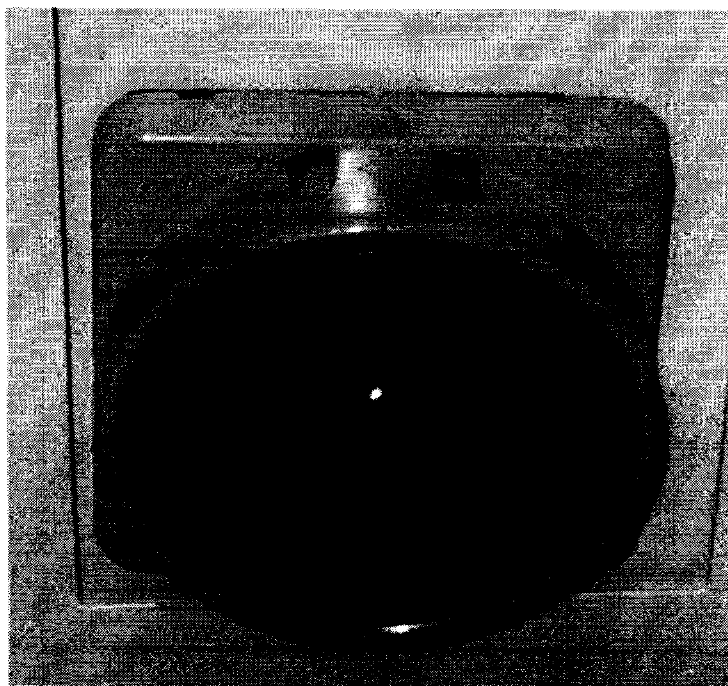

FIG. A.22. Mains power supply switch: (OFF) vertical position, (ON) horizontal position.

Reproduced with permission of the copyright owner. Further reproduction prohibited without permission.

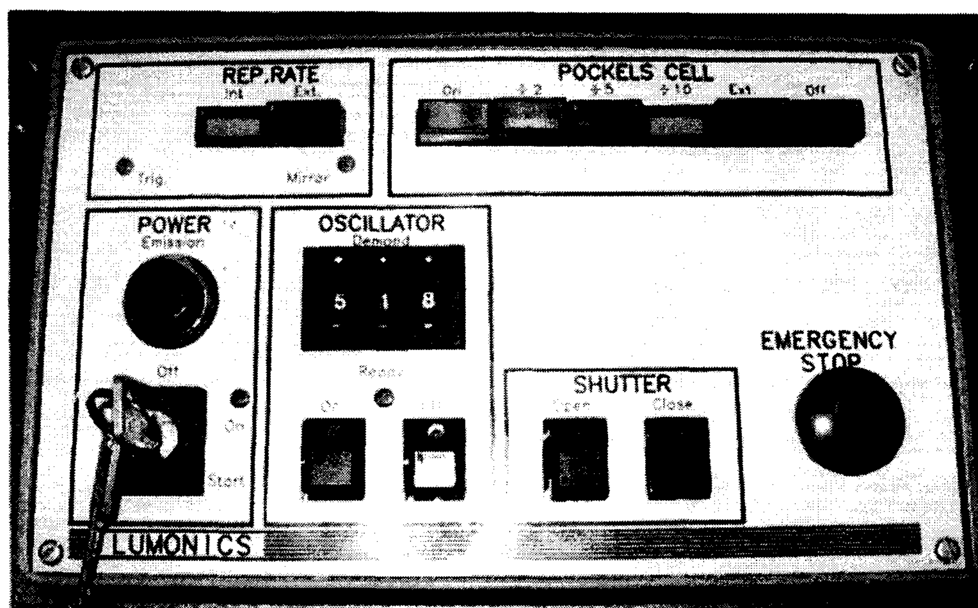

FIG. A.23. Local control unit.

Reproduced with permission of the copyright owner. Further reproduction prohibited without permission.

APPENDIX B

PULSED LASER DEPOSITION SYSTEM EQUIPPED WITH SCANNING TUNNELING MICROSCOPE

B.1. System design and components

Schematic diagrams of the system are shown in Figs. 2.6 and 7.1, while Fig B.1 is an image of the real system showing the main components of the system. Images for the rest of the components will appear later in the operation description. Remember that all UHV systems should be under vacuum at all times, even when not being used.

B.2. Pumping up and opening the system

I have designed the system such that the deposition chamber is kept under vacuum all the time. Any sample loading should be done via the custom-made load lock.

1. Make sure that the vent valve of the turbo is closed, and then turn ON both the roughing and turbo pumps.

2. Close the gate valve, Fig. B.2, separating the deposition chamber from the bolt-on STM chamber. Make sure that the valve is tightly closed.

3. Wait 5-10 minutes for the pressure in the STM bolt-on increases.

4. Open the "Right angle UHV" valve, Fig. B.3, which connects the STM bolt-on to the turbo pump.

Reproduced with permission of the copyright owner. Further reproduction prohibited without permission.

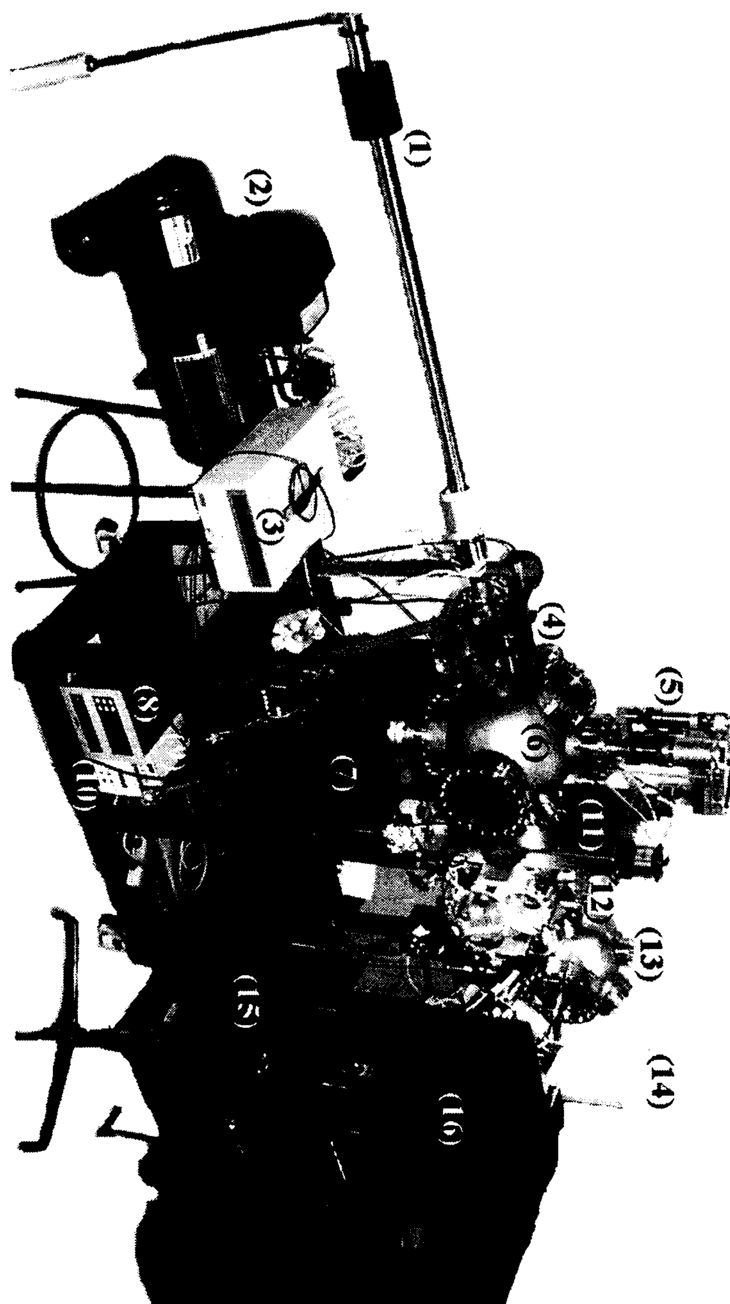

FIG. B.1. Image of the PLD system equipped with UHV STM. (1) 48" magnetic transporter, (2) air compressor to controls the gate valve, (3) power supply to heat the substrate, (4) bellow to move the transporter in X and Y directions, (5) home-made target rotator mount on a Z-translator, (6) 12" spherical deposition chamber, (7) ion pump, (8) ion pump controller, (9) convectorn gauge, (10) turbo pump controller, (11) gate valve, (12) custom-made load lock, (13) Omicron bolt-on UHV STM chamber, (14) computer monitor to control the STM, (15) optics assembly to direct laser into the chamber, (16) shield to protect the system from the Nd:YAG laser.

Reproduced with permission of the copyright owner. Further reproduction prohibited without permission.

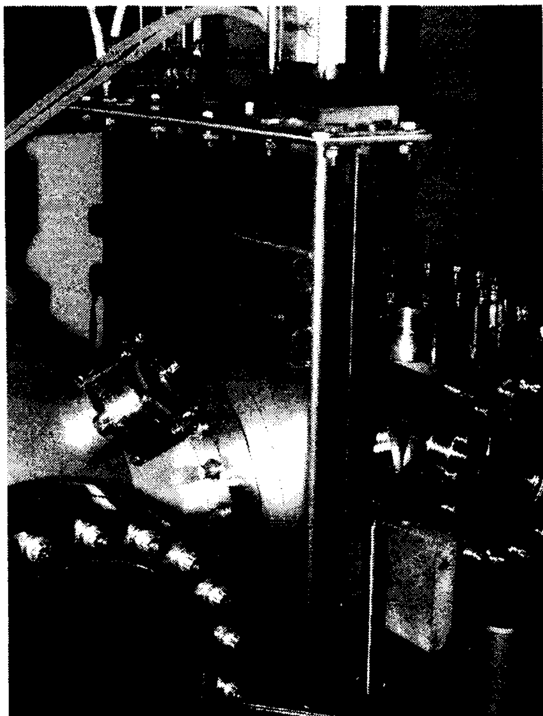

FIG. B.2. Gate valve.

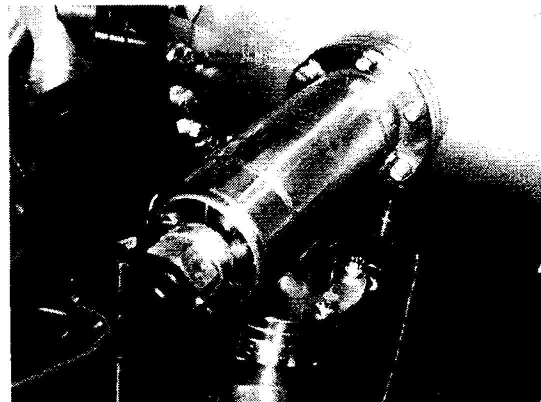

FIG. B.3. Right angle UHV valve connecting the deposition chamber to the STM chamber.

5. After a few minutes, turn OFF both the turbo and the roughing pumps.

6. After a few seconds open the turbo vent valve, Fig. A.2, very slowly until the turbo stops and the chamber is completely filled by air.

B.3. Changing the samples

1. Open the 8" flange on the load-lock, Fig. B.4.

2. With one glove-covered hand (left hand recommended) reach for the tip/sample carousel, Figs. B.5 and B.6, and take it out of the system.

3. Place the carousel on a clean holder.

Reproduced with permission of the copyright owner. Further reproduction prohibited without permission.

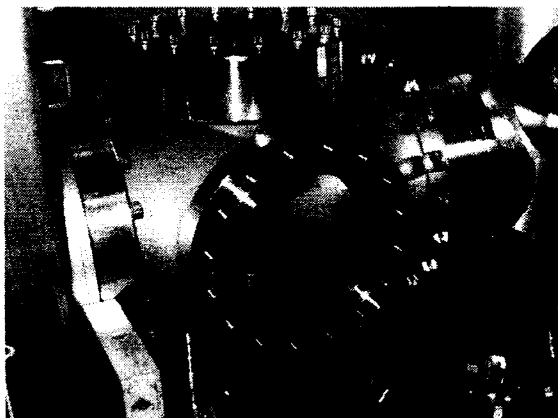

FIG. B.4. 8" flange on the load-lock.

FIG. B.5. Tip/sample carousel in its housing in the UHV STM bolt-on.

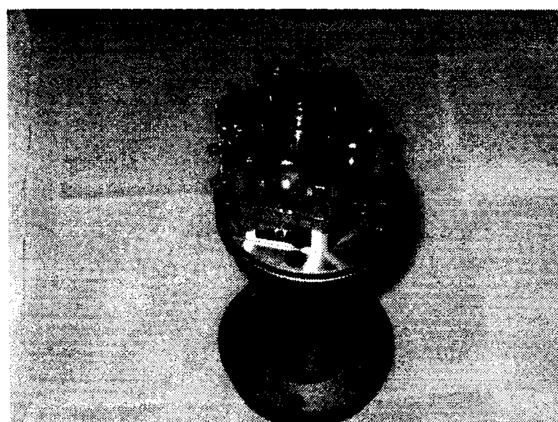

FIG. B.6. Carousel outside the chamber.

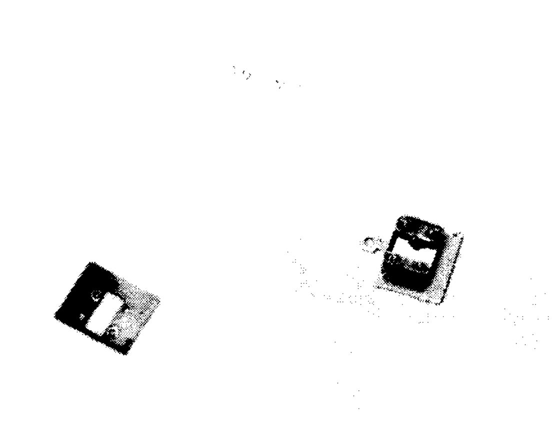

FIG. B.7. Directing heating sample holder.

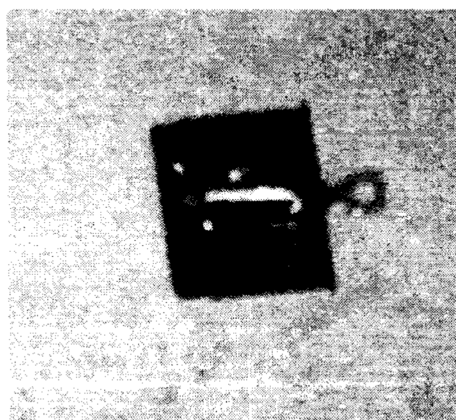

FIG. B.8. Normal sample holder.

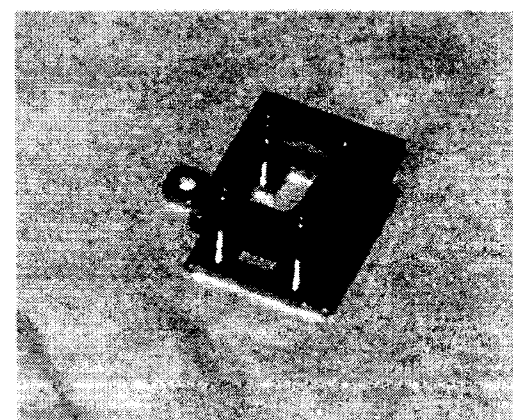

FIG. B.9. Tip holder.

Reproduced with permission of the copyright owner. Further reproduction prohibited without permission.

4. Clean and prepare the samples before installing them in the proper sample holder.

5. For Si substrates, follow the cleaning procedure in section A.3. Then, load the Si sample into a direct heating sample holder, Fig. B.7. For samples that do not require direct heating, use normal sample holders, Fig. B.8.

6. Load the samples into the carousel. Tabulate the location of each sample in the carousel compartments.

7. Load tips to the tip holders, Fig. B.9. Etched tungsten tips are recommended.

8. When all carousel compartments are filled, load it back to its place in the chamber.

9. Close the 8" flange after changing the gasket.

B.4. Pumping the system down and bakeout the system

Important:

- **Always, consult the Omicron manual for detailed instructions**.
- Bring the PPM to its upper position before bakeout.
- Never leave a sample plate in the STM during bakeout.
- Switch OFF all units and remove all cables that are not necessary during bakeout.
- To avoid charge build up during bakeout, fit all electrical feedthroughs with their short circuit plugs. To do that, remove the connection cable from the Matrix control unit, Fig. B.10, and SPM preamplifier, Fig. B.11, and replace them with the bakeout short circuit plugs, Fig. B.12.
- Maximum bakeout temperature is 170 °C.

Reproduced with permission of the copyright owner. Further reproduction prohibited without permission.

1. Make sure that you have installed a new gasket and tightly screwed all opened ports. Also, double check that the turbo vent valve is tightly closed. Use antiseize for screws.

2. Turn on the roughing pump and turbo pump. Watch the speed and temperature of the turbo during pumping down the bolt-on and the load lock.

3. After 40-60 minutes, turn off the ion pump.

4. Open the right angle UHV valve connecting the deposition chamber to the turbo pump, Fig. B.13, and watch the pressure via the ion gauge, Fig A.15.

5. After ~20 minutes, open the gate valve to connect both chambers, while being pumped by the turbo.

6. After several minutes, the pressure should be in the low 10^{-6} or high 10^{-7} Torr ranges.

7. At the above pressure range, close both right angle UHV valves and turn ON the ion pump.

8. When the ion pump is operating normally, turn OFF the turbo pump, then shut down the mechanical pump.

9. Wait for a few hours. When the pressure reaches the low 10^{-8} range, you may start baking the system. Surround the system with high power light bulbs and cover everything with aluminum foil, Fig A.16. **(<u>Caution:</u> before baking the system, make sure that it is not surrounded by anything that can be burned. Also, cover all mirrors and/or lenses that are very close to the system with aluminum foil)**. The system should be baked for 12-24 hours. You have to watch the pressure during the early stages of baking. It is normal for the pressure to increase by an order of magnitude during baking.

10. Normally, I load two Si substrates in the carousel for deposition. You may load one of them into the substrate holder, Fig. 7.2, and keep it at ~300 °C during baking. To

Reproduced with permission of the copyright owner. Further reproduction prohibited without permission.

transfer the sample from the carousel, Fig. B.5, to the substrate holder, use the wobblestick, Fig. B.14. Be careful not to hit or destroy the STM head, while using wobblestick.

11. After the baking period, turn off all the bulbs, remove the foil and leave the system to cool down. It may take several minutes to cool down to room temperature.

12. NEVER disconnect the short circuit plugs and reconnect the control connections before the system cools down to room temperature.

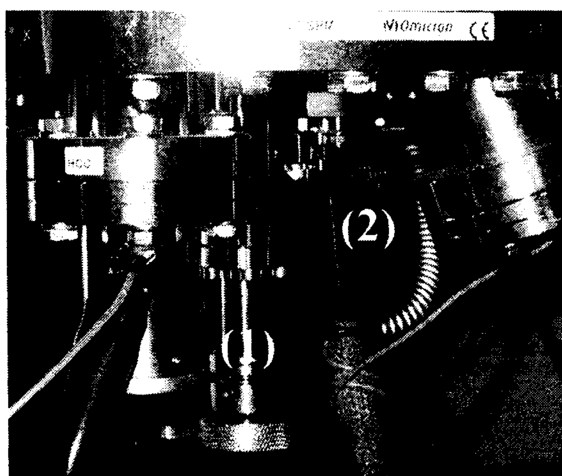

FIG. B.10. (1) PPM, (2) connection to the Matrix control unit.

FIG. B.11. SPM preamplifier.

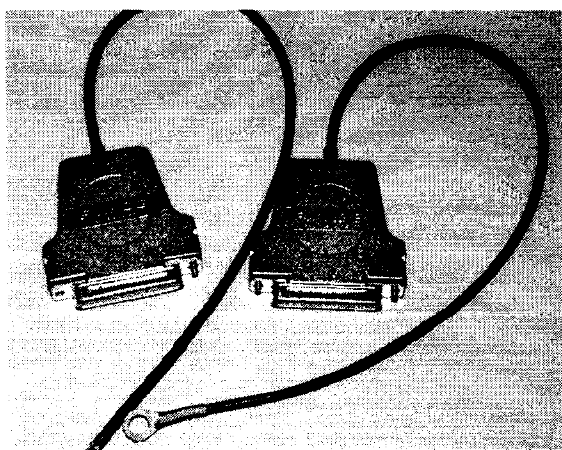

FIG. B.12. Bakeout short circuit plugs.

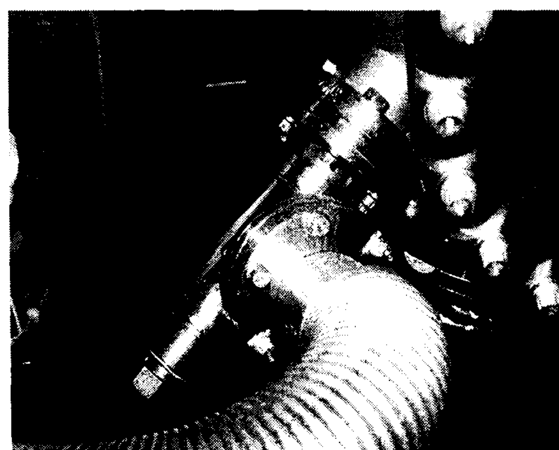

FIG. B.13. Right angle UHV valve connected to the deposition chamber.

Reproduced with permission of the copyright owner. Further reproduction prohibited without permission.

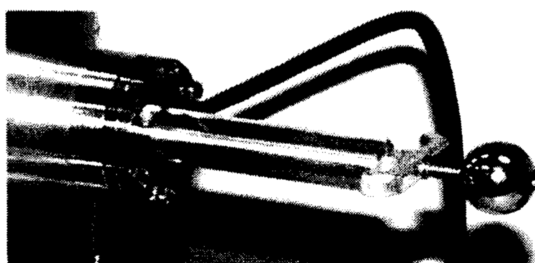

FIG. B.14. Wobblestick.

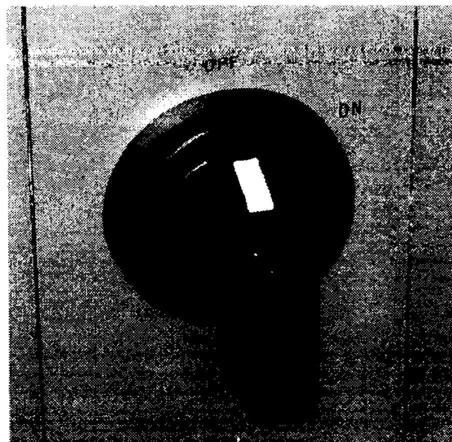

FIG. B.15. Matrix power switch.

B.5. Cleaning the Si(100) substrate

1. Use the Wobblestick to remove the sample to the direct heating stage, which is installed on the 48" magnetic transporter.

2. Follow the steps in section A.6.

3. If needed, repeat the above cleaning steps.

4. Using the wobblestick, move the sample back and forth between the deposition chamber and the STM stage to check whether more cleaning is needed. Remember to keep the PPM secure in the upper position.

Reproduced with permission of the copyright owner. Further reproduction prohibited without permission.

B.6. Starting the STM and tip approach

1. Lower the PPM all the way down and secure it by rotating it to the right or to the left.

2. Turn ON the Matrix by rotating the power switch clockwise to the ON position, Fig. B.16.

2. Log in to the computer using the username: matrix and no password.

3. Wait for ~1 minute until the communication between the PC and the Matrix is established via TFTPD32, Figs. B.16 and B.17.

4. Start Matrix software, Fig. B.18.

5. Select "STM" mode, B.19. Then select "STM V-Spec" mode, Fig. B.20.

6. In the Matrix software interface, Fig. B.21, go to the Z regulation panel, Fig. B. 22, and enter the parameters that are suitable for the sample under study. For my Si(100) samples, the parameters in the figure are found to be suitable starting parameters. **Remember: that you will need to change these parameters when you zoom in**. You will need to tune the V-gap voltage, loop gain, and I-set point until you get the best images depending on your sample and on the scanned area.

7. Adjust the parameters in the XY scanner control panel, Fig. B.23. Always start with a large scan area (4-6 μm) and then zoom in to the smaller area of interest. You will need to tune the "raster time" depending on your sample and the scanned area.

8. Use the Matrix remote box, Fig. B.24, to control the tip approach to the surface. Upon switching on the MATRIX CU the remote box display will come on and display the OMICRON logo together with the head that has been configured. Press DOWN to proceed to the BACK menu, i.e. scan piezo fully retracted and coarse positioning

Reproduced with permission of the copyright owner. Further reproduction prohibited without permission.

functions active. Operate the ±X, ±Y, APPR (approach) and RETR (retract) coarse motion buttons (±F1 to ±F3) on the remote box. Turn regulator "SPEED" to the maximum (“10”). As the coarse steps are so small (40 nm to 400 nm at room temperature) you have to look closely to see the motion. Different directions normally have different speeds (up to a factor of 3). When you are close to the sample reduce the step width and approach very slowly (speed of 3-4). Use the TV monitor to determine how close the tip is to the surface, Fig B.25.

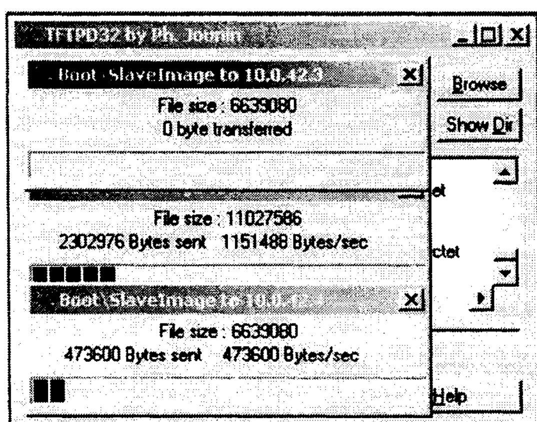

FIG. B.16. Communication is still in progress.

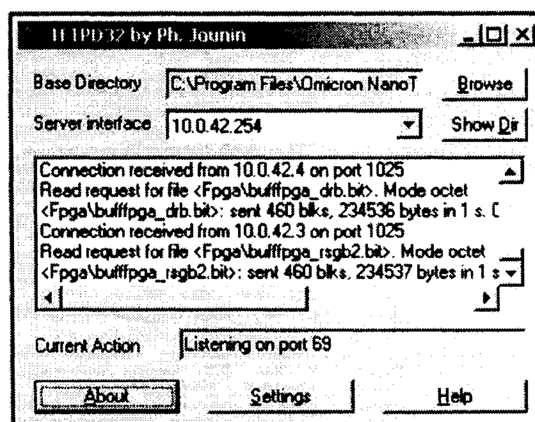

FIG. B.17. Communication is established.

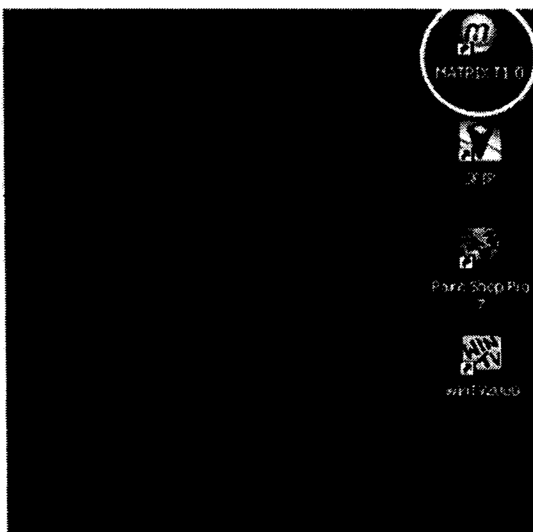

FIG. B.18. Matrix software icon.

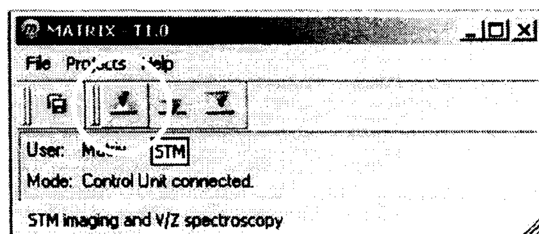

FIG. B.19. STM mode selection.

Reproduced with permission of the copyright owner. Further reproduction prohibited without permission.

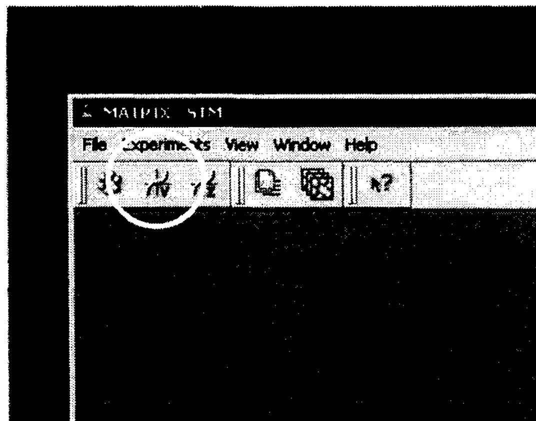

FIG. B.20. STM V-Spec mode selection, highlighted by the circle.

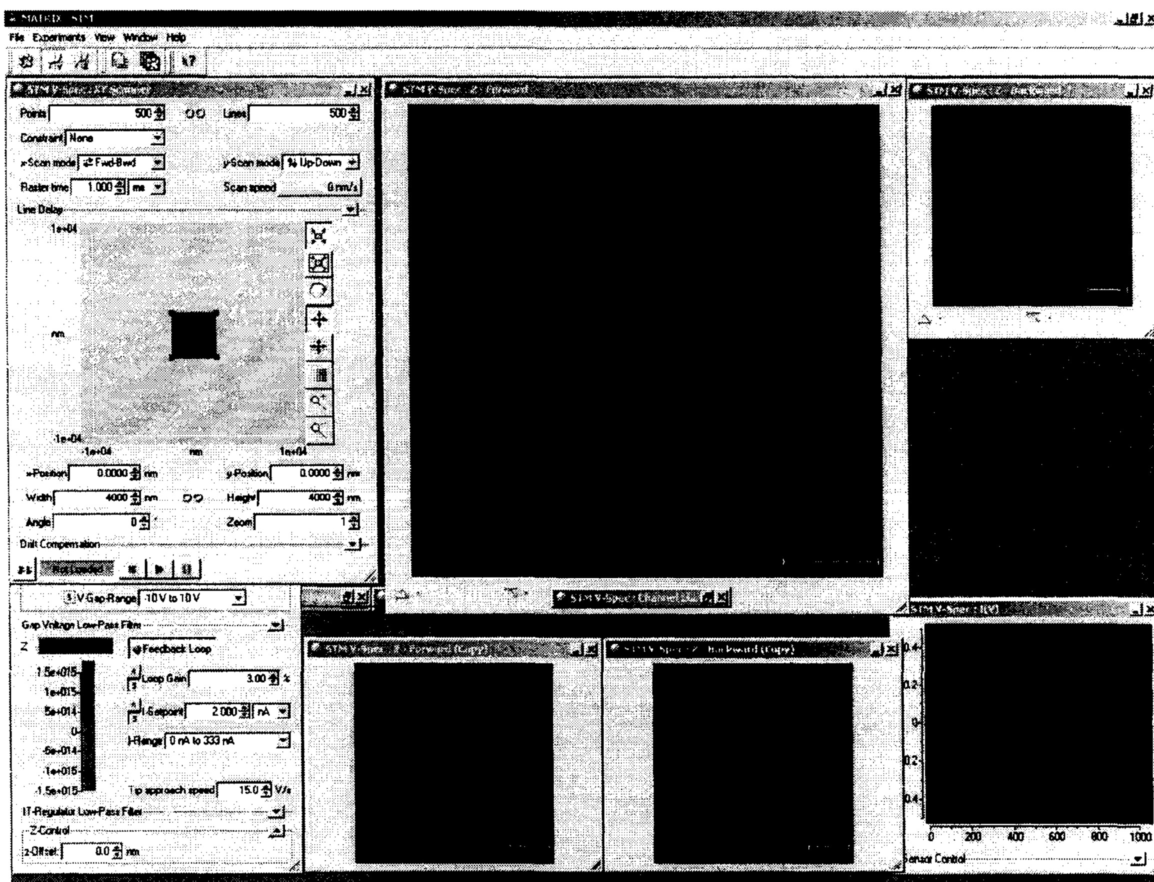

FIG. B.21. Matrix software interface.

Reproduced with permission of the copyright owner. Further reproduction prohibited without permission.

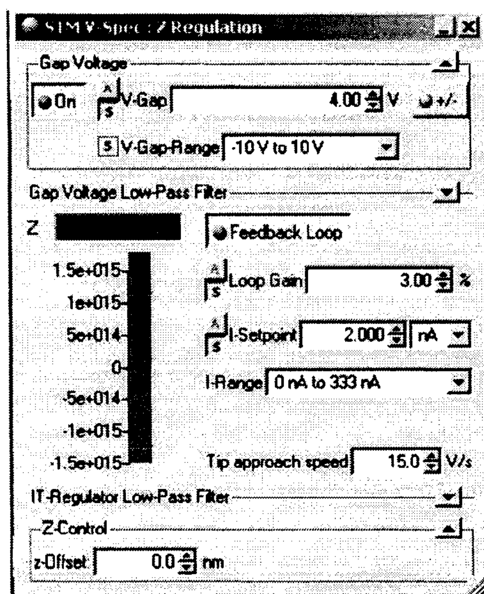

FIG. B.22. Z regulation panel.

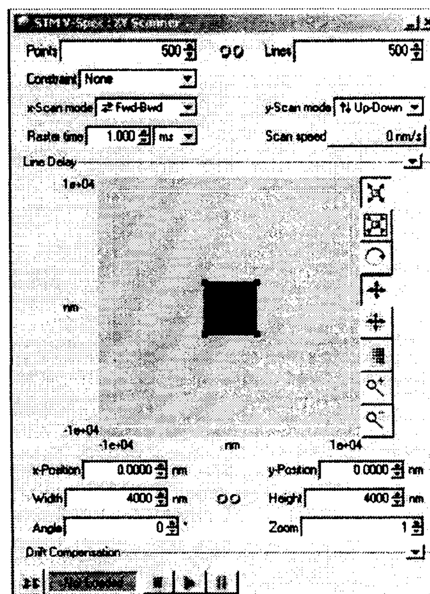

FIG. B.23. XY scanner control.

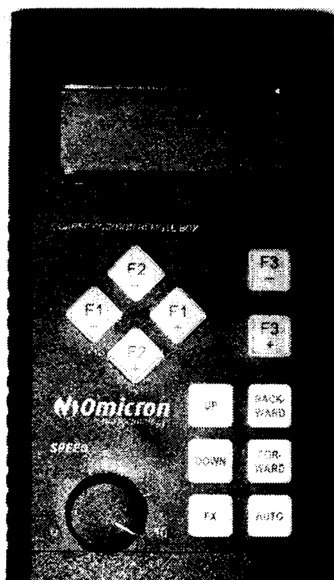

FIG. B.24. Matrix remote box.

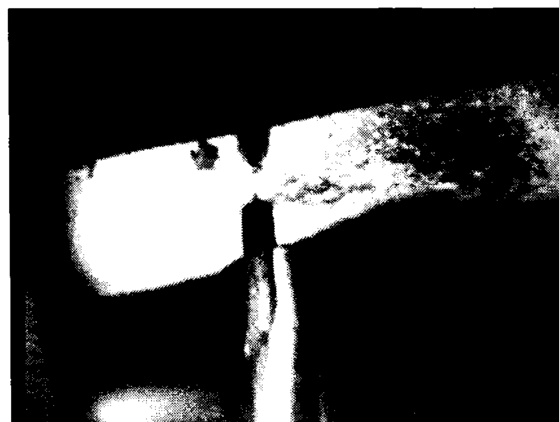

FIG. B.25. Tip approaching the sample.

Attention: The software program must have already been started and the correct experiment loaded before starting any adjustment or tip approach! Otherwise, a tip crash may be the result. Also, make sure the PPM is at its lower limit, i.e. the coarse slider stage is unlocked.

Reproduced with permission of the copyright owner. Further reproduction prohibited without permission.

Attention: The apex of a good tip cannot be resolved in an optical microscope at "x 30" magnification, i.e. it is not visible with a CD camera. In other words, the tip is normally longer than it appears. If you see the tip and its reflection from the surface touching, you have probably crashed the tip to the surface.

9. Use +Y/-Y buttons and adjust the tip position until the tip can be seen in front of the sample on the CD camera screen. You have to carefully adjust the CD camera and light source such that the sample appears bright on the screen and the tip is dark. Note: this can be quite tricky! You have to play with the light source until you achieve that.

Attention: The tip reflection can only be seen on reflecting samples. For non-reflecting sample materials keep a safe distance.

10. When the tip is at a good distance from the surface, press AUTO to activate the auto approach. Always, set the SPEED to the max value of 10 during the auto approaching process.

11. After a coarse approach the surface is only just in the reach of the tip since the coarse step width (=0.2 μm) is smaller than the z-range of the scanner (>1 μm). Hence the green tip shape of the z-meter, Fig. B.21, in the MATRIX is close to the yellow region. In order to have piezo play in both directions during scanning the green tip shape in the software Z-meter display should be in the center between the red and yellow regions. To do that, follow the following steps:

i) On the remote box set SPEED to maximum.

ii) With the remote box in forward mode watch the software z-meter.

iii) If the green tip shape is closer to yellow, switch to BACKWARD and press APPR once.

Reproduced with permission of the copyright owner. Further reproduction prohibited without permission.

iv) If the green tip shape is closer to red, switch to BACKWARD and press RETR once.

v) After each step switch to FORWARD and check the position of the green tip shape.

vi) Stop this process when the green tip shape has reached a nearly central position between yellow and red, Fig. B.21. Now you are ready for data acquisition.

B.7. Starting the STM scanning and data acquisition

A continuous scan can be started after the tip is in tunneling distance of the sample. Before you try to get small or atomic resolution you should start with large frames (> 300 nm x 300 nm) on flat samples.

1. In the scanner window choose the raster size (i.e. number of points and lines) to be measured.

2. Select frame size, frame angle, frame position and raster period time.

3. In the regulator window select a current setpoint (consult table 9 on page 64 of Omicron manual for some guiding values).

4. Do not switch the range button with the tip in tunneling condition (FORW on remote box) as this causes preamplifier relays to switch. During switching the feedback loop is undefined, which may lead to a tip crash.

5. Set a loop gain setpoint (consult table 9 on page 64 of Omicron manual for some

Reproduced with permission of the copyright owner. Further reproduction prohibited without permission.

guiding values).

6. In the Gap voltage window set a gap voltage (consult table 9 on page 64 of Omicron manual for some guiding values).

7. Start a measurement.

8. Configure the online display to suit your needs.

9. Fine-tune the loop gain and possibly the current setpoint and gap voltage.

10. To start saving measurement data check the "Store" box in the Experiment Options window.

Useful remarks:

If the obtained image does not match the expected surface structure, try adjusting the tunneling current by changing the feedback setpoint or polarity. Play with the parameters given on page 64 of the Omicron manual. You may also want to try changing the scan area by adjusting the scanner's X and Y Offset or even retracting and using the coarse motion drive.

The final solution may be changing the tip/tip material or the sample, or improving sample and tip preparation. Often additional methods along with UHV-STM operation are necessary for defining the surface condition.

STM imaging really needs patience. Sometimes, especially on relatively dirty samples, quality results are only obtained after a long period of scanning and searching for a clean area of the sample by adjusting the X and Y. Occasionally quality results are achieved at the first attempt. If this is not the case, leaving the instrument scanning a clean surface area unattended for a while may lead to a cleansing effect on the tip.

Reproduced with permission of the copyright owner. Further reproduction prohibited without permission.

B.8. Changing the tips

1. Make sure that the PPM is in its upper position.

2. Use the wobblestick to move any sample in the sample stage and store it in the carousel.

3. Use the wobblestick to move the empty tip carrier (holder) from the carousel to the sample stage. Make sure that the carrier is fully at home in the sample stage. Do not force it in. If it does not go in smoothly, remove it and start over.

4. Use the Matrix remote box to move the current tip into the empty holder. Be careful not to crash the tip. Move the tip slow enough, stop from now and then, and try to maneuver the tip to the right and to the left in order for the tip out of the holder.

5. Move the tip carrier to the carousel.

6. Fetch another tip carrier and load it into the sample stage.

7. Use the remote box to maneuver the tip down out of the carrier.

Reproduced with permission of the copyright owner. Further reproduction prohibited without permission.

APPENDIX C

USEFUL CONTACT INFORMATION

Omicron Nanotechnology			
Dave Wynia	Service Support Engineer	952-345-5244	d.wynia@omicronUS.com
Matt Roberts	Service Manager	952-345-5240	m.roberts@omicronUS.com
David Laken	Sales Engineer	704-655-8530 704-490-0334	d.laken@omicronUS.com
MDC Vacuum Products Corp.			
Richard Glazewski	Application engineer	215-822-6398	EasternVacuum@comcast.net
Amelita Camacho	Sales Administrator (MDC)	510-265-3500	ACamacho@mdcvacuum.com
Thermionics Vacuum			
Franz Witte	Regional Sales Manager	800-962-2310	franz_w@thermionics.com
Varian Inc.			
Michael Flinko	Sales Rep.	410-255-5049	mike.flinko@varianinc.com
Paul Heins	Sales Engineer	410-757-8346	paul.heins@varianinc.com
Ultrasil Corp. (Silicon vendor)*			
		800-910-0607	request_quote@ultrasil.com
Montco Silicon (Silicon vendor)*			
Kim Norris	Sales Rep.	610-948-6880	kim@silicon-wafers.com
M.T.I. Corp. (Germanium vendor)			
	Sales Rep.	510-525-3070	info@mticrystal.com
2" Ge(100), Undoped, 500 µm, single side polished			
Institute of electronic materials technology (Silicon vendor)			
M. Mroczkowska	Sales Rep.	+48228349154	malgorzata.mroczkowska@itme.edu.pl
2" Si(100), P type, B doped, 500 µm, 0.060-0.075 Ωm, cut into 10x1 mm^2 pieces, single side polished			
2" Si(111), P type, B doped, 500 µm, 0.01-0.02 Ωm, cut into 10x1 mm^2 pieces, single side polished			
Spectra Services (QICAM CCD camera vendor)			
Michael Phillips	Sales Rep.	585-265-4320	mphil@spectraservices.com

***Silicon wafers:**

Quantity	**Orientation**	**Type**	**Thick. (µm)**	**Resistivity (Ω cm)**	**Doping (cm^{-3})**
11	100	U	485-499	>>	0
5	100	P/B	500-550	10-25	6E14-1.5E15
5	100	P/B	475-575	<0.015	>6E18
11	100	P/B	475-575	0.005-0.025	3E18-1E19
25	100	N/Sb	500-550	0.025-0.05	1E17-8E17
5	111	N/As	500-550	<0.006	>8E18

Reproduced with permission of the copyright owner. Further reproduction prohibited without permission.

CURRICULUM VITA
For
MOHAMMED S. HEGAZY

DEGREES:

Master of Science (Electrical Engineering), Old Dominion University, Norfolk, VA, USA, Aug 2002.

Bachelor of Science (Physics), Cairo University, Giza, Egypt, May 1997

PROFESSIONAL CHRONOLOGY:

Department of Electrical and Computer Engineering, Old Dominion University, Norfolk, Virginia

Research Assistant, January 2000 – present
TA, spring 2000
LAN technical assistant, May 2000 – Aug 2006

Department of Physics, Cairo University, Giza, Egypt

Assistant lecturer, November 1997 – present

Micro Systems Co, New Maadi, Cairo, Egypt

Computer technical support, May 1997 – November 1997

PART TIME EMPLOYMENT:

Sphinx Co, Giza, Egypt

Computer technical support, January 1999 – December 1999

SCIENTIFIC AND PROFESSIONAL SOCIETIES MEMBERSHIP:

1. American Physical Society (APS)
2. Institute of Electrical and Electronics Engineers (IEEE/LEOS)
3. International Society of Optical Engineers (SPIE)
4. Egyptian Solid State Society

HONORS AND AWARDS:

1. Outstanding Ph.D. Research, ECE Dept., Old Dominion University (2006)
2. Supplemental Dissertation Stipend Award, Old Dominion University (2005)
3. Meredith Construction Company Scholarship, Old Dominion University (2004)
4. Highest score in Ph.D. diagnostics, ECE Dept., Old Dominion University (2003)
5. Dominion Scholarship, Old Dominion University (2000-2002)
6. Teaching Assistant of the year, ECE Dept., Old Dominion University (2000)
7. Three articles (out of seven) selected to appear on American Physical Society's Virtual Journal of Nanoscience and Technology and the Virtual Journal of Ultrafast Science

Reproduced with permission of the copyright owner. Further reproduction prohibited without permission.

COURSES TAUGHT DURING LAST FIVE YEARS:

Solid state laboratory, nuclear physics laboratory, statistical mechanics I, thermodynamics, nuclear physics, introduction to engineering

SCHOLARLY ACTIVITY COMPLETED

REFEREED JOURNAL

1. **M. S. Hegazy** and H. E. Elsayed-Ali, "Non-thermal laser induced formation of crystalline Ge quantum dots on Si(100)," Phys. Rev. Lett., *submitted.*
2. **M. S. Hegazy** and H. E. Elsayed-Ali, "Quantum-dot infrared photodetector fabrication by pulsed laser deposition technique," J. Laser Micro/Nanoengineering **1(2)**, 111 (2006).
3. **M. S. Hegazy** and H. E. Elsayed-Ali, "Growth of Ge quantum dots on Si by pulsed laser deposition," J. Appl. Phys. **99**, 054308 (2006) **[Selected to appear on the Virtual Journal of Nanoscience and Technology, Vol. 13(11) (2006)].**
4. M. A. Hafez, **M. S. Hegazy**, H. E. Elsayed-Ali, "Indium growth on Si(100)-2x1 by femtosecond pulsed laser deposition," J. Vac. Sci. Technol. A **23(6)**, 1681 (2005). **[Selected to appear on the Virtual Journal of Ultrafast Science, Vol. 4(11) (2005)].**
5. **M. S. Hegazy** and H. E. Elsayed-Ali, "Self-assembly of Ge quantum dots on Si(100) by pulsed laser deposition," Appl. Phys. Lett. **86**, 243204 (2005). **[Selected to appear on the Virtual Journal of Nanoscience and Technology, Vol. 11(24) (2005)].**
6. **M. S. Hegazy,** T. R. Refaat, M. N. Abedin, H. E. Elsayed-Ali, "Fabrication of GeSi quantum dot infrared photodetector by pulsed laser deposition," Optical Eng. Lett., **44(5)**, 59702 (2005).
7. M. K. Zayed, **M. S. Hegazy** and H. E. Elsayed-Ali, "Melting and solidification of indium nanocrystals on (002) graphite," Thin Solid Films **449**, 254-263 (2004).
8. **M. S. Hegazy** and H. E. Elsayed-Ali, "Observation of step-flow growth in femtosecond pulsed laser of Si on Si(100)-2x1," J. Vac. Sci. Technol. A **20(6)**, 2068-2071 (2002).

CONFERENCES AND MEETINGS

1. **M. S. Hegazy** and H. E. Elsayed-Ali, "Formation of Ge quantum dots by pulsed laser deposition," MRS Fall meeting (200).
2. **M. S. Hegazy** and H. E. Elsayed-Ali, "Controlling the self-assembly of Ge quantum dots grown by pulsed laser deposition," APS March meeting (2006).
3. **M. S. Hegazy,** T. R. Refaat, M. N. Abedin, H. E. Elsayed-Ali, "Quantum-dot infrared photodetector fabrication by pulsed laser deposition," 6th International Symposium on Laser Precision Microfabrication, April (2005).
4. H. E. Elsayed-Ali, M. A. Hafez, **M. S. Hegazy**, and I. El-kholy, "Real time electron diffraction studies of pulsed laser deposition," Invited talk to the Fifth International Conference on Laser Applications (ICLA), Cairo University, January (2005).

Reproduced with permission of the copyright owner. Further reproduction prohibited without permission.

5. M. A. Hafez, **M. S. Hegazy**, H. E. Elsayed-Ali, "Indium growth on Si(100) by femtosecond pulsed laser deposition," APS meeting, March (2004).
6. M. A. Hafez, **M. S. Hegazy**, H. E. Elsayed-Ali, "Growth of epitaxial two-dimensional layers of indium on Si(100) by femtosecond pulsed laser deposition," AVS 50th international symposium, November (2003).
7. **M. S. Hegazy** and H. E. Elsayed-Ali, "Femtosecond pulsed laser deposition of Si on Si(100)," CLEO (2003).
8. **M. S. Hegazy** and H. E. Elsayed-Ali, "Observation of step-flow growth in femtosecond pulsed laser deposition of Si on Si(100)-2x1," Workshop on Thin Films, Surfaces and Materials Processing, Jefferson Lab, Newport News, VA (2002).

Reproduced with permission of the copyright owner. Further reproduction prohibited without permission.